Synthesis and Application of Colloidal Substrates for In-Solution Surface Enhanced Raman Scattering

by

Casey John Rusin

A thesis submitted in partial fulfillment of the requirements for the degree of

Doctor of Philosophy

Department of Chemistry
University of Alberta

Abstract

Surface-enhanced Raman scattering (SERS) has evolved into a powerful analytical measurement technique with the potential for single molecule detection. The technological advancement of handheld Raman instrumentation is powering the development of SERS applications in a variety of industries. Moreover, it is driving the movement from laboratory-based analyses to on-site/remote analyses. As a result, a main research component from this movement is to develop compatible SERS substrates. While the market is dominated by solid-based substrates, solution-based substrates do offer some benefits. These could include low production costs, high scalability, competitive reproducibility and shorter analysis times.

The primary focus of the work in this thesis is to develop solution-based SERS substrates and explore their usage for in-solution measurements. This work highlights the development of three different types of solution-based substrates. The first substrate involves the synthesis and optimization of gold nanostars as a colloidal SERS substrate. The SERS performance is investigated and optimized using different Good's buffers, examining the buffer to gold salt concentration ratio and the use of an aggregating agent. In short, the results indicated that gold nanostars with smaller branches provided larger enhancement than those with larger branches, and this has been attributed to the Raman probe surface coverage on the nanostars rather than an electromagnetic effect. A SERS assay is also developed to quantitate methimazole in urine using a handheld Raman spectrometer.

The second and third solution-based substrates are metal decorated cellulose nanofibers, also known as plasmonic cellulose nanofibers. These chapters focus on the growth of silver and gold nanoparticles onto oxidized cellulose nanofibers, and are used as a water dispersible substrate. In the development of plasmonic cellulose nanofibers, the cellulose nanofibers have two important roles: (1) to act as a dispersant in water and (2) act as a support for metallic nanoparticles. For both substrates, centrifugation played a key role in producing significant signal enhancement. Cellulose nanofibers decorated with silver nanoparticles were used for in-solution measurements of malachite green, while cellulose nanofibers decorated with gold nanoparticles were used for in-solution measurements of methimazole. Moreover, an assay is developed to quantitate methimazole in synthetic urine with cellulose nanofibers decorated with gold nanoparticles. Measurements using plasmonic cellulose nanofibers are taken with a Raman microscope, however, examples are shown to highlight the capability of remote analysis by coupling the substrates with a handheld Raman spectrometer.

This work concludes with a comparative study between solid- and solution-based substrates. Using cellulose nanofibers decorated with gold nanoparticles, membrane- and glass- based SERS substrate are developed. This work discusses the benefits and challenges of solid- and solution-based substrates in terms of substrate development, measurement versatility and reproducibility. The primary contribution of this work is the development of multiple solution-based SERS substrates for in-solution measurements.

Preface

This thesis is an original work by Casey J. Rusin under the supervisor of Professor Mark T. McDermott and Professor Yaman Boluk. Pieces of this research have been in collaboration with others and have been published. The details for each experimental chapter are described below.

In Chapter 1, some of the instrumentation photos were taken and provided by Dr. Ahmed Mahmoud. This is specified in the figure caption throughout the chapter. The data and analysis associated with the Raman spectrometer comparison using gold nanostars was a collaborative piece with equal contribution between Dr. Mahmoud and myself (associated with Chapter 2).

Chapter 2 is reprinted and/or adapted from Mahmoud, A. Y. F.; Rusin, C. J.; McDermott, M. T. Gold nanostars as a colloidal substrate for in-solution SERS measurements using a handheld Raman spectrometer. *Analyst* **2020**, *145* (4), 1396-1407. Copyright 2020, with permission from the Royal Society of Chemistry. This chapter is a collaborative piece of work with equal contribution in its entirety between Dr. Mahmoud and myself. Manuscript writing, critical inputs, suggestions and recommendations were provided by Dr. McDermott. The synthesis of gold nanostars and extinction spectroscopy measurements were performed by Dr. Mahmoud and myself. Electron microscopy, dynamic light scattering and zeta potential measurements were performed by myself. Most of the Raman and SERS measurements were taken by Dr. Mahmoud. I was responsible for examining the impact of centrifugation on the SERS performance on the nanostars (data

not shown here). I was also responsible for a portion of the data and analysis related to the Raman spectrometer comparison (shown in Chapter 1).

Chapter 3 is reprinted and/or adapted with permission from Rusin, C. J.; El Bakkari, M.; Du, R.; Boluk, Y.; McDermott, M. T. Plasmonic cellulose nanofibers as water-dispersible surface-enhanced Raman scattering substrates. *ACS Appl. Nano Mater.* **2020**, *3* (7), 6584-6597. Copyright 2020 American Chemical Society. I was responsible for the majority of the experimental data acquisition, the data analysis and writing of the manuscript/chapter. Dr. El Bakkari was responsible for synthesizing the cellulose nanofibers and the oxidation process. The SEM image of CNF was taken and provided by Dr. El Bakkari. Dr. Du was responsible for providing critical inputs and suggestions early on in the works development. Critical inputs, suggestions and recommendations were provided by Dr. Boluk. Manuscript writing, critical inputs, suggestions and recommendations were provided by Dr. McDermott. FTIR measurements were collected by the Analytical and Instrumentation Laboratory at the Department of Chemistry. Samples for XPS were submitted and collected by the nanoFAB facility/staff. Samples for XRD were submitted to the NRC-Nano (Edmonton, AB) and collected by Steve Launspach.

I was responsible for the majority of the experimental data acquisition, the data analysis and writing of Chapter 4. Dr. El Bakkari was responsible for synthesizing the cellulose nanofibers and the oxidation process. The SEM image of CNF was taken and provided by Dr. El Bakkari. Critical inputs, suggestions and recommendations were provided by Dr. Boluk and Dr. McDermott. FTIR measurements were collected by the

Analytical and Instrumentation Laboratory at the Department of Chemistry. XPS and XRD samples were submitted and collected by the nanoFAB facility/staff.

I was responsible for the majority of the experimental data acquisition, the data analysis and writing of Chapter 5. Dr. El Bakkari was responsible for providing oxidized cellulose nanofibers. Critical inputs, suggestions and recommendations were provided by Dr. Boluk and Dr. McDermott.

Critical inputs, suggestions and recommendations were provided by Dr. McDermott, Dr. Rajput and Dr. Mahmoud regarding the future directions in Chapter 6.

Dedication

To my wife, Melanie Rusin:

Thank you for all your patience, love and support throughout all my years in school.

You are my rock throughout this process and your encouragement keeps me going!

Acknowledgements

The work in this thesis is not possible without the help and support system in the Department of Chemistry at the University of Alberta. Most importantly, I would like to thank my PhD supervisors, Dr. Mark McDermott and Dr. Yaman Boluk. I am blessed to have worked in an environment built to train phenomenal scientists. Dr. McDermott, I could not have achieved this without your help along the way. You have been patient, supportive and given continuous guidance from start to finish. This is all a student could ask for, and I am forever grateful. Dr. Boluk, 5 years ago you believed me and helped enrol in graduate studies. I am extremely grateful for giving me this opportunity. Throughout my program, you have been supportive with our weekly meetings and by asking me challenging questions to help push my research forward. Thank you, again!

I would like to thank all the members of the McDermott group, including Dr. Ahmed Mahmoud, Dr. Sunil Rajput, Thuy Nguyen, Nicole Jankovic, Taylor Lynk, Dr. Kenny Xu, Huijun Mao, Dr. Albert Cao, Khandaker Akib Shahriar, Dr. Abdelhaq Benkaddour, Dr. Rongbing Du, Dr. Greg Kaufman, Dr. Shereen Elbayomy. I thank you all for your help and support throughout my PhD program. I would like to also thank all the members of the Boluk group for their help and support. I am especially grateful for the support and guidance of Dr. Mounir El Bakkari early on in my program.

Thank you to all the staff from the Department of Chemistry, NRC-Nano and nanoFAB facilities for their support and help throughout my program.

I am extremely grateful for having the opportunity to work with a great teaching group, including Dr. Norman Gee, Dr. Greg Kiema, Dr. Charles Lucy, Dr. Mark McDermott, Dr. James Harynuk and Dr. Vladimir Michaelis. Thank you Dr. Lucy for providing me with an extraordinary teaching opportunity through the Chemical Education program. I am extremely grateful for Dr. Greg Kiema's help, support and suggestions throughout my program. Your guidance has been crucial in the development of my interpersonal skills.

I have received numerous Awards and Scholarships throughout my program and I am extremely thankful for the following: NSERC Alexander Graham Bell Canada Graduate Scholarship – Masters; Walter H. Johns Graduate Fellowship; Alberta Innovates – Technology Futures Top-Up Award; Graduate Student Association Travel Awards; Marshall Syska Chemistry Graduate Scholarship; Queen Elizabeth II Graduate Scholarship; Graduate Student Teaching Award; and Faculty of Graduate Studies and Research Travel Award. I would like to thank the Department of Chemistry, University of Alberta and all other funders/funding agencies for providing financial support throughout my program.

Thank you to my wife, Melanie Rusin, and all my family members for your support from the very beginning. Your enthusiasm and encouragement has pushed me to the finish line. I am forever indebted for your support!

Table of Contents

Abstract ..... **ii**

Preface ..... **iv**

Dedication ..... **vii**

Acknowledgements ..... **viii**

Table of Contents ..... **x**

List of Tables ..... **xvi**

List of Figures ..... **xviii**

List of Abbreviations ..... **xxii**

List of Symbols ..... **xxvi**

Chapter 1. Introduction **1**

1.1. Research Scope and Objectives 1

1.2. Raman and Surface-Enhanced Raman Scattering Theory 2

1.2.1. Raman Scattering 2

1.2.2. Surface-Enhanced Raman Scattering 3

1.2.3. SERS Enhancement Mechanisms 4

1.3. Surface-Enhanced Raman Scattering Measurements 10

1.3.1. Instrumentation for SERS Analysis 10

1.3.2. Development of SERS Substrates 17

1.4. Cellulose nanomaterials 28

1.4.1. Metal Nanoparticles on Cellulose Nanomaterials 30

1.5. Thesis Outline 31

1.6. References 34

Chapter 2. Gold Nanostars as a Colloidal Substrate for In-Solution SERS Measurements Using a Handheld Raman Spectrometer 51

2.1. Introduction 51

2.2. Experimental 54

2.2.1. Materials 54

2.2.2. Preparation of Gold Nanostars 55

2.2.3. Characterization 56

2.2.4. Raman Analysis 57

2.3. Results and Discussion 57

2.3.1. Synthesis and Characterization of AuNS using HEPES and EPPS Buffers 59

2.3.2. In-Solution SERS Performance of AuNS 63

2.3.3. Reproducibility and Additional Enhancement 68

2.3.4. Applications of AuNS for In-Solution SERS 71

2.4. Conclusions 82

2.5. References 83

Chapter 3. Plasmonic Cellulose Nanofibers as Water-Dispersible Surface-Enhanced Raman Scattering Substrates 94

3.1. Introduction 94

3.2. Experimental 97

3.2.1. Materials 97

3.2.2. Preparation of TEMPO-Oxidized Cellulose Nanofibers 98

3.2.3. Determination of Carboxyl Content of TEMPO-Oxidized Cellulose Nanofibers 98

3.2.4. Synthesis of Metal Decorated Cellulose Nanofibers 99

3.2.5. Characterization 100

3.2.6. Raman Analysis 102

3.3. Results and Discussion 103

3.3.1. Characterization of TEMPO-Oxidized Cellulose Nanofibers 103

3.3.2. Synthesis and Characterization of Plasmonic Cellulose Nanofibers 106

3.3.3. SERS Enhancement, Dispersibility and Reproducibility 115

3.3.4. Rapid In-Solution SERS Measurements 127

3.4. Conclusions 134

3.5. References 136

Chapter 4. In-Solution SERS Measurements Using Gold Nanoparticle Decorated Cellulose Nanofibers 146

4.1. Introduction 146

4.2. Experimental 149

4.2.1. Materials 149

4.2.2. Preparation of TEMPO-Oxidized Cellulose Nanofibers 149

4.2.3. Determination of Carboxyl Content of TEMPO-Oxidized Cellulose Nanofibers 150

4.2.4. Synthesis of Cellulose Nanofibers Decorated With Gold Nanoparticles 150

4.2.5. Characterization 151

4.2.6. SERS Analysis 153

4.3. Results and Discussion 154

4.3.1. Synthesis and Characterization of Gold Nanoparticle Decorated Cellulose Nanofibers 154

4.3.2. SERS Enhancement from Au-CNF 163

4.3.3. SERS Measurements and Reproducibility of Au-CNF 166

4.3.4. Measurements Using a Handheld Raman Spectrometer 177

4.4. Conclusions 180

4.5. References 182

Chapter 5. Comparison of the SERS Performance of Plasmonic Cellulose Nanofibers in Solid and Solution Format 196

5.1. Introduction 196

5.2. Experimental 198
5.2.1. Chemicals 198
5.2.2. Synthesis of Plasmonic Cellulose Nanofibers 199
5.2.3. Development of Au-CNF Planar SERS Substrates 199
5.2.4. SERS Measurements Using Solid and Solution Substrates 200
5.3. Results and Discussion 201
5.3.1. Taking Measurements on a Surface 201
5.3.2. Taking In-Solution Measurements 202
5.3.3. Performance of Solid-Based Substrates 208
5.3.4. Performance of Solution-Based SERS Substrates 216
5.3.5. Comparative Examination of Solid and Solution SERS Analysis 218
5.4. Conclusions 221
5.5. References 222
Chapter 6. Conclusion 226
6.1. Chapter Summaries 226
6.2. Future Directions 229
6.2.1. Anisotropic Nanoparticles on Cellulose Nanofibers 229
6.2.2. Specificity and Selectivity In-Solution Measurements 230
6.2.3. Other Methods for Taking Measurements In-Solution 232
6.3. References 234

Bibliography 235

List of Tables

Table 1-1. Comparison of Raman Spectrometers for the Measurement of Methimazole 13

Table 1-2. List of Companies and Handheld Raman Spectrometers Offered on the Market. 16

Table 2-1. Comparison of AuNS Synthesized using Good's Buffers for SERS Applications . 59

Table 2-2. Major Band Assignments Listed for the SERS Spectrum of 4-Mercaptobenzonitrile on AuNS 66

Table 2-3. Size and Colloidal Stability Study of AuNS Nano-Aggregates Using Dynamic Light Scattering and Zeta Potential Measurements. 71

Table 2-4. Major Bands Assignments Listed for the SERS Spectrum of Thiabendazole on AuNS..... 74

Table 2-5. Major Bands Assignments Listed for the SERS Spectrum of Malachite Green on AuNS..... 75

Table 2-6. Major Bands Assignments Listed for the SERS Spectrum of Ciprofloxacin on AuNS..... 75

Table 2-7. Major Bands Assignments Listed for the SERS Spectrum of Methimazole on AuNS..... 76

Table 2-8. Recoveries of Methimazole in Urine Using AuNS Nano-Aggregates as a SERS Substrate 81

Table 3-1. FTIR Spectroscopy Band Assignments for TEMPO-Oxidized Cellulose Nanofibers..... 105

Table 3-2. Survey Scan Data of CNF With and Without Silver Nanoparticles. 113

Table 3-3. High Resolution Data of Cellulose Nanofibers With and Without Silver Nanoparticles....113

Table 3-4. Data From the Component Fitting From the High Resolution Spectra of Cellulose Nanofibers With and Without Silver Nanoparticles.....114

Table 3-5. Determination of d-Spacing and Crystallite Size of Silver Nanoparticles on Cellulose Nanofibers From XRD Data.....115

Table 3-6. Summary of Colloidal SERS Substrates for In-Solution Measurements and Applications 116

Table 3-7. Summary of SERS Substrates and Their Performance for the Detection of Malachite Green.....133

Table 4-1. Infrared Spectroscopy Band Assignments for TEMPO-Oxidized Cellulose Nanofibers 157

Table 4-2. X-Ray Photoelectron Spectroscopy Survey Scan Data of CNF and Au-CNF.....161

Table 4-3. Determination of d-Spacing and Crystallite Size of Gold Nanoparticles on Cellulose Nanofibers From XRD Data.....163

Table 4-4. Major Bands Assignments Listed for the SERS Spectrum of 4-Mercaptobenzonitrile on Au-CNF.....165

Table 4-5. Band Assignments for the SERS Spectrum of Rhodamine 6G using Au-CNF.....170

Table 4-6. Band Assignments for the SERS Spectrum of Thiabendazole Using Au-CNF.....171

Table 4-7. Band Assignments for the SERS Spectrum of Methimazole Using Au-CNF.....172

Table 4-8. Percent Recovery of Methimazole in Urine Using Au-CNF 177

Table 4-9. Band Assignments for the SERS Spectrum of Malachite Green Using Au-CNF..180

List of Figures

Figure 1-1. Illustration of the SERS electromagnetic enhancement. 6

Figure 1-2. Illustration of the SERS chemical enhancement. 9

Figure 1-3. Photos of different Raman spectrometers. 12

Figure 1-4. SERS spectra of methimazole (1.15 μM) in water using different Raman spectrometers. 13

Figure 1-5. Handheld Raman spectrometers and their different adapters. 17

Figure 1-6. Nanosphere lithography. 19

Figure 1-7. Inkjet-printed SERS substrates. 22

Figure 1-8. Schematic demonstrating a method for controlled aggregation for in-solution SERS. 27

Figure 1-9. Illustration of the chemical and physical structure of cellulose. 29

Figure 2-1. Schematic of AuNS synthesis using Good's buffers (HEPES and EPPS). 58

Figure 2-2. Extinction spectra and TEM imaging of AuNS using Good's buffers at different [buffer] to [$HAuCl_4$] ratios. 61

Figure 2-3. UV-Vis spectrum of citrate capped gold nanoparticles (30 nm). 61

Figure 2-4. Size distribution analysis and TEM imaging of AuNS. 62

Figure 2-5. AuNS SERS optimization based on buffer type and [buffer] to [$HAuCl_4$] ratio. 65

Figure 2-6. Solution Raman spectra of water, EPPS and HEPES buffer. 66

Figure 2-7. SERS reproducibility and long-term storage of colloidal AuNS. 69

Figure 2-8. Additional SERS enhancement using NaCl. 70

Figure 2-9. Applications for in-solution SERS measurements using AuNS..... 73

Figure 2-10. Quantitation of MTZ using colloidal AuNS..... 78

Figure 2-11. Raman spectrum of solid methimazole..... 79

Figure 2-12. In-solution SERS spectrum of methimazole in urine and associated control spectra..... 81

Figure 3-1. Synthesis of cellulose nanofibers decorated with silver nanoparticles..... 100

Figure 3-2. Characterization of TEMPO-oxidized cellulose nanofibers..... 104

Figure 3-3. Conductometric titration of cellulose nanofiber carboxyl content..... 106

Figure 3-4. UV-Vis extinction optimization of Ag-CNF..... 107

Figure 3-5. SERS spectroscopy optimization of Ag-CNF. 108

Figure 3-6. Characterization of Ag-CNF synthesis using IR, UV-Vis extinction and SEM imaging..... 110

Figure 3-7. XPS and XRD analysis of CNF and Ag-CNF..... 111

Figure 3-8. XPS survey spectra of CNF and Ag-CNF..... 112

Figure 3-9. XPS high resolution spectra..... 112

Figure 3-10. Plasmonic cellulose nanofiber enhancement. 119

Figure 3-11. SERS spectra of MBN at 5 μM demonstrating the effect of substrate aging on the enhancement of plasmonic cellulose nanofibers..... 121

Figure 3-12. UV-Visible extinction of Ag-CNF at 0 hour and 72 hour..... 122

Figure 3-13. SERS spectra of MBN demonstrating the stability of Ag-CNF being stored as a pellet in the refrigerator (4 °C) over time. 122

Figure 3-14. SERS capability and reproducibility..... 123

Figure 3-15. UV-Visible extinction of commercial Ag NPs at different NaCl concentrations. 125

Figure 3-16. In-solution measurements using Ag-CNF. 128

Figure 3-17. SERS controls and powder spectra. 130

Figure 3-18. Analytical measurements using Ag-CNF. 132

Figure 3-19. SERS measurements of MG (0.1 nM to 1000 nM) in Ag-CNF solution. 132

Figure 4-1. Synthesis schematic for cellulose nanofibers decorated with gold nanoparticles. 151

Figure 4-2. Images of the Renishaw inVia Raman microscope and B&W Tek TacticID handheld Raman spectrometer. 154

Figure 4-3. Cellulose nanofibers size analysis. 155

Figure 4-4. Infrared spectroscopy of oxidized cellulose nanofibers with and without gold nanoparticles. 156

Figure 4-5. Extinction spectra of gold nanoparticle decorated on cellulose nanofibers, gold nanoparticles synthesized with ascorbic acid and controls. 159

Figure 4-6. Electron microscopy characterization of colloidal Au-CNF. 160

Figure 4-7. X-ray spectroscopy analysis of Au-CNF. 161

Figure 4-8. X-ray diffraction spectra of CNF and Au-CNF. 162

Figure 4-9. SERS capability of Au-CNF. 164

Figure 4-10. Reproducibility of colloidal Au-CNF substrates. 167

Figure 4-11. Applications of Au-CNF for SERS measurements. 169

Figure 4-12. Quantitation of methimazole using colloidal Au-CNF. 174

Figure 4-13. Enhancement factor from colloidal Au-CNF. 175

Figure 4-14. Quantitation of methimazole in urine. 177

Figure 4-15. Potential applications for colloidal Au-CNF using a handheld Raman spectrometer....179

Figure 5-1. Schematic of the development of Au-CNF solid-based SERS substrates. 200

Figure 5-2. Schematic of the experimental procedure for solid-based substrates. 202

Figure 5-3. Schematic of experimental procedure for solution-based substrates. 203

Figure 5-4. Containers for solution analysis. Raman spectra of ethanol in a quartz cuvette and glass vial using a 633 nm and 785 nm laser. 204

Figure 5-5. Liquid cell adapter components. 205

Figure 5-6. Initial placement of solution containers into the Raman spectrometer. 206

Figure 5-7. Alignment of the laser on the vial. 208

Figure 5-8. SERS performance spectrum treatment. 209

Figure 5-9. 3D plots of the SERS spectrum for rhodamine 6G (7 nmol) from Au-CNF (0.4 mL) deposited onto different types of membranes.. 210

Figure 5-10. 3D plots of the SERS spectrum for rhodamine 6G (7 nmol) from Au-CNF (2 mL) deposited onto different types of membranes. 213

Figure 5-11. Raman spectra of rhodamine 6G (7 nmol) from Au-CNF deposited onto glass slides. 216

Figure 5-12. In-solution analysis of rhodamine 6G (5 μM) using Au-CNF. 217

Figure 6-1. Introducing selectivity for in-solution measurements using colloidal plasmonic cellulose nanofibers. 232

List of Abbreviations

AA	L-ascorbic acid
AEF	Analytical enhancement factor
Ag	Silver
Ag-CNF	Cellulose nanofibers decorated with silver nanoparticles
$AgNO_3$	Silver nitrate
Ag NPs	Silver nanoparticles
AFM	Atomic force microscopy
ASH	Average-shifted histogram
Au	Gold
Au-CNF	Cellulose nanofibers decorated with gold nanoparticles
AuNS	Gold nanostars
BCTMP	Bleached chemi-thermo mechanical pulp
CCD	Charged coupled device
Cipro	Ciprofloxacin
CNC	Cellulose nanocrystals

CNF	Cellulose nanofibers
COO^-	Carboxylate
COOH	Carboxylic acid
CPS	Counts per second
CTAB	Cetrimonium bromide
Cu	Copper
DI	Deionized
DLS	Dynamic light scattering
DNA	Deoxyribonucleic acid
EPPS	4-(2-hydroxyethyl)-1-piperazinepropanesulfonic acid
FON	Film over the nanosphere
FTIR	Fourier transform infrared
$HAuCl_4$	Chloroauric acid
HCl	Hydrochloric acid
HeNe	Helium neon
HEPES	4-(2-hydroxyethyl)-1-piperazineethanesulfonic acid
IR	Infrared

LOD	Limit of detection
LOQ	Limit of quantification
LSPR	Localized surface plasmon resonance
MBN	4-mercaptobenzonitrile
MG	Malachite green
MOPS	3-(N-morpholino)propanesulfonic acid
MRL	Maximum residue limit
MRPL	Minimum required performance limit
MTZ	Methimazole
NaCl	Sodium chloride
NaBr	Sodium bromide
NaOCl	Sodium hypochlorite
NaOH	Sodium hydroxide
Ni	Nickel
NP	Nanoparticles
PAH	Polycyclic aromatic hydrocarbon
Pd	Palladium

PDI	Polydispersity index
Pt	Platinum
PVDF	Polyvinylidene fluoride
PVP	polyvinylpyrrolidone
RSD	Relative standard deviation
R6G	Rhodamine 6G
SEM	Scanning electron microscopy
SERS	Surface enhanced Raman scattering
SILAR	Successive ionic layer adsorption and reaction
TBZ	Thiabendazole
TEM	Transmission electron microscopy
TEMPO	2,2,6,6-tetramethylpyperidine-1-oxyl
US EPA	United States Environment Protection Agency
UV-Vis	UV-Visible
XPS	X-ray photoelectron spectroscopy
XRD	X-ray diffraction

List of Symbols

λ_{max}	Absorption band maximum
R	[buffer]/[$HAuCl_4$] ratio
cm	Centimeter
R^2	Coefficient of determination
c	Concentration
°	Degree
°C	Degree Celsius
ε	Dielectric constant
E	Electric field
eV	Electron volts
g	Gram
h	Hour
μ_{ind}	Induced dipole moment
I	Intensity
kV	Kilovolts

kJ mol^{-1}	Kilojoules per mole
MΩ•cm	Mega ohm centimeter
µL	Microliter
µm	Micrometer
mL	Milliliter
mW	Milli watts
min	Minute
µM	Micromolar
mM	Millimolar
mmol	Millimole
mV	Millivolts
M	Molar
mol	Moles
nm	Nanometer
nM	Nanomolar
nmol	Nanomole
N or n	Number of samples

ppb	Parts per billion
%	Percent
pM	Picomolar
α	Polarizability
rpm	Revolutions per minute
θ	Theta
cm^{-1}	Wavenumber
Wt.%	Weight percent

Chapter 1. Introduction

1.1. Research Scope and Objectives

Surface-enhanced Raman scattering (SERS) is a continuously developing qualitative and quantitative measurement technique with the capability of single molecule detection.[1-4] A major component of SERS is the development of SERS substrates. Many different types of SERS substrates have been fabricated and used for chemical sensing.[5] The opportunities for SERS substrate development remain open and continue to diversify. For example, paper- and cellulose-based substrates have drawn a lot of attention as of late.[6] The popularity around paper- and cellulose-based substrates are attributed to the abundance of cellulose, ease of surface functionalization, the ease of synthesizing nanoparticles onto the substrate, its biocompatibility, and its biodegradability.[6] Moreover, these paper-based substrates can be utilized in different ways for measurements, such as dipping in solution, or swabbing a contaminated surface.[7] Up until now, the majority of these substrates are used as a solid-based substrate. However, cellulose-based substrates could also be effective for in-solution measurements, but requires further investigation.

The motivation of this thesis is to develop colloidal SERS substrates for rapid and reproducible in-solution measurements. The work in this thesis strives to show the potential of solution-based substrates to provide qualitative and quantitative measurements, and their potential with a handheld Raman spectrometer. The experimental research objectives of this thesis are: (1) optimization of gold nanostars as an in-solution

SERS substrate; (2) development of a water dispersible SERS substrate using cellulose nanofibers decorated with silver nanoparticles for the detection of malachite green; (3) detection and quantitation of methimazole in synthetic urine using cellulose nanofibers decorated with gold nanoparticles; and (4) comparison and discussion of solid-based and in-solution SERS measurements using plasmonic cellulose nanofibers.

This chapter introduces background information and the fundamentals of Raman scattering and SERS. There is a focus on comparing different types of instrumentation and SERS substrates with an emphasis on colloidal substrates. Additionally, background information of cellulose nanomaterials is reviewed with a focus on cellulose nanofibers and metal decorated cellulose nanofibers.

1.2. Raman and Surface-Enhanced Raman Scattering Theory

1.2.1. Raman Scattering

Chandrasekhara Venkata Raman discovered the Raman scattering phenomenon in 1928, and was awarded a Nobel Prize in Physics for the discovery in 1930.[8-9] The different types of scattering can be used to describe this phenomenon. When a photon interacts with a molecule, the oscillating electric field from electromagnetic radiation creates a short lived distortion of the molecule's electron cloud producing a "virtual state".[10] When the resulting scattered photon is at the same frequency as the incident photon it is called Rayleigh scattering.[10] Rayleigh scattering is an elastic scattering phenomenon. On the other hand, when the scattered photon is at a different frequency than the incident photon it is called Raman scattering.[10] Raman scattering is an inelastic scattering phenomenon. The

frequency shift in Raman scattering is equal to a molecular vibrational transition.[10] In order for this transition to occur, there must be a change in polarizability.[10]

Raman spectroscopy has established itself as a useful technique in a variety of applications due to technological advancements in diode lasers and charge coupled devices (CCD) in the 1980s.[10] Raman spectroscopy continues to be used today for the investigation of art history and archaeology, the detection of explosives, the identification of narcotics and airport/border security.[11-13] Advantages and appealing features of Raman scattering include: (1) non-invasive technique; (2) compatible with aqueous samples; (3) provides chemical information about the sample; (4) narrow linewidths that provide multiplex capabilities; (5) easy and minimal sample preparation; and (6) remote analysis capabilities.[3, 10] However, there are two main problems that continue to plague Raman spectroscopy as a technique. First, Raman spectroscopy is considered a weak scattering technique where only one in ten million photons are Raman scattered.[14] Second, Raman scattering is approximately 10^6 to 10^{10} less efficient than fluorescence and is often overwhelmed by its interference.[3]

1.2.2. Surface-Enhanced Raman Scattering

Surface-enhanced Raman scattering (SERS) is a technique employed to amplify weak Raman scattering by several orders of magnitude. Extremely large enhancements (up to 10^{10}) and the capability for single molecule detection have empowered the evolution of SERS into an analytical measurement technique.[1-2, 4, 15]

The discovery of SERS dates back to 1974 when Fleischmann et al. were investigating the adsorption of pyridine on silver electrodes using Raman spectroscopy.[16]

The increased Raman intensities were attributed as a surface adsorption effect from an increase in surface area due to electrochemical surface roughening of the electrode.[16] A few years later two independent research groups deemed the increase in surface area cannot be the only cause for such intensity increases, and other enhancement phenomena must be responsible.[17-18] Jeanmarie and Van Duyne studied heterocyclic, aromatic, and aliphatic amines adsorbed on anodized silver electrodes, and concluded the Raman enhancement was caused from an electric field enhancement mechanism.[17] Concurrently, Albrecht and Creighton proposed a chemical surface effect upon the adsorption of pyridine to the metal surface.[18] The interaction between the surface plasmon from the metal and the adsorbed pyridine causes broadening the molecular electronic energy levels, thus resulting in an increase in the molecular Raman scattering cross-section.[18] A year later, Moskovits proposed that the enhancement is from the optical conduction resonance of surface electrons from bumps on a metal surface.[19-20] These works have led to the acceptance of two enhancement mechanisms within the scientific community: an electromagnetic and chemical enhancement mechanisms.[3, 21]

1.2.3. SERS Enhancement Mechanisms

SERS enhancement is a result of an interaction between light and matter, and an interaction between light and a metal nanostructure.[21] As noted above, there are two enhancement mechanism: (1) electromagnetic and (2) chemical enhancement. These mechanisms stem from the relationship between the Raman scattering intensity (I) and the square of the induced dipole moment (μ_{ind}).[15] An induced dipole moment is the product of the Raman polarizability (α) and the strength of the incident electromagnetic field (E).[15]

SERS enhancement mechanisms have been described and discussed extensively throughout the literature.[3, 15, 21] The following section will highlight the key aspects associated with the electromagnetic and chemical enhancement mechanisms in SERS.

The electromagnetic enhancement considered the most prominent mechanism in SERS. Figure 1-1A is a schematic demonstrating the electromagnetic enhancement mechanism in SERS using a gold nanoparticle.[21] When an incident electromagnetic wave interacts with a metal nanostructured surface, it produces a charge separation and an oscillation of the metal's surface conduction electrons.[21] This effect is called the localized surface plasmon resonance (LSPR). The LSPR is dependent on many factors including the dielectric functions of the metal (ε_{metal}) and the surrounding medium (ε_m).[21] As mentioned in the previous paragraph, the SERS enhancement mechanisms are a result of the Raman scattering intensity and the square of the induced dipole moment.[15] Mathematically, the strength of the induced dipole moment is demonstrated as in Equation 1-1:[21]

$$\boldsymbol{E}(\boldsymbol{\omega_{inc}})\colon \mu_{\boldsymbol{ind}} = \boldsymbol{\alpha_{metal}}\boldsymbol{E_0}(\boldsymbol{\omega_{inc}}) \quad \textbf{(Equation 1-1)}$$

where $E_0(\omega_{inc})$ is the incident electric field strength, μ_{ind} is the induced dipole moment, and α_{metal} is the polarizability of the metal.[21] Therefore, it is the incoming electric field strength and the polarizability of the metal that dictates the induced dipole moment strength.[21] Figure 1-1 demonstrates the interaction of a gold nanoparticle with incoming electromagnetic radiation (in green).[21] In turn, results in a charge separation and amplification in the local electric field around the metal nanoparticle.[21]

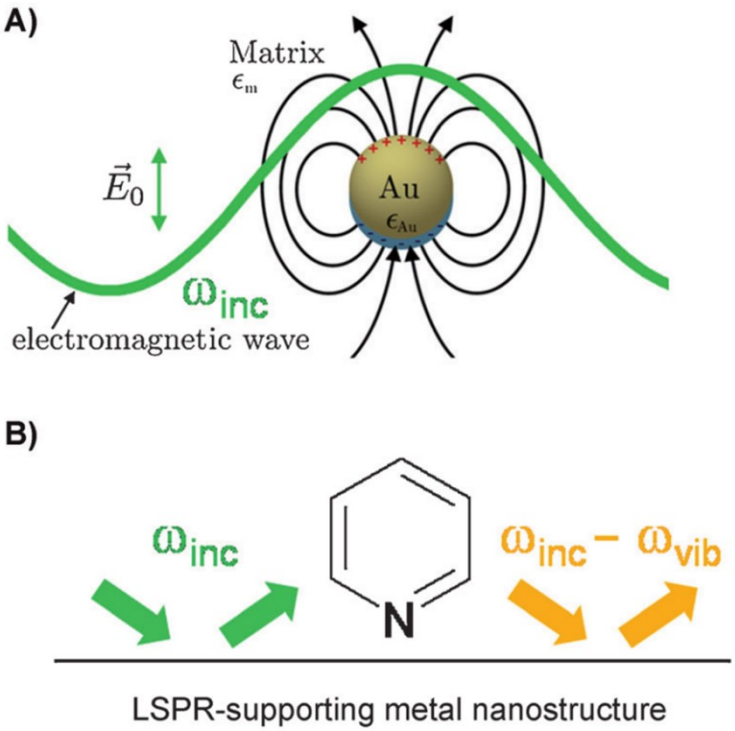

Figure 1-1. Illustration of the SERS electromagnetic enhancement. (A) Excitation of the localized surface plasmon resonance (LSPR) of a gold nanoparticle when interacting with electromagnetic radiation. (B) Enhancement of the "incoming" (ω_{inc}, green) and the "outgoing" field ($\omega_{inc} - \omega_{vib}$, orange) by elastic light scattering from the LSPR of a metallic nanostructure. Reprinted from Schlücker, S., Surface-Enhanced Raman Spectroscopy: Concepts and Chemical Applications. *Angew. Chem. Int. Ed.* **2014**, 53 (19), 4756-4795. Copyright 2014, with permission from John Wiley and Sons.[21]

Another important aspect to consider is the interaction between the electric field and the molecule at the nanoparticle surface.[21] Figure 1-1B is a schematic that illustrates this interaction with pyridine at the surface of a gold nanoparticle.[21] Similar to the scenario described above, molecules at the surface of a nanoparticle also experience induced dipole moment, and results in the inelastic scattering of the incident light.[21] This is described as $\omega_{inc} - \omega_{vib}$ in Figure 1-1B (in orange). This suggests that the SERS intensity is dependent on the incoming (ω_{inc}) and outgoing electric fields ($\omega_{inc} - \omega_{vib}$), and is mathematically expressed as:[21]

$$\boldsymbol{I_{SERS} = I_{inc}(\omega_{inc})I(\omega_{inc} - \omega_{vib}) = |E_{inc}(\omega)_{inc}|^2|E(\omega_{inc} - \omega_{vib})|^2} \quad \textbf{(Equation 1-2)}$$

Using Equation 1-2, when the ω_{inc} and $\omega_{inc}-\omega_{vib}$ radiation are close in value, the SERS enhancement is approximately $\sim E^4$.[21] This is called the E^4 approximation.

There are other important factors related to the incident laser wavelength and the metal nanostructure for SERS measurements. For example, a wavelength dependence for the LSPR exists, and ideally, the LSPR wavelength from the nanoparticle should be close to that of the excitation wavelength.[22] Van Duyne and co-workers have demonstrated that the largest SERS enhancements are when the excitation wavelength is blue-shifted from the LSPR wavelength of the nanoparticle.[23]

Another important factor related to SERS enhancement is a distance dependency. It is known that the field enhancement for a spherical nanoparticle decays with r^{-3}, where r is the distance from the surface to the adsorbate.[15, 21] Considering the E^4 approximation, the distance dependency scales by a factor of r^{-12}.[15, 21] Additionally, it is important to consider the increased surface area scaling (r^2) due to adsorbed molecules, and this results in a distance dependency of r^{-10}.[15] The distance dependency is shown mathematically in Equation 1-3:[15]

$$\boldsymbol{I_{SERS} = \left(\frac{a+r}{a}\right)^{-10}} \quad \textbf{(Equation 1-3)}$$

where I_{SERS} is the SERS intensity, a is the average size of the field-enhancing features on the surface and r is the distance between the surface and adsorbate.[15] The SERS intensity decreases by a factor of 10 when the distance between the surface and the adsorbate is ~3 nm.[15, 22] This highlights the importance of the molecule being located at the nanoparticle surface.

The formation of hot spots is another aspect to consider for the electromagnetic enhancement in SERS. Hot spots are highly spatially localized regions in between nanoparticles and are responsible for producing very large field enhancements.[21] In the case of a dimer, large field enhancements are produced because the electric field becomes polarized along the main axis of the dimer.[3] The strongest field enhancements are observed when a molecule is placed exactly in the gap between the two nanoparticles.[21] However, the likelihood of this happening is low.[21] A more moderate enhancement is generally observed from a molecule somewhere on one of the nanoparticles, rather than being exactly between them.[21] Finally, it is important to note that hot spots not only occur in the gaps between nanoparticles, but also at and in between sharp tips and edges.[3, 21] This is discussed further later in the chapter.

As previously noted above, SERS enhancement is governed by two enhancement mechanisms. The first mechanism, the electromagnetic mechanism, was discussed above. The second SERS enhancement mechanism is a chemical enhancement. The chemical enhancement mechanism is correlated to the electronic properties of the adsorbate, and is the result of an increase in molecular polarizability and change in the molecule's Raman cross-section.[21] The chemical enhancement mechanism can be described with three processes, which are molecular excitation resonances, charge-transfer resonances and nonresonant changes in the molecular polarizability upon adsorption onto the metal surface.[24-27] A charge-transfer mechanism is used to generalize and explain the chemical enhancement contribution in SERS, and is illustrated in Figure 1-2.[28] In this schematic, the metal and adsorbate create a complex where the molecular orbital energy is close to the metal's Fermi level.[28] The interaction of light with metal–adsorbate complex leads to the

formation of electron-hole pairs (Figure 1-2A).[28] The electron tunnels to the adsorbate through a charge transfer transition, and results in a molecular vibrational change (Figure 1-2B and 1-2C).[28] Electron relaxation back to the metal, or electron-hole recombination produces a Raman scattered photon with vibrational information of the adsorbate (Figure 1-2D).[28]

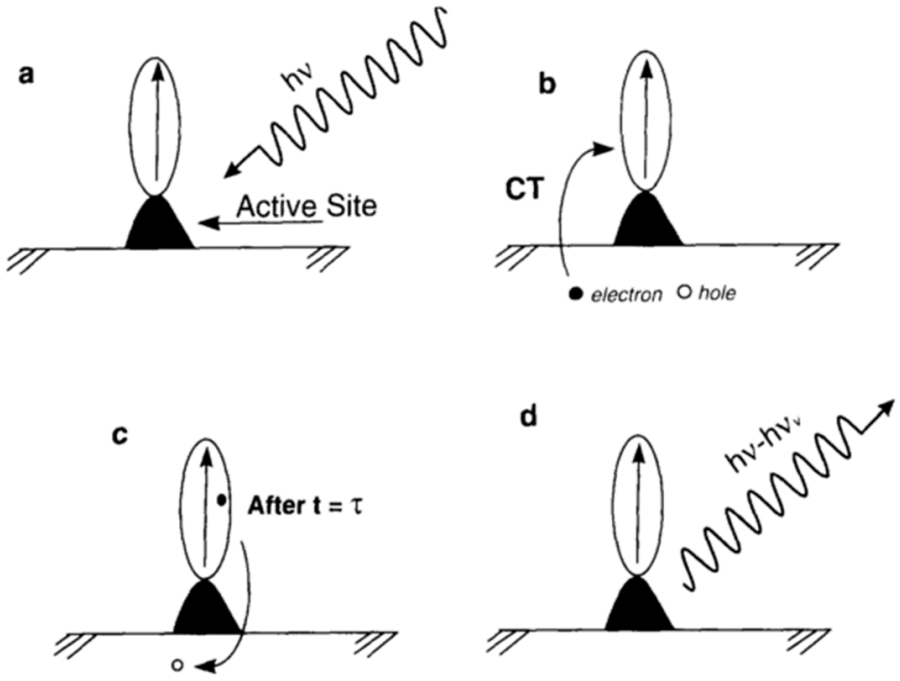

Figure 1-2. Illustration of the SERS chemical enhancement. (A) The interaction between radiation and a molecule adsorbed to metallic nanostructure active site leads to the formation of an electron-hole pair. (B) An electron is transferred from the metal nanostructure to the molecule. (C) If the transferred electron remains in the molecule long enough for a vibrational change, then this information is transferred when the electron tunnels back to the metal. (D) A Raman photon is created with an electron-hole recombination. Reprinted from Brolo, A. G.; Irish, D. E.; Smith, B. D., Applications of surface enhanced Raman scattering to the study of metal-adsorbate interactions. *J. Mol. Struct.* **1997**, 405 (1), 29-44. Copyright 1997, with permission from Elsevier.[28]

In summary, this section discussed the electromagnetic and chemical enhancement mechanisms in SERS. The electromagnetic enhancement mechanism is the primary mechanism with enhancement contributions of 10^4 to 10^8 orders.[15] The chemical

enhancement mechanism, which is equally important but to a lesser effect, has shown enhancement contributions of up to 10^2 orders.[15] Overall, these mechanisms together can result in SERS enhancement factors as high as the 10^9 to 10^{10} range.[15]

1.3. Surface-Enhanced Raman Scattering Measurements

There are two main components required to perform SERS measurements effectively: a Raman spectrometer and SERS substrates. The following sections provide an overview on the types of instrumentation and SERS substrates used for SERS measurements.

1.3.1. Instrumentation for SERS Analysis

The type of instrumentation for analysis is often a choice many do not have, and the instrument owned or available is the one used for measurements. Given the choice, there are many different types of spectrometers with many secondary options available. As an example, Figure 1-3 shows three photos of different Raman spectrometers that could be used for SERS measurements. These instruments differ vastly in cost and application. Figure 1-3A is a photo of a Renishaw inVia Raman microscope. This is an expensive and large instrument (see business cards at top of instrument for scale) that cannot be easily moved from lab to lab. It can be equipped with multiple lasers, different polarizers, different objectives and measurement setups. While it must remain stationary, there is a lot of versatility available with this type of Raman spectrometer.

Figure 1-3B is a photo of a benchtop DeltaNu Advantage NIR spectrometer. This instrument is a much smaller spectrometer in comparison to the microscope (use quarter to gauge size). This is a semi-stationary spectrometer that can easily be transported

between labs, however is not suitable for field or on-site analysis. It requires to be on a flat stable surface, and needs to be plugged into an outlet in order to function. This spectrometer can be equipped with different measurement stages for liquid and solid phase analysis. An instrument this size typically is only equipped with a single laser wavelength source.

Figure 1-3C is a photo of a B&W Tek TacticID handheld Raman spectrometer. This instrument is versatile in that it can be used in the lab, or for on-site analysis. It is intended to be held in your hand and easily transportable in a case or bag. A handheld Raman is usually battery powered. Similar to the benchtop, handheld Raman devices are usually equipped with a single laser wavelength source. These devices are also compatible with a variety of different attachments for liquid and solid phase measurements. These will be expanded on later in this chapter.

There are certainly pros and cons to using different types of Raman spectrometers. Above, the size and measurement capability beyond the laboratory were highlighted. It is important to note that there are other factors that impact the performance of the measurement and results. These include the type of laser and wavelength, the type of detector, the spectral resolution and the instrument optics.

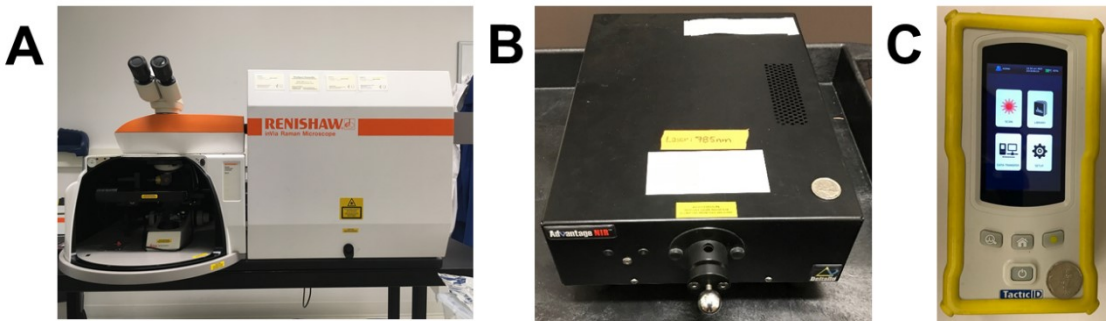

Figure 1-3. Photos of different Raman spectrometers. (A) Renishaw inVia Raman microscope. Business cards near the top of the instrument can provide insight about the instrument size. (B) Benchtop DeltaNu Advantage NIR spectrometer. (C) B&W Tek TacticID handheld Raman spectrometer. A 25¢ coin (quarter) is used to provide insight about the scale of (B) and (C). Photos for (B) and (C) are taken and provided by Dr. Ahmed Mahmoud.

An example of performance comparison between Raman spectrometers is shown in Figure 1-4. This is a qualitative comparison of the in-solution SERS spectrum of methimazole using a Renishaw inVia Raman microscope, a DeltaNu benchtop Raman spectrometer and a B&W Tek TacticID handheld Raman spectrometer. Gold nanostars were used as the SERS substrate (Chapter 2), and the concentration and volume of the gold nanostars are identical for each sample. Other sample conditions such as methimazole concentration, the total sample volume, the final NaCl concentration and mixing times were held constant to ensure consistency across each instrument. In Figure 1-4, the spectrum for each instrument has been normalized for the power and acquisition time. It is common to plot SERS spectra with units of counts/mW•s. Figure 1-4 indicates that instrumentation has some impact on the measurement performance. Table 1-1 summarizes the instrument parameters and measurement results. The Renishaw inVia microscope provides the highest peak intensities, while those from the DeltaNu benchtop and B&W Tek TacticID handheld are significantly less intense. A multiplier (×5) has been applied to the spectra for

the benchtop and handheld to demonstrate the detection and appearance of enhanced Raman bands.

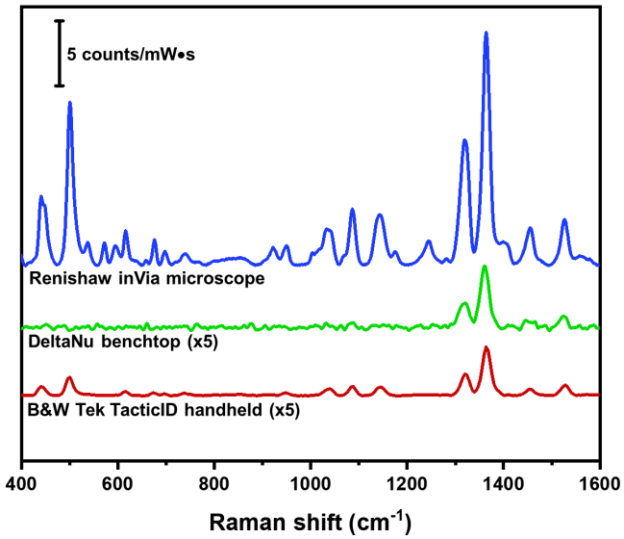

Figure 1-4. SERS spectra of methimazole (1.15 µM) in water using different Raman spectrometers. The same conditions, including the sample concentration, sample volume, NaCl concentration and mixing times were kept constant. Each instrument used a 785 nm laser. The spectra were normalized in terms of laser power and acquisition time. In collaboration with Dr. Ahmed Mahmoud.

Table 1-1. Comparison of Raman Spectrometers for the Measurement of Methimazole

		Instruments		
		Renishaw	**DeltaNu**	**TacticID***
Parameters	**Power (mW)**	115 ± 1	37 ± 1	300.0 ± 0.2
	Time (s)	15	10	N/A*
	Laser spot size (µm²)	26	491	7854
	Power density (mW/µm²)	4.4	0.076	0.038
Measurement at 1364 cm⁻¹ [a]	**Intensity (Counts/mW•s)**	18 ± 1	1.00 ± 0.07	0.75 ± 0.04
	Intensity (Counts•µm²/mW•s)	466 ± 28	493 ± 33	5915 ± 320
	%RSD	6	7	5

*TacticID does not allow user to set the acquisition time. The time varies from sample to sample, however, can be noted and accounted for in the data treatment. [a]Based on three samples measured at three different locations on the vial (n=9). In collaboration with Dr. Ahmed Mahmoud.

Peak intensity measurements at 1364 cm^{-1} indicate that the microscope provides peaks that are 18× and 24× more intense than the benchtop and handheld, respectively. However, the measurement setup (i.e., collection optics) and laser spot size have not been accounted for in these measurements. The comparison will never be completely fair as the optical setup from each instrument will differ. That being said, it is difficult to account for these differences as they are usually protected by the vendor's intellectual property rights. As for the laser spot size, it varies from instrument to instrument as shown in Table 1-1. This inherently impacts the power density of the laser at the sample. It usually uncommon and overlooked to normalize the intensity in terms of power density. Table 1-1 makes this comparison and significantly changes the peak intensities. In units of counts•μm^2/mW•s the handheld provides peak intensities that are 13× and 12× more intense than the microscope and benchtop, respectively. In this case, the handheld provides the largest signal intensities. Moreover, it is worth noting that the percent relative standard deviation is relatively consistent amongst the different instruments. The point of this comparison was to demonstrate that different instruments provide different results based on their specific parameters and measurement scenarios, that and each has its pros and cons. This thesis highlights the importance of being able to synthesize and optimize SERS substrates using expensive laboratory based equipment like a Raman microscope, and then use the substrate with a less expensive handheld Raman for remote analysis.

Handheld Raman spectrometers are more than capable of being coupled with SERS substrates for remote measurements and analysis. Given that larger laboratory-based instruments are expensive (>$100,000), purchasing a handheld Raman spectrometer for academic and industrial purposes in and out of the lab is a feasible option. There are many

options available on the market. Table 1-2 is a short list of some of the handheld Raman spectrometers available on the market. There are many options with varying costs (~tens of thousands of dollars). The range in instrument cost likely comes down to specific features that are often protected by the vendor's intellectual property rights. For example, the Bruker BRAVO handheld contains specialized technology such as Sequentially Shifted Excitation (SSE™, patented fluorescence mitigation), Duo LASER™ Excitation and IntelliTip™ (automated measuring tip recognition). There is some commonality amongst all the manufacturers when it comes to selling their spectrometers. These descriptors include: user-friendly/minimal training, rugged, versatile, transportability, fast identification, on-board validation and calibration, extensive libraries, reproducible data acquisition, Wi-Fi capabilities, document tracking and the detection of coloured samples, detection through packaging. Moreover, almost all manufacturers claim their device is compliant with management systems and good manufacturing practices to some extent. Also, many companies have also developed devices tailored for law enforcement, border security, hazmat response, etc. For example, the B&W Tek TacticID®-N Plus was specifically designed for forensic analysis of narcotics. It is important to consider the purpose and functionality of the device, and whether specific parameters such as laser wavelength, instrument size, adapter compatibility, etc. are suitable for the intended purpose, i.e. SERS analysis.

Table 1-2. List of Companies and Handheld Raman Spectrometers Offered on the Market

Company	Devices
Agilent	Resolve[29], Vaya[30]
Anton Paar	Cora 100[31]
B&W Tek	NanoRam®-1064[32], NanoRam®[33-34], TacticID®-1064[35], TacticID®-N Plus[36], TacticID®-GP Plus[37]
Bruker	BRAVO[38]
Metrohm	Mira DS[39-40], Mira P[41]
Rigaku	Models: Basic, Flex, Advanced Progeny ResQ[42], Progeny ResQ FLX[43], ResQ CQL[44], Progeny[45]
SciAps	CHEM-500[46], CHEM-200[47], Inspector 500[48], Inspector 300[49], ReporteR[50], ObserveR[51]
ThermoFisher Scientific	TruScan RM[52-53], TruNarc[54-55], FirstDefender RMX[56-57], Gemini[58-60]

This thesis will demonstrate the potential capability of using a handheld Raman spectrometer and a solution-based SERS substrate. Figure 1-5 shows both handheld Raman devices that are used throughout the chapters to come. Figure 1-5A is a B&W Tek TacticID Raman spectrometer and is shown with multiple handheld Raman adapters. Each adapter will have different functionalities. For example, the point and shoot could be used for taking measurements of solid material within a container. The vial adapter could be used for taking measurements of solutions. This is demonstrated in Figure 1-5B using a B&W Tek NanoRam handheld Raman spectrometer. Finally, a membrane adapter would commonly be used in conjunction with a membrane- or paper-based SERS substrate. These type of adapters add a lot of measurement versatility and functionality.

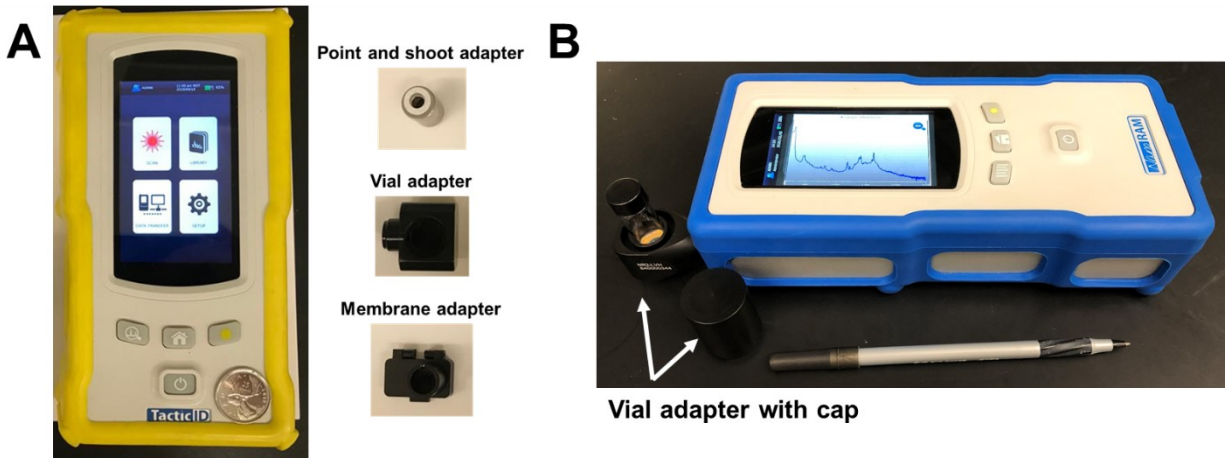

Figure 1-5. Handheld Raman spectrometers and their different adapters. (A) B&W Tek TacticID with a point and shoot, vial and membrane adapters. (B) B&W Tek NanoRam handheld Raman spectrometer demonstrating how to use the vial adapter. A 25¢ coin (quarter) and pen is used to provide insight about the scale of the instruments. Photos in (A) were taken and provided by Dr. Ahmed Mahmoud.

1.3.2. Development of SERS Substrates

SERS substrates are responsible for providing enhancement of weak intensity Raman scattered photons, thus are a vital component to developing any type of SERS measurement platform. SERS substrates often fall under three main categories: (1) ordered array of nanostructures on solid surfaces; (2) deposition of nanoparticles on surfaces; and (3) nanoparticles in suspension.[61] The performance of SERS substrates is evaluated based on a set of well-established standards. An ideal SERS substrate should: (i) demonstrate good spot-to-spot and substrate-to-substrate reproducibility (<20%); (ii) provide large enhancements for rapid and sensitive analyses; (iii) have good long-term stability; (iv) have a clean surface for strong and weak adsorbates; and (v) be easily produced and at a low cost.[3, 62-63] The diversity of SERS substrates is extensive and only a select few examples will be highlighted. Since this work focuses on solution-based substrates, more emphasis will be placed on nanoparticles in suspension.

1.3.2.1. Ordered Nanostructure and Nanoparticle Arrays on Solid Substrates

The fabrication of highly ordered nanostructure arrays often used micro and nanofabrication techniques. There are many reviews that summarize the different types of fabrication processes.[3, 5, 61, 64-65] These techniques are generally broken down into top-down, bottom-up and templating techniques.[65] A couple of examples of top-down fabrication methods include electron beam lithography and focused ion-beam lithography.[65] These techniques are capable of creating highly ordered geometric structures on a substrate with a high degree of reproducibility.[3] For example, Yue et al. used electron beam lithography to produce gold nanostructures with controlled geometries and arrangements for SERS analysis.[66] However, top-down techniques are generally expensive, time consuming, and struggle at producing sub-5 nm structures.[65] Another nanofabrication technique worth noting is nanosphere lithography. This is a technique developed by the Van Duyne Group, and is used to fabricate arrays with controlled nanoparticles sizes, shapes and interparticle spacing.[67-68] These substrates are prepared by first self-assembling polymer nanospheres onto a solid substrate, and then depositing metal onto the nanospheres mask (15-100 nm).[22, 67] Figure 1-6A is an illustration of a polymer nanosphere mask.[67] The substrate is then sonicated in solvent to remove the mask, and leaves behind any metal deposited in between the nanospheres.[22, 67] Figure 1-6B is an AFM image demonstrating the silver triangular nanoparticle array resulting from this process.[67] Another possibility is to deposit a thicker layer of metal (~200 nm) onto the nanosphere mask to produce a metal film over the nanosphere (FON).[22] In this case the mask is not removed afterwards.

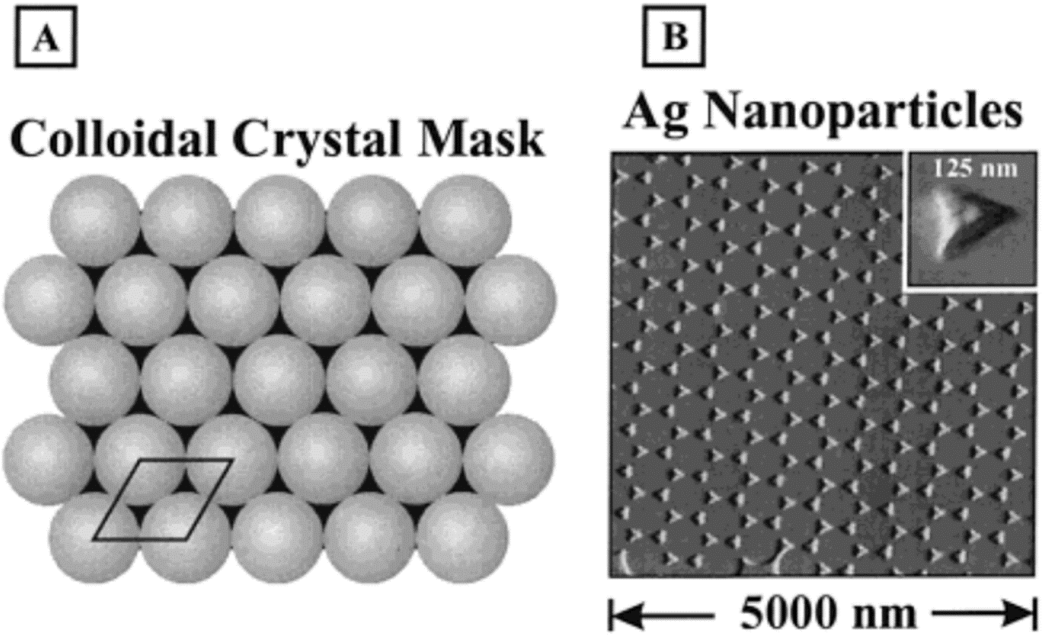

Figure 1-6. Nanosphere lithography. (A) Schematic illustration and (B) atomic force microscopy image of single layer periodic particle arrays. Reprinted with permission from Haynes, C. L.; Van Duyne, R. P., Nanosphere Lithography: A Versatile Nanofabrication Tool for Studies of Size-Dependent Nanoparticle Optics. *J. Phys. Chem. B* **2001**, 105 (24), 5599-5611. Copyright 2001 American Chemical Society.[67]

Bottom-up approaches, such as Langmuir–Blodgett, Langmuir–Schaefer and other interface assembly protocols are commonly employed to assemble smaller nanoparticles into an ordered array.[65] Tao et al. used a Langmuir–Blodgett technique to assemble aligned silver nanowires on a surface for SERS molecular sensing.[69] These methods are capable of achieving moderate reproducibility.[65] Templating fabrication techniques, such as anodized aluminium oxide templating, are a lower cost option for producing high throughput and highly reproducible substrates.[65] Moskovits and co-workers developed silver nanowire bundles using a porous aluminium oxide template and AC electrodeposition for SERS applications.[70]

1.3.2.2. Nanoparticles on Flexible Substrates

The deposition of nanoparticles into flexible substrates are a highly sought after alternative due to their cost-effectiveness and versatility in taking measurements. Many types of platforms, such as paper, polymer membranes and fabrics have been incorporated with metallic nanoparticles and used for SERS applications.[71-72] The use of paper-based SERS dates back as far as the mid-1980s.[73-75] Over time, the use of cellulose-based (paper) substrates for SERS applications has grown immensely.[6] In general, many different protocols have been developed to synthesize flexible substrates. Some of these protocols include in-situ synthesis, drop-casting, dip-coating/immersion, electrospinning, additive manufacturing and filtration.[6, 71-72] For example, Kim et al. used an in-situ synthesis/immersion protocol to develop a SERS biosensing paper strip.[76] In their work, the substrates are developed by immersing filter papers into a gold salt solution, and then immersing in sodium borohydride solution to form gold nanoparticles directly on the filter paper.[76] The synthesis used a technique called successive ionic layer absorption and reaction (SILAR) to maximize the SERS activity and enhancement of their substrates.[76] In short, this technique essentially exposes the filter paper to multiple reaction cycles. These types of substrate are capable of producing high enhancement factors ($\sim 10^8$) and provide good reproducibility ($\sim$7.5% relative standard deviation).[76] However, the requirement to immerse the substrate in multiple solutions followed by multiple rinsing steps can be tedious and time consuming, and this makes having a high production throughput difficult.[72]

The deposition of nanoparticles through additive manufacturing consists of inkjet printing, spraying and screen printing processes.[72] For example, the White group has developed a cost-effective paper-based SERS substrate using an inkjet-printing approach.[7, 77-86] Initially, silver nanoparticles were inkjet-printed onto chromatography paper using a commercially available inkjet printer.[82] The substrates have also been printed with gold nanoparticles and have proven to be versatile in acquiring measurements.[86] These substrates can be used for lateral flow assays, to wipe surfaces, dip into solutions, etc.[86] Figure 1-7 shows images of the White's group paper-based substrates and the different styles of substrates.[86] However, there are some drawback in the development of these substrate. In the production of these substrates, the paper needs to be treated so it is hydrophobic, the nanoparticles need to be concentrated, the solution viscosity needs to be corrected for printing and multiple deposition cycles are usually needed.[72, 82]

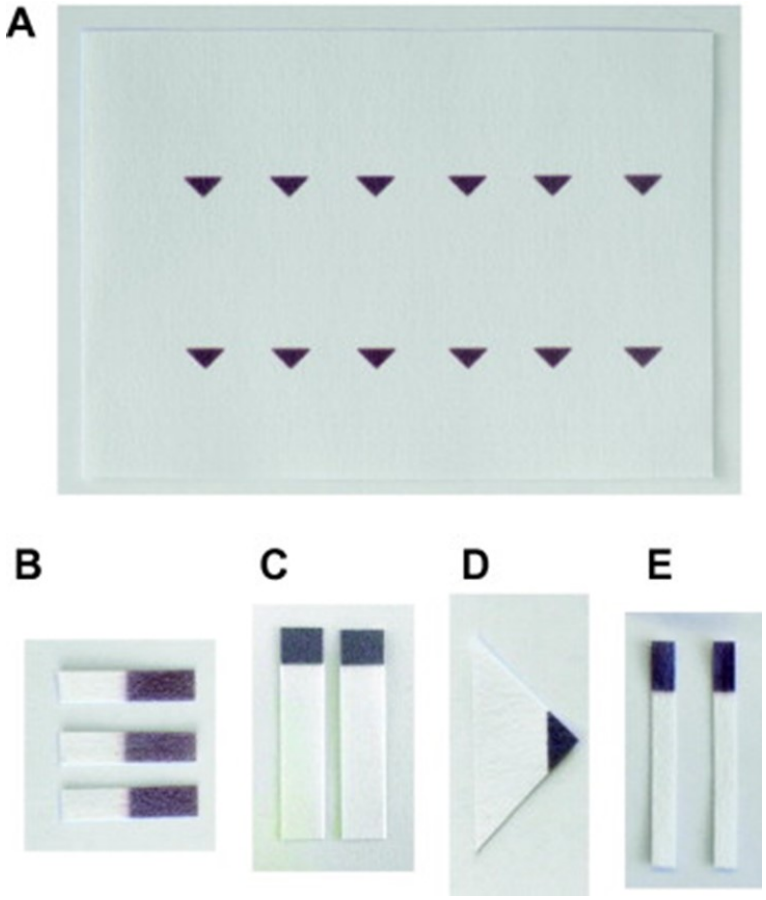

Figure 1-7. Inkjet-printed SERS substrates. (A) Printed array of SERS substrates that can be cut and adapted to meet specific analyte collection, concentration and detection requirements as required by the application. (B) General SERS substrates fabricated using inkjet-printed gold nanoparticles. (C) SERS substrates used for lateral flow concentration experiments. (D) Large wicking region allows for the substrate to be used as a dipstick. (E) Surface swab SERS substrates. Reprinted from Hoppmann, E. P.; Yu, W. W.; White, I. M., Highly sensitive and flexible inkjet printed SERS sensors on paper. *Methods* **2013**, 63 (3), 219-224. Copyright 2013, with permission from Elsevier.[86]

Another simple and straightforward approach to incorporate nanoparticles into flexible substrates is through filtration. For example, Yu and White loaded pre-aggregated silver nanoparticles into nylon and polyvinylidene fluoride (PVDF) filter membranes using a syringe filtration process.[87] Gao et al. performed a similar study and loaded pre-aggregated silver nanoparticles into PVDF membrane filters.[88] These reports showed good SERS measurement capabilities. An alternative is to use a vacuum filtration approach.

Zhang et al. vacuum filtered a cellulose nanofiber layer onto polycarbonate filter membrane before adding gold nanorods.[89] Their substrate demonstrated molecular and cellular SERS detection capabilities.[89]

In general, the development of flexible SERS substrates are a cost-effective alternative to ordered nanostructure arrays on rigid substrates. The synthesis is relatively straightforward and does not require the use of expensive equipment. The measurement versatility is also an appealing added feature. The SERS performance of nanoparticles on flexible substrates have moderate reproducibility, enhancement factors between 10^4-10^9 and detection limits in the nM to pM range.[6, 71]

1.3.2.3. Nanoparticles in Suspension

Colloidal plasmonic nanoparticles for in-solution measurements offer two distinct advantages over the substrates described above. The first advantage is the decrease in the adsorption time of the analyte to the nanoparticle surface due to dynamic solution mixing. Second, solution homogeneity offers the potential for reproducible analysis. Colloidal plasmonic nanoparticles, such as silver and gold nanoparticles, are the most common examples of solution-based SERS substrates. The ease and scalability of nanoparticle synthesis make their use as a substrate viable and appealing. The most simple synthesis of silver and gold nanoparticles is prepared by reducing and stabilizing a metal precursor, such as $AgNO_3$ or $HAuCl_4$, with a reducing agent and capping agent (e.g., sodium citrate).[90] There are plenty of alternative methods that use different reducing and capping agents, and these ultimately result in nanoparticles of different shapes and sizes with unique optical properties.

There are many important factors that contribute to the nanoparticles surface plasmon resonance properties and SERS enhancement capability. These factors include the nanoparticle size, the type of metal and the nanoparticle shape. For example, the size of gold and silver nanoparticles have an impact on the LSPR and the SERS performance.[91-92] Generally, nanoparticles between 10-100 nm are used for SERS analysis purposes.[93] In terms of the metal type, silver nanoparticles provide signals as much as 10 to 100 times more intense than those from gold nanoparticles.[94] However, gold nanoparticles have a higher biocompatibility in comparison to silver nanoparticles, and are often used in biological applications.[94-95] The shape of the nanoparticle is also an important factor to consider. A variety of nanoparticle shapes have been investigated throughout the literature, including spheres, nanorods, nanotriangles, nanostars, etc.[96-105] One benefit of using anisotropic nanoparticles is the capability to tune the LSPR over a range of wavelengths.[106] Another benefit is that large enhancements are produced at sharp edges and points of anisotropic nanoparticles, and this is called the "lightning rod" effect.[106-107] Tian et al. examined the effect of different nanoparticle shapes on the SERS enhancement of rhodamine 6G by comparing gold spheres, aggregated spheres, nanotriangles and nanostars.[105] Briefly, their results demonstrated that the nanostars provided the highest signal enhancement, whereas the non-aggregated spheres provided little signal enhancement.[105]

It is well understood that the enhancement from dispersed single particle is considered weak/low in comparison to dimers and small clusters.[93] Hence, many aggregation strategies have been investigated to increase the number of hot spots in solution and improve the SERS enhancement.[3, 108] A variety of different aggregating agents,

such as poly(L-lysine), halide ions, spermine, nitric acid, magnesium sulfate, etc. have been investigated.[98, 108] However, controlling the aggregation process is difficult and could lead to irreproducible results. There have been attempts to control the aggregation process in the past. For example, Meyer et al. studied the formation of long-lived metastable silver nanoparticle clusters with the addition of potassium chloride for SERS applications.[109] Their results showed the possibility to produce partially aggregated nanoparticles for long term usage with reproducible signals.[109] In another example, Cummingham et al. investigated the aggregation of citrate reduced silver nanoparticles with the controlled addition of poly(L-lysine).[96] Larmour et al. examined the use magnesium sulfate as an aggregating agent to produce silver nanoparticle dimers.[110] The authors suggest that silver nanoparticle dimers are still supported by weakly bound citrate due to a weaker binding affinity between sulfate anions and silver.[110]

Another interesting example investigated strategies to improve the reproducibility of colloidal SERS.[111] Tantra et al. synthesized citrate capped silver nanoparticles, used potassium chloride to aggregate the nanoparticles and rhodamine 6G as a Raman probe.[111] Some of the key parameters that were studied include storage conditions, filtration and solution vortexing time.[111] Their results indicated that filtration and storage conditions had little to no effect on the SERS, however, longer vortexing time improved the SERS reproducibility.[111] These improvements were attributed to the formation of reproducible clusters under forced convection, rather than random collisions via natural convection.[111]

Some other approaches to produce dimers and nanoparticle clusters in solution include the self-assembly of nanoparticles using molecular linkers.[108] Molecular linkers are

often classified into groups: (1) bifunctional molecules (e.g., dithiol) and selective recognition molecules (e.g. DNA hybridization).[108] The detection of polycyclic aromatic hydrocarbons (PAHs) have been quite successful with colloidal nanoparticles and bifunctional molecules.[112-115] For example, Guerrini et al. created nanosensors capable of detecting PAHs using viologen functionalized nanoparticles.[113, 115] The viologens were responsible for creating intermolecular hot spots and cavities for molecular detection.[113, 115] While multiple viologens were investigated, the authors found that lucigenin provided the best SERS results due to its large aromatic character and bifunctional properties.[115] Moreover, Guerrini et al. also investigated the use of dithiocarbamate calix[4]arene functionalized nanoparticles for PAH detection.[112, 114] The dithiocarbamate has a strong affinity to metal surfaces, while the calix[4]arene component creates a cavity at the nanoparticle surface for PAH adsorption.[112] In the presence of a PAH, such as coronene, functionalized nanoparticles form host–guest complexes and trap the PAHs in the interparticle hot spot.[114]

Biological linkers, such as antibodies, antigens and DNA, have been used to induce nanoparticle assemblies and introduce molecular recognition capabilities.[108] For example, Graham et al. developed a DNA-based nanoparticle assembly process for controlled SERS.[99] Silver nanoparticles were labelled with a dye molecules (Raman reporter) and surface functionalized with DNA probes.[99] Aggregation of the nanoparticles and formation of hot spots is caused by sequence-specific DNA hybridization in the presence of the complementary DNA strand.[99] This results in a large SERS enhancement in comparison to dye-coded single nanoparticles.[99]

Another more recent approach is to control and prevent nanoparticle sedimentation using a polymer solution. Van Duyne and co-workers developed a method using polyvinylpyrrolidone (PVP) to prevent the sedimentation of gold nanoparticles for the SERS detection of neurotransmitters.[116] A schematic of the method used is shown in Figure 1-8. In their approach, gold nanoparticles are mixed with neurotransmitters (epinephrine, dopamine, serotonin, histamine and norepinephrine) in salty buffer solution, and PVP is added to the solution immediately afterwards to control and halt any significant aggregation.[116] The PVP encapsulates the gold nanoparticle clusters with analyte, and demonstrates detection in the nM range.[116]

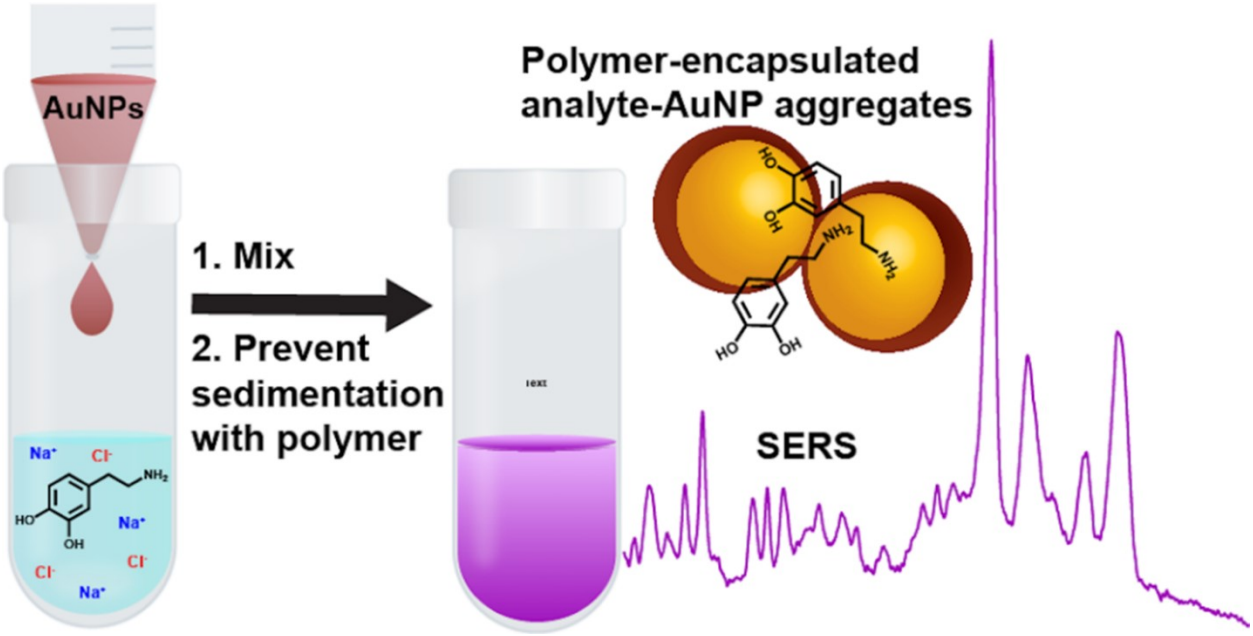

Figure 1-8. Schematic demonstrating a method for controlled aggregation for in-solution SERS. Reprinted with permission from Vander Ende, E.; Bourgeois, M. R.; Henry, A.-I.; Chávez, J. L.; Krabacher, R.; Schatz, G. C.; Van Duyne, R. P., Physicochemical Trapping of Neurotransmitters in Polymer-Mediated Gold Nanoparticle Aggregates for Surface-Enhanced Raman Spectroscopy. *Anal. Chem.* **2019**, 91 (15), 9554-9562. Copyright 2019 American Chemical Society.[116]

The deposition and growth of nanoparticles onto larger dispersible support structures is another approach for reproducible in-solution SERS measurements. For example, Li et al. coated poly(styrene-co-acrylic acid) nanosphere with silver nanoparticles and stabilized with PVP for the detection of trace melamine in solution.[117] Ogundare and van Zyl synthesized silver nanoparticles onto cellulose nanocrystals (CNC) for the detection of riboflavin.[118] Silver nanoparticles were also deposited onto a silica/CNC nanocomposite material for the in-solution SERS measurement of malachite green.[119] In these examples, the larger structures act as a support for the nanoparticles and bring nanoparticles in close proximity to one another. This produces potential hot spots for SERS measurements. This thesis investigates a similar approach using cellulose nanofibers as a dispersible support.

1.4. Cellulose nanomaterials

Cellulose is the world's most abundant renewable polymer and known as the main component found in cell walls.[120] Cellulose has become a widely used material with a variety of different applications, particularly in forest products, pulp and paper and textile industries.[121] It was not until 1838 that French chemist Anselme Payen first discovered the material "cellulose".[120, 122] Since then, much effort has been invested into characterizing and understanding its structure.[121, 123-124] Figure 1-9 shows an illustration of the chemical and physical structure of cellulose. Cellulose is chemically composed of two anhydroglucose units (cellobiose; repeating segment) adjoined by a β 1–4 glucosidic bond.[120-121, 124] Van der Waals and intermolecular hydrogen bonding between the hydroxyl and oxygen groups result in stable cellulose chains.[121] Cellulose chains are composed of elementary fibrils and bundles of fibrils (as known as microfibrillated or nanofibrillated cellulose) (see Figure 1-

9).[121, 124] These fibrils are generally several micrometres in length with a diameter range of 5-50 nm.[121, 124] Moreover, the makeup of elementary fibrils consist of highly orders (crystalline) and disordered (amorphous) regions (Figure 1-9).[121, 124] The diversity in cellulose is controlled by two factors: (1) source of the cellulose material (i.e., wood, plant, tunicates, algae, bacteria, etc.) and (2) the extraction process (e.g., pre-treatment, disintegration or deconstruction).[121]

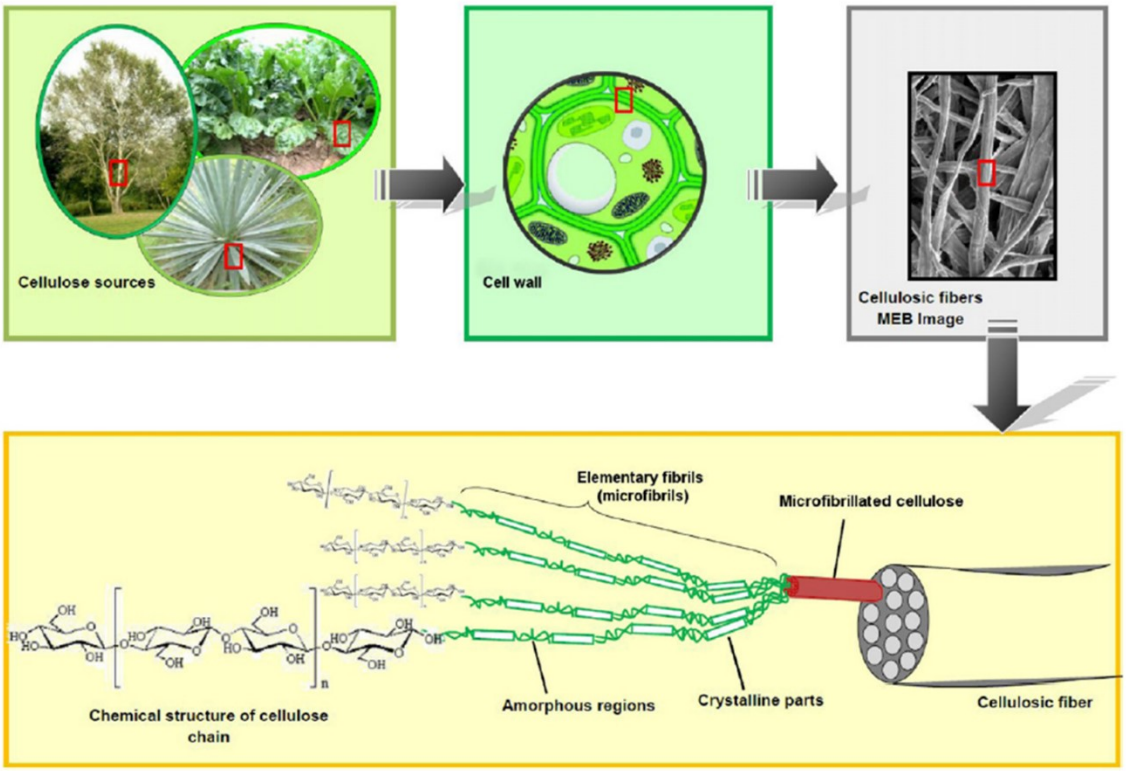

Figure 1-9. Illustration of the chemical and physical structure of cellulose. Demonstration of cellulose breakdown from cellulose sources to cellulose molecules with an emphasis on the cellulose microfibrils. Reprinted from Lavoine, N.; Desloges, I.; Dufresne, A.; Bras, J., Microfibrillated cellulose – Its barrier properties and applications in cellulosic materials: A review. *Carbohydr. Polym.* **2012**, 90 (2), 735-764. Copyright 2012, with permission from Elsevier.[124]

The extraction of nanocellulose has led to the use of cellulose nanomaterials in numerous areas, such as polymers, biomedical, pharmaceuticals, separation membranes, etc.[121] It is important to distinguish between the different types of nanomaterials, and in general can be broken down into two main categories: (1) cellulose nanocrystals (CNC) and (2) cellulose nanofibers (CNF). CNC's are rod-like nanoparticles with widths of 3-5 nm and lengths of 50-500 nm depending on the cellulose source.[121] The first report of colloidal suspension of CNCs was by Ränby in the 1950s after treating cellulose fibrils with sulfuric acid.[120] Acid hydrolysis treatment is used to hydrolyse the disordered regions on the cellulose fibrils, leaving behind the crystalline regions.[120] Conversely, CNF typically have sizes ranging from 4-20 nm in width and 500-2000 nm in length.[121] These materials are finer cellulose fibers consisting of both the crystalline and amorphous regions.[121] Unlike CNCs production which requires an acid hydrolysis treatment, CNFs are usually produced using a mechanical process to defibrillate the fibers.[121] CNFs are used throughout this thesis and will be discussed more throughout the chapters.

1.4.1. Metal Nanoparticles on Cellulose Nanomaterials

Cellulose nanomaterials have been used in a wide range of applications as described above. This section specifically discusses the synthesis and use of cellulose nanomaterial and metal particle nanocomposites. Islam et al. have written an excellent review on cellulose-based inorganic hybrid systems.[125] Some of the key features of cellulose nanomaterials, such as the large surface area, reductive surface functional groups and water dispersibility, have allowed for its ability to act as a scaffold for metallic nanoparticle nucleation and deposition.[125] Many types of nanoparticles have been used in the synthesis of metal-

cellulose nanocomposites. Some examples of the nanoparticles include Ag, Au, Cu, Pt, Pd, Ni, etc. [125-131] Moreover, a wide range of different synthesis processes have been used including hydrothermal, UV reduction, electrostatic assembly, reduction with external reducing agents, etc.[125-126, 132-139] It is believed that oxygen containing moieties are responsible for acting as a nucleation and/or support/stabilizer for metal nanoparticles.[125] Depending on the type of nanoparticle synthesized onto the cellulose nanomaterial, there have been many applications for these materials. These metal-cellulose hybrid nanomaterials have been used in many applications, including antimicrobial, biosensing, catalytic and SERS applications.[125, 127, 131, 136-137] For example, Wu et al. synthesized silver nanoparticles onto bacterial cellulose and applied their material as a wound dressing.[136] Gopiraman et al. synthesized Au, Ag and Ni onto cellulose nanofiber composites and used these nanocomposites as a catalyst for the reduction of nitrophenol in water.[127] In another example, Jiang and Hsieh developed a solid substrate composed of cellulose nanofibrils and silver nanoprisms for SERS applications.[137] These are just a few of many application examples for metal-cellulose hybrid nanomaterials, and many more can be found in this review article.[125] In this thesis, silver and gold nanoparticles will be synthesized with CNF, and will be used for SERS measurement applications.

1.5. Thesis Outline

This thesis describes the synthesis and development of SERS substrates for in-solution analysis. Two different SERS substrate templates were investigated in this thesis. The first uses Good's buffer to synthesize and support gold nanostars for in-solution analysis (Chapter 2). The second SERS substrate uses cellulose nanofibers decorated with silver and

gold nanoparticles (Chapter 3 and 4). The cellulose nanofibers are used as a template for nanoparticle growth and as a support for colloidal stability for in-solution analysis. This thesis concludes with a comparison between in-solution and solid-based analyses using cellulose-based substrates (Chapter 5).

Chapter 2 investigates the use of gold nanostars as an in-solution SERS substrate using a handheld Raman spectrometer. The SERS performance is optimized based on different Good's buffers and the gold to buffer molar ratios. The impact of using salt to aggregate the nanostars is investigated and potential applications are shown. An assay is developed with these nanostars to quantitate methimazole, an anti-thyroid pharmaceutical, in urine.

Chapter 3 investigates the development of a water dispersible SERS substrate using cellulose nanofibers to provide rapid and reproducible measurement of solution-borne analytes. The substrate synthesis conditions were optimized based on SERS performance. A centrifugal entanglement process is used to produce colloidally stable bundles of plasmonic cellulose nanofibers. This process brings silver nanoparticles in-close proximity to each other creating hot spots for SERS analysis. Plasmonic cellulose nanofibers are examined using chemisorb and physisorb analytes. The substrates were used to detect malachite green below the recommended limit in less than 2 minutes.

Chapter 4 examines the synthesis of gold nanoparticles on cellulose nanofibers as a water dispersible SERS substrate. The stability and reproducibility of cellulose nanofibers decorated with gold nanoparticles were investigated. Methimazole in urine was quantitatively measured and compared to the gold nanostars. The field deployability of

metal decorated cellulose nanofibers is investigated by taking measurements using a handheld Raman spectrometer.

Chapter 5 is a comparative study using cellulose nanofibers decorated with gold nanoparticles as a solution-based and solid-based SERS substrate. In this chapter the advantages and disadvantages of using a solution-based and solid-based substrate are highlighted. These are discussed in terms of the synthesis and preparation of the substrate, the instrumentation setup and optimization, substrate treatment before analysis, the measurement style and technique, and the substrate reproducibility.

1.6. References

1. Kneipp, K.; Wang, Y.; Kneipp, H.; Perelman, L. T.; Itzkan, I.; Dasari, R. R.; Feld, M. S., Single Molecule Detection Using Surface-Enhanced Raman Scattering (SERS). *Phys. Rev. Lett.* **1997,** *78* (9), 1667-1670.

2. Nie, S.; Emory, S. R., Probing Single Molecules and Single Nanoparticles by Surface-Enhanced Raman Scattering. *Science* **1997,** *275* (5303), 1102-1106.

3. Pilot, R.; Signorini, R.; Durante, C.; Orian, L.; Bhamidipati, M.; Fabris, L., A Review on Surface-Enhanced Raman Scattering. *Biosensors* **2019,** *9* (2), 57.

4. Goodacre, R.; Graham, D.; Faulds, K., Recent developments in quantitative SERS: Moving towards absolute quantification. *TrAC, Trends Anal. Chem.* **2018,** *102*, 359-368.

5. Mosier-Boss, P. A., Review of SERS Substrates for Chemical Sensing. *Nanomaterials* **2017,** *7* (6), 142.

6. Ogundare, S. A.; van Zyl, W. E., A review of cellulose-based substrates for SERS: fundamentals, design principles, applications. *Cellulose* **2019,** *26* (11), 6489-6528.

7. Hoppmann, E. P.; White, I. M., A paper-based inkjet-fabricated substrate for SERS detection and differentiation of PCR products. In *Advanced Environmental, Chemical, and Biological Sensing Technologies X*, VoDinh, T.; Lieberman, R. A.; Gauglitz, G. G., Eds. 2013; Vol. 8718.

8. Raman, C. V.; Krishnan, K. S., A New Type of Secondary Radiation. *Nature* **1928,** *121* (3048), 501-502.

9. Krishnan, R. S.; Shankar, R. K., Raman effect: History of the discovery. *J. Raman Spectrosc.* **1981,** *10* (1), 1-8.

10. McCreery, R. L., Raman spectroscopy for chemical analysis. John Wiley & Sons: New York :, 2000.

11. Bouchard, M.; Smith, D. C., Catalogue of 45 reference Raman spectra of minerals concerning research in art history or archaeology, especially on corroded metals and coloured glass. *Spectrochim. Acta, Part A* **2003,** *59* (10), 2247-2266.

12. Hargreaves, M. D.; Page, K.; Munshi, T.; Tomsett, R.; Lynch, G.; Edwards, H. G. M., Analysis of seized drugs using portable Raman spectroscopy in an airport environment—a proof of principle study. *J. Raman Spectrosc.* **2008,** *39* (7), 873-880.

13. Moore, D. S., Instrumentation for trace detection of high explosives. *Rev. Sci. Instrum.* **2004,** *75* (8), 2499-2512.

14. Liang, D.; Bowers, J. E., Recent progress in lasers on silicon. *Nat. Photonics* **2010,** *4* (8), 511-517.

15. Stiles, P. L.; Dieringer, J. A.; Shah, N. C.; Duyne, R. P. V., Surface-Enhanced Raman Spectroscopy. *Annu. Rev. Anal. Chem.* **2008,** *1* (1), 601-626.

16. Fleischmann, M.; Hendra, P. J.; McQuillan, A. J., Raman spectra of pyridine adsorbed at a silver electrode. *Chem. Phys. Lett.* **1974,** *26* (2), 163-166.

17. Jeanmaire, D. L.; Van Duyne, R. P., Surface raman spectroelectrochemistry: Part I. Heterocyclic, aromatic, and aliphatic amines adsorbed on the anodized silver electrode. *J. Electroanal. Chem. Interfacial Electrochem.* **1977,** *84* (1), 1-20.

18. Albrecht, M. G.; Creighton, J. A., Anomalously intense Raman spectra of pyridine at a silver electrode. *J. Am. Chem. Soc.* **1977,** *99* (15), 5215-5217.

19. Moskovits, M., Surface roughness and the enhanced intensity of Raman scattering by molecules adsorbed on metals. *J. Chem. Phys.* **1978,** *69* (9), 4159-4161.

20. Moskovits, M., Surface-enhanced spectroscopy. *Rev. Mod. Phys.* **1985,** *57* (3), 783-826.

21. Schlücker, S., Surface-Enhanced Raman Spectroscopy: Concepts and Chemical Applications. *Angew. Chem. Int. Ed.* **2014,** *53* (19), 4756-4795.

22. Willets, K. A.; Van Duyne, R. P., Localized surface plasmon resonance spectroscopy and sensing. *Annu. Rev. Phys. Chem.* **2007,** *58*, 267-97.

23. McFarland, A. D.; Young, M. A.; Dieringer, J. A.; Van Duyne, R. P., Wavelength-Scanned Surface-Enhanced Raman Excitation Spectroscopy. *J. Phys. Chem. B* **2005,** *109* (22), 11279-11285.

24. Kambhampati, P.; Child, C. M.; Foster, M. C.; Campion, A., On the chemical mechanism of surface enhanced Raman scattering: Experiment and theory. *J. Chem. Phys.* **1998,** *108* (12), 5013-5026.

25. Lombardi, J. R.; Birke, R. L., A Unified Approach to Surface-Enhanced Raman Spectroscopy. *J. Phys. Chem. C* **2008,** *112* (14), 5605-5617.

26. Morton, S. M.; Ewusi-Annan, E.; Jensen, L., Controlling the non-resonant chemical mechanism of SERS using a molecular photoswitch. *PCCP* **2009,** *11* (34), 7424-7429.

27. Valley, N.; Greeneltch, N.; Van Duyne, R. P.; Schatz, G. C., A Look at the Origin and Magnitude of the Chemical Contribution to the Enhancement Mechanism of Surface-Enhanced Raman Spectroscopy (SERS): Theory and Experiment. *J. Phys. Chem. Lett.* **2013,** *4* (16), 2599-2604.

28. Brolo, A. G.; Irish, D. E.; Smith, B. D., Applications of surface enhanced Raman scattering to the study of metal-adsorbate interactions. *J. Mol. Struct.* **1997,** *405* (1), 29-44.

29. Agilent. Handheld Chemical Identification - Resolve Handheld Through-Barrier Identification System. https://www.agilent.com/en/products/raman-spectroscopy/raman-spectroscopy-systems/handheld-chemical-identification/resolve (accessed April 18, 2020).

30. Agilent. Pharmaceutical Analysis - Vaya Raman Raw Material Identity Verification System. https://www.agilent.com/en/products/raman-spectroscopy/raman-spectroscopy-systems/pharmaceutical-analysis/vaya-raman-raw-material-identity-verification-system (accessed April 18, 2020).

31. Anton Paar. Handheld Raman spectrometer: Cora 100. https://www.anton-paar.com/ca-en/products/details/handheld-raman-spectrometer-cora-100/ (accessed April 18, 2020).

32. B&W Tek. NanoRam - 1064 Handheld Raman Spectrometer. https://bwtek.com/products/nanoram-1064/ (accessed April 18, 2020).

33. B&W Tek. NanoRam Handheld Raman Spectrometer. https://bwtek.com/products/nanoram/ (accessed April 18, 2020).

34. VWR. NanoRam Handheld RAMAN System, B&W Tek. https://ca.vwr.com/store/product/en/13244534/nanoram-handheld-raman-system-b-w-tek (accessed April 18, 2020).

35. B&W Tek. TacticID-1064 All-Inclusive Handheld Raman for Identification of Explosives, Hazmat, Narcotics & More. https://bwtek.com/products/tacticid-1064/ (accessed April 18, 2020).

36. B&W Tek. TacticID-N Plus Handheld Raman Analyzer for Narcotics Identification. https://bwtek.com/products/tacticid-n/ (accessed April 18, 2020).

37. B&W Tek. TacticID-GP Plus All-Inclusive Handheld Analyzer for Hazmat, Narcotics and More. https://bwtek.com/products/tacticid-gp/ (accessed April 18, 2020).

38. Bruker. BRAVO Handheld Raman Spectrometer. https://www.bruker.com/products/infrared-near-infrared-and-raman-spectroscopy/raman/bravo.html (accessed April 18, 2020).

39. Metrohm. Mira DS: Identify hazardous and illicit substances quickly and safely. https://www.metrohm.com/en/products/spectroscopy/mira-handheld-raman-spectrometers/mira-ds-landing-page/ (accessed April 19, 2020).

40. Metrohm. Mira DS Basic. https://www.metrohm.com/en/products-overview/spectroscopy/mira%20handheld%20raman%20spectrometer/29260010?fromProductFinder=true (accessed April 19, 2020).

41. Metrohm. Mira P Basic. https://www.metrohm.com/en/products-overview/spectroscopy/mira%20handheld%20raman%20spectrometer/29270010?fromProductFinder=true (accessed April 19, 2020).

42. Rigaku. Progeny ResQ. https://www.rigaku.com/products/raman/resq (accessed April 19, 2020).

43. Rigaku. Progeny ResQ FLX. https://www.rigaku.com/products/raman/flx (accessed April 19, 2020).

44. Rigaku. ResQ CQL. https://www.rigaku.com/products/raman/cql (accessed April 19, 2020).

45. Rigaku. Progeny. https://www.rigaku.com/products/raman/progeny (accessed April 19, 2020).

46. CBRNE Tech Index. Chem 500. https://www.cbrnetechindex.com/p/4131/SciAps-Inc/Chem-500 (accessed April 19, 2020).

47. SciAps. CHEM-200 Raman Analyzer. https://www.sciaps.com/raman-spectrometers/chem-200/ (accessed April 19, 2020).

48. SciAps. Inspector 500. https://www.sciaps.com/raman-spectrometers/inspector-500/ (accessed April 19, 2020).

49. SciAps. Inspector 300. https://www.sciaps.com/raman-spectrometers/legacy-products/inspector-300 (accessed April 19, 2020).

50. SciAps. ReporteR. https://www.sciaps.com/raman-spectrometers/legacy-products/ (accessed April 19, 2020).

51. SciAps. ObserveR. https://www.sciaps.com/raman-spectrometers/legacy-products/ (accessed April 19, 2020).

52. ThermoFisher Scientific. TruScan RM Handheld Raman Analyzer. https://www.thermofisher.com/order/catalog/product/TRUSCANRM#/TRUSCANRM (accessed April 19, 2020).

53. Fisher Scientific. Raman Handheld Analyzers. https://www.fishersci.com/us/en/products/I9C8KOH0/raman-handheld-analyzers.html (accessed April 19, 2020).

54. Fisher Scientific. Thermo Scientific TruNarc. https://www.fishersci.com/shop/products/thermo-scientific-trunarc-4/p-4351112 (accessed April 19, 2020).

55. ThermoFisher Scientific. TruNarc Handheld Narcotics Analyzer. https://www.thermofisher.com/order/catalog/product/TRUNARC?SID=srch-srp-TRUNARC#/TRUNARC?SID=srch-srp-TRUNARC (accessed April 19, 2020).

56. ThermoFisher Scientific. FirstDefender RMX Handheld Chemical Identification. https://www.thermofisher.com/order/catalog/product/FIRSTDEFENDERRMX?SID=srch-srp-FIRSTDEFENDERRMX#/FIRSTDEFENDERRMX?SID=srch-srp-FIRSTDEFENDERRMX (accessed April 19, 2020).

57. Fisher Scientific. Thermo Scientific First Defender RMX Handheld Chemical Identification. https://www.fishersci.com/shop/products/thermo-scientific-firstdefender-rmx-handheld-chemical-identification-5/p-4006497 (accessed April 19, 2020).

58. Fisher Scientific. Thermo Scientific Gemini Analyzer. https://www.fishersci.com/shop/products/gemini-analyzer/18001149 (accessed April 19, 2020).

59. ThermoFisher Scientific. Gemini Analyzer https://www.thermofisher.com/order/catalog/product/GEMINI?SID=srch-srp-GEMINI#/GEMINI?SID=srch-srp-GEMINI (accessed April 19, 2020).

60. ThermoFisher Scientific Gemini handheld analyzer - Integrated Raman and FTIR for chemical and explosives ID. https://www.thermofisher.com/document-connect/document-connect.html?url=https%3A%2F%2Fassets.thermofisher.com%2FTFS-Assets%2FCAD%2Fbrochures%2Fgemini-analyzer-brochure.pdf&title=QnJvY2h1cmU6IEdlbWluaSBIYW5kaGVsZCAgQW5hbHl6ZXI= (accessed April 19, 2020).

61. Fan, M.; Andrade, G. F. S.; Brolo, A. G., A review on the fabrication of substrates for surface enhanced Raman spectroscopy and their applications in analytical chemistry. *Anal. Chim. Acta* **2011,** *693* (1), 7-25.

62. Lin, X.-M.; Cui, Y.; Xu, Y.-H.; Ren, B.; Tian, Z.-Q., Surface-enhanced Raman spectroscopy: substrate-related issues. *Anal. Bioanal. Chem.* **2009,** *394* (7), 1729-1745.

63. Natan, M. J., Concluding Remarks Surface enhanced Raman scattering. *Faraday Discuss.* **2006,** *132* (0), 321-328.

64. Fan, M.; Andrade, G. F. S.; Brolo, A. G., A review on recent advances in the applications of surface-enhanced Raman scattering in analytical chemistry. *Anal. Chim. Acta* **2020,** *1097*, 1-29.

65. Shi, R.; Liu, X.; Ying, Y., Facing Challenges in Real-Life Application of Surface-Enhanced Raman Scattering: Design and Nanofabrication of Surface-Enhanced Raman Scattering Substrates for Rapid Field Test of Food Contaminants. *J. Agric. Food. Chem.* **2018,** *66* (26), 6525-6543.

66. Yue, W.; Wang, Z.; Yang, Y.; Chen, L.; Syed, A.; Wong, K.; Wang, X., Electron-beam lithography of gold nanostructures for surface-enhanced Raman scattering. *J. Micromech. Microeng.* **2012,** *22* (12), 125007.

67. Haynes, C. L.; Van Duyne, R. P., Nanosphere Lithography: A Versatile Nanofabrication Tool for Studies of Size-Dependent Nanoparticle Optics. *J. Phys. Chem. B* **2001,** *105* (24), 5599-5611.

68. Hulteen, J. C.; Duyne, R. P. V., Nanosphere lithography: A materials general fabrication process for periodic particle array surfaces. *J. Vac. Sci. Technol., A* **1995,** *13* (3), 1553-1558.

69. Tao, A.; Kim, F.; Hess, C.; Goldberger, J.; He, R.; Sun, Y.; Xia, Y.; Yang, P., Langmuir−Blodgett Silver Nanowire Monolayers for Molecular Sensing Using Surface-Enhanced Raman Spectroscopy. *Nano Lett.* **2003,** *3* (9), 1229-1233.

70. Lee, S. J.; Morrill, A. R.; Moskovits, M., Hot Spots in Silver Nanowire Bundles for Surface-Enhanced Raman Spectroscopy. *J. Am. Chem. Soc.* **2006,** *128* (7), 2200-2201.

71. Prikhozhdenko, E. S.; Bratashov, D. N.; Gorin, D. A.; Yashchenok, A. M., Flexible surface-enhanced Raman scattering-active substrates based on nanofibrous membranes. *Nano Research* **2018,** *11* (9), 4468-4488.

72. Restaino, S. M.; White, I. M., A critical review of flexible and porous SERS sensors for analytical chemistry at the point-of-sample. *Anal. Chim. Acta* **2019,** *1060*, 17-29.

73. Tran, C. D., Subnanogram detection of dyes on filter paper by surface-enhanced Raman scattering spectrometry. *Anal. Chem.* **1984,** *56* (4), 824-826.

74. Vo-Dinh, T.; Hiromoto, M. Y. K.; Begun, G. M.; Moody, R. L., Surface-enhanced Raman spectrometry for trace organic analysis. *Anal. Chem.* **1984,** *56* (9), 1667-1670.

75. Vo-Dinh, T.; Uziel, M.; Morrison, A. L., Surface-Enhanced Raman Analysis of Benzo[A]Pyrene-DNA Adducts on Silver-Coated Cellulose Substrates. *Appl. Spectrosc.* **1987,** *41* (4), 605-610.

76. Kim, W.; Lee, J.-C.; Shin, J.-H.; Jin, K.-H.; Park, H.-K.; Choi, S., Instrument-Free Synthesizable Fabrication of Label-Free Optical Biosensing Paper Strips for the Early Detection of Infectious Keratoconjunctivitides. *Anal. Chem.* **2016,** *88* (10), 5531-5537.

77. Berger, A. G.; Restaino, S. M.; White, I. M., Vertical-flow paper SERS system for therapeutic drug monitoring of flucytosine in serum. *Anal. Chim. Acta* **2017,** *949*, 59-66.

78. Betz, J. F.; Yu, W. W.; Cheng, Y.; White, I. M.; Rubloff, G. W., Simple SERS substrates: powerful, portable, and full of potential. *PCCP* **2014,** *16* (6), 2224-2239.

79. Hoppmann, E. P.; Yu, W. W.; White, I. M., Inkjet-Printed Fluidic Paper Devices for Chemical and Biological Analytics Using Surface Enhanced Raman spectroscopy. *IEEE J. Sel. Top. Quantum Electron.* **2014,** *20* (3).

80. Hoppmann, E. P.; Yu, W. W.; White, I. M., Detection of Deoxyribonucleic Acid (DNA) Targets Using Polymerase Chain Reaction (PCR) and Paper Surface-Enhanced Raman Spectroscopy (SERS) Chromatography. *Appl. Spectrosc.* **2014,** *68* (8), 909-915.

81. White, I. M., Optofluidic SERS on inkjet-fabricated paper-based substrates. In *Integrated Optics: Devices, Materials, and Technologies Xvi*, Broquin, J. E.; Conti, G. N., Eds. 2012; Vol. 8264.

82. Yu, W. W.; White, I. M., Inkjet Printed Surface Enhanced Raman Spectroscopy Array on Cellulose Paper. *Anal. Chem.* **2010,** *82* (23), 9626-9630.

83. Yu, W. W.; White, I. M., Paper-based optofluidic SERS using ink-jet-printed substrates. In *Plasmonics in Biology and Medicine Viii*, VoDinh, T.; Lakowicz, J. R., Eds. 2011; Vol. 7911.

84. Yu, W. W.; White, I. M., Inkjet-printed paper-based SERS dipsticks and swabs for trace chemical detection. *Analyst* **2013,** *138* (4), 1020-1025.

85. Yu, W. W.; White, I. M., Chromatographic separation and detection of target analytes from complex samples using inkjet printed SERS substrates. *Analyst* **2013,** *138* (13), 3679-3686.

86. Hoppmann, E. P.; Yu, W. W.; White, I. M., Highly sensitive and flexible inkjet printed SERS sensors on paper. *Methods* **2013,** *63* (3), 219-224.

87. Yu, W. W.; White, I. M., A simple filter-based approach to surface enhanced Raman spectroscopy for trace chemical detection. *Analyst* **2012,** *137* (5), 1168-1173.

88. Gao, S. Y.; Glasser, J.; He, L. L., A Filter-based Surface Enhanced Raman Spectroscopic Assay for Rapid Detection of Chemical Contaminants. *J. Visualized Exp.* **2016,** (108).

89. Zhang, S.; Xiong, R.; Mahmoud, M. A.; Quigley, E. N.; Chang, H.; El-Sayed, M.; Tsukruk, V. V., Dual-Excitation Nanocellulose Plasmonic Membranes for Molecular and Cellular SERS Detection. *ACS Appl. Mater. Interfaces* **2018,** *10* (21), 18380-18389.

90. Lee, P. C.; Meisel, D., Adsorption and surface-enhanced Raman of dyes on silver and gold sols. *J. Phys. Chem.* **1982,** *86* (17), 3391-3395.

91. Njoki, P. N.; Lim, I. I. S.; Mott, D.; Park, H.-Y.; Khan, B.; Mishra, S.; Sujakumar, R.; Luo, J.; Zhong, C.-J., Size Correlation of Optical and Spectroscopic Properties for Gold Nanoparticles. *J. Phys. Chem. C* **2007,** *111* (40), 14664-14669.

92. Seney, C. S.; Gutzman, B. M.; Goddard, R. H., Correlation of Size and Surface-Enhanced Raman Scattering Activity of Optical and Spectroscopic Properties for Silver Nanoparticles. *J. Phys. Chem. C* **2009,** *113* (1), 74-80.

93. Moskovits, M., Surface-enhanced Raman spectroscopy: a brief retrospective. *J. Raman Spectrosc.* **2005,** *36* (6-7), 485-496.

94. Abalde-Cela, S.; Aldeanueva-Potel, P.; Mateo-Mateo, C.; Rodríguez-Lorenzo, L.; Alvarez-Puebla, R. A.; Liz-Marzán, L. M., Surface-enhanced Raman scattering biomedical applications of plasmonic colloidal particles. *J. R. Soc. Interface* **2010,** *7* (suppl_4), S435-S450.

95. Murphy, C. J.; Gole, A. M.; Stone, J. W.; Sisco, P. N.; Alkilany, A. M.; Goldsmith, E. C.; Baxter, S. C., Gold Nanoparticles in Biology: Beyond Toxicity to Cellular Imaging. *Acc. Chem. Res.* **2008,** *41* (12), 1721-1730.

96. Cunningham, D.; Littleford, R. E.; Smith, W. E.; Lundahl, P. J.; Khan, I.; McComb, D. W.; Graham, D.; Laforest, N., Practical control of SERRS enhancement. *Faraday Discuss.* **2006,** *132* (0), 135-145.

97. Docherty, J.; Mabbott, S.; Smith, E.; Faulds, K.; Davidson, C.; Reglinski, J.; Graham, D., Detection of potentially toxic metals by SERS using salen complexes. *Analyst* **2016,** *141* (20), 5857-5863.

98. Faulds, K.; Smith, W. E.; Graham, D.; Lacey, R. J., Assessment of silver and gold substrates for the detection of amphetamine sulfate by surface enhanced Raman scattering (SERS). *Analyst* **2002,** *127* (2), 282-286.

99. Graham, D.; Thompson, D. G.; Smith, W. E.; Faulds, K., Control of enhanced Raman scattering using a DNA-based assembly process of dye-coded nanoparticles. *Nat. Nanotechnol.* **2008,** *3* (9), 548-551.

100. Lu, G.; Forbes, T. Z.; Haes, A. J., SERS detection of uranyl using functionalized gold nanostars promoted by nanoparticle shape and size. *Analyst* **2016,** *141* (17), 5137-5143.

101. Mahmoud, A. Y. F.; Rusin, C. J.; McDermott, M. T., Gold nanostars as a colloidal substrate for in-solution SERS measurements using a handheld Raman spectrometer. *Analyst* **2020,** *145* (4), 1396-1407.

102. Saute, B.; Premasiri, R.; Ziegler, L.; Narayanan, R., Gold nanorods as surface enhanced Raman spectroscopy substrates for sensitive and selective detection of ultra-low levels of dithiocarbamate pesticides. *Analyst* **2012,** *137* (21), 5082-5087.

103. Yu, Z.; Grasso, M. F.; Sorensen, H. H.; Zhang, P., Ratiometric SERS detection of polycyclic aromatic hydrocarbons assisted by β-cyclodextrin-modified gold nanoparticles. *Microchim. Acta* **2019,** *186* (6), 391.

104. Zhao, Y.; Tian, Y.; Ma, P.; Yu, A.; Zhang, H.; Chen, Y., Determination of melamine and malachite green by surface-enhanced Raman scattering spectroscopy using starch-coated silver nanoparticles as substrates. *Anal. Methods* **2015,** *7* (19), 8116-8122.

105. Tian, F.; Bonnier, F.; Casey, A.; Shanahan, A. E.; Byrne, H. J., Surface enhanced Raman scattering with gold nanoparticles: effect of particle shape. *Anal. Methods* **2014,** *6* (22), 9116-9123.

106. Murphy, C. J.; Gole, A. M.; Hunyadi, S. E.; Stone, J. W.; Sisco, P. N.; Alkilany, A.; Kinard, B. E.; Hankins, P., Chemical sensing and imaging with metallic nanorods. *Chem. Commun.* **2008,** (5), 544-557.

107. Gersten, J. I., The effect of surface roughness on surface enhanced Raman scattering. *J. Chem. Phys.* **1980,** *72* (10), 5779-5780.

108. Guerrini, L.; Graham, D., Molecularly-mediated assemblies of plasmonic nanoparticles for Surface-Enhanced Raman Spectroscopy applications. *Chem. Soc. Rev.* **2012,** *41* (21), 7085-7107.

109. Meyer, M.; Le Ru, E. C.; Etchegoin, P. G., Self-Limiting Aggregation Leads to Long-Lived Metastable Clusters in Colloidal Solutions. *J. Phys. Chem. B* **2006,** *110* (12), 6040-6047.

110. Larmour, I. A.; Faulds, K.; Graham, D., Improved Versatility of Silver Nanoparticle Dimers for Surface-Enhanced Raman Spectroscopy. *J. Phys. Chem. C* **2010,** *114* (31), 13249-13254.

111. Tantra, R.; Brown, R. J. C.; Milton, M. J. T., Strategy to improve the reproducibility of colloidal SERS. *J. Raman Spectrosc.* **2007,** *38* (11), 1469-1479.

112. Guerrini, L.; Garcia-Ramos, J. V.; Domingo, C.; Sanchez-Cortes, S., Functionalization of Ag Nanoparticles with Dithiocarbamate Calix[4]arene As an Effective Supramolecular Host for the Surface-Enhanced Raman Scattering Detection of Polycyclic Aromatic Hydrocarbons. *Langmuir* **2006,** *22* (26), 10924-10926.

113. Guerrini, L.; Garcia-Ramos, J. V.; Domingo, C.; Sanchez-Cortes, S., Building Highly Selective Hot Spots in Ag Nanoparticles Using Bifunctional Viologens: Application to the SERS Detection of PAHs. *J. Phys. Chem. C* **2008,** *112* (20), 7527-7530.

114. Guerrini, L.; Garcia-Ramos, J. V.; Domingo, C.; Sanchez-Cortes, S., Sensing Polycyclic Aromatic Hydrocarbons with Dithiocarbamate-Functionalized Ag Nanoparticles by Surface-Enhanced Raman Scattering. *Anal. Chem.* **2009,** *81* (3), 953-960.

115. Guerrini, L.; Garcia-Ramos, J. V.; Domingo, C.; Sanchez-Cortes, S., Nanosensors Based on Viologen Functionalized Silver Nanoparticles: Few Molecules Surface-Enhanced Raman Spectroscopy Detection of Polycyclic Aromatic Hydrocarbons in Interparticle Hot Spots. *Anal. Chem.* **2009,** *81* (4), 1418-1425.

116. Vander Ende, E.; Bourgeois, M. R.; Henry, A.-I.; Chávez, J. L.; Krabacher, R.; Schatz, G. C.; Van Duyne, R. P., Physicochemical Trapping of Neurotransmitters in Polymer-Mediated Gold Nanoparticle Aggregates for Surface-Enhanced Raman Spectroscopy. *Anal. Chem.* **2019,** *91* (15), 9554-9562.

117. Li, J.-M.; Ma, W.-F.; Wei, C.; You, L.-J.; Guo, J.; Hu, J.; Wang, C.-C., Detecting Trace Melamine in Solution by SERS Using Ag Nanoparticle Coated Poly(styrene-co-acrylic acid) Nanospheres as Novel Active Substrates. *Langmuir* **2011,** *27* (23), 14539-14544.

118. Ogundare, S. A.; van Zyl, W. E., Nanocrystalline cellulose as reducing- and stabilizing agent in the synthesis of silver nanoparticles: Application as a surface-enhanced Raman scattering (SERS) substrate. *Surf. Interfaces* **2018,** *13*, 1-10.

119. Ogundare, S. A.; van Zyl, W. E., Amplification of SERS "hot spots" by silica clustering in a silver-nanoparticle/nanocrystalline-cellulose sensor applied in malachite green detection. *Colloids Surf., A* **2019,** *570*, 156-164.

120. Habibi, Y.; Lucia, L. A.; Rojas, O. J., Cellulose Nanocrystals: Chemistry, Self-Assembly, and Applications. *Chem. Rev.* **2010,** *110* (6), 3479-3500.

121. Moon, R. J.; Martini, A.; Nairn, J.; Simonsen, J.; Youngblood, J., Cellulose nanomaterials review: structure, properties and nanocomposites. *Chem. Soc. Rev.* **2011,** *40* (7), 3941-3994.

122. History of the Division: Cellulose, Paper and Textile. ACS: Cellulose and Renewable Materials Division. https://cell.sites.acs.org/history.htm (accessed May 5, 2020).

123. O'Sullivan, A. C., Cellulose: the structure slowly unravels. *Cellulose* **1997,** *4* (3), 173-207.

124. Lavoine, N.; Desloges, I.; Dufresne, A.; Bras, J., Microfibrillated cellulose – Its barrier properties and applications in cellulosic materials: A review. *Carbohydr. Polym.* **2012,** *90* (2), 735-764.

125. Islam, M. S.; Chen, L.; Sisler, J.; Tam, K. C., Cellulose nanocrystal (CNC)-inorganic hybrid systems: synthesis, properties and applications. *J. Mater. Chem. B* **2018,** *6* (6), 864-883.

126. Padalkar, S.; Capadona, J. R.; Rowan, S. J.; Weder, C.; Won, Y.-H.; Stanciu, L. A.; Moon, R. J., Natural Biopolymers: Novel Templates for the Synthesis of Nanostructures. *Langmuir* **2010,** *26* (11), 8497-8502.

127. Gopiraman, M.; Deng, D.; Saravanamoorthy, S.; Chung, I.-M.; Kim, I. S., Gold, silver and nickel nanoparticle anchored cellulose nanofiber composites as highly active catalysts for the rapid and selective reduction of nitrophenols in water. *RSC Adv.* **2018,** *8* (6), 3014-3023.

128. Liu, P.; Oksman, K.; Mathew, A. P., Surface adsorption and self-assembly of Cu(II) ions on TEMPO-oxidized cellulose nanofibers in aqueous media. *J. Colloid Interface Sci.* **2016,** *464*, 175-182.

129. Zhang, K.; Shen, M.; Liu, H.; Shang, S.; Wang, D.; Liimatainen, H., Facile synthesis of palladium and gold nanoparticles by using dialdehyde nanocellulose as template and reducing agent. *Carbohydr. Polym.* **2018,** *186*, 132-139.

130. Zhu, C.; Soldatov, A.; Mathew, A. P., Advanced microscopy and spectroscopy reveal the adsorption and clustering of Cu(ii) onto TEMPO-oxidized cellulose nanofibers. *Nanoscale* **2017,** *9* (22), 7419-7428.

131. Zhang, T.; Wang, W.; Zhang, D.; Zhang, X.; Ma, Y.; Zhou, Y.; Qi, L., Biotemplated Synthesis of Gold Nanoparticle–Bacteria Cellulose Nanofiber Nanocomposites and Their Application in Biosensing. *Adv. Funct. Mater.* **2010,** *20* (7), 1152-1160.

132. Guo, J.; Filpponen, I.; Su, P.; Laine, J.; Rojas, O. J., Attachment of gold nanoparticles on cellulose nanofibrils via click reactions and electrostatic interactions. *Cellulose* **2016,** *23* (5), 3065-3075.

133. Eisa, W. H.; Abdelgawad, A. M.; Rojas, O. J., Solid-State Synthesis of Metal Nanoparticles Supported on Cellulose Nanocrystals and Their Catalytic Activity. *ACS Sustainable Chem. Eng.* **2018,** *6* (3), 3974-3983.

134. Lokanathan, A. R.; Uddin, K. M. A.; Rojas, O. J.; Laine, J., Cellulose Nanocrystal-Mediated Synthesis of Silver Nanoparticles: Role of Sulfate Groups in Nucleation Phenomena. *Biomacromolecules* **2014,** *15* (1), 373-379.

135. Uddin, K. M. A.; Arcot Raghupathi, L.; Liljeström, A.; Chen, X.; Rojas, O. J.; Laine, J., Silver nanoparticle synthesis mediated by carboxylated cellulose nanocrystals. *Green Mater.* **2014,** *2* (4), 183-192.

136. Wu, C.-N.; Fuh, S.-C.; Lin, S.-P.; Lin, Y.-Y.; Chen, H.-Y.; Liu, J.-M.; Cheng, K.-C., TEMPO-Oxidized Bacterial Cellulose Pellicle with Silver Nanoparticles for Wound Dressing. *Biomacromolecules* **2018,** *19* (2), 544-554.

137. Jiang, F.; Hsieh, Y.-L., Synthesis of Cellulose Nanofibril Bound Silver Nanoprism for Surface Enhanced Raman Scattering. *Biomacromolecules* **2014,** *15* (10), 3608-3616.

138. Nabeela, K.; Thomas, R. T.; Nair, J. B.; Maiti, K. K.; Warrier, K. G. K.; Pillai, S., TEMPO-Oxidized Nanocellulose Fiber-Directed Stable Aqueous Suspension of Plasmonic Flower-like Silver Nanoconstructs for Ultra-Trace Detection of Analytes. *ACS Appl. Mater. Interfaces* **2016,** *8* (43), 29242-29251.

139. Omrani, A. A.; Taghavinia, N., Photo-induced growth of silver nanoparticles using UV sensitivity of cellulose fibers. *Appl. Surf. Sci.* **2012,** *258* (7), 2373-2377.

Chapter 2. Gold Nanostars as a Colloidal Substrate for In-Solution SERS Measurements Using a Handheld Raman Spectrometer

*Reproduced and/or adapted from Mahmoud, A. Y. F.; Rusin, C. J.; McDermott, M. T., Gold nanostars as a colloidal substrate for in-solution SERS measurements using a handheld Raman spectrometer. *Analyst* **2020**, *145* (4), 1396-1407. Copyright 2020, with permission from the Royal Society of Chemistry.

2.1. Introduction

Raman spectroscopy has evolved from an instrument intensive, high-cost research lab-based methodology to an inexpensive, routine analysis technique.[1-3] One main driving force behind this evolution was the development of high-performance yet lower-cost, compact instrument components such as lasers, wavelength selectors and detectors.[1] This has led to commercial bench top Raman systems with a small footprint as well as handheld Raman devices.[1, 3] Another driving force of analytical measurement applications has been advances in platforms that enhance Raman signals, specifically surface enhanced Raman scattering (SERS).[4] A significant area of advancement has been in the synthesis of noble metal nanoparticles (NP) of controlled size and shape.[5] Computational models and experiments have both opened pathways for the application of plasmonic metal NPs in quantitative SERS measurements.[6-7] Further introduction of SERS into a wider range of analytical measurements will rely on the pairing of appropriate SERS substrates with compact instrumentation.

Anisotropic gold nanostructures have been synthesized in many different shapes such as rods,[8-9] cubes,[10] bipyramids,[11] cages,[12] prisms,[13] nanostars,[14-16] etc. The localized surface plasmon resonance (LSPR) of these structures is tunable over a wide wavelength range when compared to spherical nanoparticles.[17-20] Previous reports have shown that plasmonic excitation of anisotropic nanoparticles result in intense electric fields characteristically localized at their sharp edges.[17-20] This phenomenon is called the "lightning rod" effect[21] and can significantly improve SERS enhancement provided that the shape and the size of these particles are uniform.[17-20]

Gold nanostars (AuNS) are examples of anisotropic nanoparticles that have attracted interest as a SERS substrate because of their multiple branches. Byrne and co-workers have shown that the SERS enhancement of R6G adsorbed to AuNS was more pronounced than that of nanotriangles and nanospheres.[22] Rodríguez-Lorenzo et al. reported a zeptomole detection limit of 1,5-naphtalenedithiol by sandwiching the molecule between a gold substrate and the tips of AuNS.[23] Indrasekara et al. attached AuNS to a thin gold film using a short amine terminated alkanethiol.[24] The substrate had an enhancement factor up to 5 orders of magnitude higher than that of gold nanospheres and achieved femtomolar level of detection of 4-mercaptobenzoic acid.[24] These nanostructures have also been integrated into sandwich lateral flow SERS assays for the detection of human immunoglobulin G, Zika and dengue biomarkers.[25-26] All these SERS applications of AuNS have been in the solid state, where the spectra were collected in air at a substrate surface. Haes and co-workers have used AuNS functionalized with carboxylic acid terminated alkanethiols for uranyl detection.[27-28] The initial study in this series reported the use of AuNS in colloidal form with the measurements being made in solution.

AuNS are synthesized via two main approaches; seed-mediated and seedless growth protocols. The seed-mediated protocol is a two-step approach that requires the synthesis of isotropic gold nanoseeds, where anisotropic structures are grown on the seeds.[22-24, 29-31] For example, the nanoseeds are grown into AuNS by the reduction of $HAuCl_4$ using ascorbic acid in the presence of cetyltrimethylammonium bromide and $AgNO_3$.[22, 30] In addition, nanoseeds can be grown into AuNS when $HAuCl_4$ is reduced using N,N-dimethylformamide in the presence of poly(vinylpyrrolidone).[23, 29] Gold nanoseeds can also be grown into AuNS by the reduction of $HAuCl_4$ using ascorbic acid in the presence of HCl and $AgNO_3$.[24, 31]

The seedless protocol is a single step one-pot synthesis approach. In this approach, AuNS are synthesized by the reduction of $HAuCl_4$ using Good's buffers. 4-(2-hydroxyethyl)-1-piperazineethanesulfonic acid (HEPES)[14, 16, 32-33] and 4-(2-hydroxyethyl)-1-piperazinepropanesulfonic acid (EPPS)[32-34] are the most commonly used Good's buffer to synthesize AuNS. 3-(N-morpholino)propanesulfonic acid (MOPS)[32] has also been used to synthesize AuNS. The tertiary amines from the piperazine group form cationic free radicals and acts as the reducing agent for Au ions.[14, 32, 35-36] The terminal alkanesulfonate group acts as a shaping-directing agent and promotes bilayer formation on the AuNS.[32-33, 37] The terminal hydroxyl groups promote bilayer formation and shape stability via hydrogen bonding.[32-33] The hydrophilic nature of the hydroxyl groups also provide water dispersibility and colloidal stability of the AuNS.[33] The simplicity of the one-pot seedless synthesis approach of AuNS using Good's buffers has attracted attention for various applications.[25-28, 34, 38] These nanostars have been applied in many SERS applications using different synthesis conditions.[25-28] The plasmonic behaviour of AuNS has been systematically optimized by varying experimental conditions such as the concentration

ratio of Good's buffer to $HAuCl_4$, choice of Good's buffer and pH of the reaction.[32] However, the effect of these various conditions on the SERS performance has not been investigated.[32]

Herein, we report the colloidal SERS performance of AuNS substrates using a handheld Raman spectrometer. In-solution SERS measurements were carried out with AuNS synthesized using HEPES and EPPS buffer at numerous ratios with and without using an aggregating agent (NaCl). This is to determine the optimal buffer and buffer to gold ratio for colloidal SERS analysis. The AuNS are characterized based on their LSPR, shape and size, and Raman intensity enhancement with and without NaCl. Following optimization with a chemisorbed Raman probe, the AuNS are used as a dispersible substrate to detect and quantify methimazole (MTZ) in synthetic urine. All Raman analyses are performed using a handheld Raman device to show the field deployability aspect of a colloidal AuNS substrate and to demonstrate rapid measurement performance.

2.2. Experimental

2.2.1. Materials

Gold (III) chloride trihydrate (99.995%, $HAuCl_4$), 4-(2-hydroxyethyl)-1-piperazineethanesulfonic acid buffer solution (1 M in H_2O, HEPES), 4-(2-Hydroxyethyl)-1-piperazinepropanesulfonic acid (99.5%, EPPS), sodium chloride (≥ 99.5%, NaCl), malachite green oxalate salt technical grade (MG), methimazole (analytical standard, MTZ), ciprofloxacin (≥ 98%, Cipro) and Surine™ negative urine control were purchased from Sigma-Aldrich Canada (Oakville, Ontario). 4-mercaptobenzonitrile (MBN) was purchased from Combi-Blocks, Inc. (San Diego, California, USA). Sodium hydroxide (NaOH) was

purchased from Fisher Scientific Canada. Transmission electron microscopy (TEM) grids (400-mesh carbon) were purchased from Electron Microscopy Sciences. Fisherbrand™ Class A clear glass threaded vials (1 dram) were purchased from Fisher Scientific Canada. The gold nanoparticles (30 nm) were purchased from Ted Pella, Inc. Deionized (DI) water (18.2 MΩ·cm) was used for all syntheses and measurements in this work.

2.2.2. Preparation of Gold Nanostars

AuNS were synthesized according to previously developed methods with slight modifications.[32] The pH of the 1 M HEPES buffer solution was adjusted to 7.20 ± 0.01 using a solution of 1 M NaOH and a Fisher Scientific accumet research AR15 pH meter. Similarly, a solution of 0.5 M EPPS buffer was prepared in DI water and the pH was also adjusted to 7.20 ± 0.01. A stock solution of $HAuCl_4$ (26 mM) was prepared in DI water. The synthesis of AuNS is governed by the ratio of the precursors in solution and is defined as R = [Buffer]/[$HAuCl_4$], where [Buffer] is the concentration of HEPES or EPPS, and [$HAuCl_4$] is held constant at 0.2 mM. The ratios assessed for each buffer in this work are 100, 300, 500, 700 and 1000 (buffer concentration = 20, 60, 100, 140 and 200 mM, respectively). The Good's buffer is initially mixed with DI water at 400 rpm. $HAuCl_4$ solution is then added to the solution and mixed for 5 minutes. The solution is then removed and stored in a dark environment for 24 hours. The AuNS concentration at HR100 and ER100 is estimated to be ~2.2 and 1.2 nM, respectively, as calculated using a previously published method.[39] Throughout this manuscript, a codename is used to describe the AuNS such as HR100. The first letter (in this case H) is the buffer used, where H stands for HEPES and E stands for EPPS, the R represents ratio, and the numbers represent the ratio being examined.

2.2.3. Characterization

UV-Vis spectroscopy experiments were completed using a PerkinElmer Lambda 35 spectrometer. All experiments used a slit width of 1 nm and a scan rate of 960 nm/min. The samples were analyzed in 1.5 mL BRAND® polystyrene disposable cuvettes (unless stated otherwise) and monitored from 400 to 1000 nm.

Transmission electron microscopy (TEM) imaging was performed using a JEOL JEM-ARM200CF S/TEM. Samples underwent a washing step to remove excess buffer by centrifuging three times: 12000 rpm for 10 minutes, 9000 rpm for 10 minutes and 6000 rpm for 10 minutes (Eppendorf Centrifuge 5417 R). The samples were re-dispersed in water and sonicated for 2 minutes between centrifugation steps. After the final centrifugation step the sample was concentrated by a factor of 10 for imaging. The sample (10 µL) was drop-casted onto a TEM grid for 10 minutes and the excess solution was wicked away. Samples were imaged at 200 kV. Image processing and analysis was completed using Gatan Digital Micrograph software.

Dynamic light scattering (DLS) and zeta potential measurements of AuNS were determined using a Malvern Zetasizer Nano-ZS. The instrument is equipped with a 4 mW HeNe laser (633 nm) and 173 ° backscattering angle. The 1 mL aliquot samples were measured in 2.5 mL BRAND® polystyrene disposable cuvettes (pathlength=1cm). Each measurement was performed with an equilibrium time of 120 seconds and at a temperature of 25 °C. For the DLS experiment, the standard deviation is representative of n=5 with each measurement consisting of 13 sub-runs. For the zeta potential experiment,

the standard deviation is representative of n=3 with each measurement consisting of 20 sub-runs.

2.2.4. Raman Analysis

Raman analysis using the AuNS was completed with a B&W Tek TacticID handheld Raman device with 785 nm laser (spot size 100 μm). The handheld was standardized using a polystyrene standard and all samples were analyzed using a liquid cell adapter at 100% power (300 mW). All measurements were performed in 1 dram vials. The analytes were mixed with the AuNS for 2 minutes using a vortex before analysis. In some experiments, NaCl was used as an aggregating agent to produce additional enhancement. Studies using salt were mixed for an additional 2 minutes after the addition of NaCl (total of 4 minutes) before taking the measurement. All samples contained the same concentration of AuNS and a total sample volume of 1 mL. Care was taken to choose an analyte concentration range that would not aggregate the AuNS before the addition of salt. This range was investigated by assessing low concentrations to concentrations that visibly aggregate the AuNS. This ensured partial control over the aggregation throughout the analyses. The acquisition time from the handheld cannot be user controlled. All Raman spectra were normalized to the device acquisition time. The spectral analysis was done using Spectragryph open-source software.[40]

2.3. Results and Discussion

A combination of easy-to-use, solution based SERS substrates and handheld Raman instrumentation has the potential to be a powerful portable measurement platform.

Anisotropic metal nanoparticles, such as AuNS, have shown a great deal of promise as in-solution SERS substrates. The influence of the type of buffer and the [buffer]/[$HAuCl_4$] ratio (R) on the structure and plasmonic behaviour of AuNS has been explored by Odom and co-workers.[32] Although their work provides a clear set of design rules for achieving a certain shape and optical properties, the effect of buffer type and R on the performance of colloidal AuNS as a water dispersible SERS substrate has not been fully explored to the best of our knowledge. In this work, AuNS synthesized in two different Good's buffers (HEPES and EPPS) with a R ranging from 100 to 1000 were investigated (Figure 2-1). AuNS used in SERS applications are usually prepared in this buffer ratio range as shown in Table 2-1.[25-28, 34, 41-42] In the work described here, we characterize the structure of AuNS from HEPES and EPPS at various ratios. The in-solution SERS performance of the AuNS is then investigated using a probe molecule and a handheld Raman device. Finally, we present results for the measurement of the anti-thyroid pharmaceutical drug, methimazole (MTZ) in urine.

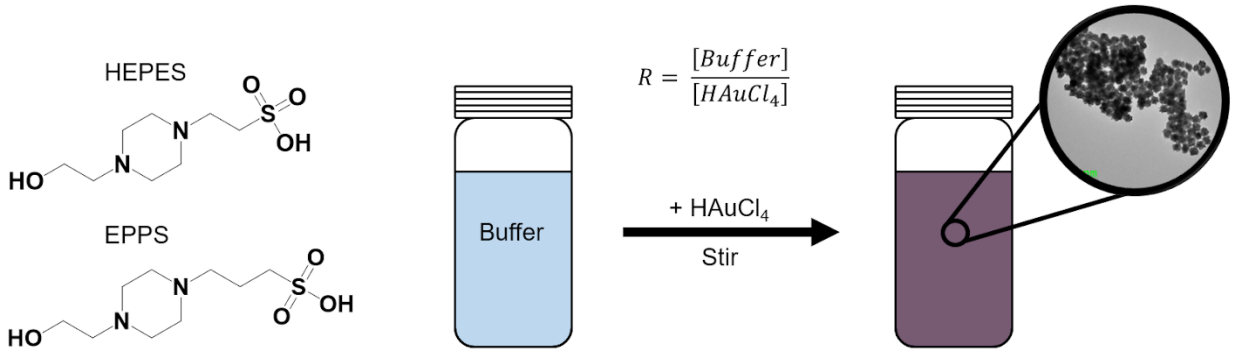

Figure 2-1. Schematic of AuNS synthesis using Good's buffers (HEPES and EPPS).

Table 2-1. Comparison of AuNS Synthesized using Good's Buffers for SERS Applications

Type of synthesis	Buffer type and ratio	Platform	Application	Reference
Seedless/seeded	EPPS R = ~300	Cellular	SERS imaging of breast cancer cells	34
Seedless/seeded	EPPS R = 400	Colloidal	Detection of uranyl	27
Seedless/seeded	EPPS R = 200	Surface	Detection of uranyl	28
Seedless	HEPES R = ~310	Surface	Lateral flow assay	25
Seedless	HEPES R = ~625	Surface	Lateral flow assay	26
Seedless	HEPES R = 200	Surface	Development of SERS graphene-nanostar composite nanoprobe	41
Seedless	HEPES R = 83 - 500	Surface	Synthesis of graphene nanostar nanocomposite	42
Seedless	HEPES/EPPS R = 100-1000	Colloidal	SERS optimization and detection	This work

*Seedless/seeded – AuNS are initially synthesized using a seedless method. Then AuNS are used as seeds to produce nanostars with longer branches via further addition of $HAuCl_4$.

2.3.1. Synthesis and Characterization of AuNS using HEPES and EPPS Buffers

The synthesis of AuNS in Good's buffers was performed using previously reported methods.[16, 32] The size and shape of the AuNS were manipulated based on R.[32] Figure 2-2 shows the extinction spectra and TEM images of AuNS synthesized using HEPES and EPPS. The AuNS extinction spectra is at ratios of 100, 300, 500, 700 and 1000, while only the AuNS extremities were imaged. The inset photographs are a visualization of the LSPR red-shift through a solution colour change from purple/blue to grey as the ratio is increased. Figure 2-2A are the results for HEPES. It is known that low R values for HEPES result in more spherical particles with short branches and higher R mixtures yield longer branches.[32] It has also been reported that HEPES induces branch growth in the [111]

crystal plane direction.[32] The extinction spectrum of HR100 in Figure 2-2A exhibits a single LSPR mode centred at 566 nm. This mode is attributed to the near-spherical core of the AuNS (Figure 2-3).[16, 32, 43] The TEM image of the HR100 shows a near-spherical structure with a size of 39 ± 11 nm (tip-to-tip) and branches of 7 ± 2 nm in length (size distribution found in Figure 2-4). The lattice spacing within the branches measured from high-resolution TEM images (Figure 2-4) is 0.235 ± 0.003 nm and is consistent with branch growth along the [111] direction.[16, 32, 44] The extinction spectra of AuNS prepared with R 300 to 1000 all exhibit a primary band that is associated with the branches that red-shifts as R increases. The red-shift has previously been attributed to the change in branch length and the branch tip sharpness.[16] As shown in the TEM image of the HR1000, a high R produces anisotropic AuNS containing branches up to 100 nm in length with sharper tips. A low intensity band between 520 and 550 nm is also observed for R > 100 that is attributed to spherical by-products that are minimized with stirring.[32] The results in Figure 2-2A agree with those reported by Odom and co-workers for AuNS synthesized from HEPES.[32]

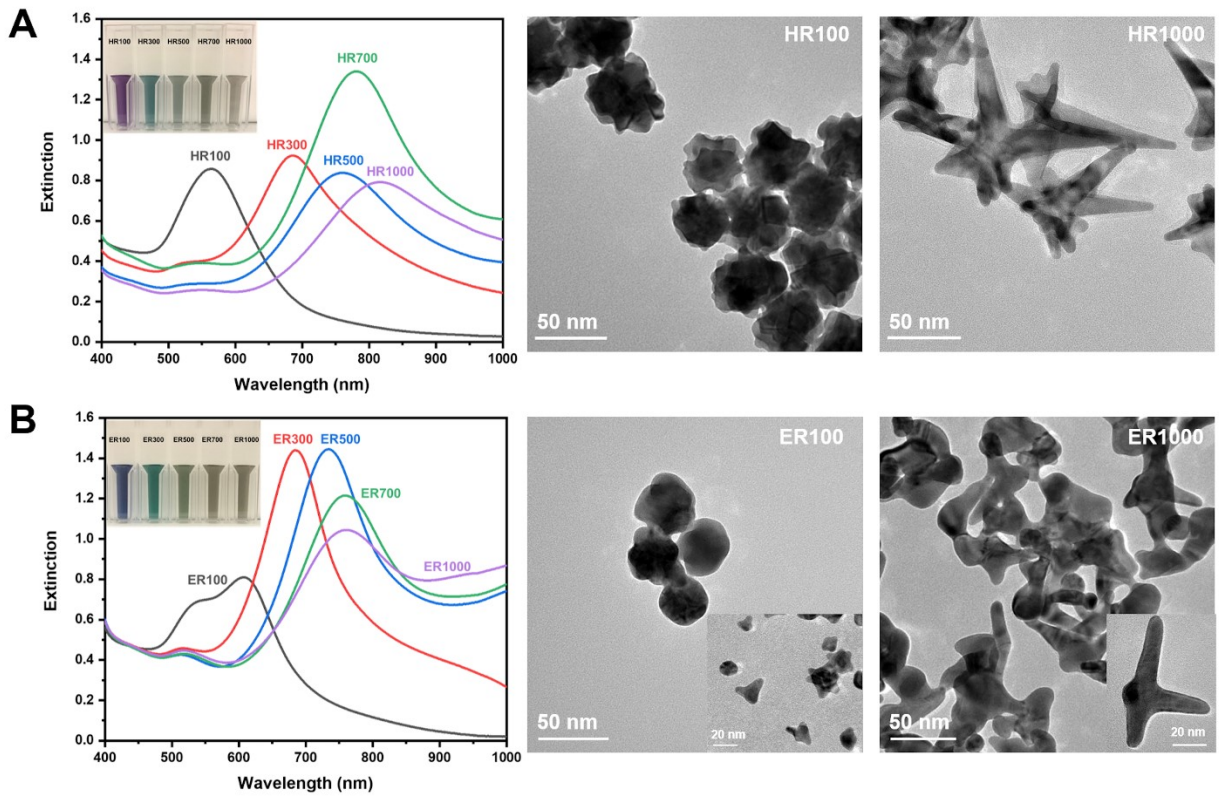

Figure 2-2. Extinction spectra and TEM imaging of AuNS using Good's buffers at different [buffer] to [$HAuCl_4$] ratios. Extinction spectra of (A) HEPES and (B) EPPS buffers. The inset images show the colour of the AuNS solutions at the given ratios. TEM images correspond to AuNS at R 100 and 1000.

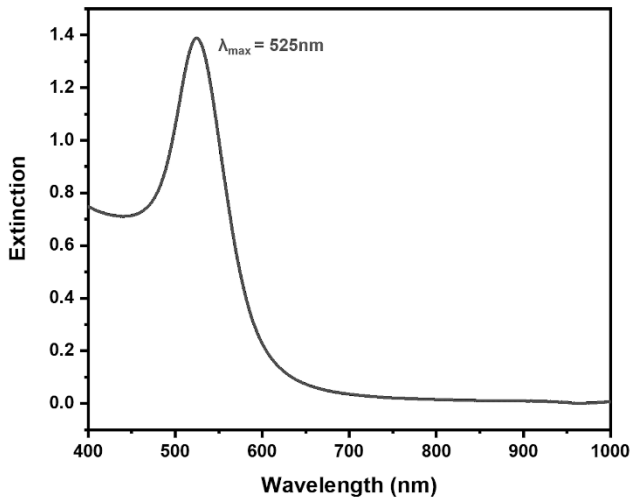

Figure 2-3. UV-Vis spectrum of citrate capped gold nanoparticles (30 nm).

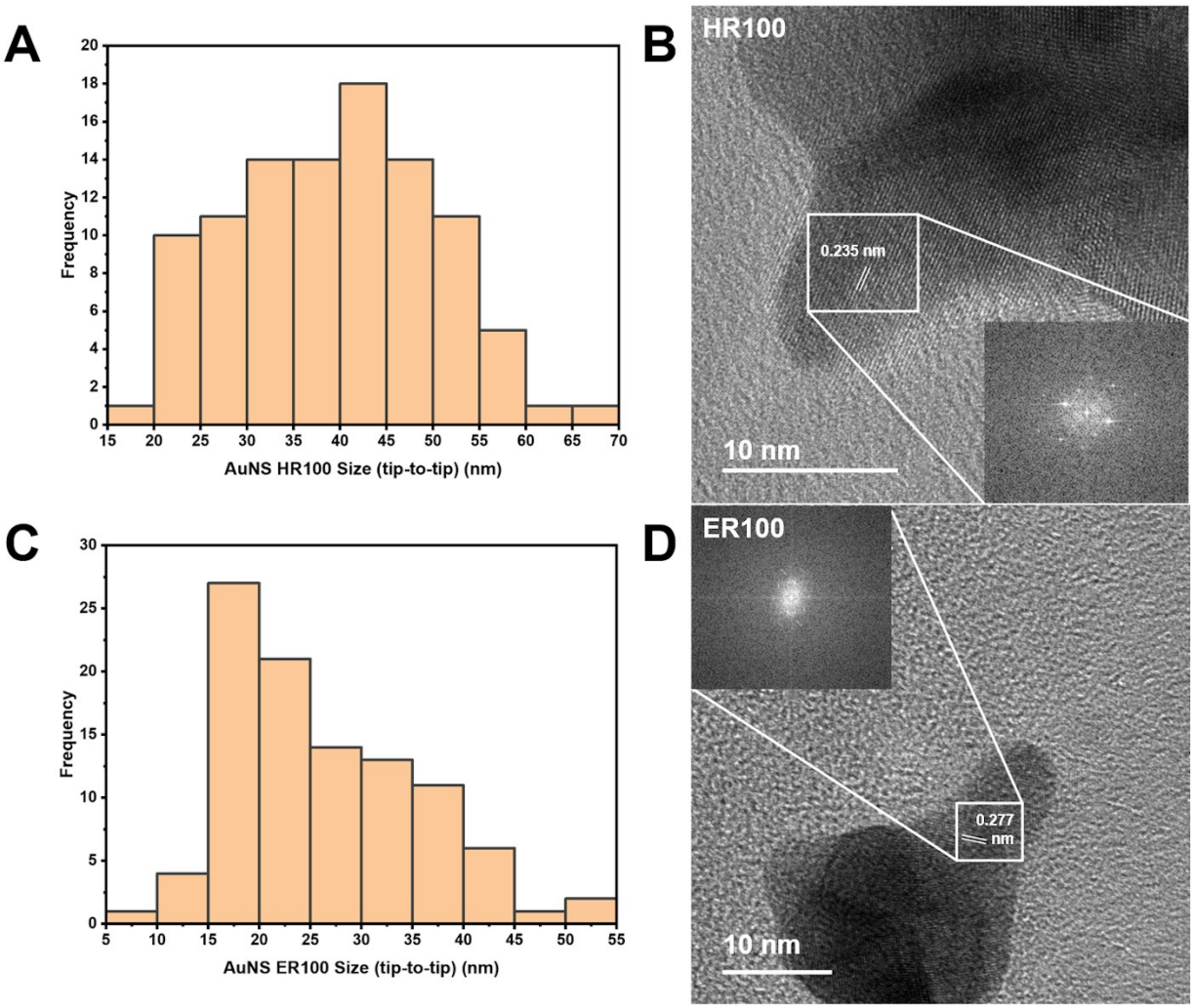

Figure 2-4. Size distribution analysis and TEM imaging of AuNS. Histograms and TEM images of AuNS using HEPES (A and B) and EPPS (C and D) at R 100. The white boxes represent the area where FFT analysis was performed.

The optical properties of AuNS synthesized using EPPS buffer are qualitatively similar to those from HEPES as shown in Figure 2-2B. The primary mode is red-shifted as R is increased from 100 to 1000. One notable difference between the HEPES and EPPS is the presence of two plasmon modes for ER100. This suggests a spherical core (26 ± 9 nm, tip-to-tip, or furthest tip points) with smaller branch lengths (6 ± 2 nm) in comparison to nanostars synthesized at higher ratios. Odom and co-workers have thoroughly examined the extinction spectra of AuNS synthesized using EPPS, including subtle changes at higher

ratios.[32] Our results are consistent with their observations. The TEM images for ER100 and ER1000 indicate a shape evolution from more spherical NPs with small branches to NPs dominated by long branches. In general, the λ_{max} for NPs synthesized in EPPS is lower than those in HEPES for a given R. It has been reported that the branches grow in the [110] direction in EPPS[32] and the difference in λ_{max} is likely due to the variations in crystal structure of the branches. The results in Figure 2-2 are qualitatively similar to those reported in the literature[32] and describe the evolution of both the shape and optical properties of AuNS with buffer type and concentration.

2.3.2. In-Solution SERS Performance of AuNS

In-solution SERS using colloidal NPs has proven to be a challenge. Spherical NPs do not yield substantial SERS intensities without inducing aggregation.[45-46] Nanoparticles with shapes such as rods[47] and dog-bones[48-49] have demonstrated promise as colloidal SERS substrates. As shown in Table 2-1, most of the SERS applications of AuNS have been in the solid-state with the exception of work by Haes and co-workers in the measurement of uranyl with functionalized AuNS.[27] In the work presented here, we examine the SERS performance of AuNS synthesized using HEPES and EPPS buffers with different R and using a handheld Raman instrument. Mercaptobenzonitrile (MBN) was chosen as a Raman probe due to its ability to specifically adsorb to the AuNS surface. We chose to conduct our measurements without any centrifugation or cleaning steps following synthesis. This represents a facile approach of performing SERS measurements directly after NP synthesis. Figure 2-5 shows the SERS spectra of 5 μM MBN mixed with AuNS prepared from R100 solutions for both HEPES and EPPS buffers. The spectra were collected with a handheld

instrument following 2 min of stirring (vortex). The major Raman bands are identified in Table 2-2 according to previously published papers.[50-52] Note that the only evidence of the buffer itself is the shoulder at 1044 cm^{-1} (Figure 2-6). Both buffers yield AuNS that provide in-solution SERS spectra with reasonable signal-to-noise without the need to form aggregate generated hot-spots.

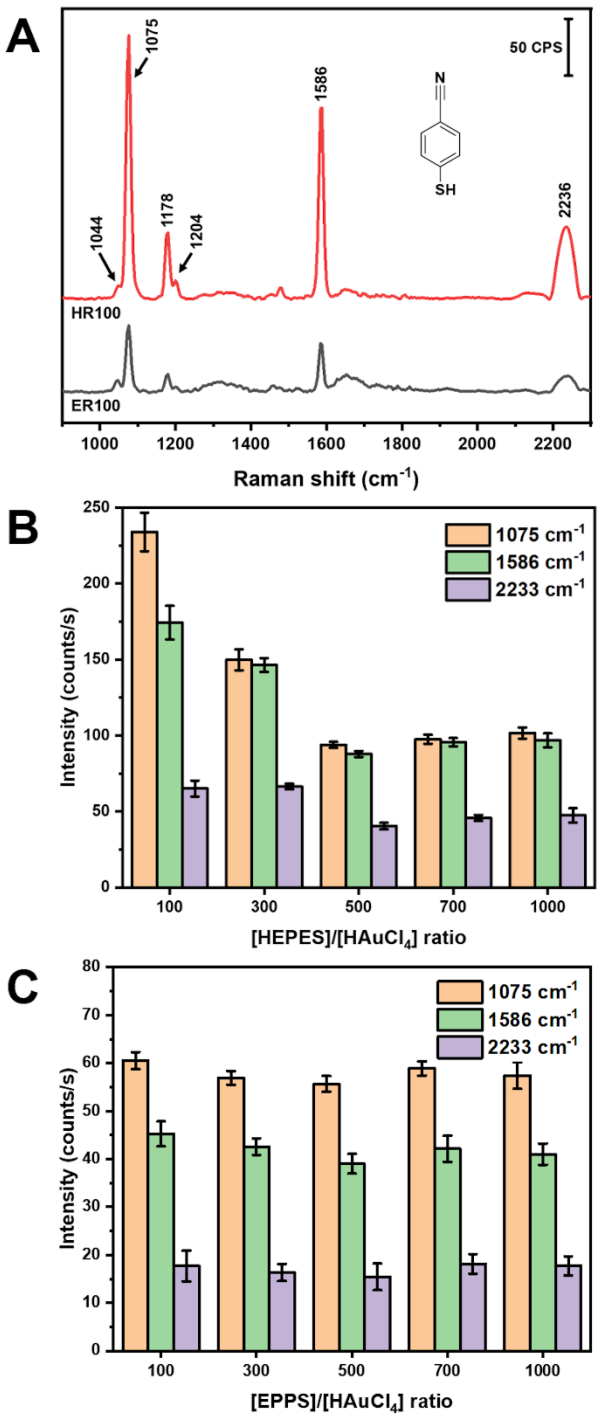

Figure 2-5. AuNS SERS optimization based on buffer type and [buffer] to [$HAuCl_4$] ratio. (A) SERS spectra of 5 μM MBN comparing AuNS HR100 ([AuNS] = 2.2 nM) and ER100 ([AuNS] = 1.2 nM). Column graph of the peak height of different vibrational modes of MBN at different ratios using (B) HEPES and (C) EPPS.

Table 2-2. Major Band Assignments Listed for the SERS Spectrum of 4-Mercaptobenzonitrile on AuNS

Band position (cm^{-1})	Assignment[50-52]
1075	C–S and C–C stretch
1178	C–H bend and C–C stretch
1204	C–H bend and C–C≡N stretch
1586	C–C stretch
2233	C≡N stretch

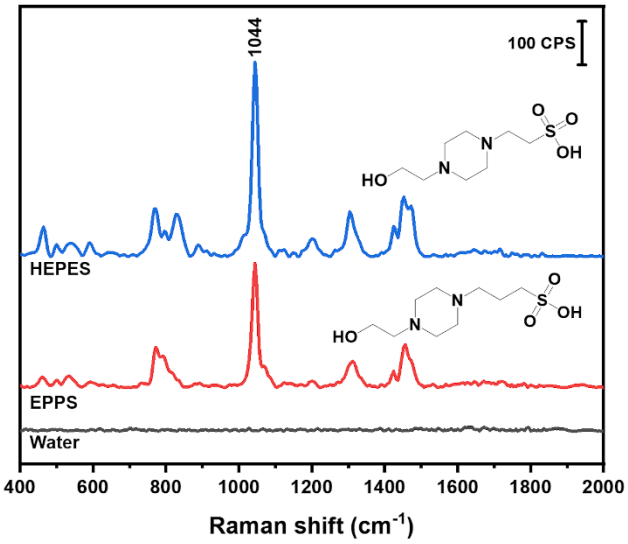

Figure 2-6. Solution Raman spectra of water, EPPS and HEPES buffer.

The band intensities observed in Figure 2-5A for the AuNS from HEPES are approximately 4× more intense than those in EPPS. A summary of the intensities of the three major bands at 1075 cm^{-1} (C–S stretch, ν_{CS}, and C–C stretch, ν_{CC}), 1586 cm^{-1} (C–C stretch, ν_{CC}), and 2233 cm^{-1}(C≡N stretch, ν_{CN}) of MBN for the different buffers and concentration ratios are shown in parts B and C of Figure 2-5.[50-52] The results for HEPES show a dependence on R, while the intensity is insensitive to R for EPPS. In Figure 2-5B, the intensity of all bands decrease as R increases with the highest intensities observed at

HR100 and are 2× that of HR1000. This is surprising considering the shapes of the AuNS, where the longer and sharper branches formed from higher R may be expected to yield higher SERS intensity. However, the variations of the SERS intensities observed are, at most, a factor of 4, and as described below, we believe these differences are primarily due to surface coverage of the probe MBN rather than any large electromagnetic differences.

HEPES and EPPS both act as a reducing, shape directing and stabilizing agent in the synthesis of AuNS.[32, 37] The piperazine moiety contains two cationic free radical tertiary amines that can reduce Au^{3+} to Au^{0}.[32, 36] Additionally, the terminal alkanesulfonate group interacts with the AuNS surface and acts as a shape directing agent, while the terminal hydroxyl group acts as a stabilizing agent and facilitates bilayer formation of the buffer ligand.[32-33, 37] MBN will have to compete with the HEPES or EPPS for surface sites. Previous studies suggest that at lower HEPES concentration the formation of a bilayer is incomplete or collapsed.[33, 37] Conversely, at high HEPES concentration (>100 mM) the formation of a bilayer inhibits the adsorption of MBN. Thus, MBN can compete more favourably for AuNS surface sites when R = 100.

Figure 2-5 plots the intensities of the MBN bands for ER100 to ER1000. A comparison of the intensities between parts B and C of Figure 2-5 shows that the AuNS prepared from HEPES provide more intense SERS signals for all R values. This difference is a factor of 4 for R100 and a factor of 2 for higher buffer concentrations. Again, we believe these modest differences in SERS intensities are due to the amount of probe adsorbed in each case. The additional methylene group in EPPS may promote a more densely packed monolayer on the AuNS through hydrophobic interactions similar to alkanethiols

monolayers leading to less available surface sites for Raman active molecules.[53] Another factor involves the growth direction of the AuNS branches in each buffer. As previously noted, it has been shown that HEPES induces branch growth in the [111] direction while EPPS results in branches in the [110] direction.[32] It is known that the surface coverage of thiol-derived monolayers depends on the gold crystal face.[54] Thus, surface coverage of MBN binding to the AuNS will be influenced by these different crystal faces. Another observation from Figure 2-5C is that the peak intensities of MBN are relatively constant regardless of the EPPS buffer to gold ratio. One possible explanation involves the energetics of bilayer formation for HEPES-HEPES vs. EPPS-EPPS. A computational study using the polarizable continuum model determined that HEPES-HEPES and EPPS-EPPS dimers have a binding energy of 25.7 and -1.0 KJ/mol, respectively.[33] Thus, while HEPES can form stable bilayers at higher concentrations, bilayer formation with EPPS is less favourable. The AuNS formed in EPPS are thus coated with a more densely packed monolayer of stabilizing agent that does not vary with concentration of EPPS. In summary, colloidal AuNS prepared from HR100 solutions provide the highest in-solution SERS intensity for the MBN probe and overall greater enhancement than EPPS. The experiments described in the next section are all carried out with HR100 AuNS.

2.3.3. Reproducibility and Additional Enhancement

One of the potential benefits of using a colloidal SERS substrate and in-solution measurements is high reproducibility provided by sample homogeneity. Figure 2-7A shows SERS spectra of MBN from AuNS within the same batch on different days. The peak intensity from the C-S stretching vibration on different days is plotted in Figure 2-7B. The

AuNS HR100 were exposed to 5 µM MBN and measured on Day 0. The samples were then measured after being stored at 4 °C for the given period of time. Slight deviations in intensity may be the result of several factors. The initial spectra (Day 0) is obtained after 2 minutes of mixing and the thiolate layer may be incomplete. Additionally, over 78 days adsorption/desorption of the thiolate, changes in molecular orientation and gold surface reconstruction could result in slight variations in intensity. However, any significant destabilization of the AuNS would result in substantial changes in intensity. Over a period of 78 days, the AuNS showed a percent relative standard deviation (%RSD) range (1-5%) within the same day and %RSD of 8% over the entire time period suggesting an excellent colloidal stability and a long-term storage capability at 4 °C. This demonstrates the applicability to store functionalized AuNS long-term.

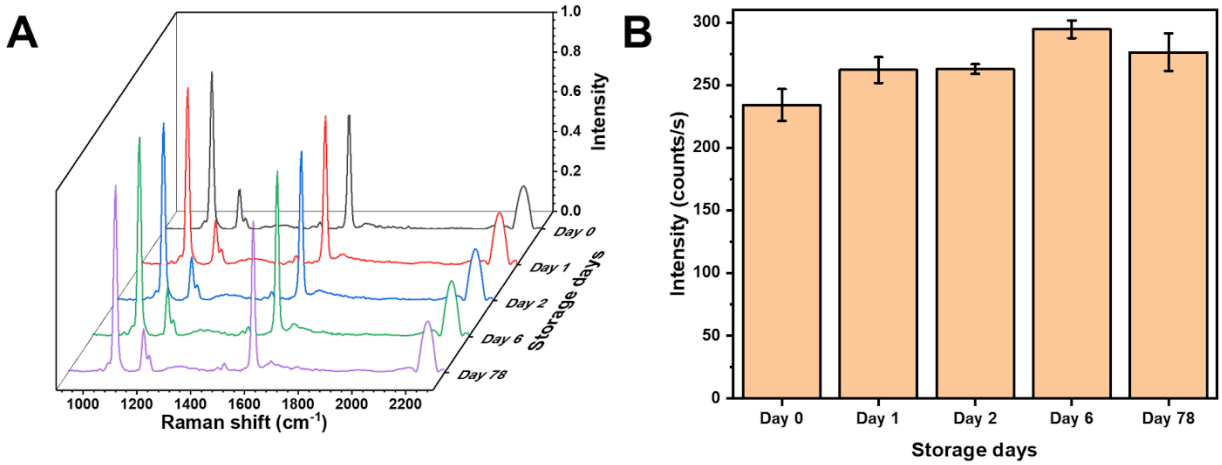

Figure 2-7. SERS reproducibility and long-term storage of colloidal AuNS. (A) SERS spectra of MBN showing signal reproducibility from AuNS substrates. (B) Bar chart of MBN C-S stretch peak intensity showing stability of AuNS at 4 °C.

Aggregating agents are commonly used to enhance the SERS signals in solution by entrapping molecules between interstitial hot spots.[55-56] We explored the possibility of

increasing the observed signals by adding NaCl (200 mM) to produce dispersible AuNS nano-aggregates. Figure 2-8A shows in-solution SERS spectra of MBN in AuNS HR100 before and after the addition of NaCl. The addition of NaCl results in a significant increase in peak intensity; a factor of about 10 for the C-S stretch at 1075 cm^{-1}. The extinction spectra in Figure 2-8B provides evidence for the formation of salt induced nano-aggregates. The AuNS HR100 exhibits a LSPR λ_{max} at 566 nm. The addition of MBN indicates a slight decrease in the extinction and the appearance of a tail in the 600-775 nm range of the spectrum. There is also a slight colour change from light purple to dark purple. This is attributed to MBN adsorbing to the AuNS surface and changing the local dielectric constant. After the addition of NaCl, there is a large red-shift and broadening of the LSPR peak indicating the formation of AuNS aggregates. The colour of the AuNS changes from a dark purple to a light blue/grey. The UV-Vis extinction results are consistent with the formation of AuNS nano-aggregates with the addition of NaCl, and this explains the large enhancement observed in the SERS data.

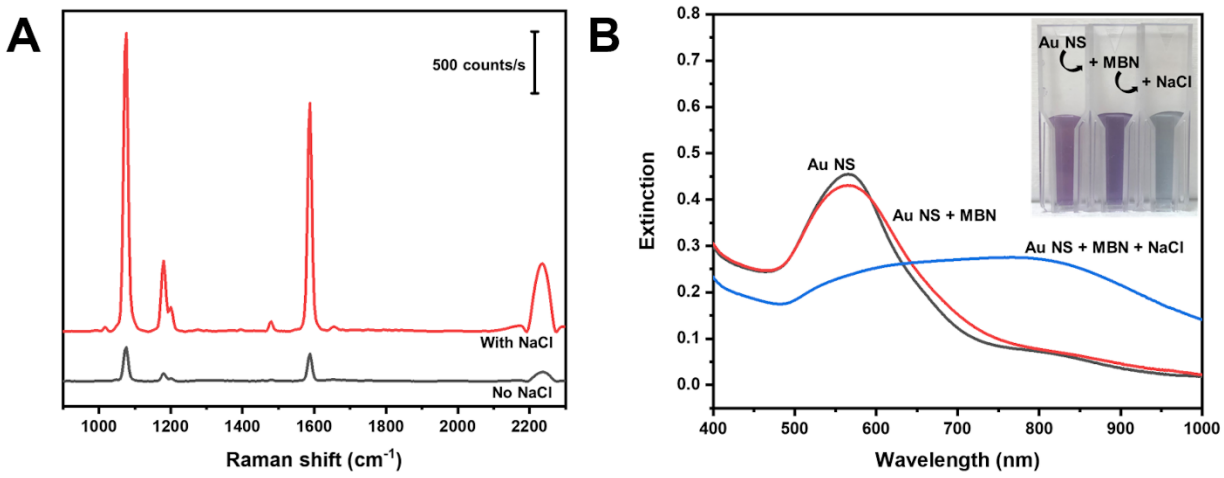

Figure 2-8. Additional SERS enhancement using NaCl. (A) SERS spectra of MBN using AuNS HR100 before and after salt addition. (B) UV-Vis spectra showing the extinction of AuNS HR100, after the addition of MBN and after the addition of MBN and NaCl.

The size and colloidal stability of the AuNS nano-aggregates were studied using DLS and zeta potential measurements, and the results are shown in Table 2-3. The AuNS HR100 have a z-average diameter of 49.4 ± 0.9 nm. With the addition of MBN, we observe an increase in the z-average diameter due to the adsorption of MBN onto the AuNS surface through a gold-thiol linkage. Addition of NaCl causes the z-average diameter to increase to 379 nm indicating the formation of AuNS nano-aggregates. The polydispersity index (PDI) decreases with the addition of MBN and NaCl indicating the AuNS become more uniformly dispersed. The zeta potential remains relatively constant with the addition of MBN and NaCl.

Table 2-3. Size and Colloidal Stability Study of AuNS Nano-Aggregates Using Dynamic Light Scattering and Zeta Potential Measurements.

AuNS HR100	z-average diameter (nm)[a]	PDI[a]	Zeta potential (mV)[b]
Unmodified	49.4 ± 0.9	0.38 ± 0.04	-35 ± 1
+ MBN	54.7 ± 0.4	0.29 ± 0.01	-36.9 ± 0.9
+ NaCl	379 ± 54	0.23 ± 0.03	-34 ± 2

[a] n=5 with each measurement consisting of 13 sub-measurements. Analysis is based on a measurement time of 8 minutes. [b] n=5 with each measurement consisting of 20 sub-measurements. Analysis is based on a measurement time of 5 minutes. pH values of the AuNS solutions were at 6.5-7 and were measured using Accumet pH paper.

2.3.4. Applications of AuNS for In-Solution SERS

In the absence of any programmed molecular recognition, analytes will have to adsorb onto the AuNS in order to be detected. In this work, different adsorption mechanisms were investigated. Figure 2-9 contains the in-solution SERS spectra of four different analytes, before and after nano-aggregate formation, that are expected to interact with the AuNS via different mechanisms. All analytes were detected in solution within five minutes of mixing.

Thiabendazole (TBZ) (Figure 2-9A) and methimazole (MTZ) (Figure 2-9B) are examples of sulfur containing molecules which adsorb on AuNS by chemisorption through a S-Au interaction. Malachite green (MG) (Figure 2-9C) and ciprofloxacin (Cipro) (Figure 2-9D) are examples of non-sulfur containing molecules that will likely physisorb through the aromatic rings or N groups. All of these analytes can be rapidly measured (within 5 minutes) in the low μM range using colloidal AuNS via either chemisorption or physisorption mechanisms using the handheld Raman device. This points to the ability of a range of molecular structures to compete with HEPES for surface sites on the AuNS surface. As shown in Figure 2-9, the analytes are detectable with un-aggregated AuNS. However, with the addition of NaCl the analyte signal is significantly enhanced due to aggregation and the subsequent formation of SERS hot spots.

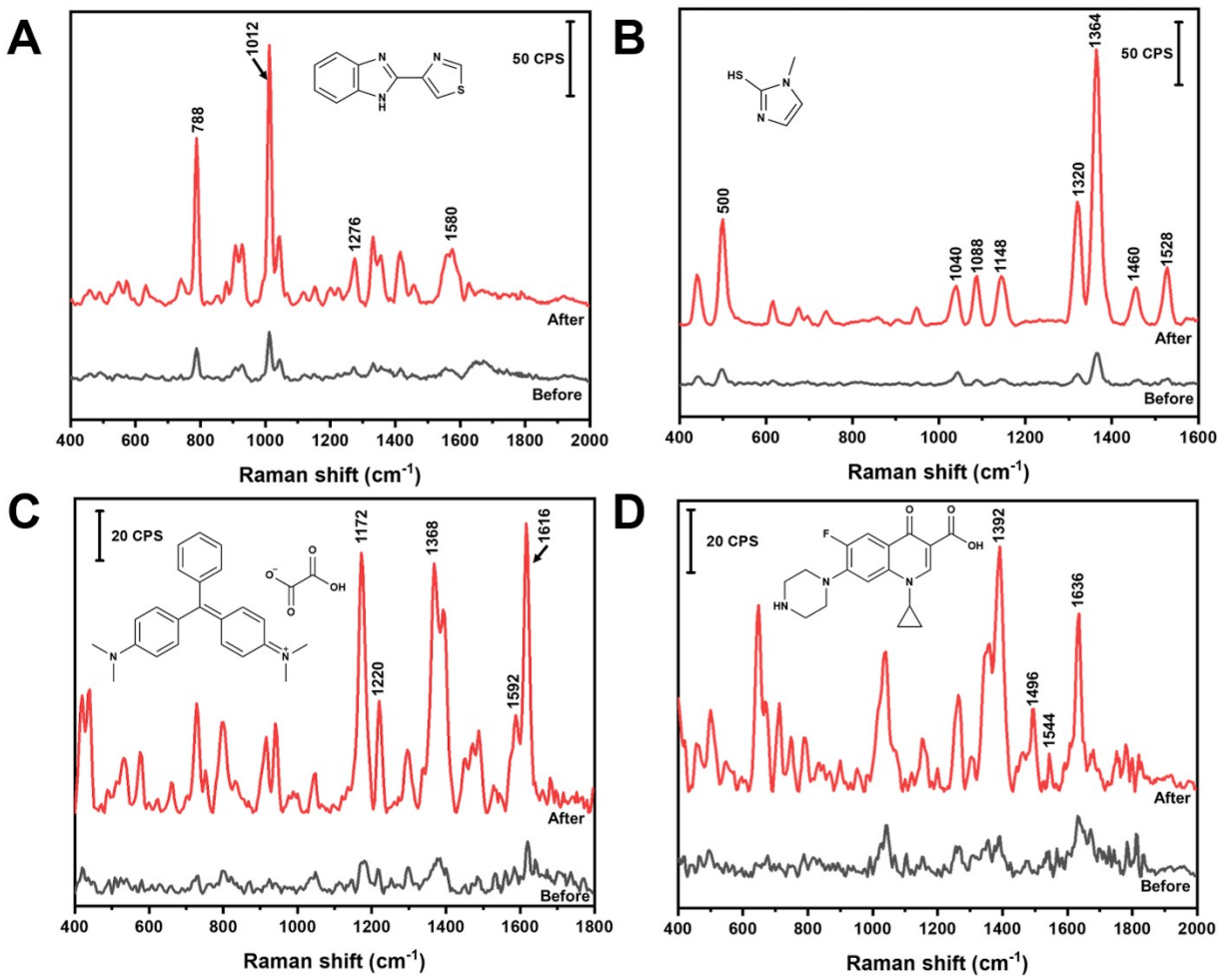

Figure 2-9. Applications for in-solution SERS measurements using AuNS. (A) 5 µM thiabendazole in 0.1 M HCl, (B) 1 µM methimazole in water, (C) 0.5 µM malachite green in water and (D) 5 µM ciprofloxacin in 0.1 M HCl using a colloidal AuNS HR100 substrate before and after the addition of NaCl (200 mM).

Thiabendazole (TBZ) is a common fungicide applied after harvest to prevent mould and rot on fruit and vegetables.[57] The use of TBZ has been classified as likely to be carcinogenic at high concentrations and poses thyroid hormone production imbalance risks.[58-59] Since TBZ is a widely used on fruits and vegetables ranging from applesauce to sweet potatoes, the maximum residue limit (MRL) will differ per commodity. For example, the United States Environmental Protection Agency (US EPA) has set a tolerance limit of 5 ppm and 10 ppm for applesauce and sweet potatoes, respectively (~25-50 µM).[60] Figure 2-

9A shows the SERS spectrum of 5 μM TBZ adsorbed on AuNS before and after the addition of NaCl (200 mM). The major bands are summarized in Table 2-4 according to a previously published paper.[61]

Table 2-4. Major Bands Assignments Listed for the SERS Spectrum of Thiabendazole on AuNS

Band position (cm^{-1})	Assignment[61]
788	C–H out-of-plane bend
1012	C–H out-of-plane bend
1276	Ring stretch
1580	Ring stretch and C=N stretch

Malachite green (MG) is a highly effective fungicide used to mitigate fungi and parasite growth in the aquaculture industry.[62] In Canada, MG is approved for use on aquarium fish only, and is not permitted for use on food-producing animals/fish.[63] MG and its metabolite, leucomalachite green, are known to reside in fish tissue and are known to have mutagenic and teratogenic effects on humans.[62-63] While its use on aquarium fish is approved, improper disposal or careless treatment of aquarium fish could lead to accidental contamination of surrounding bodies of water and fish. Figure 2-9C shows the in-solution SERS spectrum of 0.5 μM MG adsorbed on colloidal AuNS before and after the addition of NaCl. These bands are summarized in Table 2-5 according to a previously published paper.[64] MG was used as an example of a fluorescent dye to show the capability of AuNS to detect such a molecule.

Table 2-5. Major Bands Assignments Listed for the SERS Spectrum of Malachite Green on AuNS

Band position (cm^{-1})	Assignment[64]
1172	In-plane C–H ring vibration
1220	C–H rock
1368	N-phenyl stretch
1592	C–C stretch
1616	C–C stretch

Ciprofloxacin (Cipro) is a fluoroquinolone antibiotic used to treat bacterial infections relating to the urinary tract, prostatitis, sinusitis, bones and joints.[65] Figure 2-9D shows the SERS spectrum of Cipro adsorbed on AuNS before and after the addition of NaCl at a concentration of 5 μM. These bands are summarized in Table 2-6 according to previously published papers.[66-67]

Table 2-6. Major Bands Assignments Listed for the SERS Spectrum of Ciprofloxacin on AuNS

Band position (cm^{-1})	Assignment[66-67]
1392	Symmetric O–C–O stretch
1496	Asymmetric O–C–O stretch
1544	Quinolone ring stretch
1636	Asymmetric aromatic ring stretch

Further development of a quantitative method and measurement in a complex matrix was carried out for MTZ. MTZ is commonly used as an anti-hormone pharmaceutical to treat hyperthyroidism by regulating the production of thyroxine and triiodothyronine.[68-69] Moreover, MTZ is often illegally applied to animal feed to promote animal weight gain by

increasing water retention in tissues.[68, 70] Monitoring and limiting human exposure is important as MTZ is known to have multiple negative side effects. These side effects include skin irritation, allergic reactions, impaired taste, pharyngitis, nephritis and liver cirrhosis.[68-69, 71] In addition, metabolization of MTZ leads to further MTZ intermediates known to have cytotoxic effects in the body.[71] Chromatography is commonly used to detect and quantify MTZ in urine.[69] However, the chromatographic method requires instrumental expertise, sample extraction, pre-concentration, or derivatization treatment before analysis.[68-69] The limit of detection of MTZ by liquid chromatography methods can range from a concentration of nM to μM.[68-69] A simple and less labour intensive method that can competitively quantify MTZ in urine would be useful. Figure 2-9B shows the SERS spectrum of 1 μM MTZ before and after the addition of NaCl adsorbed on AuNS. This demonstrates the promise of in-solution SERS with a handheld device to measure this analyte. The band assignments are summarized in Table 2-7.

Table 2-7. Major Bands Assignments Listed for the SERS Spectrum of Methimazole on AuNS

Band position (cm^{-1})	Assignment[72-77]
500	S–C–N in plane bend
616	Ring out-of-plane bend, ring C–H and N–H out-of-plane bend
1037	Ring bend, ring C–H bend and C–S–H bend
1086	Ring C–N stretch and ring C–H bend
1145	C–S stretch, ring C–H bend and C–N stretch
1320	Ring C–N stretch, ring bend and ring C–H bend
1364	C–N stretch, ring bend and ring C–H bend

Figure 2-10 contains the results for the method development and quantitation of MTZ using in-solution SERS. First, we estimated the in-solution SERS enhancement factor of the MTZ AuNS system with the handheld device. Figure 2-10A contains the SERS spectra of MTZ in water in the absence and presence of AuNS. The band intensity at 1364 cm^{-1} is low and only slightly visible above the background for 16 mM MTZ in water. The MTZ (0.917 μM)-AuNS nano-aggregate mixture exhibit a large enhancement at 1364 cm^{-1}. The enhancement factor for AuNS HR100 was determined using the analytical enhancement factor formula[78], as shown in Equation 2-1:

$$\boldsymbol{A.E.F.} = \frac{I_{SERS}/c_{SERS}}{I_{Raman}/c_{Raman}} \quad \textbf{Equation 2-1}$$

where I_{SERS} and I_{Raman} are the peak intensities at 1364 cm^{-1} of MTZ in the presence and in the absence of AuNS HR100, respectively. The c_{SERS} and c_{Raman} terms are the solution concentrations of MTZ in the SERS and normal Raman measurements (0.917 μM and 16 mM), respectively. The enhancement factor from the AuNS was calculated to be 5.2×10^5. This value is comparable to those measured for both solid[79] and in-solution[29, 80] substrates and indicates sufficient signal intensity for quantitative analysis.[78] The Raman spectrum for solid MTZ can be found in Figure 2-11.

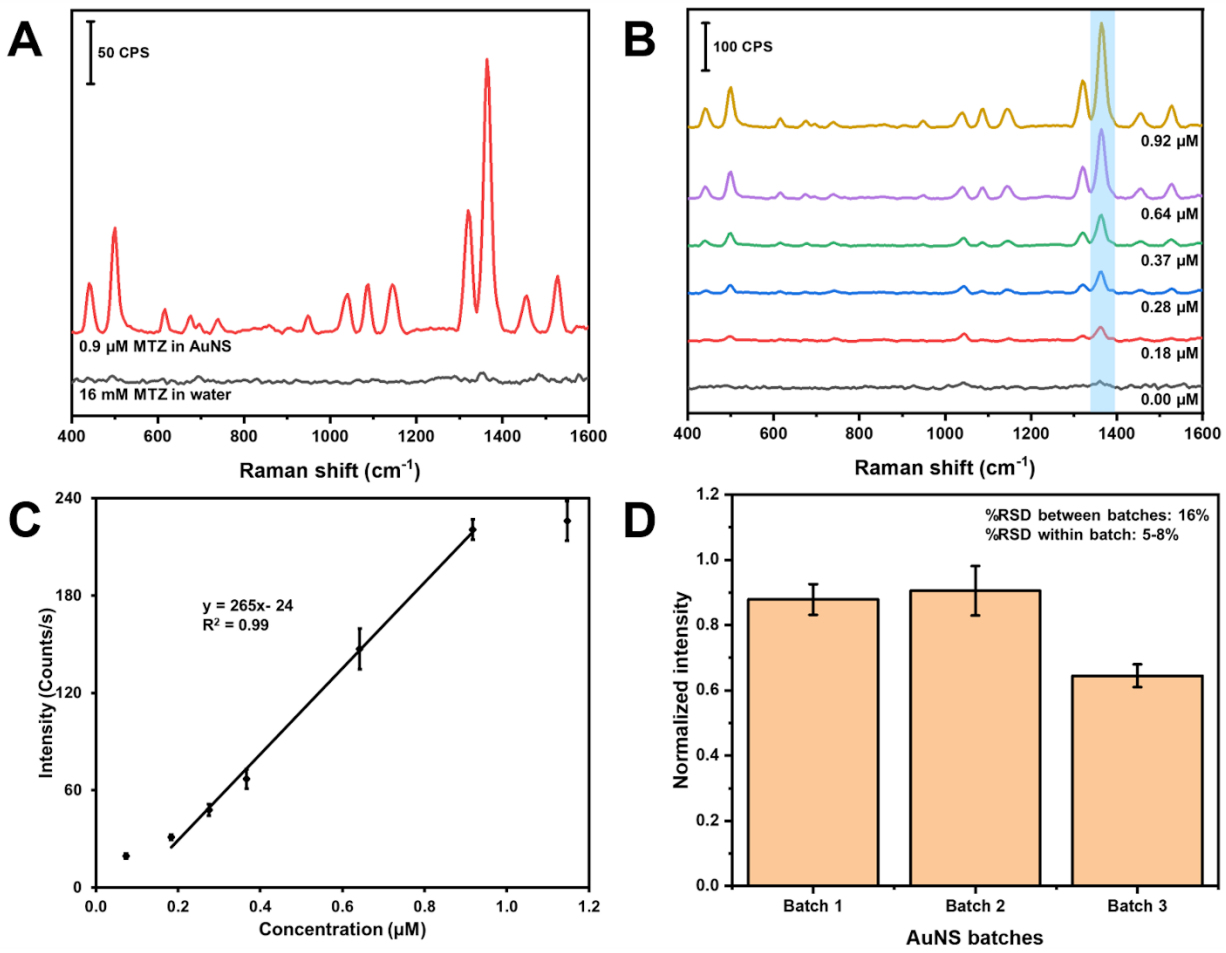

Figure 2-10. Quantitation of MTZ using colloidal AuNS. (A) SERS spectra showing the enhancement of MTZ in the presence of AuNS HR100. (B) SERS spectra of MTZ at various concentrations using AuNS HR100 and NaCl. (C) Calibration curve of MTZ using colloidal AuNS HR100. (D) Bar graph of the batch to batch reproducibility of AuNS using MTZ.

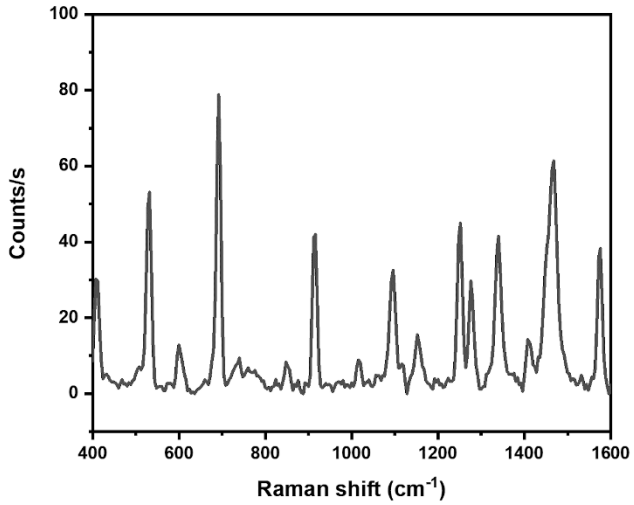

Figure 2-11. Raman spectrum of solid methimazole.

Parts B and C of Figure 2-10 demonstrate quantitation of MTZ using colloidal AuNS nano-aggregates as a water dispersible SERS substrate. The SERS spectra of MTZ at different concentrations in water is shown in Figure 2-10B. Each concentration is represented by an average spectrum composed of three samples measured three times at different spots in a glass vial (n=9). The N-C stretching band at 1364 cm^{-1} used for quantitation is highlighted in light blue and band intensities increase with concentration.

Figure 2-10C is a plot of the intensity of the 1364 cm^{-1} band versus concentration. The plot exhibits a linear portion and curves at low and high concentration. The curvature at lower concentration indicates the limit of the measurement. The "levelling-off" observed at high concentrations likely indicates that the adsorption sites on the AuNS nano-aggregates are saturated. A linear least squares fit of a portion of the plot can be used as a calibration curve. From this linear portion, the limit of detection and limit of quantification were calculated to be 0.1 and 0.3 μM. The dynamic range is determined to be between 0.3 and 0.9 μM.

The batch-to-batch reproducibility of the AuNS was monitored using the peak intensity at 1364 cm^{-1} of MTZ. Figure 2-10D shows a bar chart of the peak intensity using three different AuNS batches. Each batch consists of three samples analyzed three times at different spots on the vial (n=9). The %RSD between samples within the same batch was between 5-8%, while the %RSD between different batches was 16%. The %RSD for SERS substrates is generally reported up to about 15-20%.[81]

Human urine is a complex matrix consisting of non-protein nitrogenous compounds (e.g., urea), inorganic ions and salts, water soluble toxins and haemoglobin by-products.[82] Individuals that use MTZ to treat hyperthyroidism will excrete excess amounts in their urine.[68-69] The amount of MTZ retained in tissues can be harmful to the individuals health.[68] The amount of MTZ retained in tissues can be quantified by monitoring the amount of MTZ excreted in urine. In this study, we spiked synthetic urine with MTZ and used our colloidal AuNS SERS substrate to quantify the amount of MTZ. Figure 2-12 shows the Raman spectra of MTZ found in urine along with the corresponding control experiments. A band at 1008 cm^{-1} is prominent in the spectrum of pure urine that likely corresponds to the symmetrical CN stretch of urea.[82]

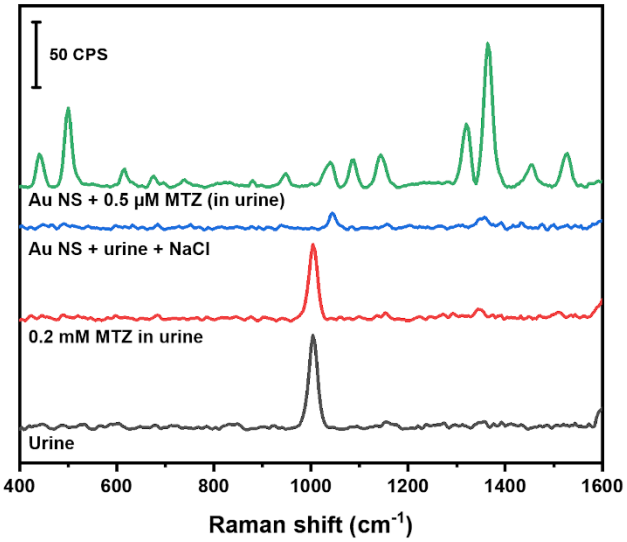

Figure 2-12. In-solution SERS spectrum of methimazole in urine and associated control spectra.

When urine is spiked with MTZ (0.2 mM as the final concentration), no bands corresponding to MTZ are observed. When urine is mixed with the AuNS nanoaggregate substrate, only a band from the HEPES buffer is visible. The disappearance of the 1008 cm^{-1} is due to the 200× dilution of the urine into the AuNS. The urine sample spiked with MTZ (0.5 µM final concentration) mixed with the AuNS nanoaggregates shows a large enhancement of MTZ Raman bands. Using the calibration curve obtained in water (Figure 2-10C), MTZ in urine was examined at 0.5 and 0.8 µM and our method provided recoveries of nearly 100% (Table 2-8).

Table 2-8. Recoveries of Methimazole in Urine Using AuNS Nano-Aggregates as a SERS Substrate

Spiked amount of MTZ (µM)	Calc. amount of MTZ (µM)	% Recovery	% RSD
0.5	0.495 ± 0.009	99 ± 2	2%
0.8	0.83 ± 0.05	104 ± 6	5%

2.4. Conclusions

The synthesis of AuNS using HEPES and EPPS buffer were systematically explored to determine the optimal buffer and buffer-to-gold ratio for in-solution SERS analysis. Differences in SERS intensities between HEPES and EPPS at different R values are primarily due to surface coverage of MBN on the AuNS instead of enhanced electromagnetic effects. AuNS synthesized using HEPES at R 100 produced the highest signal intensities. The AuNS showed a %RSD of 8% in signal intensity over 78 days at 4 °C and the ability to detect a variety of analytes in under 5 minutes through chemisorption and physisorption mechanisms. The addition of NaCl to the AuNS increases the SERS intensity by a factor of about 10 through the formation of nanoaggregates. A SERS assay was developed for the detection and quantitation of MTZ. The assay showed a limit of detection of 0.1 μM and a recovery of nearly 100% when MTZ was spiked in urine. The merging of in-solution substrates and handheld Raman spectrometers open new avenues for rapid and reproducible on-site SERS analysis.

2.5. References

1. Crocombe, R. A., Portable Spectroscopy. *Appl. Spectrosc.* **2018,** *72* (12), 1701-1751.

2. Deidda, R.; Sacre, P.-Y.; Clavaud, M.; Coïc, L.; Avohou, H.; Hubert, P.; Ziemons, E., Vibrational spectroscopy in analysis of pharmaceuticals: Critical review of innovative portable and handheld NIR and Raman spectrophotometers. *TrAC, Trends Anal. Chem.* **2019,** *114*, 251-259.

3. Pilot, R., SERS detection of food contaminants by means of portable Raman instruments. *J. Raman Spectrosc.* **2018,** *49* (6), 954-981.

4. Langer, J.; Jimenez de Aberasturi, D.; Aizpurua, J.; Alvarez-Puebla, R. A.; Auguié, B.; Baumberg, J. J.; Bazan, G. C.; Bell, S. E. J.; Boisen, A.; Brolo, A. G.; Choo, J.; Cialla-May, D.; Deckert, V.; Fabris, L.; Faulds, K.; García de Abajo, F. J.; Goodacre, R.; Graham, D.; Haes, A. J.; Haynes, C. L.; Huck, C.; Itoh, T.; Käll, M.; Kneipp, J.; Kotov, N. A.; Kuang, H.; Le Ru, E. C.; Lee, H. K.; Li, J.-F.; Ling, X. Y.; Maier, S. A.; Mayerhöfer, T.; Moskovits, M.; Murakoshi, K.; Nam, J.-M.; Nie, S.; Ozaki, Y.; Pastoriza-Santos, I.; Perez-Juste, J.; Popp, J.; Pucci, A.; Reich, S.; Ren, B.; Schatz, G. C.; Shegai, T.; Schlücker, S.; Tay, L.-L.; Thomas, K. G.; Tian, Z.-Q.; Van Duyne, R. P.; Vo-Dinh, T.; Wang, Y.; Willets, K. A.; Xu, C.; Xu, H.; Xu, Y.; Yamamoto, Y. S.; Zhao, B.; Liz-Marzán, L. M., Present and Future of Surface-Enhanced Raman Scattering. *ACS Nano* **2020,** *14* (1), 28-117.

5. Xia, Y.; Halas, N. J., Shape-Controlled Synthesis and Surface Plasmonic Properties of Metallic Nanostructures. *MRS Bull.* **2011,** *30* (5), 338-348.

6. Hao, E.; Schatz, G. C., Electromagnetic fields around silver nanoparticles and dimers. *J. Chem. Phys.* **2004,** *120* (1), 357-366.

7. Stiles, P. L.; Dieringer, J. A.; Shah, N. C.; Duyne, R. P. V., Surface-Enhanced Raman Spectroscopy. *Annu. Rev. Anal. Chem.* **2008,** *1* (1), 601-626.

8. Gole, A.; Murphy, C. J., Seed-Mediated Synthesis of Gold Nanorods: Role of the Size and Nature of the Seed. *Chem. Mater.* **2004,** *16* (19), 3633-3640.

9. Nikoobakht, B.; El-Sayed, M. A., Preparation and Growth Mechanism of Gold Nanorods (NRs) Using Seed-Mediated Growth Method. *Chem. Mater.* **2003,** *15* (10), 1957-1962.

10. Sau, T. K.; Murphy, C. J., Room Temperature, High-Yield Synthesis of Multiple Shapes of Gold Nanoparticles in Aqueous Solution. *J. Am. Chem. Soc.* **2004,** *126* (28), 8648-8649.

11. Kou, X.; Ni, W.; Tsung, C. K.; Chan, K.; Lin, H. Q.; Stucky, G. D.; Wang, J., Growth of Gold Bipyramids with Improved Yield and Their Curvature-Directed Oxidation. *Small* **2007,** *3* (12), 2103-2113.

12. Skrabalak, S. E.; Au, L.; Li, X.; Xia, Y., Facile synthesis of Ag nanocubes and Au nanocages. *Nat. Protoc.* **2007,** *2* (9), 2182-2190.

13. Pelaz, B.; Grazu, V.; Ibarra, A.; Magen, C.; del Pino, P.; de la Fuente, J. M., Tailoring the Synthesis and Heating Ability of Gold Nanoprisms for Bioapplications. *Langmuir* **2012,** *28* (24), 8965-8970.

14. Ahsan, H.; Masaaki, T.; Guang, W. Y., Formation of Gold Nanoparticles by Good's Buffers. *Bull. Chem. Soc. Jpn.* **2005,** *78* (2), 262-269.

15. Nehl, C. L.; Hafner, J. H., Shape-dependent plasmon resonances of gold nanoparticles. *J. Mater. Chem.* **2008,** *18* (21), 2415-2419.

16. Xie, J.; Lee, J. Y.; Wang, D. I. C., Seedless, Surfactantless, High-Yield Synthesis of Branched Gold Nanocrystals in HEPES Buffer Solution. *Chem. Mater.* **2007,** *19* (11), 2823-2830.

17. Banholzer, M. J.; Millstone, J. E.; Qin, L.; Mirkin, C. A., Rationally designed nanostructures for surface-enhanced Raman spectroscopy. *Chem. Soc. Rev.* **2008,** *37* (5), 885-897.

18. Huang, X.; Neretina, S.; El-Sayed, M. A., Gold Nanorods: From Synthesis and Properties to Biological and Biomedical Applications. *Adv. Mater.* **2009,** *21* (48), 4880-4910.

19. Murphy, C. J.; Gole, A. M.; Hunyadi, S. E.; Stone, J. W.; Sisco, P. N.; Alkilany, A.; Kinard, B. E.; Hankins, P., Chemical sensing and imaging with metallic nanorods. *Chem. Commun.* **2008,** (5), 544-557.

20. Rycenga, M.; Langille, M. R.; Personick, M. L.; Ozel, T.; Mirkin, C. A., Chemically Isolating Hot Spots on Concave Nanocubes. *Nano Lett.* **2012,** *12* (12), 6218-6222.

21. Gersten, J. I., The effect of surface roughness on surface enhanced Raman scattering. *J. Chem. Phys.* **1980,** *72* (10), 5779-5780.

22. Tian, F.; Bonnier, F.; Casey, A.; Shanahan, A. E.; Byrne, H. J., Surface enhanced Raman scattering with gold nanoparticles: effect of particle shape. *Anal. Methods* **2014,** *6* (22), 9116-9123.

23. Rodríguez-Lorenzo, L.; Álvarez-Puebla, R. A.; Pastoriza-Santos, I.; Mazzucco, S.; Stéphan, O.; Kociak, M.; Liz-Marzán, L. M.; García de Abajo, F. J., Zeptomol Detection Through Controlled Ultrasensitive Surface-Enhanced Raman Scattering. *J. Am. Chem. Soc.* **2009,** *131* (13), 4616-4618.

24. Indrasekara, A. S. D. S.; Meyers, S.; Shubeita, S.; Feldman, L. C.; Gustafsson, T.; Fabris, L., Gold nanostar substrates for SERS-based chemical sensing in the femtomolar regime. *Nanoscale* **2014,** *6* (15), 8891-8899.

25. Sánchez-Purrà, M.; Carré-Camps, M.; de Puig, H.; Bosch, I.; Gehrke, L.; Hamad-Schifferli, K., Surface-Enhanced Raman Spectroscopy-Based Sandwich Immunoassays for Multiplexed Detection of Zika and Dengue Viral Biomarkers. *ACS Infect. Dis.* **2017,** *3* (10), 767-776.

26. Sánchez-Purrà, M.; Roig-Solvas, B.; Rodriguez-Quijada, C.; Leonardo, B. M.; Hamad-Schifferli, K., Reporter Selection for Nanotags in Multiplexed Surface Enhanced Raman Spectroscopy Assays. *ACS Omega* **2018,** *3* (9), 10733-10742.

27. Lu, G.; Forbes, T. Z.; Haes, A. J., SERS detection of uranyl using functionalized gold nanostars promoted by nanoparticle shape and size. *Analyst* **2016,** *141* (17), 5137-5143.

28. Lu, G.; Johns, A. J.; Neupane, B.; Phan, H. T.; Cwiertny, D. M.; Forbes, T. Z.; Haes, A. J., Matrix-Independent Surface-Enhanced Raman Scattering Detection of Uranyl Using Electrospun Amidoximated Polyacrylonitrile Mats and Gold Nanostars. *Anal. Chem.* **2018,** *90* (11), 6766-6772.

29. Nalbant Esenturk, E.; Hight Walker, A. R., Surface-enhanced Raman scattering spectroscopy via gold nanostars. *J. Raman Spectrosc.* **2009,** *40* (1), 86-91.

30. Senthil Kumar, P.; Pastoriza-Santos, I.; Rodríguez-González, B.; Javier García de Abajo, F.; Liz-Marzán, L. M., High-yield synthesis and optical response of gold nanostars. *Nanotechnology* **2007,** *19* (1), 015606.

31. Yuan, H.; Khoury, C. G.; Hwang, H.; Wilson, C. M.; Grant, G. A.; Vo-Dinh, T., Gold nanostars: surfactant-free synthesis, 3D modelling, and two-photon photoluminescence imaging. *Nanotechnology* **2012,** *23* (7), 075102.

32. Chandra, K.; Culver, K. S. B.; Werner, S. E.; Lee, R. C.; Odom, T. W., Manipulating the Anisotropic Structure of Gold Nanostars using Good's Buffers. *Chem. Mater.* **2016,** *28* (18), 6763-6769.

33. Liu, H.; Xu, Y.; Qin, Y.; Sanderson, W.; Crowley, D.; Turner, C. H.; Bao, Y., Ligand-Directed Formation of Gold Tetrapod Nanostructures. *J. Phys. Chem. C* **2013,** *117* (33), 17143-17150.

34. Cai, J.; Raghavan, V.; Bai, Y. J.; Zhou, M. H.; Liu, X. L.; Liao, C. Y.; Ma, P.; Shi, L.; Dockery, P.; Keogh, I.; Fan, H. M.; Olivo, M., Controllable synthesis of tetrapod gold nanocrystals with precisely tunable near-infrared plasmon resonance towards highly efficient surface enhanced Raman spectroscopy bioimaging. *J. Mater. Chem. B* **2015,** *3* (37), 7377-7385.

35. Chen, R.; Wu, J.; Li, H.; Cheng, G.; Lu, Z.; Che, C.-M., Fabrication of gold nanoparticles with different morphologies in HEPES buffer. *Rare Met.* **2010,** *29* (2), 180-186.

36. Grady, J. K.; Chasteen, N. D.; Harris, D. C., Radicals from "Good's" buffers. *Anal. Biochem.* **1988,** *173* (1), 111-115.

37. Xi, W.; Haes, A. J., Elucidation of HEPES Affinity to and Structure on Gold Nanostars. *J. Am. Chem. Soc.* **2019,** *141* (9), 4034-4042.

38. Dam, D. H. M.; Lee, J. H.; Sisco, P. N.; Co, D. T.; Zhang, M.; Wasielewski, M. R.; Odom, T. W., Direct Observation of Nanoparticle–Cancer Cell Nucleus Interactions. *ACS Nano* **2012,** *6* (4), 3318-3326.

39. de Puig, H.; Tam, J. O.; Yen, C.-W.; Gehrke, L.; Hamad-Schifferli, K., Extinction Coefficient of Gold Nanostars. *J. Phys. Chem. C* **2015,** *119* (30), 17408-17415.

40. Menges, F. Spectragryph - optical spectroscopy software. http://www.effemm2.de/spectragryph/ (accessed February 20, 2020).

41. Jalani, G.; Cerruti, M., Nano graphene oxide-wrapped gold nanostars as ultrasensitive and stable SERS nanoprobes. *Nanoscale* **2015,** *7* (22), 9990-9997.

42. Nergiz, S. Z.; Gandra, N.; Singamaneni, S., Self-assembled high aspect ratio gold nanostar/graphene oxide hybrid nanorolls. *Carbon* **2014,** *66*, 585-591.

43. Hao, F.; Nehl, C. L.; Hafner, J. H.; Nordlander, P., Plasmon Resonances of a Gold Nanostar. *Nano Lett.* **2007,** *7* (3), 729-732.

44. Webb, J. A.; Erwin, W. R.; Zarick, H. F.; Aufrecht, J.; Manning, H. W.; Lang, M. J.; Pint, C. L.; Bardhan, R., Geometry-Dependent Plasmonic Tunability and Photothermal Characteristics of Multibranched Gold Nanoantennas. *J. Phys. Chem. C* **2014,** *118* (7), 3696-3707.

45. Faulds, K.; Littleford, R. E.; Graham, D.; Dent, G.; Smith, W. E., Comparison of Surface-Enhanced Resonance Raman Scattering from Unaggregated and Aggregated Nanoparticles. *Anal. Chem.* **2004,** *76* (3), 592-598.

46. Graham, D.; Thompson, D. G.; Smith, W. E.; Faulds, K., Control of enhanced Raman scattering using a DNA-based assembly process of dye-coded nanoparticles. *Nat. Nanotechnol.* **2008,** *3* (9), 548-551.

47. Saute, B.; Premasiri, R.; Ziegler, L.; Narayanan, R., Gold nanorods as surface enhanced Raman spectroscopy substrates for sensitive and selective detection of ultra-low levels of dithiocarbamate pesticides. *Analyst* **2012,** *137* (21), 5082-5087.

48. Saute, B.; Narayanan, R., Solution-based direct readout surface enhanced Raman spectroscopic (SERS) detection of ultra-low levels of thiram with dogbone shaped gold nanoparticles. *Analyst* **2011,** *136* (3), 527-532.

49. Saute, B.; Narayanan, R., Solution-based SERS method to detect dithiocarbamate fungicides in different real-world matrices. *J. Raman Spectrosc.* **2013,** *44* (11), 1518-1522.

50. Gkogkou, D.; Schreiber, B.; Shaykhutdinov, T.; Ly, H. K.; Kuhlmann, U.; Gernert, U.; Facsko, S.; Hildebrandt, P.; Esser, N.; Hinrichs, K.; Weidinger, I. M.; Oates, T. W. H., Polarization- and Wavelength-Dependent Surface-Enhanced Raman Spectroscopy Using Optically Anisotropic Rippled Substrates for Sensing. *ACS Sens.* **2016,** *1* (3), 318-323.

51. Holze, R., Competition of anchoring groups in adsorption on gold electrodes—a comparative spectroelectrochemical study of 4-mercaptobenzonitrile and aromatic nitriles. *J. Solid State Electrochem.* **2013,** *17* (7), 1869-1879.

52. Villarreal, E.; Li, G. G.; Zhang, Q.; Fu, X.; Wang, H., Nanoscale Surface Curvature Effects on Ligand–Nanoparticle Interactions: A Plasmon-Enhanced Spectroscopic Study of Thiolated Ligand Adsorption, Desorption, and Exchange on Gold Nanoparticles. *Nano Lett.* **2017,** *17* (7), 4443-4452.

53. Porter, M. D.; Bright, T. B.; Allara, D. L.; Chidsey, C. E. D., Spontaneously organized molecular assemblies. 4. Structural characterization of n-alkyl thiol monolayers on gold by optical ellipsometry, infrared spectroscopy, and electrochemistry. *J. Am. Chem. Soc.* **1987,** *109* (12), 3559-3568.

54. III, N. C.; Chidsey, C. E. D.; Liu, G. y.; Scoles, G., Substrate dependence of the surface structure and chain packing of docosyl mercaptan self-assembled on the (111), (110), and (100) faces of single crystal gold. *J. Chem. Phys.* **1993,** *98* (5), 4234-4245.

55. Bell, S. E. J.; Sirimuthu, N. M. S., Surface-Enhanced Raman Spectroscopy (SERS) for Sub-Micromolar Detection of DNA/RNA Mononucleotides. *J. Am. Chem. Soc.* **2006,** *128* (49), 15580-15581.

56. Yaffe, N. R.; Ingram, A.; Graham, D.; Blanch, E. W., A multi-component optimisation of experimental parameters for maximising SERS enhancements. *J. Raman Spectrosc.* **2010,** *41* (6), 618-623.

57. Alsammarraie, F. K.; Lin, M.; Mustapha, A.; Lin, H.; Chen, X.; Chen, Y.; Wang, H.; Huang, M., Rapid determination of thiabendazole in juice by SERS coupled with novel gold nanosubstrates. *Food Chem.* **2018,** *259*, 219-225.

58. Liou, P.; Nayigiziki, F. X.; Kong, F.; Mustapha, A.; Lin, M., Cellulose nanofibers coated with silver nanoparticles as a SERS platform for detection of pesticides in apples. *Carbohydr. Polym.* **2017,** *157*, 643-650.

59. USEPA EPA reregistration eligibility decision thiabendazole. United States Environmental Protection Agency: 2002. https://archive.epa.gov/pesticides/reregistration/web/pdf/thiabendazole_red.pdf (accessed March 31, 2019).

60. USDA Pesticide Data Program Annual Summary, Calendar Year 2017. United States Department of Agriculture: 2017. https://www.ams.usda.gov/sites/default/files/media/2017PDPAnnualSummary.pdf (accessed March 31, 2019).

61. Kim, M. S.; Kim, M. K.; Lee, C. J.; Jung, Y. M.; Lee, M.-S., Surface-enhanced Raman Spectroscopy of Benzimidazolic Fungicides: Benzimidazole and Thiabendazole. *Bull. Korean Chem. Soc.* **2009,** *30* (12), 2930-2934.

62. Zhao, Y.; Tian, Y.; Ma, P.; Yu, A.; Zhang, H.; Chen, Y., Determination of melamine and malachite green by surface-enhanced Raman scattering spectroscopy using starch-coated silver nanoparticles as substrates. *Anal. Methods* **2015,** *7* (19), 8116-8122.

63. CFIA Malachite Green - Questions and Answers. Canadian Food Inspection Agency. http://www.inspection.gc.ca/food/information-for-consumers/fact-sheets-and-infographics/products-and-risks/chemical-hazards/malachite-green/eng/1332268890141/1332268947157 (accessed April 2, 2019).

64. Chamuah, N.; Bhuyan, N.; Das, P. P.; Ojah, N.; Choudhary, A. J.; Medhi, T.; Nath, P., Gold-coated electrospun PVA nanofibers as SERS substrate for detection of pesticides. *Sens. Actuators, B* **2018,** *273*, 710-717.

65. Hidi, I. J.; Heidler, J.; Weber, K.; Cialla-May, D.; Popp, J., Ciprofloxacin: pH-dependent SERS signal and its detection in spiked river water using LoC-SERS. *Anal. Bioanal. Chem.* **2016,** *408* (29), 8393-8401.

66. Neugebauer, U.; Szeghalmi, A.; Schmitt, M.; Kiefer, W.; Popp, J.; Holzgrabe, U., Vibrational spectroscopic characterization of fluoroquinolones. *Spectrochim. Acta, Part A* **2005,** *61* (7), 1505-1517.

67. Yang, L.; Qin, X.; Jiang, X.; Gong, M.; Yin, D.; Zhang, Y.; Zhao, B., SERS investigation of ciprofloxacin drug molecules on TiO2 nanoparticles. *PCCP* **2015,** *17* (27), 17809-17815.

68. Ebrahimzadeh, H.; Asgharinezhad, A. A.; Adlnasab, L.; Shekari, N., Optimization of ion-pair based hollow fiber liquid phase microextraction combined with HPLC–UV for the determination of methimazole in biological samples and animal feed. *J. Sep. Sci.* **2012,** *35* (16), 2040-2047.

69. Kuśmierek, K.; Bald, E., Determination of methimazole in urine by liquid chromatography. *Talanta* **2007,** *71* (5), 2121-2125.

70. Kong, D.; Chi, Y.; Chen, L.; Dong, Y.; Zhang, L.; Chen, G., Determination of thyreostatics in animal feeds by CE with electrochemical detector. *Electrophoresis* **2009,** *30* (19), 3489-3495.

71. Genter, M. B., Evaluation of olfactory and auditory system effects of the antihyperthyroid drug carbimazole in the Long-Evans rat. *J. Biochem. Mol. Toxicol.* **1998,** *12* (5), 305-314.

72. Fei, J.; Wu, L.; Zhang, Y.; Zong, S.; Wang, Z.; Cui, Y., Pharmacokinetics-on-a-Chip Using Label-Free SERS Technique for Programmable Dual-Drug Analysis. *ACS Sens.* **2017,** *2* (6), 773-780.

73. Ma, P.; Liang, F.; Yang, Q.; Wang, D.; Sun, Y.; Wang, X.; Gao, D.; Song, D., Highly sensitive SERS probe for mercury(II) using cyclodextrin-protected silver nanoparticles functionalized with methimazole. *Microchim. Acta* **2014,** *181* (9), 975-981.

74. Muniz-Miranda, M.; Muniz-Miranda, F.; Pedone, A., Raman and DFT study of methimazole chemisorbed on gold colloidal nanoparticles. *PCCP* **2016,** *18* (8), 5974-5980.

75. Saleh, T. A.; Al-Shalalfeh, M. M.; Al-Saadi, A. A., Graphene Dendrimer-stabilized silver nanoparticles for detection of methimazole using Surface-enhanced Raman scattering with computational assignment. *Sci. Rep.* **2016,** *6*, 32185.

76. Saleh, T. A.; Al-Shalalfeh, M. M.; Al-Saadi, A. A., Silver nanoparticles for detection of methimazole by surface-enhanced Raman spectroscopy. *Mater. Res. Bull.* **2017,** *91*, 173-178.

77. Saleh, T. A.; Al-Shalalfeh, M. M.; Onawole, A. T.; Al-Saadi, A. A., Ultra-trace detection of methimazole by surface-enhanced Raman spectroscopy using gold substrate. *Vib. Spectrosc* **2017,** *90*, 96-103.

78. Le Ru, E. C.; Blackie, E.; Meyer, M.; Etchegoin, P. G., Surface Enhanced Raman Scattering Enhancement Factors: A Comprehensive Study. *J. Phys. Chem. C* **2007,** *111* (37), 13794-13803.

79. Osinkina, L.; Lohmüller, T.; Jäckel, F.; Feldmann, J., Synthesis of Gold Nanostar Arrays as Reliable, Large-Scale, Homogeneous Substrates for Surface-Enhanced Raman Scattering Imaging and Spectroscopy. *J. Phys. Chem. C* **2013,** *117* (43), 22198-22202.

80. Kneipp, K.; Kneipp, H.; Manoharan, R.; Hanlon, E. B.; Itzkan, I.; Dasari, R. R.; Feld, M. S., Extremely Large Enhancement Factors in Surface-Enhanced Raman Scattering for Molecules on Colloidal Gold Clusters. *Appl. Spectrosc.* **1998,** *52* (12), 1493-1497.

81. Panneerselvam, R.; Liu, G.-K.; Wang, Y.-H.; Liu, J.-Y.; Ding, S.-Y.; Li, J.-F.; Wu, D.-Y.; Tian, Z.-Q., Surface-enhanced Raman spectroscopy: bottlenecks and future directions. *Chem. Commun.* **2018,** *54* (1), 10-25.

82. Moreira, L. P.; Silveira, L.; Pacheco, M. T. T.; da Silva, A. G.; Rocco, D. D. F. M., Detecting urine metabolites related to training performance in swimming athletes by means of Raman spectroscopy and principal component analysis. *J. Photochem. Photobiol., B* **2018,** *185*, 223-234.

Chapter 3. Plasmonic Cellulose Nanofibers as Water-Dispersible Surface-Enhanced Raman Scattering Substrates

3.1. Introduction

The progression of substrate development continues to evolve surface-enhanced Raman scattering (SERS) into a more effective chemical sensing and sensitive analytical measurement technique.[1-2] SERS measurement platforms are generally categorized into solid-based and solution-based substrates. Highly reproducible nanostructured rigid substrates are effective for chemical sensing, however, these substrates can be associated with high costs, and can require specialized equipment and expertise in nano-lithographic fabrication methods.[3-4] The in-situ synthesis and deposition of nanoparticles on light-weight and flexible supports, such as cellulose and polymer, are economical alternatives for SERS measurements.[3, 5] For example, Kim et al. have developed low-cost and high-performance cellulose-based plasmonic nanocomposites.[6-7] There are, however, some intrinsic challenges pertaining to solid-based substrates, and these include spot-to-spot irreproducibility and slow-mass transport of the nanoparticle and/or analyte to the surface. Crawford et al. have shown that SERS measurement reproducibility is impacted by the laser spot size, and that smaller spot sizes can lead to greater measurement imprecision.[8]

Colloidal nanoparticles of different shapes and sizes, such as spheres, nanorods, dog-bone shapes and nanostars, have been used as solution-based SERS substrates.[9-19] The synthesis of colloids is relatively straightforward and can be scaled up economically.[11] Long adsorption periods and tedious washing/drying steps associated with solid-based substrates are not necessary for in-solution SERS. Dynamic solution mixing decreases the necessary adsorption time of the analyte to the nanoparticle surface and solution homogeneity can provide the potential for reproducible analysis. However, individual colloidal nanoparticles do not provide strong SERS signals in solution, and assembly into dimers and larger clusters is generally required to generate SERS hot-spots.[20] Controlling nanoparticle aggregation and the stability of aggregated nanoparticles in solution is challenging.[21] Methods involving various aggregating agents and DNA hybridization have been reported.[9, 11-12] Moreover, buffer and polymer solutions have been used to maintain the stability of aggregated nanoparticles in solution.[13-14, 22] Another approach for in-solution SERS is to deposit metallic nanoparticles onto larger dispersible support structures. For example, a high density of silver nanoparticles were grown onto poly(styrene-co-acrylic acid) nanospheres and supported with polyvinylpyrrolidone for in-solution measurements of melamine.[23] In another example, silver nanoparticles were grown onto cellulose nanocrystals (CNC) for in-solution measurements of riboflavin.[24] Silver nanoparticles have also been grown onto silica/CNC nanocomposites for in-solution measurements of malachite green.[25] These latter two reports demonstrate the potential of metal nanoparticle/CNC hybrid materials for in-solution SERS. The work presented here describes the optimization of a substrate based on high aspect ratio cellulose nanomaterials and highlights the value of this substrate for in-solution SERS.

Cellulose nanofibers (CNF) are a class of cellulose nanomaterials well known for their high aspect ratio with a length of >1 μm and width of 20-100 nm.[26-27] Surface modification with 2,2,6,6-tetramethylpyperidine-1-oxyl (TEMPO) oxidization produces CNF rich in surface carboxylate groups and this provides excellent colloidal stability in water.[28-29] Cellulose nanomaterials have previously been used for the synthesis of metal nanoparticles where the oxygen containing moieties of cellulose act as nucleation and stabilization sites for nanoparticle growth.[30] For example, CNF has been used as a capping agent in the synthesis of various nanoparticle shapes.[31-32] These nanocomposites are almost exclusively deposited onto a solid substrate to form a thin film on glass or flexible substrate.[5, 31-34] The benefit of using CNF as a support is the opportunity to produce multiple nanoparticles in close proximity to each other producing hot spots for SERS analysis. However, application of these materials suffers from an intrinsic solid-based SERS substrate limitation; spot-to-spot irreproducibility. Moreover, the analysis is generally time consuming because of the two-dimensional diffusion-limited adsorption of the analyte to the metal nanoparticle. A water dispersible substrate can improve on these limitations by offering higher reproducibility because of solution homogeneity and faster analysis time due to three-dimensional diffusion of the analyte to the nanoparticle. There is one example of liquid phase SERS measurements using metal decorated CNF that employs a drop on a glass slide.[32] However, this method falls short of ideal SERS solution measurements. To the best of our knowledge, metal decorated CNF has not been explored as a water-dispersible SERS substrate.

Herein, we developed a water-dispersible SERS substrate featuring Ag nanoparticles (Ag NP) on CNF. The synthesis of Ag NPs on CNF is accomplished using ascorbic acid (AA)

as a reducing agent. We demonstrate that CNF plays an important role in the synthesis of plasmonic cellulose nanofibers (Ag-CNF) by acting as a support for Ag NPs and a dispersing agent for Ag-CNF. The nanoparticles are anchored in close proximity and well dispersed in solution, and this results in large and reproducible SERS enhancement. Furthermore, analysis using aqueous Ag-CNF provides rapid detection of analytes (~2 minutes) due to faster mass transport of the analyte to the nanoparticle surface in comparison to planar SERS substrates. Ag-CNF is optimized in terms of its SERS intensity using mercaptobenzonitrile (MBN) as a Raman active molecule. Reagent mixing, temperature and CNF concentration are a controlling factor in the size of Ag NPs. The nanofibers form nano-sized bundles upon centrifugation but re-disperse in water and remain colloidally stable. We show rapid analysis of analytes using both chemisorption and physisorption that could be used to detect pesticides and fungicides.

3.2. Experimental

3.2.1. Materials

Commercial Bleached Chemi-Thermo Mechanical Pulp (BCTMP, 60% water content) from a local company was used to synthesize CNF. Hydrochloric acid (HCl, 37.5%), laboratory grade 2,2,6,6-tetramethylpiperidinyl-1-oxyl radical (TEMPO), sodium hypochlorite solution (NaOCl, 13%), sodium bromide (NaBr, 99.0%), sodium chloride (NaCl, 99%), malachite green oxalate salt technical grade (MG) and rhodamine 6G (R6G, 95%) were purchased from Sigma-Aldrich Canada. Silver nitrate ($AgNO_3$) and sodium hydroxide (NaOH) were purchased from Fisher-Scientific Canada. L-ascorbic acid (AA) was purchased from Anachemia and 4-mercaptobenzonitrile (MBN) was purchased from Combi-Blocks.

Commercial citrate capped NanoXact silver nanoparticles (Ag NP, 40 nm, 0.02 mg/mL) were purchased from nanoComposix. The 400-mesh carbon transmission electron microscopy (TEM) grids were purchased from Electron Microscopy Sciences and clear shell vials (1 mL) were purchased from VWR. Deionized (DI) water (18.2 MΩ·cm) was obtained from a MilliQ^{UV} Plus purification system and all reagents were used without further purification.

3.2.2. Preparation of TEMPO-Oxidized Cellulose Nanofibers

TEMPO-oxidation of CNF followed a similar method with slight modifications.[28-29] An aqueous solution of BCTMP (7 wt %) was mixed with TEMPO (0.1 mmol/g of BCTMP) and NaBr (1 mmol/g of BCTMP) at room temperature and stirred at 500 rpm. NaOCl (10 mmol/g of BCTMP) was added dropwise to the solution and maintained at a pH of 10.5 using HCl or NaOH. The reaction was complete when no pH variation was observed. The resulting CNF was washed three times via Büchner funnel filtration followed by disintegration using a Vitamix® Professional Series 300 blender (10 minutes; setting #10). The CNF was then stored at 4 °C for further use.

3.2.3. Determination of Carboxyl Content of TEMPO-Oxidized Cellulose Nanofibers

The carboxyl content of the CNF was determined via a conductometric titration with slight modifications using a conductivity meter (Meter Star, A212).[28-29] A CNF slurry was made by stirring freeze-dried CNF (0.2 g) with DI water (55 mL) and NaCl (5 mL, 10 mM). The initial pH of the slurry was adjusted to 2.5 using HCl (1 M) and was titrated to a pH of 11 using NaOH (0.05 M). The carboxyl content was determined using Equation 3-1:

$$\boldsymbol{COOH}\ \left(\frac{\boldsymbol{mmol}}{\boldsymbol{g}}\right) = \frac{[\boldsymbol{C}](\boldsymbol{V_2}-\boldsymbol{V_1})}{\boldsymbol{m_{CNF}}} \quad \textbf{(Equation 3-1)}$$

where C is the concentration of NaOH (mol/L), V_1 and V_2 is the volume of NaOH (mL) at the inflection points determined graphically and m_{CNF} is the mass of CNF (g). Titration was performed in triplicates.

3.2.4. Synthesis of Metal Decorated Cellulose Nanofibers

Figure 3-1 illustrates the experimental procedure for the synthesis of Ag-CNF. Aqueous solution of CNF was heated to 70 °C and $AgNO_3$ (0.2 mM) was added to the solution and mixed for 5 minutes at 400 rpm. AA was then added to the solution and mixed for another 5 minutes. The sample was then cooled to room temperature and aged for 0, 24, 48 and 72 hours in the dark. After aging, the sample was centrifuged at 14000 rpm for 10 minutes and re-dispersed to the same volume. The substrate was visually dispersed using a water bath sonicator. The substrate synthesis was optimized in terms of its SERS enhancement, and the concentration of CNF and AA were monitored at 0.01, 0.02, 0.04, 0.1 and 0.2 % and 0.002, 0.02, 0.2 and 2 mM, respectively.

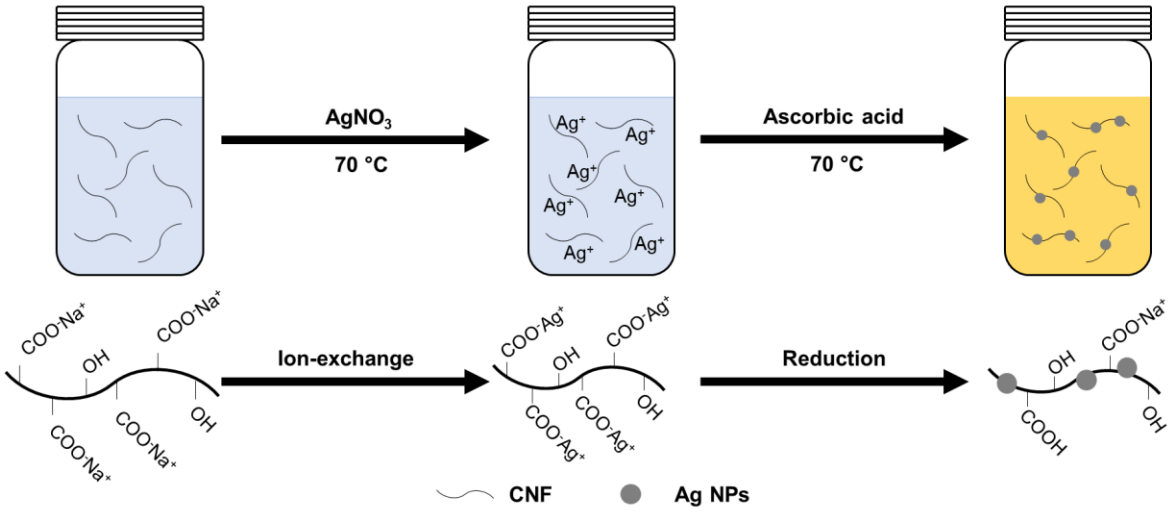

Figure 3-1. Synthesis of cellulose nanofibers decorated with silver nanoparticles.

3.2.5. Characterization

Scanning electron microscopy (SEM) images were taken using a Hitachi S-4800 field emission scanning electron microscope. Samples (10 µL) were drop-casted on a TEM grid, and after 2 minutes excess solution was wicked away and dried overnight. All samples were imaged at 30 keV and 20 µA. Images were processed using Gatan Digital Micrograph and analyzed with ImageJ software. The particle size distribution was created with an open-source program and represented as an average-shifted histogram (ASH).[35]

Atomic force microscopy (AFM) images were taken using a Digital Instruments Nanoscope III Multimode microscope. Images and data were acquired using Nanoscope in tapping mode at a scan size of 2.5 µm and scan rate of 1.969 Hz. CNF ($1x10^{-4}$ %) solution was drop-casted on a silicon substrate and left to dry overnight. Image processing and height profiling were completed using Gwyddion software. The height was determined from 20 single stranded fiber locations.

Zeta potential was measured using a Malvern Zetasizer Nano-ZS. Samples (1 mL) were analyzed in 2.5 mL BRAND® polystyrene disposable cuvettes using a zeta dip cell. Each sample was measured in triplicates consisting of 12 sub-runs and with an equilibrium time of 120 seconds and a temperature of 25 °C. The pH measurements were estimated using Hydrion pH paper (1-12).

Fourier transform infrared (FTIR) analysis was completed using a Nicolet 8700 continuum FTIR microscope. Samples were flattened on a silicon wafer and analyzed using a solid state FTIR microscope transmittance from 4000 to 650 cm^{-1} at 128 sample scans and a resolution of 4.000.

UV-Vis spectroscopy was completed using a PerkinElmer Lambda 35 with a slit of 1 nm and a scan rate of 960 nm/min from 300-900 nm. All samples were cooled to room temperature after synthesis and 1 mL of sample was analyzed in 2.5 mL BRAND® polystyrene disposable cuvettes.

X-ray photoelectron spectroscopy (XPS) analysis was performed on a Kratos AXIS-165 spectrometer with a monochromatic Al Kα source (1486.69 eV) at 140 W. Samples (200 µL) were drop-casted on a copper substrate and left overnight to dry. Survey and high resolution spectra of carbon, oxygen and silver were obtained for CNF and Ag-CNF. The instrument was run using a hybrid lens mode and iris slot with a magnification of 1e+37. For the survey scans, a dwell time of 0.1 seconds, a 400 meV step and a 160 eV analyzer pass energy was used. The acquisition time was a total of 600 seconds for a total of two sweeps. For the high-resolution spectra, a dwell time of 0.2 seconds, a 100 meV step and a 20 eV analyzer pass energy was used. The acquisition time was a total of 282 and 451 seconds for a total of 10 and 16 sweeps for CNF and Ag-CNF, respectively. The charge

neutralizer was on during acquisition of survey and high-resolution spectra. All data processing was completed using CasaXPS software. The library used for analysis was CasaXPS_KratosAxis-F1.lib and the survey and high-resolution scans were adjusted by setting the C 1s peak to 285.0 eV binding energy. All peaks were fitted with a Gaussian-Lorentzian line shape and a Shirley background.

X-ray diffraction (XRD) analysis was completed using a Bruker D8 Discover with an IμS Cu Kα source and Vantec 500 2D detector. Samples were analyzed with a 2θ coverage from 4 frames (120 seconds per frame), a scan range of 5-95 ° and a step size of 0.2 °. The Ag-CNF spectrum was scaled by a factor of ~4.4 based on the value at a 2θ of 18.2 ° in the CNF spectrum.

3.2.6. Raman Analysis

Raman experiments were completed using a Renishaw inVia Raman Microscope. The laser source is a RL633 50 mW HeNe laser. The microscope configuration was modified with a liquid cell adapter and an f=30 mm objective. Clear shell vials (1 mL) were used as the sampling container with a sampling volume of 1 mL. All samples were analyzed using the following spectral acquisition settings (unless stated otherwise): 632.8 nm laser, 100% power (4-5 mW), 5 seconds and 20 accumulations. Laser power was measured after each experiment and spectra were normalized in terms of power and time. The data was acquired using Wire 3.4 software and analyzed using open-source Spectragryph software.[36] Analyte adsorption time for Raman experiments was 2 minutes.

A B&W Tek NanoRam handheld Raman spectrometer (785 nm, 300 mW) was used to obtain a SERS spectrum of malachite green. Before analysis, the device was standardized using a polystyrene standard. A measurement was taken in a 1 dram vial and the handheld

was equipped with a liquid cell adapter. Malachite green had an adsorption time of 2 minutes before analysis.

3.3. Results and Discussion

3.3.1. Characterization of TEMPO-Oxidized Cellulose Nanofibers

High aspect ratio CNF that are colloidally stable in aqueous solutions serve as a Ag NP support for solution-based SERS applications. The size and morphology of the CNF fibers produced via TEMPO-oxidation were evaluated in images such as those shown in Figure 3-2. Analysis of SEM images (Figure 3-2A) reveals fibers that are 300 to 2000 nm in length. Cross-sectional analysis of intermittent-contact AFM images (Figure 3-2B) reveals a fiber width of 8 ± 2 nm. CNF sizes reported in the literature have high aspect ratios and widths as small as 3 nm.[37-38]

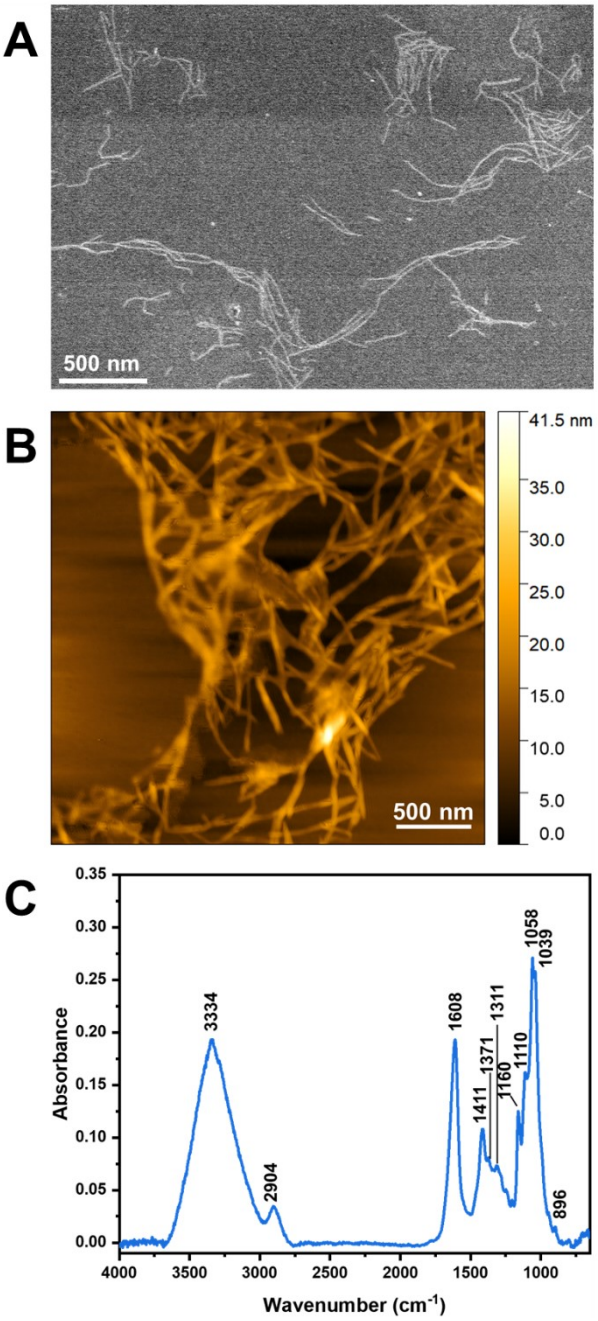

Figure 3-2. Characterization of TEMPO-oxidized cellulose nanofibers. (A) SEM and (B) AFM image of cellulose nanofibers. (C) FTIR spectrum of freeze-dried cellulose nanofibers at pH ~7-8.

TEMPO-oxidation of CNF is known to selectively convert the primary surface hydroxyl groups to carboxylic acid/carboxylate groups.[28] This surface chemistry and interfacial charge of the resulting CNF was characterized by IR analysis, titration and zeta

potential. Figure 3-2C contains the FTIR spectrum of the oxidized fibers. Assignment of the majority of the bands observed is found in Table 3-1. The primary feature in Figure 3-2C is the sharp peak at 1608 cm^{-1} that is assigned to the COO^- antisymmetric stretch.[37, 39-40] The measured pH of the stock CNF solution (~1 %) following TEMPO oxidation is ~7-8 and thus we expect the majority of the carboxylic acid groups to be deprotonated. The band at 3334 cm^{-1} corresponds to the O–H stretching of secondary alcohols on the CNF that are not expected to react with TEMPO. The zeta potential of a diluted solution of the CNF (0.02 %) is -51.3 ± 0.6 mV. This value is consistent with a high-density of surface carboxylate groups and is characteristic of colloidal stability.

Table 3-1. FTIR Spectroscopy Band Assignments for TEMPO-Oxidized Cellulose Nanofibers.

Wavenumber (cm^{-1})	IR band assignment[26, 37, 39-42]
3334	O–H stretch
2904	CH_2 stretch
1608	COO^- antisymmetric stretch
1411	COO^- symmetric stretch
1371	C–H bend
1311	CH_2 wag
1160	C–O–C glycosidic antisymmetric stretch
1110	C–O stretch
1058	C–O stretch
1039	C–O stretch
896	β-glycosidic linkage

The carboxyl content of the CNF was quantitated by conductometric titration. Excess strong acid (HCl) was added to protonate all the carboxylate groups and then the mixture was titrated with NaOH. An example titration curve is shown in Figure 3-3. After

neutralization of excess HCl in the CNF slurry, the plateau region between the two inflection points is used to quantify the amount of carboxylic acids groups present on the CNF.[26, 28-29] Using Equation 3-1, the CNF carboxyl content is calculated to be 1.12 ± 0.03 mmol/gram. Values of 0.6 to 1.7 mmol/gram have been reported for the carboxyl content of TEMPO oxidized CNF and the material used here is in that range.[38, 43] The carboxyl groups on the CNF surface provide colloidal stability and potential nucleation sites for metal nanoparticles.[38, 44]

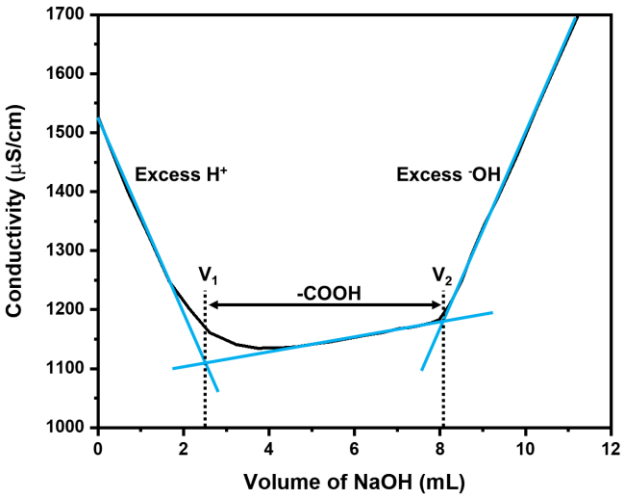

Figure 3-3. Conductometric titration of cellulose nanofiber carboxyl content.

3.3.2. Synthesis and Characterization of Plasmonic Cellulose Nanofibers

It is known that CNF is capable of acting as a template for the synthesis of Ag NPs.[31-32, 44] The synthesis of Ag NPs has been driven both thermally and chemically in the presence of CNF.[30, 44-48] Chemical synthesis has utilized external reducing agents, such as trisodium

citrate, sodium borohydride and AA.[31-32, 45, 49] Our synthesis follows a two-step procedure with AA as the reducing agent as shown as in Figure 3-1. Several parameters were optimized in this synthesis including mixing time, temperature, CNF concentration and AA concentration. The effect of these parameters on the density and functionality of the Ag NPs were tracked by visible extinction and Raman spectroscopies (Figures 3-4 and 3-5). The optimized conditions for Ag deposition onto the CNF were: 5 minutes mixing times for both steps, 70 °C, 0.2 mM AA and 0.02 % CNF.

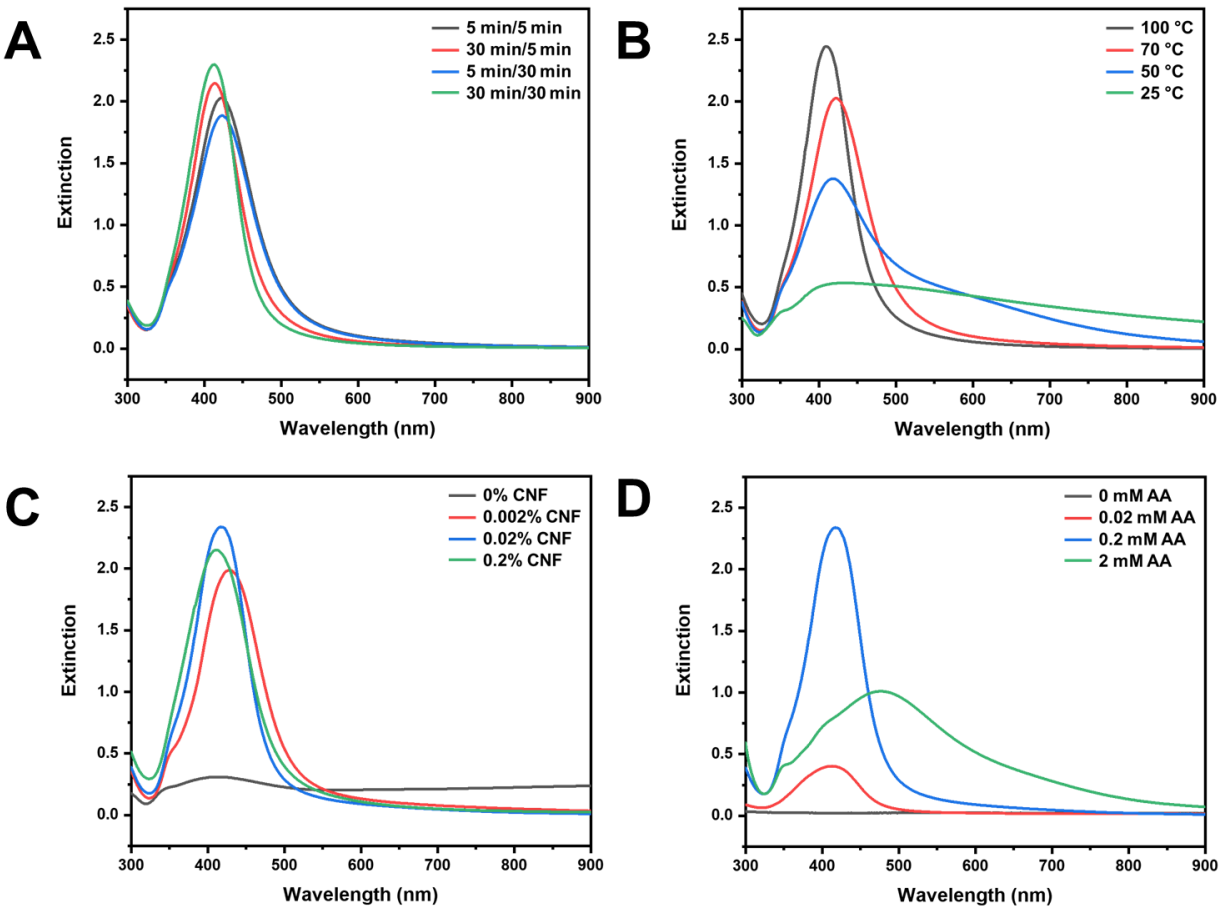

Figure 3-4. UV-Vis extinction optimization of Ag-CNF. UV-Visible extinction spectra of Ag-CNF synthesized at different (A) mixing times in step 1/step 2 (0.02% CNF; 0.2 mM AA; 0.2 mM $AgNO_3$), (B) temperatures (0.02% CNF; 0.2 mM AA; 0.2 mM $AgNO_3$; 5 min/5 min mixing), (C) CNF concentration (0.2 mM AA; 0.2 mM $AgNO_3$; 70 °C; 5 min/5 min mixing) and (D) AA concentration (0.02% CNF; 0.2 mM $AgNO_3$; 70 °C; 5 min/5 min mixing).

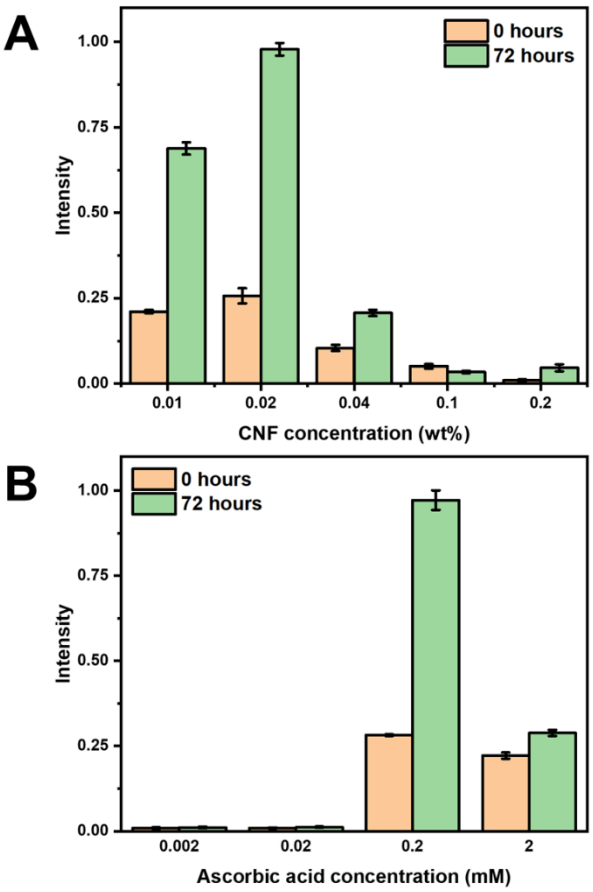

Figure 3-5. SERS spectroscopy optimization of Ag-CNF. Bar charts of the C≡N stretch peak intensity measured at 2230 cm^{-1} as a function of (A) CNF concentration (0.2 mM AA; 0.2 mM $AgNO_3$; 70 °C; 5 min/5 min mixing) and (B) AA concentration (0.02 % CNF; 0.2 mM $AgNO_3$; 70 °C; 5 min/5 min mixing). Analysis (SERS measurements) was done in triplicates.

The synthesis of Ag-CNF was tracked with IR spectroscopy as shown as in Figure 3-6A. Shifts in the COO^- antisymmetric stretch (ν_{a,COO^-}) and symmetric stretch (ν_{s,COO^-}) are observed after each step. The ν_{a,COO^-} and ν_{s,COO^-} are observed at 1608 and 1411 cm^{-1} for unmodified CNF, respectively. After the addition of $AgNO_3$, the ν_{a,COO^-} shifts to 1606 cm^{-1}, the ν_{s,COO^-} shifts to 1409 cm^{-1} and a band at 1730 cm^{-1} emerges. We assign the band at 1730 cm^{-1} to the carbonyl stretch ($\nu_{C=O}$) of protonated acid groups due to a decrease in pH upon dilution of the CNF to 0.02% from the stock solution of ~1 % CNF (from pH ~7-8 to ~5-6).

It has been shown that the COO^- sites on TEMPO oxidized CNF will preferentially bind Ag^+ over Na^+ through an ion-exchange process.[50] Thus, we interpret the slight shift in ν_{a,COO^-} from 1608 to 1606 cm^{-1} to be due to the ion-exchange between Na^+ and Ag^+ at the COO^- on CNF.[44] Ag NPs are formed with the addition of AA, and the ν_{s,COO^-} shifts to 1425 cm^{-1} while the ν_{a,COO^-} becomes broadened due to a variety of environments consisting of Ag NPs and Na^+ ionic interactions. Finally, the increase in intensity of the $\nu_{C=O}$ at 1730 cm^{-1} is due to a further decrease in pH from ~5-6 to ~4-5 due to the addition of AA. The various chemical steps consistent with the IR spectra are shown on the right of Figure 3-6A.

The mechanism described by the IR results above involves modification of the surface charge of the material in each step. As noted above, the zeta potential of the diluted CNF at a pH ~5-6 is -51.3 ± 0.6 mV. Upon addition of $AgNO_3$ the zeta potential is -38 ± 1 mV which is attributed to the complex coordination of Ag^+ to COO^- resulting in the lowering of the magnitude of the surface potential due to shielding. After reduction of the Ag cations, the zeta potential of Ag-CNF is -41.5 ± 0.5 mV at a pH of ~4-5. The change in zeta potential upon Ag NP formation is due to AA adsorbing to the surface of the nanoparticles, providing additional surface charge and colloidal stability.[51]

The extinction spectrum for the material produced from optimal reaction conditions is shown in Figure 3-6B. A band due to the localized surface plasmon of the Ag-CNF is observed at 417 nm. Control experiments without CNF or AA produce solutions with negligible extinction at 417 nm. The extinction spectrum of the Ag-CNF is consistent with the synthesis of discrete Ag NPs that are well dispersed on the fibers and colloidally stable in solution. The shape and size of the Ag NPs are revealed in the SEM images in parts C and D of Figure 3-6. These images show the presence of Ag NPs with an average diameter of

~45 nm anchored to the CNF. A more in-depth discussion of the size distribution of the Ag NPs is below. There is no evidence of nanoparticles on the background grid and all particles are attached to the fibers. There is a clear indication of CNF bundling as well as nanoparticle dimers, trimers and larger clusters. These are potential hot spot locations that can provide enhancement for SERS analysis.

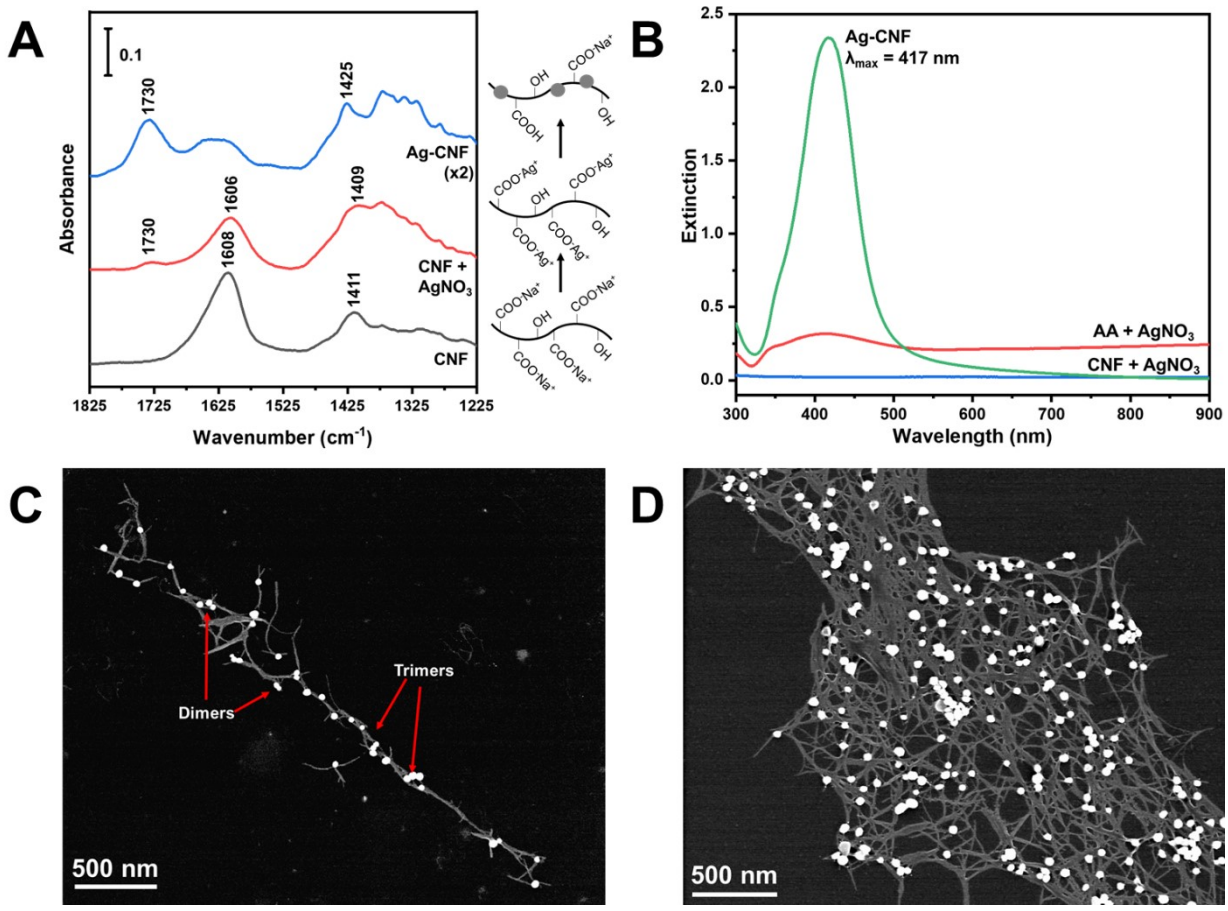

Figure 3-6. Characterization of Ag-CNF synthesis using IR, UV-Vis extinction and SEM imaging. (A) Examination of silver/carboxylate complexation with IR spectroscopy. (B) UV-Visible extinction of Ag-CNF and controls. (C) and (D) are SEM images of Ag-CNF.

The elemental composition of CNF and Ag-CNF is examined using XPS analysis. Figure 3-7A is a XPS spectrum of the Ag 3d binding energy. No Ag is observed in CNF and Ag-CNF shows the Ag 3d doublet at 368.5 and 374.5 eV. This peak separation of 6.0 eV is characteristic of the spin-orbit component of Ag metal.[52] The total amount of Ag metal in Ag-CNF is 1.7 %. Survey scans and high-resolution deconvolution data can be found in Figures 3-8 and 3-9, and Tables 3-2, 3-3, and 3-4. Deconvolution assignments are based on previously published works.[42, 52-53]

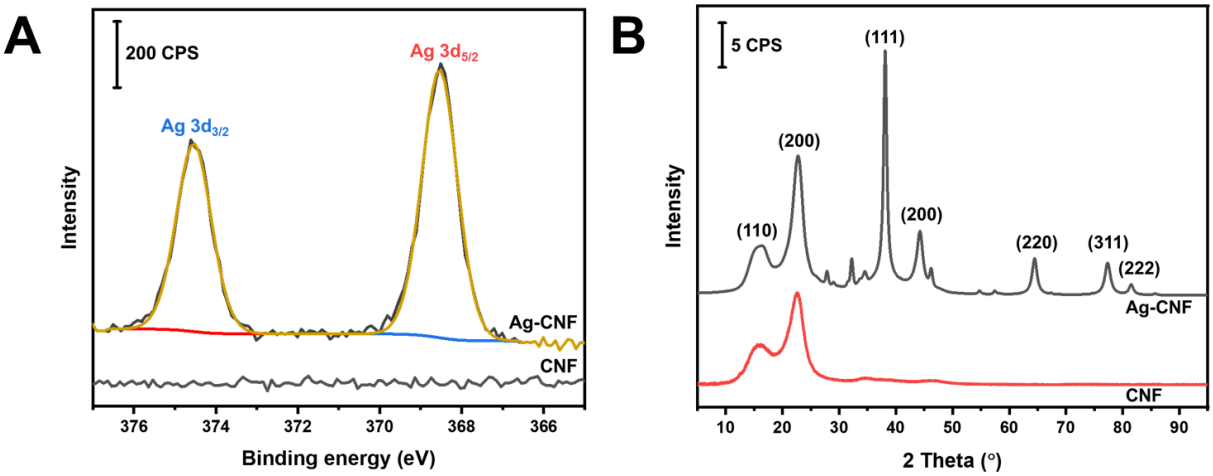

Figure 3-7. XPS and XRD analysis of CNF and Ag-CNF. (A) High resolution XPS and (B) XRD analysis of CNF and Ag-CNF.

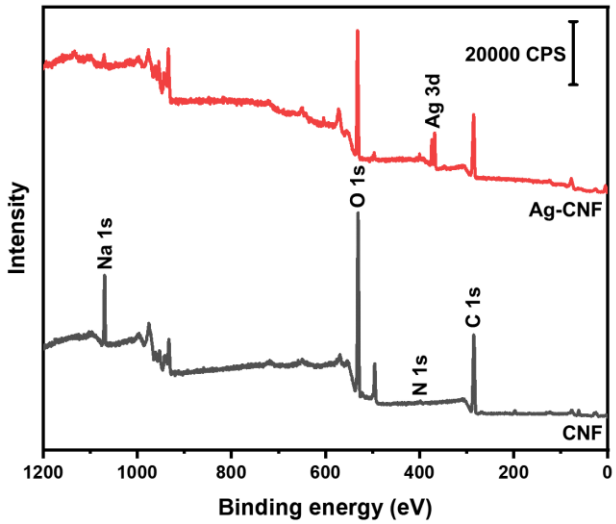

Figure 3-8. XPS survey spectra of CNF and Ag-CNF.

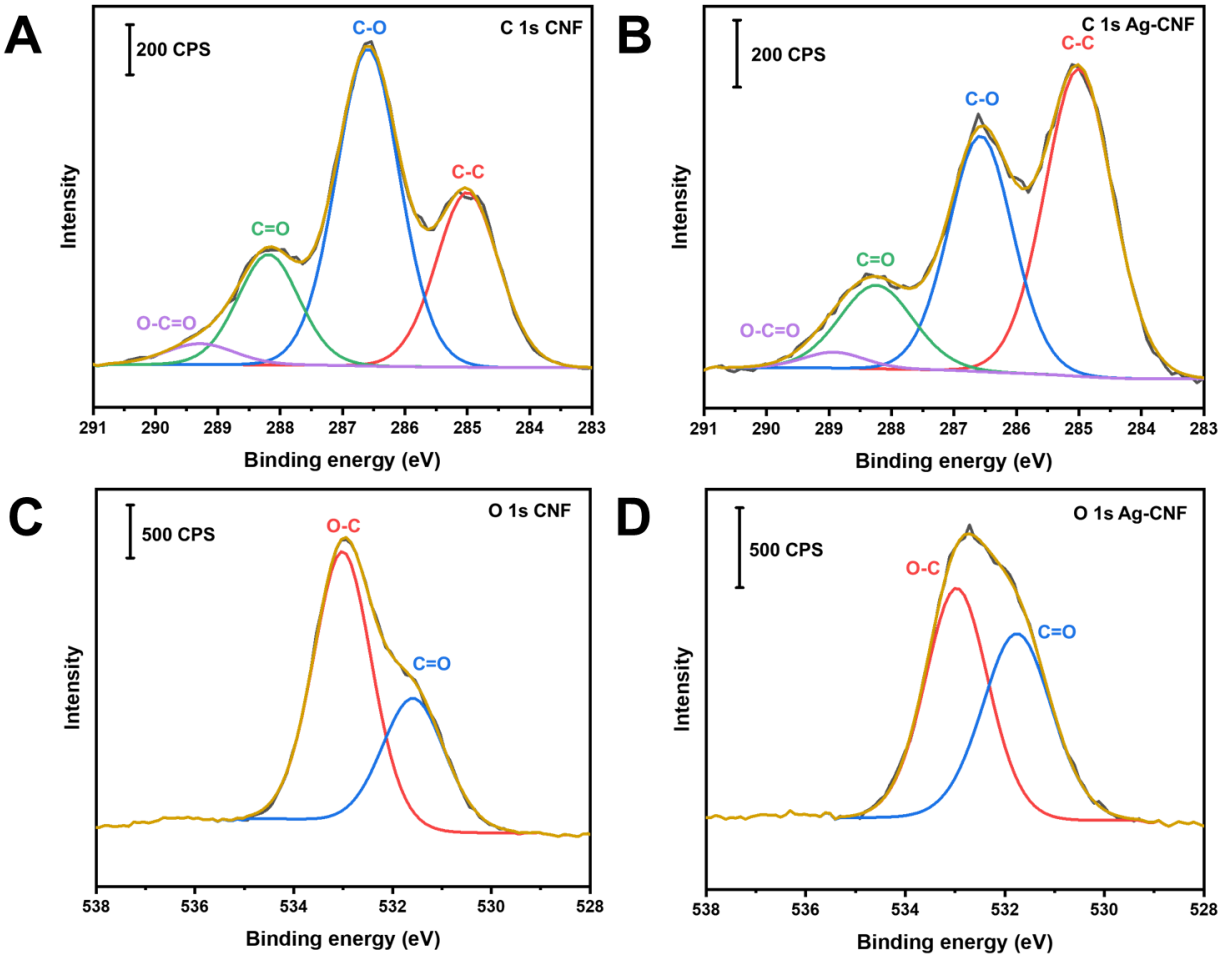

Figure 3-9. XPS high resolution spectra. C 1s for (A) CNF and (B) Ag-CNF, and of O1s for (C) CNF and (D) Ag-CNF.

Table 3-2. Survey Scan Data of CNF With and Without Silver Nanoparticles.

Sample	Peak	Position	FWHM	Area	At%	R.S.F
CNF	C 1s	285.0	3.63	5575	56.7	0.278
	O 1s	531.0	2.92	10279	37.3	0.780
	N 1s	398.2	2.45	159	0.9	0.477
	Na 1s	1069.4	2.37	3019	5.1	1.690
Ag-CNF	C 1s	285.0	3.84	4661	60.6	0.278
	O 1s	531.8	3.02	7231	33.5	0.780
	N 1s	400.2	2.07	379	2.9	0.477
	Na 1s	1071.0	3.27	594	1.3	1.690
	Ag 3d	368.2	2.33	2790	1.7	5.99

Table 3-3. High Resolution Data of Cellulose Nanofibers With and Without Silver Nanoparticles.

Sample	Peak	Position	FWHM	Area
CNF	C 1s	286.5	1.34	3065
	O 1s	532.9	2.22	5418
	Ag 3d	-	-	-
Ag-CNF	C 1s	285.1	2.71	2500
	O 1s	532.7	2.35	4037
	Ag 3d	368.5	0.97	1462

Table 3-4. Data From the Component Fitting From the High Resolution Spectra of Cellulose Nanofibers With and Without Silver Nanoparticles.

Sample	Peak	Name	Position	FWHM	Area	%Area
CNF	C 1s	C–C/C–H	285.0	1.18	851	27.7
		C–O	286.6	1.20	1569	51.2
		O–C–O/C=O	288.2	1.16	522	17.0
		O–C=O	289.3	1.39	125	4.1
	O 1s	C=O	531.6	1.51	1887	34.7
		C–O	533.0	1.38	3557	65.3
	Ag 3d	-	-	-	-	-
Ag-CNF	C 1s	C–C/C–H	285.0	1.28	1216	48.4
		C–O	286.6	1.21	884	35.2
		O–C–O/C=O	288.2	1.39	357	14.1
		O–C=O	288.9	1.15	57	2.3
	O 1s	C=O	531.8	1.64	1904	47.2
		C–O	533.0	1.48	2133	52.8
	Ag 3d	Ag 3d 5/2	368.5	1.02	843	58.9
		Ag 3d 3/2	374.5	1.01	588	41.1

The crystallinity of CNF and Ag-CNF is examined using XRD analysis. Figure 3-7B shows the diffraction spectrum of CNF and Ag-CNF. The spectrum of the CNF contains two broad band peaks at 16.34 ° and 22.74 ° which are due to the (110) and (200) crystallographic planes, respectively, and are characteristic of cellulose I structure.[38, 54] In the spectrum of the Ag-CNF sample, the Ag metal lattice peaks are observed at 38.11 °, 44.24 °, 64.45 °, 77.34 ° and 81.48 °, and are attributed to (111), (200), (220), (311) and (222) lattice facets.[31] The d-spacing and crystallite size of the Ag NPs can be found in Table 3-5.

Table 3-5. Determination of d-Spacing and Crystallite Size of Silver Nanoparticles on Cellulose Nanofibers From XRD Data.

Lattice facet	2θ	d-spacing (Å)	Crystallite size (nm)
111	38.11	2.36	12.5
200	44.24	2.05	7.1
220	64.45	1.44	9.3
311	77.34	1.23	8.8
222	81.48	1.18	11.5

The calculated d-spacing values were calculated using the Bragg equation as shown as in Equation 3-2:[55]

$$\boldsymbol{d = \frac{n\lambda}{2sin\theta}} \quad \textbf{(Equation 3-2)}$$

where d is the interatomic distance (Å), n is the order of diffraction, λ is the source wavelength (1.5406 Å) and θ is the angle of incident. The crystallite size (nm) was calculated using the Scherrer equation as shown in Equation 3-3:[55]

$$\boldsymbol{t = \frac{0.9\lambda}{Bcos\theta}} \quad \textbf{(Equation 3-3)}$$

where t is the crystallite size, 0.9 is a constant, λ is the source wavelength (1.5406 Å), B is the full width at half maximum and θ is the angle of incident.

3.3.3. SERS Enhancement, Dispersibility and Reproducibility

The use of colloidal nanoparticles as a viable SERS substrate is often overlooked due to difficulties in controlling the aggregation process. Table 3-6 is a summary of colloidal nanoparticles used for in-solution SERS measurements.[9-19, 22-25] These studies highlight a

range of examples from controlling the aggregation process to developing dispersible support structures for nanoparticles. As noted previously, cellulose nanomaterials are often used as a template/support for nanoparticles.[30] However, the majority of cellulose-based SERS substrates are used as a solid-based SERS substrate.[5] Our work highlights the use of oxidized CNF as a water-dispersible SERS substrate.

Table 3-6. Summary of Colloidal SERS Substrates for In-Solution Measurements and Applications

Type of nanomaterial	Nanoparticle support	Application	Reference
Ag NP	Citrate-capped	Investigation of aggregation control	9
Ag NP	Citrate-capped	Detection of toxic metals using salen complexes	10
Ag and Au NP	Citrate-capped	Detection of amphetamine sulfate	11
Ag NP	Oligonucleotide - functionalized NP in buffer conditions	Controlled NP assembly using DNA hybridization	12
Au nanostars	Good's buffer	Detection of uranyl	13
Au nanostars	Good's buffer	Detection of methimazole in urine	14
Au dogbone-shaped NP	CTAB-capped	Detection of thiram	15
Au dogbone shaped NP	CTAB-capped	Detection of dithiocarbamate fungicides	16
Au nanorods	CTAB-capped	Detection of dithiocarbamate pesticides	17
β-cyclodextrin modified Au NP	Citrate-capped	Detection of polycyclic aromatic hydrocarbons	18
Starch-coated Ag NP	Starch and citrate	Detection of melamine and malachite green	19
Polymer-mediated Au NP aggregates	PVP	Detection of neurotransmitters	22
Ag NP coated poly(styrene-co-acrylic acid) nanospheres	Poly(styrene-co-acrylic acid) nanospheres and PVP	Detection of trace melamine	23
Ag NP/CNC	CNC	Detection of riboflavin	24
Ag NP/SiO_2/CNC and Ag NP/CNC	SiO_2 and CNC	Detection of malachite green	25
Ag-CNF	CNF	Detection of malachite green	This work

PVP – polyvinylpyrrolidone; CTAB – cetrimonium bromide.

We are introducing the Ag-CNF material synthesized as described above as an in-solution SERS substrate. During our evaluation of this application we discovered two important factors in the treatment of the material for observing strong SERS signals. MBN adsorbed to the Ag NPs was used as a Raman probe. It was observed that centrifugation of the material after synthesis and resuspension is crucial for the observation of intense SERS bands. Figure 3-10A show aqueous phase SERS spectra of MBN treated Ag-CNF samples without centrifugation and after centrifugation. The band intensities for the re-suspended sample are ~30× more intense than for the samples that were not centrifuged. The bands observed are characteristic of MBN and are C≡N stretch at 2230 cm^{-1}, C–C stretch at 1585 cm^{-1}, C–H bend and C–C stretch at 1180 cm^{-1}, and the C–S stretch and C–C stretch at 1072 cm^{-1}.[56-57] It is clear from Figure 3-10A that centrifugation and resuspension of the Ag-CNF material provides a more active SERS substrate for solution analysis.

Insights into the effect of centrifugation/resuspension on the structure of the Ag-CNF are provided in parts B-D of Figure 3-10. Figure 3-10B are the extinction spectra and Figures 3-10C and 3-10D are SEM images taken for each sample. The extinction spectrum of the material without centrifugation is characteristic of well-dispersed Ag NPs. As noted above, the zeta potential of the Ag-CNF at this point is -41.5 mV. Although both solutions, i.e., with and without centrifugation/resuspension, appear clear and yellow in color as shown in the inset of Figure 3-10B, the extinction spectrum of the centrifuged sample contains a tail at higher wavelength that indicates some degree of aggregation. The zeta potential of the material taken immediately after resuspension is -30 ± 3 mV (pH of ~5-6). While this value is consistent with colloidal stability, it is clear from Figure 3-10B that Ag

aggregates are present in the re-suspended material. We note that the solutions of the centrifuged/re-suspended Ag-CNF remain visually similar for at least 24 hours.

Figure 3-10C is a SEM image for a sample without centrifugation. In this image, a single nanofiber with a single nanoparticle is observed. While other images of the non-centrifuged samples show some fiber and particle bunching (Figure 3-10C inset), it is not to the extent observed after centrifugation. Considering Figure 3-10C and the SERS spectrum in Figure 3-10A and the extinction spectrum in Figure 3-10B, we hypothesize that the Ag-CNF solution directly after the synthesis consists of well dispersed individual fibers containing one or a few Ag NPs. Figure 3-10D is a SEM image of Ag-CNF after centrifugation. The image shows a bundle of nanofibers with many nanoparticles. Centrifugation of the Ag-CNF solution introduces an intertwinement of the CNF that gathers the Ag NPs in close proximity to one another. The groupings of Ag NPs contain numerous regions of potential SERS hot spots. We attribute the large increase in the MBN SERS signal observed in Figure 3-10A to clusters of the Ag-CNF material that remain suspended in aqueous solutions.

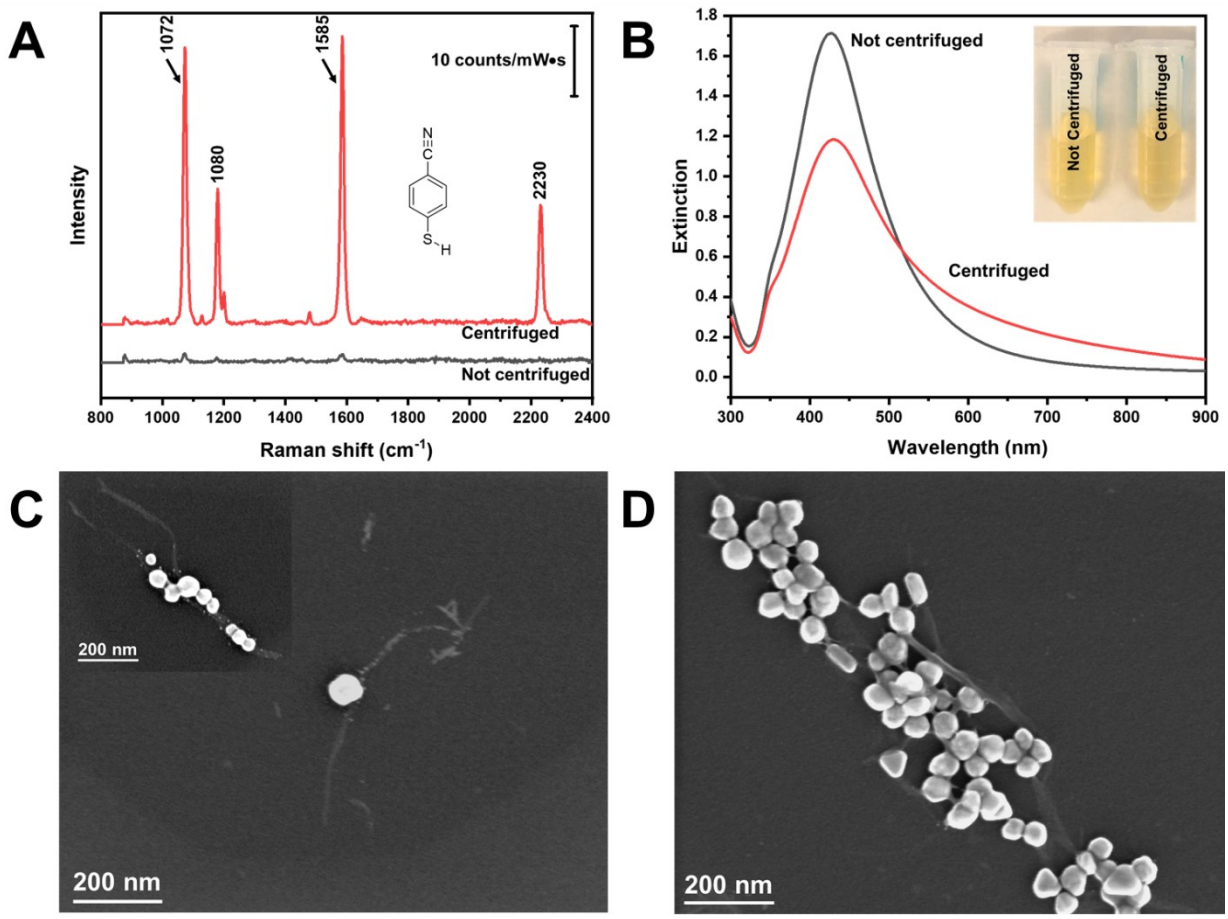

Figure 3-10. Plasmonic cellulose nanofiber enhancement. (A) SERS spectrum of MBN demonstrating the effect of centrifugation on the enhancement of plasmonic cellulose nanofibers. (B) UV-Visible extinction of Ag-CNF before and after centrifugation. SEM images of Ag-CNF (C) before centrifugation and (D) after centrifugation.

The second factor observed to influence the solution-based SERS intensity is room temperature aging of the sample after synthesis and before centrifugation/resuspension. SERS spectra for aging periods of 0, 24, 48 and 72 hours are in Figure 3-11A. The sample is centrifuged/re-suspended after the indicated aging period and then MBN is introduced for SERS analysis. As the aging period increases, the signal intensity also increases. We do not observe the same effect if the aging is carried out after centrifugation/resuspension (Figure 3-11B). While there are slight deviations in intensity, particularly from 0 to 24 hours, this is

attributed to the settling of Ag-CNF bundles after centrifugation. There are no significant changes in the signal intensity with increased aging time. SEM imaging was used to investigate the influence of aging on Ag NP size. ASH plots are used to examine the nanoparticle size distribution at 0 and 72 hours (Figure 3-11). Over the aging period the nanoparticle size remained constant; however, the size distribution shifted to a narrower profile. Moreover, the rug plot below the distribution indicates consumption of smaller Ag NPs. This suggests a mixture of intraparticle and Ostwald ripening.[58-59] Thus, we conclude that the optimal substrate preparation should include a 72 hour aging period prior to centrifugation. UV-Vis extinction of Ag-CNF at 0 and 72 hours are shown in Figure 3-12. In terms of storage and handling of the material, the centrifuged pellet can be stored in a refrigerator (4 °C) for over 10 days and resuspension carried out directly before usage without loss of signal (Figure 3-13).

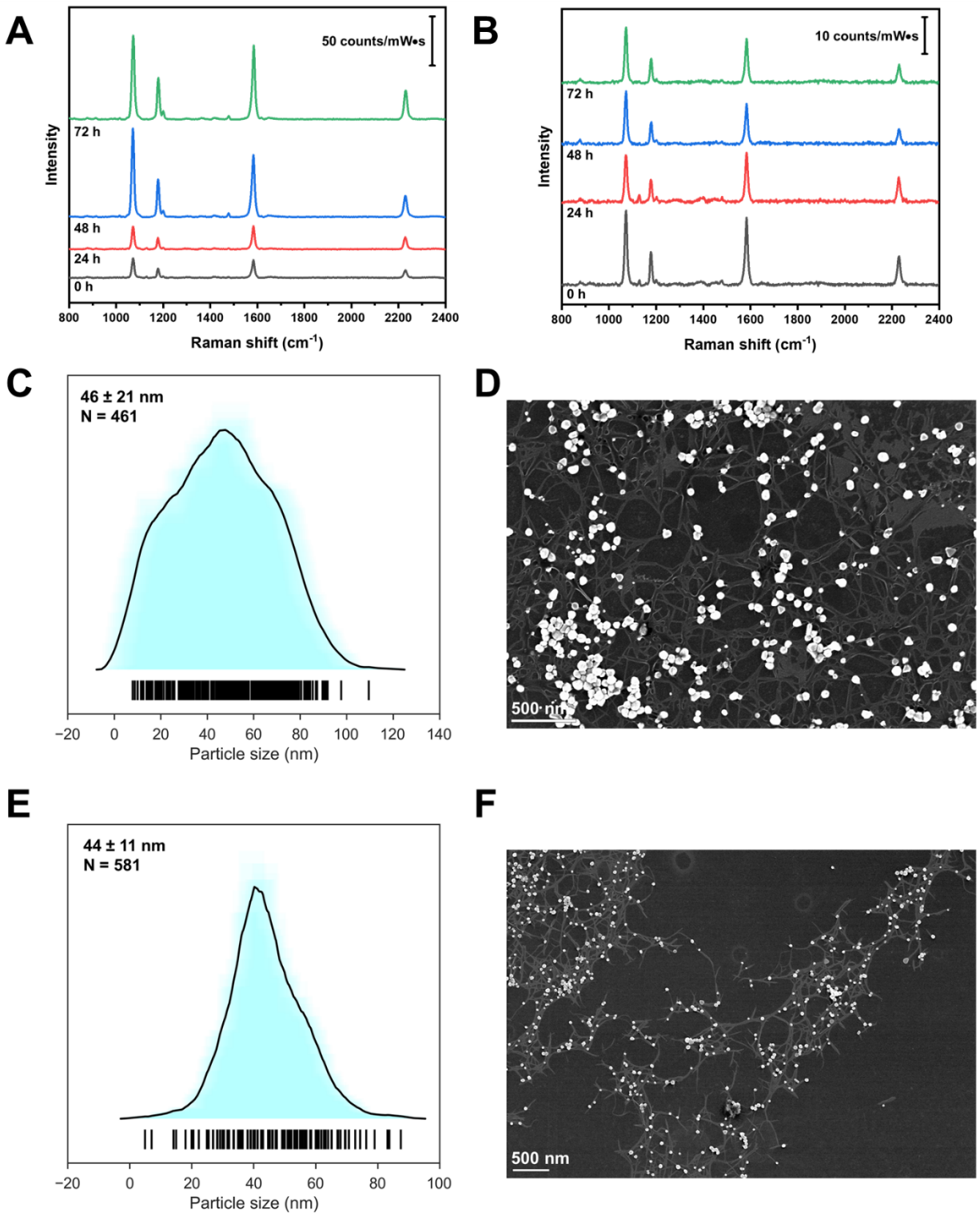

Figure 3-11. SERS spectra of MBN at 5 µM demonstrating the effect of substrate aging on the enhancement of plasmonic cellulose nanofibers. Aging of Ag-CNF (A) before and (B) after centrifugation for 0 hours, 24 hours, 48 hours and 72 hours. Silver nanoparticle size distribution and SEM of Ag-CNF at (C-D) 0 hours and (E-F) 72 hours.

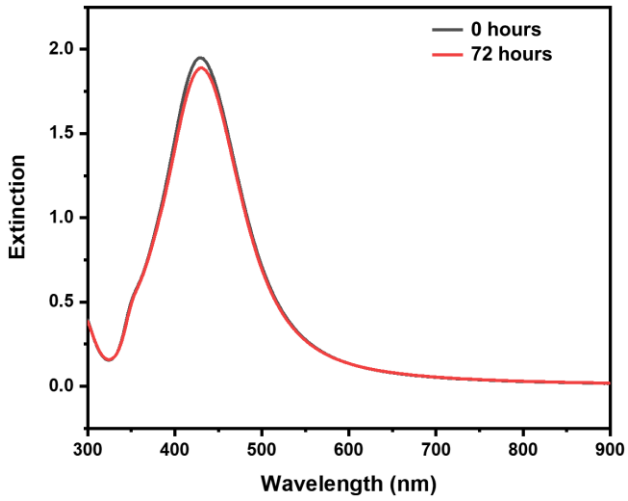

Figure 3-12. UV-Visible extinction of Ag-CNF at 0 hour and 72 hour.

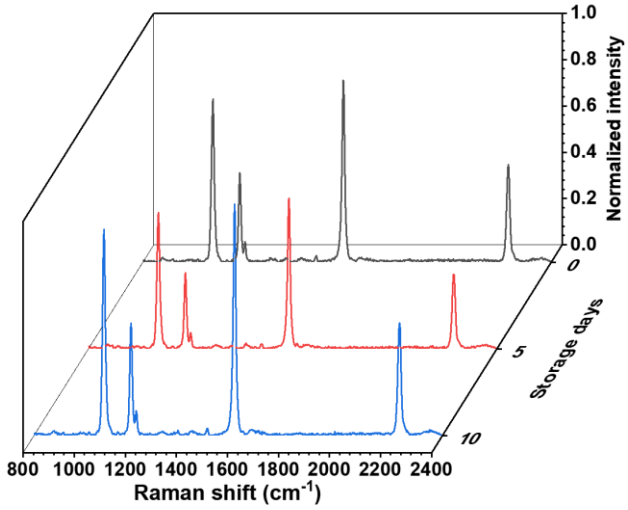

Figure 3-13. SERS spectra of MBN demonstrating the stability of Ag-CNF being stored as a pellet in the refrigerator (4 °C) over time. Normalized to the highest peak intensity (C–C stretch).

The capability of the Ag-CNF material for in-solution SERS analyses is demonstrated in Figure 3-14. Figure 3-14A are spectra that compare the material with commercial citrate capped Ag NPs of similar size (40 nm) as well as some control spectra. A SERS signal is not observed for dispersed CNF or MBN in solution under the conditions employed here

(bottom spectrum of Figure 3-14A). The Ag-CNF without a Raman reporter yields a slightly enhanced spectrum for CNF. We attribute the band at 1614 cm^{-1} to the ν_{a,COO^-}. The bands between 1000-1200 cm^{-1} and 1300-1500 are associated with the C-O/C-C stretching and CH_2/CH_2OH bending, respectively.[60-61] The observation of the CNF bands indicates that the Ag NPs are indeed attached to the CNF and that the CNF bands are being enhanced by the Ag NPs.

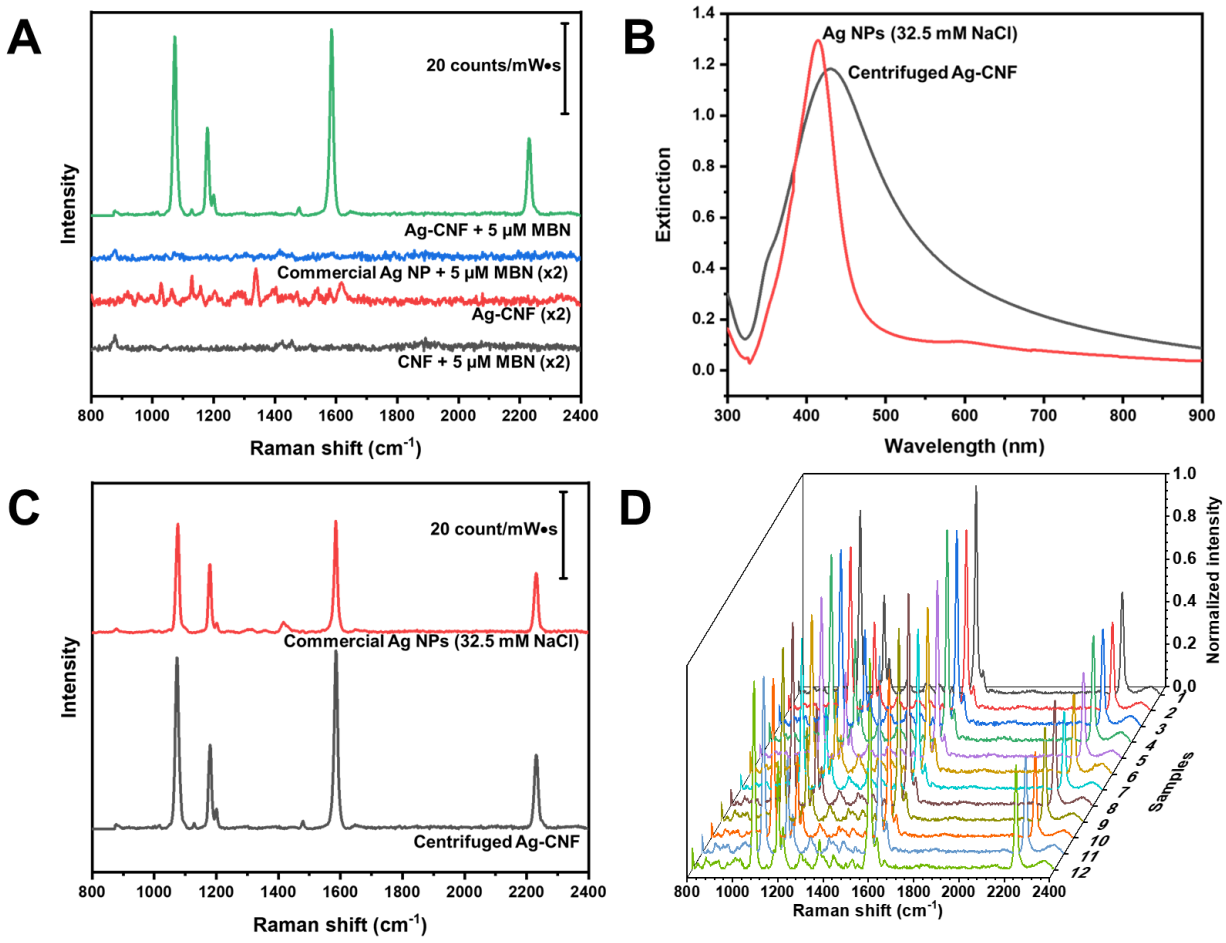

Figure 3-14. SERS capability and reproducibility. (A) Demonstration of SERS capability of Ag-CNF with MBN. (B) Comparison of Ag-CNF and aggregated Ag NP (32.5 mM NaCl) using UV-Vis extinction. (C) SERS spectra of MBN using centrifuged Ag-CNF and aggregated Ag NP. (D) SERS spectra of MBN demonstrating the reproducibility of Ag-CNF. Each sample was analyzed three times at different locations on the vial. Normalized to the highest peak intensity (C–C stretch).

A comparison of the Ag-CNF substrate and commercial Ag NPs is given in the top two spectra in Figure 3-14A. The spectrum of commercial Ag NPs mixed with MBN contains no observable bands characteristic of the reporter molecule. When MBN is adsorbed to Ag-CNF a clear spectrum is observed indicating significant enhancement. The weak enhancement from dispersed Ag NPs is presumably due to the lack of electromagnetic coupling between particles in a well-dispersed system. Indeed, solution-based SERS using colloidal nanoparticles is typically conducted in the presence of an aggregating agent. Additives such as sodium chloride, sodium nitrate, poly(L-lysine), nitric acid and spermine have been used to induce aggregation.[9, 11] It has also been shown that SERS can be controlled via assembly of DNA functionalized nanoparticles.[12] Thus, a more level comparison of the in-solution SERS performance of Ag-CNF is with aggregated colloidal Ag NP.

Aggregation of spherical Ag NPs was induced with the addition of NaCl. Figure 3-15 contains the extinction spectra of spherical Ag NPs at different NaCl concentrations to monitor the aggregation. We note that the NaCl concentration range for the formation of aggregates that are temporarily colloidally stable is narrow and at all NaCl concentrations, the aggregated nanoparticles will sediment over time. The performance of the Ag-CNF was compared to an aggregated Ag NP solution. We used a concentration of NaCl that produces an extinction spectrum similar to that of the centrifuged Ag-CNF. Figure 3-14B contains the extinction spectrum of commercial Ag NPs aggregated using 32.5 mM NaCl and that of centrifuged Ag-CNF. The two materials are fairly close in extinction intensity. The Ag-CNF exhibits a slightly broader extinction that we attribute to a wider nanoparticle size distribution in Ag-CNF and a wider variation in local dielectric constant. The centrifugation

step produces Ag-CNF bundles which increases the CNF density that will impact the local environment around the nanoparticles and broaden the localized surface plasmon resonance curve.

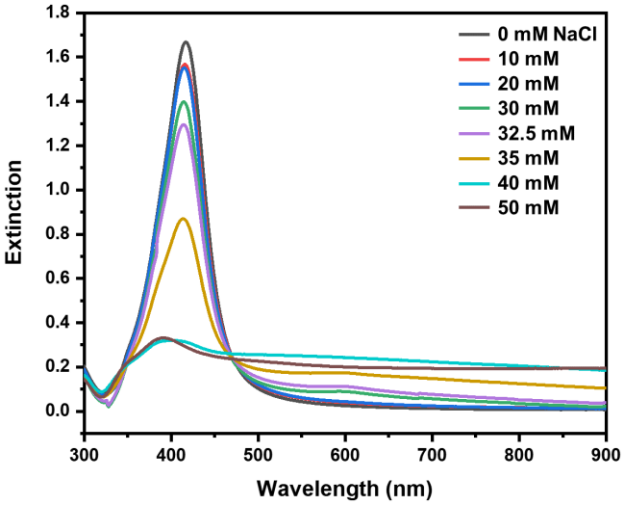

Figure 3-15. UV-Visible extinction of commercial Ag NPs at different NaCl concentrations.

The SERS comparison of the two solution-based substrates is shown in Figure 3-14C. The spectra of MBN adsorbed to Ag-CNF and to aggregated Ag NPs are similar in intensity despite the difference in the mechanism in which hot spots are generated. The interparticle coupling in the Ag-CNF system is driven by fiber bundling while nanoparticle association is driven by salt induced collapse of the electrical double layer. It is worth noting that the Ag NPs in the Ag-CNF system are not coated with a capping species and are not involved in aggregation so that their surface is relatively free for the adsorption of analyte species. In addition, the Ag-CNF remains colloidally stable after centrifugation for ~24 hours before sedimentation is observed, while Ag NPs in the presence of NaCl will

eventually destabilize and sediment out of solution within an hour. Thus, the Ag-CNF serves as a colloidally stable SERS substrate for in-solution analysis.

Spot-to-spot irreproducibility remains a persistent issue in the development of SERS substrates. Intensity fluctuation across a solid substrate surface can be due to a number of factors including inhomogeneous distribution of nanoparticles or analyte that are drop-casted, e.g., the coffee-ring effect. Solution-based analysis struggles with the random aggregation and instability of colloidal nanoparticles. However, with the aid of a dispersible support (i.e., CNF) for the nanoparticles, the solution homogeneity eliminates issues pertaining to spot-to-spot irreproducibility typically observed on a surface. The reproducibility of in-solution measurements using Ag-CNF is monitored in Figure 3-14D. The SERS spectrum is monitored using 12 different samples from the same batch of Ag-CNF. Each Ag-CNF sample is monitored at 3 different locations within the sample vial and the average MBN spectrum is shown. The percent relative standard deviation (%RSD) was examined using the C≡N, C–C and C–S stretching vibrational bands. The average %RSD for spot-to-spot on the same vial was observed to be ~3%. The %RSD for sample-to-sample was determined to be 9%. These results are comparable to where measurements have been taken on a solid-based CNF/gold nanocomposite substrates.[6-7] It is well understood that achieving reproducible SERS measurements using aggregated colloidal nanoparticles is challenging, and Tantra et al. present guidelines and measurement strategies to improve the SERS reproducibility of in-solution measurements.[62] A measurement reproducibility of less than 20% is generally accepted for SERS analyses and the reproducibility of Ag-CNF falls well below this threshold.[63]

3.3.4. Rapid In-Solution SERS Measurements

Developing SERS substrates capable of providing rapid measurements is essential for on-site analysis. Analysis times for solid substrates are limited by two key factors, namely two-dimensional diffusion-limited adsorption of the analyte to the substrate, and successive rinsing and drying of the substrate. For example, Jiang and Hsieh immerse their CNF/Ag nanocomposite film in analyte solution for 1 hour, followed by a rinsing and drying step before a SERS spectrum was collected.[31] An in-solution SERS platform with a dispersible substrate does not suffer from these time consuming issues. Upon mixing of the analyte with the substrate, mass transport to the nanoscale substrate will take place via radial diffusion that is more rapid than planar diffusion. In addition, simply shaking the vial will increase mass transport via convection. Also, and obviously, rinsing and drying is not necessary. For example, Ogundare and van Zyl perform measurements using their Ag NP/SiO_2/CNC substrate after an incubation period of 30 minutes.[25] The necessary adsorption time for analysis using Ag-CNF is determined by monitoring the peak intensity of MBN at a series of different adsorption times. An aliquot of MBN is added to Ag-CNF solution and initially vortexed for 2 minutes. The first SERS spectrum is taken at this point. The sample is then re-analyzed at 10, 30, 60, 130 and 180 minutes of adsorption. Figure 3-16A is a 3D plot of the MBN spectrum at each adsorption time interval. Figure 3-16B is a column graph describing the peak intensity at 2230 cm^{-1} as adsorption time increases. There is nearly no change in peak intensity as the MBN adsorption time increases. This is attributed to dynamic mixing and three-dimensional diffusion of the analyte to the nanoparticle. Performing analysis in solution overcomes the limitation of two-dimensional diffusion often found when a solid-based substrate is used.

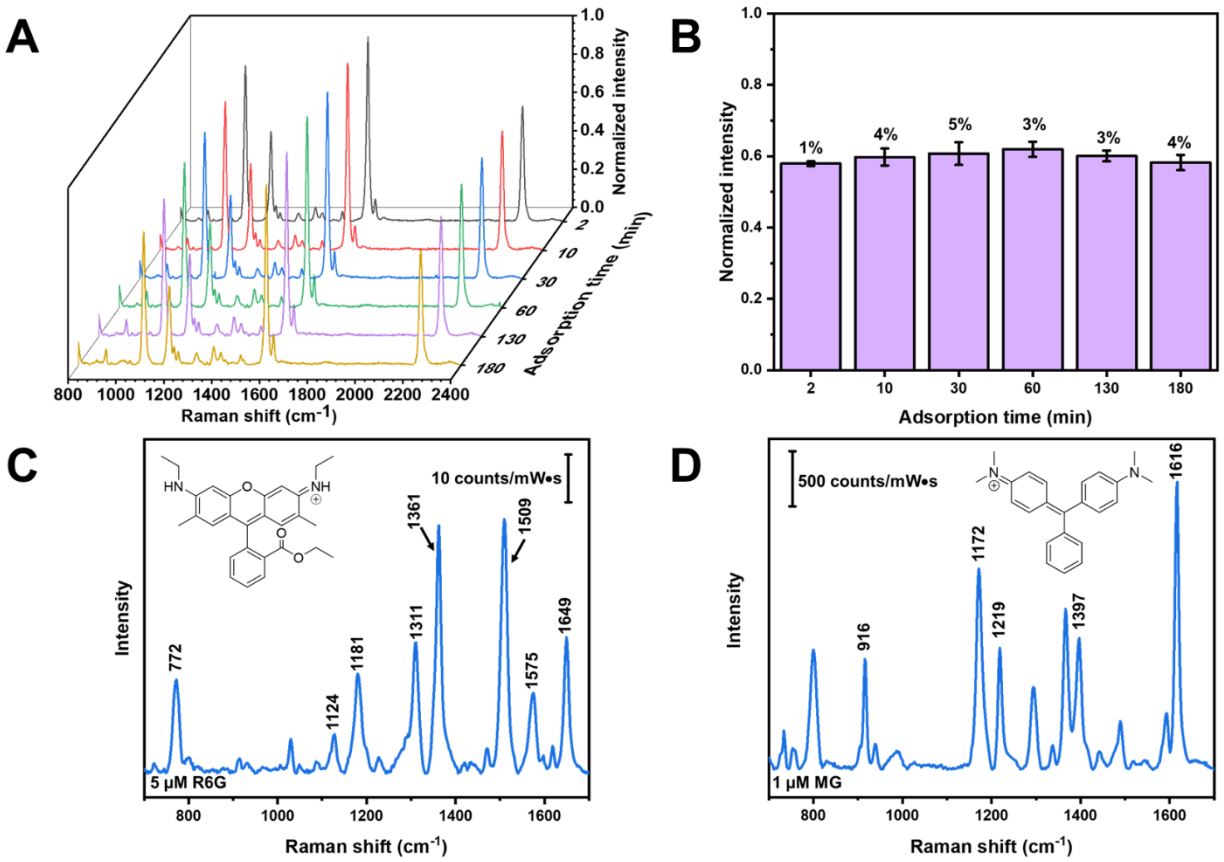

Figure 3-16. In-solution measurements using Ag-CNF. The adsorption of MBN (5 μM) to Ag-CNF is monitored over time. (A) SERS spectra of MBN spectra in Ag-CNF solution and (B) column graph of MBN peak intensity at 2230 cm^{-1}. Each spectrum is the average of five different Ag-CNF samples. Normalized to the highest peak intensity (C–C stretch). SERS spectrum of (C) 5 μM rhodamine 6G and (D) 1 μM malachite green.

MBN serves as an excellent Raman reporter due to its specific chemisorption to Ag through the thiolate group. However, many potential analytes will interact to the substrate via physisorption. Figure 3-16C and 3-16D demonstrate the measurement of non-thiol containing analytes, rhodamine 6G (R6G) and malachite green (MG). The spectrum in Figure 3-16C was collected under the same acquisition conditions as MBN in Figure 6 after 2 minutes of adsorption time (final concentration of 5 μM). The Raman peaks at 1649, 1575, 1509, 1361, 1311 and 1181 cm^{-1} are attributed to the symmetric in-plane C–C stretching vibrations.[31, 64] The Raman peaks at 1124 and 772 cm^{-1} are attributed to the in-

and out-of-plane C–H bending vibrations.[31] The spectrum in Figure 3-16D was collected under slightly different acquisition conditions (1 second, 10 accumulations) to avoid detector saturation. Note that MG can be measured with low acquisition time (1 second) partially due to its absorbance at ~624 nm.[65] The Raman bands at 1616, 1397, 1219, 1172 and 916 cm^{-1} are the C–C ring stretching, N–phenyl ring stretching, C–H rocking, in-plane ring C–H stretching and the in-plane ring C–H bending, respectively.[19, 66-67] Thus SERS measurements with Ag-CNF are not dependent on a metal-thiol interaction and the substrate can be used for rapid analysis of physisorbed molecules. Figure 3-17 contains control and powder spectra.

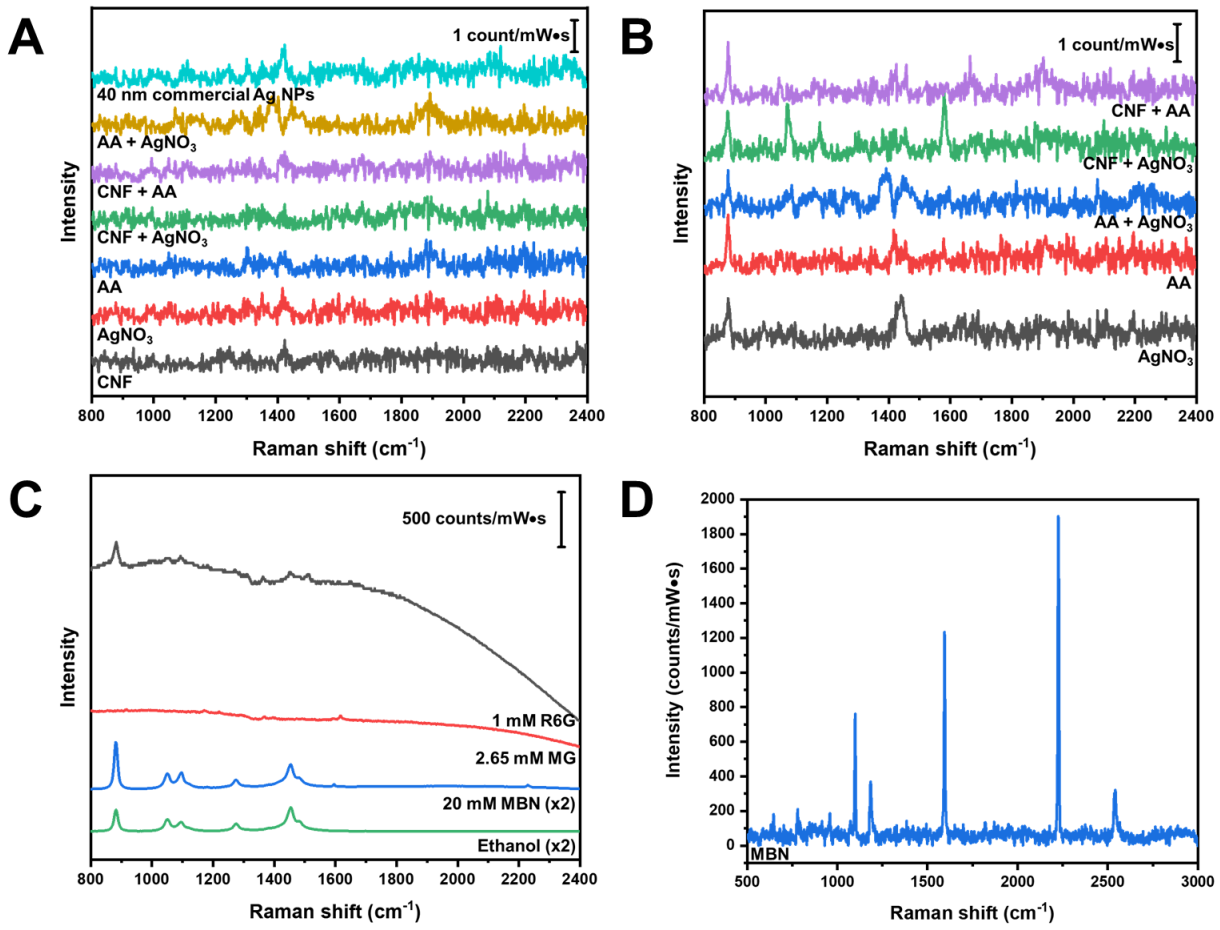

Figure 3-17. SERS controls and powder spectra. (A) Raman spectra controls. (B) Raman spectra controls with 5 μM MBN. (C) Raman spectra of ethanol, 20 mM MBN in ethanol, 2.65 mM MG in ethanol and 1 mM R6G in ethanol. (D) Powder spectrum of MBN using 633 nm laser, 10% power, 10 seconds, 1 accumulations on a gold coated glass slide.

Ag-CNF is envisioned as a water-dispersible substrate for the detection of pesticides and fungicides. MG is commonly found in water and is thus an ideal proof-of-concept analyte to measure using a water-dispersible SERS substrate. MG is a fungicide that is now banned due to its genotoxic and carcinogenic properties. However, the material is still used illegally from time to time in the aquaculture industry due to its effectiveness in preventing infection.[65-66] The European Commission has set a minimum required performance limit (MRPL) of 2 μg/kg (~5 nM in solution) in the collective detection of MG and leucomalachite

green.[66-67] Figure 3-18A shows SERS spectra of MG at different concentrations (0.1 nM to 100 nM) with an adsorption time of 2 minutes. Figure 3-18B is a plot of the peak intensity from the C–C ring stretch at 1616 cm^{-1} versus MG concentration. The peak intensity of MG increases linearly as the solution concentration increases. Beyond 100 nM, measurements of MG follow a Langmuir adsorption isotherm (Figure 3-19). The calibration curve yields a line equation of y = 10.2x + 18.6 and a coefficient of determination of 0.997. The limit of detection and limit of quantification is 0.08 and 0.27 nM based on 3 and 10 standard deviations of the blank signal, respectively. The dynamic range is determined to be between 0.27 and 100 nM. The detection of MG using other SERS substrates is compared in Table 3-7.[19, 25, 66-72] SERS has also been coupled with other techniques and methods for the detection of MG. For example, Lee and co-workers have developed a SERS microfluidic sensor for the detection of MG, and determined a limit of detection of 2.74 to 5.48 nM (1-2 ppb) and linear response between 2.74 and 274 nM (1-100 ppb).[73] In their work, they also performed a comparative study with a liquid chromatography mass spectrometry method, and found similar results.[73] The dispersible Ag-CNF substrate achieves a lower limit of detection (LOD) compared to that reported by Lee and coworkers. In addition, our LOD is lower or comparable to that of any of the SERS methods listed in Table 3-7.

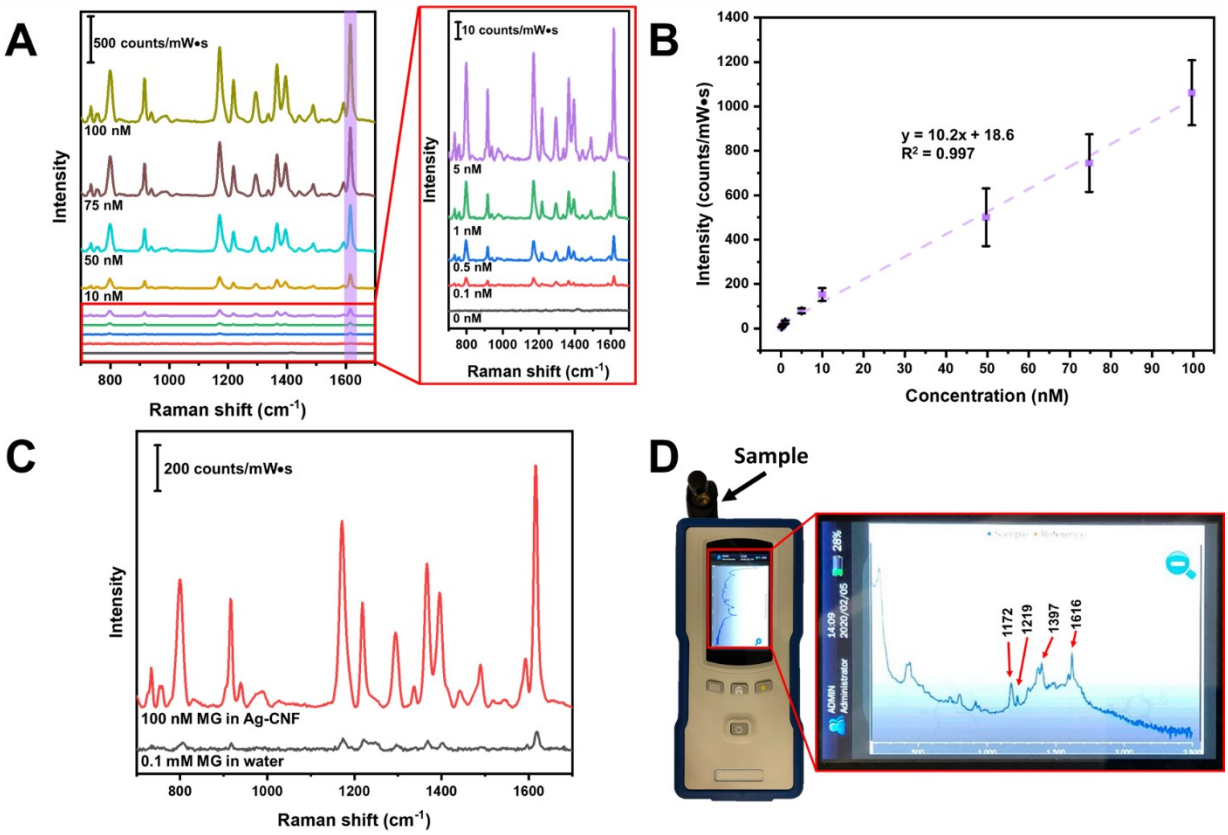

Figure 3-18. Analytical measurements using Ag-CNF. (A) Stacked SERS spectra and (B) calibration curve of malachite green in Ag-CNF solution. Each concentration is representative of three Ag-CNF samples measured three times at different locations on the vial (n=9) (633 nm, 4.55 mW, 1 second, 10 accumulations). (C) Comparison of 100 nM malachite green in Ag-CNF solution versus 0.1 mM malachite green in water. (D) Measurements taken using a handheld Raman spectrometer in 2 minutes. The Raman spectrum is from malachite green (1 μM) in Ag-CNF solution (785 nm, 300 mW).

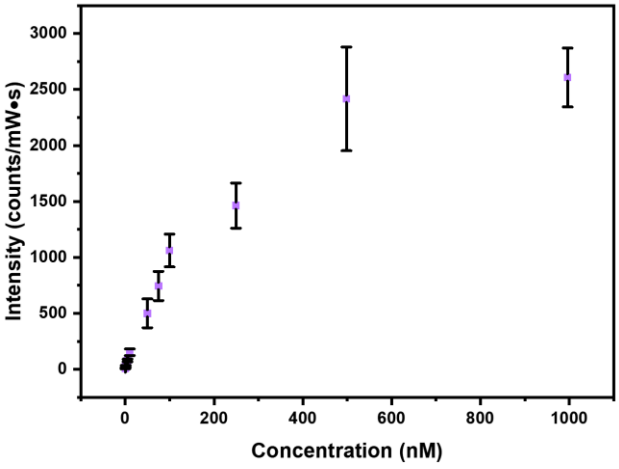

Figure 3-19. SERS measurements of MG (0.1 nM to 1000 nM) in Ag-CNF solution.

Table 3-7. Summary of SERS Substrates and Their Performance for the Detection of Malachite Green

Type of substrate	Detection platform	Limit of detection	Enhancement factor	Reference
Starch-coated Ag NP	Solution	1.7×10^{-10} M[a] (0.08 μg/L)	5.1×10^{5} [b]	19
Ag NP/SiO_2/CNC and Ag NP/CNC	Solution	9×10^{-10} M and 5.2×10^{-9} M	n.d.	25
Au NP	Solution	2.2×10^{-10} M[a] (0.1 μg/L)	1.5×10^{6} [b]	66
Ag NP on gold electrode	Solid	2.4×10^{-16} M	n.d.	67
Ag NP on glass fiber paper	Solid	5×10^{-10} M	n.d.	68
Au NP on paper	Solid	1×10^{-9} M	n.d.	69
Ag NP on a TiO_2 nanorod scaffold	Solid	1×10^{-12} M	4.4×10^{5} [c]	70
S-RGO/Ag NP on weighing paper	Solid	1×10^{-7} M	1.4×10^{9} [d]	71
Ag NP on TiO_2 inverse opal film	Solid	1×10^{-9} M	4.1×10^{4} [d]	72
Ag-CNF	Solution	8×10^{-11} M	1.3×10^{4}[b]	This work

n.d. – not determined; CNC – cellulose nanocrystals; S-RGO – sulfonated reduced graphene oxide. [a]Malachite green reagent is not specified and the conversion to molar concentration is approximated using malachite green oxalate. [b]Based on malachite green. [c]Based on p-mercaptobenzoic acid. [d]Based on rhodamine 6G.

The performance of colloidal Ag-CNF for in-solution measurements is further investigated by determining the enhancement factor. Figure 3-18C compares Raman spectra of MG in the presence and absence of Ag-CNF. A spectrum with intense peaks is produced when MG (100 nM final concentration) is in Ag-CNF solution. Conversely, a spectrum with low intensity peaks is shown when MG (0.1 mM final concentration) is only in water. The analytical enhancement factor (AEF) formula is used calculate the enhancement factor for Ag-CNF (Equation 3-4)[74]:

$$AEF = \frac{I_{SERS}/c_{SERS}}{I_{Raman}/c_{Raman}} \quad \textbf{(Equation 3-4)}$$

where I_{SERS} and I_{Raman} are the MG peak intensities at 1616 cm^{-1} and c_{SERS} and c_{Raman} are the MG solution concentrations in the presence and absence of Ag-CNF, respectively. The AEF

was determined to be $1.3x10^4$. Table 3-7 summaries the enhancement factor of other SERS substrates.[19, 66, 70-72]

Technological advancements in Raman spectrometers such as the development of handheld Raman devices has enticed researchers to produce field deployable SERS substrates. An important advantage of solution-based substrates is that they are easily compatible with handheld Raman platforms. We have recently reported on the combination of colloidal gold nanostars and a handheld Raman device for in-solution SERS.[14] Figure 3-18D is an image demonstrating the use of colloidal Ag-CNF and a handheld Raman spectrometer with a liquid cell adapter for the detection of MG. The screen of the device has been expanded to show that the major peaks of MG are easily distinguishable without additional data manipulation. We feel that portable instrumentation and solution-based substrates will be an important combination for SERS measurements in a number of settings moving forward.

3.4. Conclusions

We have developed a water-dispersible hybrid nanomaterial SERS substrate consisting of CNF decorated with Ag NPs. The synthesis of Ag-CNF produces well-controlled spherical nanoparticles. It is confirmed by UV-Vis, SEM, XRD, XPS and FTIR that Ag NPs with an average diameter of 45 nm are anchored to the CNF. We demonstrate that CNF plays a significant role as a support and dispersing agent in the synthesis of this hybrid nanomaterial. With the nanoparticles anchored to the CNF, we found that centrifugation results in bundles of fibers that bring the Ag NPs into close proximity, resulting in interparticle coupling and hot spots. Ostwald ripening and intraparticle growth was

observed after substrate aging which resulted in an increase in SERS intensity. SERS measurements with water-dispersible Ag-CNF are rapid (2 minutes) and reproducible (9% RSD). The detection of the banned fungicide, MG, was demonstrated at a level of 80 pM, which is below the required method sensitivity limit. Methods to control the fiber intertwinement and to introduce selectivity via chemical modification of the CNF are currently being developed.

3.5. References

1. Bell, S. E. J.; Sirimuthu, N. M. S., Quantitative surface-enhanced Raman spectroscopy. *Chem. Soc. Rev.* **2008,** *37* (5), 1012-1024.

2. Mosier-Boss, P. A., Review of SERS Substrates for Chemical Sensing. *Nanomaterials* **2017,** *7* (6), 142.

3. Shi, R.; Liu, X.; Ying, Y., Facing Challenges in Real-Life Application of Surface-Enhanced Raman Scattering: Design and Nanofabrication of Surface-Enhanced Raman Scattering Substrates for Rapid Field Test of Food Contaminants. *J. Agric. Food. Chem.* **2018,** *66* (26), 6525-6543.

4. Lin, X.-M.; Cui, Y.; Xu, Y.-H.; Ren, B.; Tian, Z.-Q., Surface-enhanced Raman spectroscopy: substrate-related issues. *Anal. Bioanal. Chem.* **2009,** *394* (7), 1729-1745.

5. Ogundare, S. A.; van Zyl, W. E., A review of cellulose-based substrates for SERS: fundamentals, design principles, applications. *Cellulose* **2019,** *26* (11), 6489-6528.

6. Kim, D.; Ko, Y.; Kwon, G.; Choo, Y.-M.; You, J., Low-cost, high-performance plasmonic nanocomposites for hazardous chemical detection using surface enhanced Raman scattering. *Sensors and Actuators B: Chemical* **2018,** *274*, 30-36.

7. Kim, D.; Ko, Y.; Kwon, G.; Kim, U.-J.; Lee, J. H.; You, J., 2,2,6,6-Tetramethylpiperidine-1-oxy-Oxidized Cellulose Nanofiber-Based Nanocomposite Papers for Facile In Situ Surface-Enhanced Raman Scattering Detection. *ACS Sustainable Chem. Eng.* **2019,** *7* (18), 15640-15647.

8. Crawford, A. C.; Skuratovsky, A.; Porter, M. D., Sampling Error: Impact on the Quantitative Analysis of Nanoparticle-Based Surface-Enhanced Raman Scattering Immunoassays. *Anal. Chem.* **2016,** *88* (12), 6515-6522.

9. Cunningham, D.; Littleford, R. E.; Smith, W. E.; Lundahl, P. J.; Khan, I.; McComb, D. W.; Graham, D.; Laforest, N., Practical control of SERRS enhancement. *Faraday Discuss.* **2006,** *132* (0), 135-145.

10. Docherty, J.; Mabbott, S.; Smith, E.; Faulds, K.; Davidson, C.; Reglinski, J.; Graham, D., Detection of potentially toxic metals by SERS using salen complexes. *Analyst* **2016,** *141* (20), 5857-5863.

11. Faulds, K.; Smith, W. E.; Graham, D.; Lacey, R. J., Assessment of silver and gold substrates for the detection of amphetamine sulfate by surface enhanced Raman scattering (SERS). *Analyst* **2002,** *127* (2), 282-286.

12. Graham, D.; Thompson, D. G.; Smith, W. E.; Faulds, K., Control of enhanced Raman scattering using a DNA-based assembly process of dye-coded nanoparticles. *Nat. Nanotechnol.* **2008,** *3* (9), 548-551.

13. Lu, G.; Forbes, T. Z.; Haes, A. J., SERS detection of uranyl using functionalized gold nanostars promoted by nanoparticle shape and size. *Analyst* **2016,** *141* (17), 5137-5143.

14. Mahmoud, A. Y. F.; Rusin, C. J.; McDermott, M. T., Gold nanostars as a colloidal substrate for in-solution SERS measurements using a handheld Raman spectrometer. *Analyst* **2020,** *145* (4), 1396-1407.

15. Saute, B.; Narayanan, R., Solution-based direct readout surface enhanced Raman spectroscopic (SERS) detection of ultra-low levels of thiram with dogbone shaped gold nanoparticles. *Analyst* **2011,** *136* (3), 527-532.

16. Saute, B.; Narayanan, R., Solution-based SERS method to detect dithiocarbamate fungicides in different real-world matrices. *J. Raman Spectrosc.* **2013,** *44* (11), 1518-1522.

17. Saute, B.; Premasiri, R.; Ziegler, L.; Narayanan, R., Gold nanorods as surface enhanced Raman spectroscopy substrates for sensitive and selective detection of ultra-low levels of dithiocarbamate pesticides. *Analyst* **2012,** *137* (21), 5082-5087.

18. Yu, Z.; Grasso, M. F.; Sorensen, H. H.; Zhang, P., Ratiometric SERS detection of polycyclic aromatic hydrocarbons assisted by β-cyclodextrin-modified gold nanoparticles. *Microchim. Acta* **2019,** *186* (6), 391.

19. Zhao, Y.; Tian, Y.; Ma, P.; Yu, A.; Zhang, H.; Chen, Y., Determination of melamine and malachite green by surface-enhanced Raman scattering spectroscopy using starch-coated silver nanoparticles as substrates. *Anal. Methods* **2015,** *7* (19), 8116-8122.

20. Moskovits, M., Surface-enhanced Raman spectroscopy: a brief retrospective. *J. Raman Spectrosc.* **2005,** *36* (6-7), 485-496.

21. Langer, J.; Jimenez de Aberasturi, D.; Aizpurua, J.; Alvarez-Puebla, R. A.; Auguié, B.; Baumberg, J. J.; Bazan, G. C.; Bell, S. E. J.; Boisen, A.; Brolo, A. G.; Choo, J.; Cialla-May, D.; Deckert, V.; Fabris, L.; Faulds, K.; García de Abajo, F. J.; Goodacre, R.; Graham, D.; Haes, A. J.; Haynes, C. L.; Huck, C.; Itoh, T.; Käll, M.; Kneipp, J.; Kotov, N. A.; Kuang, H.; Le Ru, E. C.; Lee, H. K.; Li, J.-F.; Ling, X. Y.; Maier, S. A.; Mayerhöfer, T.; Moskovits, M.; Murakoshi, K.; Nam, J.-M.; Nie, S.; Ozaki, Y.; Pastoriza-Santos, I.; Perez-Juste, J.; Popp, J.; Pucci, A.; Reich, S.; Ren, B.; Schatz, G. C.; Shegai, T.; Schlücker, S.; Tay, L.-L.; Thomas, K. G.; Tian, Z.-Q.; Van Duyne, R. P.; Vo-Dinh, T.; Wang, Y.; Willets, K. A.; Xu, C.; Xu, H.; Xu, Y.; Yamamoto, Y. S.; Zhao, B.; Liz-Marzán, L. M., Present and Future of Surface-Enhanced Raman Scattering. *ACS Nano* **2020,** *14* (1), 28-117.

22. Vander Ende, E.; Bourgeois, M. R.; Henry, A.-I.; Chávez, J. L.; Krabacher, R.; Schatz, G. C.; Van Duyne, R. P., Physicochemical Trapping of Neurotransmitters in Polymer-Mediated Gold Nanoparticle Aggregates for Surface-Enhanced Raman Spectroscopy. *Anal. Chem.* **2019,** *91* (15), 9554-9562.

23. Li, J.-M.; Ma, W.-F.; Wei, C.; You, L.-J.; Guo, J.; Hu, J.; Wang, C.-C., Detecting Trace Melamine in Solution by SERS Using Ag Nanoparticle Coated Poly(styrene-co-acrylic acid) Nanospheres as Novel Active Substrates. *Langmuir* **2011,** *27* (23), 14539-14544.

24. Ogundare, S. A.; van Zyl, W. E., Nanocrystalline cellulose as reducing- and stabilizing agent in the synthesis of silver nanoparticles: Application as a surface-enhanced Raman scattering (SERS) substrate. *Surf. Interfaces* **2018,** *13*, 1-10.

25. Ogundare, S. A.; van Zyl, W. E., Amplification of SERS "hot spots" by silica clustering in a silver-nanoparticle/nanocrystalline-cellulose sensor applied in malachite green detection. *Colloids Surf., A* **2019,** *570*, 156-164.

26. Foster, E. J.; Moon, R. J.; Agarwal, U. P.; Bortner, M. J.; Bras, J.; Camarero-Espinosa, S.; Chan, K. J.; Clift, M. J. D.; Cranston, E. D.; Eichhorn, S. J.; Fox, D. M.; Hamad, W. Y.; Heux, L.; Jean, B.; Korey, M.; Nieh, W.; Ong, K. J.; Reid, M. S.; Renneckar, S.; Roberts, R.; Shatkin, J. A.; Simonsen, J.; Stinson-Bagby, K.; Wanasekara, N.; Youngblood, J., Current characterization methods for cellulose nanomaterials. *Chem. Soc. Rev.* **2018,** *47* (8), 2609-2679.

27. Siró, I.; Plackett, D., Microfibrillated cellulose and new nanocomposite materials: a review. *Cellulose* **2010,** *17* (3), 459-494.

28. Saito, T.; Isogai, A., TEMPO-Mediated Oxidation of Native Cellulose. The Effect of Oxidation Conditions on Chemical and Crystal Structures of the Water-Insoluble Fractions. *Biomacromolecules* **2004,** *5* (5), 1983-1989.

29. Saito, T.; Kimura, S.; Nishiyama, Y.; Isogai, A., Cellulose Nanofibers Prepared by TEMPO-Mediated Oxidation of Native Cellulose. *Biomacromolecules* **2007,** *8* (8), 2485-2491.

30. Islam, M. S.; Chen, L.; Sisler, J.; Tam, K. C., Cellulose nanocrystal (CNC)-inorganic hybrid systems: synthesis, properties and applications. *J. Mater. Chem. B* **2018,** *6* (6), 864-883.

31. Jiang, F.; Hsieh, Y.-L., Synthesis of Cellulose Nanofibril Bound Silver Nanoprism for Surface Enhanced Raman Scattering. *Biomacromolecules* **2014,** *15* (10), 3608-3616.

32. Nabeela, K.; Thomas, R. T.; Nair, J. B.; Maiti, K. K.; Warrier, K. G. K.; Pillai, S., TEMPO-Oxidized Nanocellulose Fiber-Directed Stable Aqueous Suspension of Plasmonic Flower-like Silver Nanoconstructs for Ultra-Trace Detection of Analytes. *ACS Appl. Mater. Interfaces* **2016,** *8* (43), 29242-29251.

33. Liou, P.; Nayigiziki, F. X.; Kong, F.; Mustapha, A.; Lin, M., Cellulose nanofibers coated with silver nanoparticles as a SERS platform for detection of pesticides in apples. *Carbohydr. Polym.* **2017,** *157*, 643-650.

34. Xiong, Z.; Lin, M.; Lin, H.; Huang, M., Facile synthesis of cellulose nanofiber nanocomposite as a SERS substrate for detection of thiram in juice. *Carbohydr. Polym.* **2018,** *189*, 79-86.

35. Anderson, S. L.; Luber, E. J.; Olsen, B. C.; Buriak, J. M., Substance over Subjectivity: Moving beyond the Histogram. *Chem. Mater.* **2016,** *28* (17), 5973-5975.

36. Menges, F. Spectragryph - optical spectroscopy software. http://www.effemm2.de/spectragryph/ (accessed April 23, 2020).

37. Soni, B.; Hassan, E. B.; Mahmoud, B., Chemical isolation and characterization of different cellulose nanofibers from cotton stalks. *Carbohydr. Polym.* **2015,** *134*, 581-589.

38. Isogai, A.; Saito, T.; Fukuzumi, H., TEMPO-oxidized cellulose nanofibers. *Nanoscale* **2011,** *3* (1), 71-85.

39. Yu, L.; Lin, J.; Tian, F.; Li, X.; Bian, F.; Wang, J., Cellulose nanofibrils generated from jute fibers with tunable polymorphs and crystallinity. *J. Mater. Chem. A* **2014,** *2* (18), 6402-6411.

40. Miao, X.; Lin, J.; Tian, F.; Li, X.; Bian, F.; Wang, J., Cellulose nanofibrils extracted from the byproduct of cotton plant. *Carbohydr. Polym.* **2016,** *136*, 841-850.

41. Kafy, A.; Kim, H. C.; Zhai, L.; Kim, J. W.; Hai, L. V.; Kang, T. J.; kim, J., Cellulose long fibers fabricated from cellulose nanofibers and its strong and tough characteristics. *Sci. Rep.* **2017,** *7* (1), 17683.

42. Zhu, C.; Soldatov, A.; Mathew, A. P., Advanced microscopy and spectroscopy reveal the adsorption and clustering of Cu(ii) onto TEMPO-oxidized cellulose nanofibers. *Nanoscale* **2017,** *9* (22), 7419-7428.

43. Liu, P.; Oksman, K.; Mathew, A. P., Surface adsorption and self-assembly of Cu(II) ions on TEMPO-oxidized cellulose nanofibers in aqueous media. *J. Colloid Interface Sci.* **2016,** *464*, 175-182.

44. Ifuku, S.; Tsuji, M.; Morimoto, M.; Saimoto, H.; Yano, H., Synthesis of Silver Nanoparticles Templated by TEMPO-Mediated Oxidized Bacterial Cellulose Nanofibers. *Biomacromolecules* **2009,** *10* (9), 2714-2717.

45. Eisa, W. H.; Abdelgawad, A. M.; Rojas, O. J., Solid-State Synthesis of Metal Nanoparticles Supported on Cellulose Nanocrystals and Their Catalytic Activity. *ACS Sustainable Chem. Eng.* **2018,** *6* (3), 3974-3983.

46. Lokanathan, A. R.; Uddin, K. M. A.; Rojas, O. J.; Laine, J., Cellulose Nanocrystal-Mediated Synthesis of Silver Nanoparticles: Role of Sulfate Groups in Nucleation Phenomena. *Biomacromolecules* **2014,** *15* (1), 373-379.

47. Uddin, K. M. A.; Arcot Raghupathi, L.; Liljeström, A.; Chen, X.; Rojas, O. J.; Laine, J., Silver nanoparticle synthesis mediated by carboxylated cellulose nanocrystals. *Green Mater.* **2014,** *2* (4), 183-192.

48. Wu, C.-N.; Fuh, S.-C.; Lin, S.-P.; Lin, Y.-Y.; Chen, H.-Y.; Liu, J.-M.; Cheng, K.-C., TEMPO-Oxidized Bacterial Cellulose Pellicle with Silver Nanoparticles for Wound Dressing. *Biomacromolecules* **2018,** *19* (2), 544-554.

49. Padalkar, S.; Capadona, J. R.; Rowan, S. J.; Weder, C.; Won, Y.-H.; Stanciu, L. A.; Moon, R. J., Natural Biopolymers: Novel Templates for the Synthesis of Nanostructures. *Langmuir* **2010,** *26* (11), 8497-8502.

50. Saito, T.; Isogai, A., Ion-exchange behavior of carboxylate groups in fibrous cellulose oxidized by the TEMPO-mediated system. *Carbohydr. Polym.* **2005,** *61* (2), 183-190.

51. Malassis, L.; Dreyfus, R.; Murphy, R. J.; Hough, L. A.; Donnio, B.; Murray, C. B., One-step green synthesis of gold and silver nanoparticles with ascorbic acid and their versatile surface post-functionalization. *RSC Adv.* **2016,** *6* (39), 33092-33100.

52. Gopiraman, M.; Deng, D.; Saravanamoorthy, S.; Chung, I.-M.; Kim, I. S., Gold, silver and nickel nanoparticle anchored cellulose nanofiber composites as highly active catalysts

for the rapid and selective reduction of nitrophenols in water. *RSC Adv.* **2018,** *8* (6), 3014-3023.

53. Pawcenis, D.; Chlebda, D. K.; Jędrzejczyk, R. J.; Leśniak, M.; Sitarz, M.; Łojewska, J., Preparation of silver nanoparticles using different fractions of TEMPO-oxidized nanocellulose. *Eur. Polym. J.* **2019,** *116*, 242-255.

54. Jiang, F.; Hsieh, Y.-L., Super water absorbing and shape memory nanocellulose aerogels from TEMPO-oxidized cellulose nanofibrils via cyclic freezing-thawing. *J. Mater. Chem. A* **2014,** *2* (2), 350-359.

55. Pope, C. G., X-Ray Diffraction and the Bragg Equation. *J. Chem. Educ.* **1997,** *74* (1), 129.

56. Gkogkou, D.; Shaykhutdinov, T.; Kratz, C.; Oates, T. W. H.; Hildebrandt, P.; Weidinger, I. M.; Ly, K. H.; Esser, N.; Hinrichs, K., Gradient metal nanoislands as a unified surface enhanced Raman scattering and surface enhanced infrared absorption platform for analytics. *Analyst* **2019,** *144* (17), 5271-5276.

57. Villarreal, E.; Li, G. G.; Zhang, Q.; Fu, X.; Wang, H., Nanoscale Surface Curvature Effects on Ligand–Nanoparticle Interactions: A Plasmon-Enhanced Spectroscopic Study of Thiolated Ligand Adsorption, Desorption, and Exchange on Gold Nanoparticles. *Nano Lett.* **2017,** *17* (7), 4443-4452.

58. Qin, Y.; Ji, X.; Jing, J.; Liu, H.; Wu, H.; Yang, W., Size control over spherical silver nanoparticles by ascorbic acid reduction. *Colloids Surf., A* **2010,** *372* (1), 172-176.

59. Thanh, N. T. K.; Maclean, N.; Mahiddine, S., Mechanisms of Nucleation and Growth of Nanoparticles in Solution. *Chem. Rev.* **2014,** *114* (15), 7610-7630.

60. Joke, D. G.; Kris, D. G.; Peter, V.; Luc, M., Reference database of Raman spectra of biological molecules. *J. Raman Spectrosc.* **2007,** *38* (9), 1133-1147.

61. Sacui, I. A.; Nieuwendaal, R. C.; Burnett, D. J.; Stranick, S. J.; Jorfi, M.; Weder, C.; Foster, E. J.; Olsson, R. T.; Gilman, J. W., Comparison of the Properties of Cellulose Nanocrystals and Cellulose Nanofibrils Isolated from Bacteria, Tunicate, and Wood Processed Using Acid, Enzymatic, Mechanical, and Oxidative Methods. *ACS Appl. Mater. Interfaces* **2014,** *6* (9), 6127-6138.

62. Tantra, R.; Brown, R. J. C.; Milton, M. J. T., Strategy to improve the reproducibility of colloidal SERS. *J. Raman Spectrosc.* **2007,** *38* (11), 1469-1479.

63. Panneerselvam, R.; Liu, G.-K.; Wang, Y.-H.; Liu, J.-Y.; Ding, S.-Y.; Li, J.-F.; Wu, D.-Y.; Tian, Z.-Q., Surface-enhanced Raman spectroscopy: bottlenecks and future directions. *Chem. Commun.* **2018,** *54* (1), 10-25.

64. Nie, S.; Emory, S. R., Probing Single Molecules and Single Nanoparticles by Surface-Enhanced Raman Scattering. *Science* **1997,** *275* (5303), 1102-1106.

65. An, L.; Deng, J.; Zhou, L.; Li, H.; Chen, F.; Wang, H.; Liu, Y., Simultaneous spectrophotometric determination of trace amount of malachite green and crystal violet in water after cloud point extraction using partial least squares regression. *J. Hazard. Mater.* **2010,** *175* (1), 883-888.

66. Jin, Y.; Ma, P.; Liang, F.; Gao, D.; Wang, X., Determination of malachite green in environmental water using cloud point extraction coupled with surface-enhanced Raman scattering. *Anal. Methods* **2013,** *5* (20), 5609-5614.

67. Xu, K.-X.; Guo, M.-H.; Huang, Y.-P.; Li, X.-D.; Sun, J.-J., Rapid and sensitive detection of malachite green in aquaculture water by electrochemical preconcentration and surface-enhanced Raman scattering. *Talanta* **2018,** *180*, 383-388.

68. Deng, D.; Lin, Q.; Li, H.; Huang, Z.; Kuang, Y.; Chen, H.; Kong, J., Rapid detection of malachite green residues in fish using a surface-enhanced Raman scattering-active glass fiber paper prepared by in situ reduction method. *Talanta* **2019,** *200*, 272-278.

69. Liao, W.-J.; Roy, P. K.; Chattopadhyay, S., An ink-jet printed, surface enhanced Raman scattering paper for food screening. *RSC Adv.* **2014,** *4* (76), 40487-40493.

70. Tan, E.-Z.; Yin, P.-G.; You, T.-t.; Wang, H.; Guo, L., Three Dimensional Design of Large-Scale TiO2 Nanorods Scaffold Decorated by Silver Nanoparticles as SERS Sensor for Ultrasensitive Malachite Green Detection. *ACS Appl. Mater. Interfaces* **2012,** *4* (7), 3432-3437.

71. Xiao, G.; Li, Y.; Shi, W.; Shen, L.; Chen, Q.; Huang, L., Highly sensitive, reproducible and stable SERS substrate based on reduced graphene oxide/silver nanoparticles coated weighing paper. *Appl. Surf. Sci.* **2017,** *404*, 334-341.

72. Zhao, J.; Lin, J.; Li, X.; Zhao, G.; Zhang, W., Silver nanoparticles deposited inverse opal film as a highly active and uniform SERS substrate. *Appl. Surf. Sci.* **2015,** *347*, 514-519.

73. Lee, S.; Choi, J.; Chen, L.; Park, B.; Kyong, J. B.; Seong, G. H.; Choo, J.; Lee, Y.; Shin, K.-H.; Lee, E. K.; Joo, S.-W.; Lee, K.-H., Fast and sensitive trace analysis of malachite green using a surface-enhanced Raman microfluidic sensor. *Anal. Chim. Acta* **2007,** *590* (2), 139-144.

74. Le Ru, E. C.; Blackie, E.; Meyer, M.; Etchegoin, P. G., Surface Enhanced Raman Scattering Enhancement Factors: A Comprehensive Study. *J. Phys. Chem. C* **2007,** *111* (37), 13794-13803.

Chapter 4. In-Solution SERS Measurements Using Gold Nanoparticle Decorated Cellulose Nanofibers

4.1. Introduction

Surface-enhanced Raman scattering (SERS) is a non-destructive and sensitive technique used in qualitative and quantitative measurement applications.[1-2] Potential uses and applications for SERS measurement platforms include biosensing, environmental monitoring, law enforcement (i.e., narcotics and explosives) and pharmaceutical quality control.[2-8] A lot of attention has been drawn towards SERS platforms due to its compatibility with aqueous samples, minimal sample preparation time and ability to provide chemical information through molecular vibrational modes.[9] Moreover, with the technological advancement of handheld Raman spectrometers, remote SERS analysis has become appealing and more common.[10-11] However, whether measurements are performed in or out of the laboratory, SERS analysis relies on the use of SERS substrates.

SERS substrates can provide enhancement of weak Raman scattered photons of up to 10^{10} times and the capability for single molecule detection.[9, 12-13] The desired features of a good substrate include high average enhancement ($\sim 10^5$), uniformity and reproducibility (<20%), large measurement areas (mm^2), good storage stability, low cost, ease of synthesis, and a clean surface for analysis.[9, 14-15] The list of substrates for SERS measurements is extensive.[9, 16] Briefly, these substrates can include, but are not limited to, highly ordered

nanostructured substrates fabricated using nanolithography techniques, colloidal nanoparticles of different shapes and sizes for in-solution measurements, and adsorption or deposition of nanoparticles on a solid surface.[6, 9]

Cellulose-based substrates have attracted attention due to low cost, ease of synthesis, transportability and measurement flexibility (i.e., analyte deposition, wiping and dipping).[17-18] There are plenty of cellulose-based substrates used for SERS measurements.[19] For example, White and co-workers developed substrates by ink-jet printing nanoparticles onto cellulose paper.[17-18] Lin and co-workers have grown silver nanoparticles onto cellulose nanofiber (CNF)/polyvinyl alcohol films for the detection of thiabendazole.[20] In another example, a flexible jellylike substrate developed from nanocellulose decorated with silver nanoparticles was used for the analysis of pesticides on the surface of fruits and vegetables.[21] Other examples show the development of cellulose nanocomposite materials being deposited onto glass slides and membranes.[22-25] The large majority of substrates are considered to be a planar substrates. To date, the use of colloidal cellulose-based substrates for in-solution SERS measurements is an area open to expansion.

In-solution SERS measurements using colloidal nanoparticles remains challenging because of the need for controlled nanoparticle aggregation. Many approaches have been used to control nanoparticle aggregation, such as the use of different aggregating agents, the self-assembly of nanoparticles and the use of polymers/surfactants to support nanoparticle clusters.[26-31] Examples of support structures used in the literature include poly(styrene-co-acrylic acid) nanospheres, CNC, CNC/SiO_2 nanocomposites and CNF.[32-35] In

our previous work, we developed a water dispersible SERS substrate using CNF decorated with silver nanoparticles (Ag-CNF) for the detection and quantification of malachite green (Chapter 3). In this work, oxidized CNF provided excellent colloidal stability in water and centrifugation produced Ag-CNF bundles that provided intense Raman enhancement. Moving forward, there are benefits to developing a water dispersible substrate using gold nanoparticles (AuNPs). AuNPs are, in general, more commonly used in the development of SERS substrates and SERS applications for a variety of reasons. AuNPs are resistant to oxidation and have good chemical stability.[36] Another benefit to using AuNPs in SERS applications is its significantly higher biocompatibility.[37-38] Additionally, the localized surface plasmon resonance (LSPR) of AuNPs is red-shifted in comparison to silver nanoparticles, which has a larger overlap with red and near infrared lasers. Many Raman spectrometers are equipped with longer wavelength lasers, particularly handheld Raman devices. To the best of our knowledge, CNF decorated with gold nanoparticles (Au-CNF) has not been explored as a water dispersible SERS substrate.

Herein, we report the development of a colloidal SERS substrate using CNF decorated with gold nanoparticles (Au-CNF). We demonstrate that CNF has a significant impact on the colloidal stability by acting as a support for AuNPs. Large and reproducible SERS enhancement is the result of the formation of a nanofiber capture network upon centrifugation. This colloidally stable nanofiber network brings AuNPs in close proximity to one another and produces many SERS hot spots. Colloidal Au-CNF used for in-solution measurements is capable of detecting analytes through chemisorption and physisorption mechanisms within 2 minutes. An assay is developed to detect and quantify methimazole (MTZ) in synthetic urine. As a proof-of-concept, colloidal Au-CNF is coupled with a

handheld Raman spectrometer to demonstrate the potential to rapidly detect pesticides and fungicides remotely.

4.2. Experimental

4.2.1. Materials

The CNF was synthesized using commercial Bleached Chemi-Thermo Mechanical Pulp (BCTMP, 60% water content) obtained from a local company. Gold (III) chloride trihydrate (99.995%, $HAuCl_4$), hydrochloric acid (HCl, 37.5%), sodium chloride (NaCl, 99%), sodium bromide (NaBr, 99%), laboratory grade 2,2,6,6-tetramethylpiperidinyl-1-oxyl radical (TEMPO), sodium hypochlorite solution (NaOCl, 13%), rhodamine 6G (R6G, 95%), malachite green oxalate salt technical grade (MG), thiabendazole (TBZ, 99%), methimazole (MTZ, analytical standard) and Surine™ negative urine control were purchased from Sigma-Aldrich Canada (Oakville, Ontario). Sodium hydroxide (NaOH) was purchased from Fisher Scientific Canada and the L-ascorbic acid (AA) was purchased from Anachemia. 4-Mercaptobenzonitrile (MBN) was purchased from Combi-Blocks, Inc. (San Diego, California, USA). 400-mesh carbon transmission electron microscopy (TEM) grids were purchased from Electron Microscopy Sciences. All syntheses and measurements were completed using deionized (DI) water (18.2 MΩ·cm).

4.2.2. Preparation of TEMPO-Oxidized Cellulose Nanofibers

The preparation of TEMPO-oxidation followed previously published methods.[39-40] A BCTMP (7 wt. %) solution was mixed at 500 rpm with NaBr (1 mmol/g of BCTMP) and TEMPO (0.1 mmol/g of BCTMP). While maintaining the solution pH at 10.5, NaOCl (10

mmol/g BCTMP) was added dropwise. When no pH variation was observed, the reaction was considered complete. The oxidized CNF solution was washed three times using Büchner funnel filtration. A Vitamix® Professional Series 300 blender was used for fiber disintegration (10 min; setting #10). The CNF was stored in the refrigerator (4 °C).

4.2.3. Determination of Carboxyl Content of TEMPO-Oxidized Cellulose Nanofibers

A conductometric titration was used to determine the carboxyl content of the CNF.[39-40] Freeze-dried CNF (0.2 g) was mixed with DI water (55 mL) and NaCl (5 mL, 10 mM) until the CNF was well-dispersed. The solution pH was adjusted to 2.5 using 1M HCl and was titrated to a pH of 11 using 0.05 M NaOH. The titration was performed in triplicates.

4.2.4. Synthesis of Cellulose Nanofibers Decorated With Gold Nanoparticles

Figure 4-1 is a schematic illustration of the synthesis for cellulose nanofibers decorated with AuNPs (Au-CNF). This synthesis has been adapted from my previous work (Chapter 3). An aqueous CNF solution (0.02 %) was heated to 70 °C and $HAuCl_4$ (0.2 mM final concentration) was mixed at 400 rpm for 5 minutes. AA (0.3 mM final concentration) was then added and mixed for an additional 5 minutes.

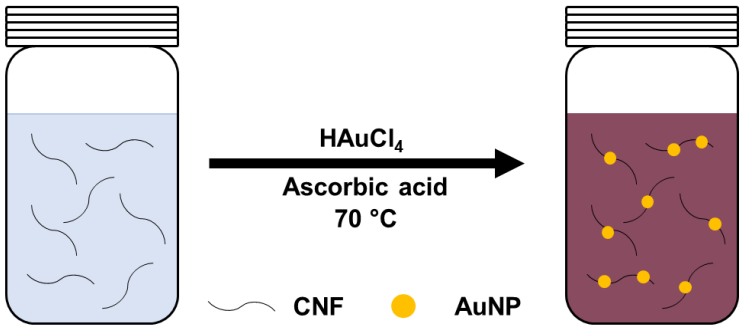

Figure 4-1. Synthesis schematic for cellulose nanofibers decorated with gold nanoparticles.

4.2.5. Characterization

A Nicolet 8700 continuum Fourier transform infrared (FTIR) spectrometer was used for FTIR analysis. Freeze-dried samples were flattened onto a KBr pellet and were examined from 4000 to 500 cm^{-1} with a resolution of 4 cm^{-1} and 32 sample scans.

UV-Visible spectroscopy experiments were performed using a PerkinElmer Lamdba 35 spectrometer. All measurements were made in 2.5 mL BRAND® polystyrene disposable cuvettes. The instrument settings were as followed: slit width of 1 nm and scan rate of 960 nm/min.

Scanning electron microscopy (SEM) and transmission electron microscopy (TEM) images were taken using a Hitachi S-4800 field emission SEM and a JEOL JEM-ARM200CF S/TEM, respectively. Images were taken at 30 keV and 20 μA (SEM) and 200 keV (TEM). The images were processed and analyzed using Gatan Digital Micrograph. An average-shifted histogram (ASH) was used to demonstrate the particle size distribution and was generated using an open-source program.[41]

Atomic force microscopy (AFM) images were taken with a Digital Instruments Nanoscope III Multimode microscope. The sample was prepared by drop-casting CNF ($1x10^{-4}$ %) onto a silicon substrate and left to dry overnight. The image shown was acquired using Nanoscope in tapping mode at a scan size of 2.0 μm and a scan rate of 1.7 Hz. Gwyddion software was used for image processing and height profiling. The height was determined using 20 different single stranded fiber locations.

A Kratos AXIS-165 spectrometer with a monochromatic Al Kα source (1486.69 eV) at 126 W was used for x-ray photoelectron spectroscopy (XPS) analysis. Survey and high resolution spectra were obtained for CNF and Au-CNF. Data processing was completed using CasaXPS software. The library was set to CasaXPS_KratosAxis-F1.lib, and the survey and high resolution spectra were adjusted by setting C 1s to 285.00 eV binding energy. A Gaussian-Lorentzian line shape and Shirley background were used for all peak fittings.

X-ray diffraction (XRD) analysis was completed using a Rigaku XRD Ultima IV equipped with a Cu Kα source (40 kV and 44 mA). Samples were analyzed using a continuous scan mode, a 2θ scan range of 10 to 90 ° and scan speed of 2 °/minute. The Au-CNF spectrum was scaled by a factor of ~2.3 based on the values at a 2θ of 18.2 ° in the CNF spectrum.

Zeta potential measurements of Au-CNF were obtained using a Malvern Zetasizer Nano-ZS. Samples (1 mL) were measured in 2.5 mL BRAND® polystyrene disposable cuvettes (pathlength=1cm) with an equilibrium time of 120 seconds and at a temperature of 25 °C. The pH measurements was estimated with Fisherbrand™ 0-14.0 pH paper.

4.2.6. SERS Analysis

SERS measurements were taken using a Renishaw inVia Raman microscope equipped with a RL633 50 mW HeNe laser and a 300 mW 785 nm diode laser. The microscope was modified using a 90 ° liquid cell adapter (f=30mm objective). Samples were centrifuged at 14000 rpm for 10 minutes (Eppendorf Centrifuge 5417 R) and re-dispersed in water. The majority of the spectra were obtained using the following setting conditions: 632.8 mW – 100% power (4-5 mW), 5 seconds and 10 accumulations; 785 nm – 100% power (95-100 mW). Analytes had an adsorption time of 2 minutes before analysis. The data was acquired using Wire 3.4 software and analyzed using open-source Spectragryph software.[42]

SERS measurements were taken using a B&W Tek TacticID handheld Raman spectrometer equipped with a 785 nm diode laser (300 mW). The handheld device was calibrated (in the x-axis) using a polystyrene standard before each experiment. A liquid cell adapter was used to measure analytes in solution using 1 dram vials at 100% laser power. Similar to above, the analytes were mixed for 2 minutes before taking a measurement. Data files were extracted from the handheld and analyzed using open-source Spectragryph software.[42] Figure 4-2 is an image comparing the Renishaw inVia Raman microscope and B&W Tek TacticID handheld Raman spectrometer.

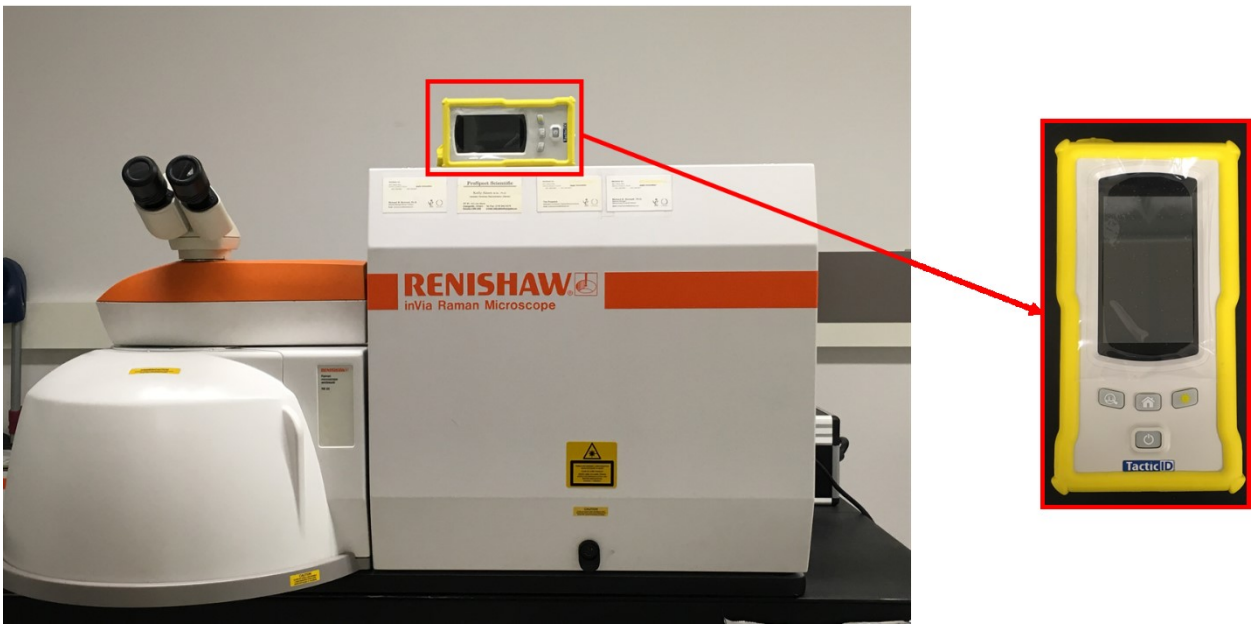

Figure 4-2. Images of the Renishaw inVia Raman microscope and B&W Tek TacticID handheld Raman spectrometer.

4.3. Results and Discussion

4.3.1. Synthesis and Characterization of Gold Nanoparticle Decorated Cellulose Nanofibers

Cellulose nanomaterials have been previously used for the synthesis and stabilization of metallic nanoparticles.[43] In this work, CNF is used to synthesize and support AuNPs. The CNF characterizations in this chapter are similar to Chapter 3, and is re-evaluated in this chapter for the sake of completeness. CNF is considered a subset of cellulose nanomaterials, and is defined as a high aspect ratio material with a length ranging up to the micrometre regime and a width of 20-100 nm.[44-45] Size and morphology analysis of the CNF used here is shown in Figure 4-3. SEM imaging shows that CNF's length ranges from 300-2000 nm (Figure 4-3A). AFM imaging and cross-sectional height profiling was used to

determine the height/width of the nanofibers (Figure 4-3B). The width of the CNF was measured as 8 ± 2 nm. Research has shown that CNF have high aspect ratios and fiber widths as low as 3 nm.[46-47]

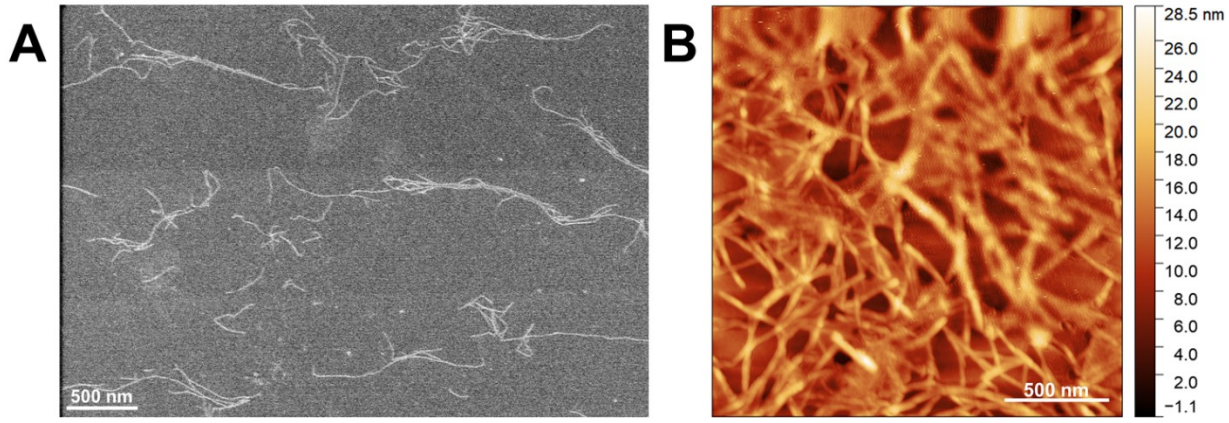

Figure 4-3. Cellulose nanofibers size analysis. (A) SEM and (B) AFM images of cellulose nanofibers. The SEM image of CNF in (A) was taken and provided by Dr. Mounir El Bakkari.

Many types of surface modification of CNF have been used to change the functionality before the defibrillation of the nanomaterial.[44, 48] Surface modification with 2,2,6,6-tetramethylpiperidinyl-1-oxyl (TEMPO) oxidation is a process used to selectively convert primary hydroxyl groups into carboxylic acid/carboxylate groups.[39-40] TEMPO oxidation of CNF results in nanofibers rich in surface carboxylate groups providing excellent water dispersibility.[40, 49] Infrared spectroscopy, a conductometric titration and zeta potential measurements were used to investigate the surface functionality and charge after the oxidation process. Figure 4-4 shows the IR spectrum of oxidized CNF (blue curve). Table 4-1 shows the major band assignments according to previously published articles.[44, 46-47, 50-52] The major band at 1613 cm^{-1} is associated to the COO^- antisymmetric stretch (ν_{as},

COO^-).[46-47, 51] The carboxylate content is quantified using a conductometric titration, and is calculated to be 1.12 ± 0.03 mmol/gram. TEMPO-oxidized CNF with values ranging between 0.6 and 1.7 mmol/gram have been demonstrated in the literature, and our value is well within this range.[49, 53] The zeta potential for CNF (0.02 %, pH 5-6) was measured at -51.3 ± 0.6 mV. This is representative of a high-density of surface carboxylate groups and characteristic of a colloidally stable solution.

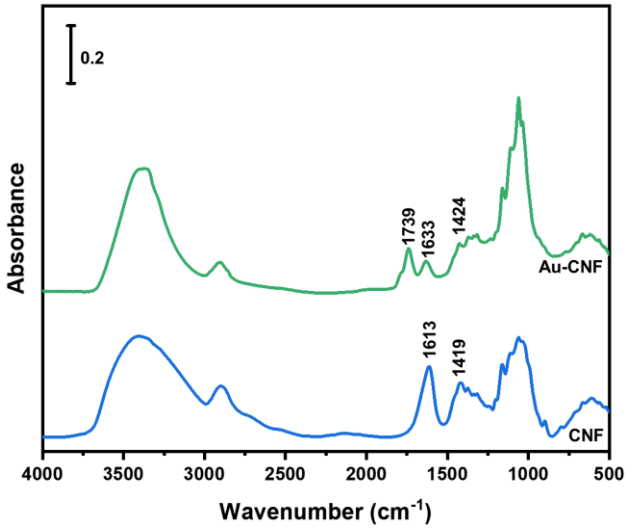

Figure 4-4. Infrared spectroscopy of oxidized cellulose nanofibers with and without gold nanoparticles.

Table 4-1. Infrared Spectroscopy Band Assignments for TEMPO-Oxidized Cellulose Nanofibers

Wavenumber (cm^{-1})	IR band assignment[44, 46-47, 50-52]
3408	O–H stretch
2899	CH_2 stretch
1613	COO^- antisymmetric stretch
1419	COO^- symmetric stretch
1371	C–H bend
1309	CH_2 wag
1162	C–O–C glycosidic antisymmetric stretch
1111	C–O stretch
1060	C–O stretch
1035	C–O stretch
898	β-glycosidic linkage

The synthesis of cellulose and AuNP hybrid nanomaterials is well-established and discussed throughout the literature.[43, 54-59] Past research has shown that the nucleation and growth of AuNPs can occur at any oxygen containing moiety from CNF.[43, 54-59] In my work, the deposition of AuNPs onto CNF was examined using IR spectroscopy. Figure 4-4 shows the IR spectrum of freeze-dried CNF (blue curve) and Au-CNF (green curve). The region between 1750 cm^{-1} and 1400 cm^{-1} of the spectrum is of interest due to interactions between the AuNPs and the carboxylate groups.[57, 59] In the CNF spectrum, the antisymmetric (ν_{as, COO^-}) and symmetric carboxylate (ν_{s, COO^-}) stretch are observed at 1613 and 1419 cm^{-1}, respectively.[52] After the synthesis of AuNPs, a band at 1739 cm^{-1} emerges. This is associated with a carbonyl stretch ($\nu_{C=O}$) of carboxylic acid groups.[59] The emergence of this band is due to a decrease in pH with the addition of AA (from pH ~6-7 to ~5). The ν_{as, COO^-} and ν_{s, COO^-} shift to 1633 and 1424 cm^{-1}. These shifts can be attributed to the interaction and reduction of Au^{3+} at the COO^- groups on CNF. The interaction between AuNPs and the carboxylate group has been suggested to be through complexing or electrostatic interactions.[54] Zeta potential measurements of Au-CNF indicate an increase in

zeta potential from -51.3 mV (pH ~5-6) to -25 ± 2 mV (pH ~5). While the increase in zeta potential indicates a lower colloidal stability suggests that the AuNPs could be occupying negatively charged carboxylate sites.

Extinction spectroscopy is used to examine the formation of plasmonic gold nanoparticles. Figure 4-5 shows the extinction spectra for Au-CNF, AuNPs formed with AA and necessary controls. The band for Au-CNF (in green) observed at 533 nm is caused by the localized surface plasmon resonance (LSPR) of AuNPs. In the absence of CNF, AuNPs are formed when AA and $HAuCl_4$ are mixed together. The LSPR band for AuNPs without CNF (in blue) is observed at 529 nm. Through visual inspection, the inset image shows slightly different colours for AuNP and Au-CNF. AuNP solution is red in colour, while Au-CNF is a darker red solution. Through spectroscopic inspection, the Au-CNF LSPR is red-shifted by 4 nm and slightly broader. We attribute these extinction changes to the interaction between the AuNP and CNF. It has been shown that shifts in the LSPR λ_{max} is likely due to a change in the medium's refractive index around the nanoparticle.[60-61] AA is a well-known reducing agent in the reduction of gold salt and a weak stabilization agent.[62-65] The other controls produce solutions with negligible extinction at ~530 nm.

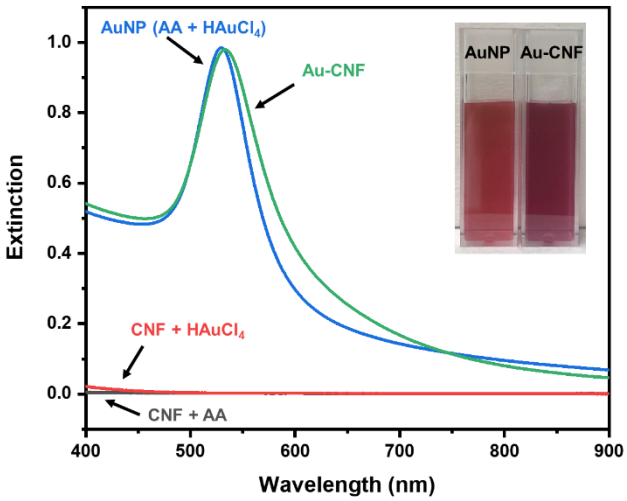

Figure 4-5. Extinction spectra of gold nanoparticle decorated on cellulose nanofibers, gold nanoparticles synthesized with ascorbic acid and controls.

Imaging techniques are used to confirm the interaction between AuNPs and CNF, and determine the shape and size of the AuNPs. Figure 4-6 shows images of Au-CNF and a size distribution ASH plot. The SEM (Figure 4-6A) and STEM (Figure 4-6B) images shows that the large majority of spherical nanoparticles are associated with CNF. This implies that the nanoparticles either nucleated on the fiber, or that nanoparticles that formed in solution attached to the CNF. The size and shape of the AuNPs on the CNF is determined using TEM imaging. Figure 4-6C is a TEM image showing the size and shape of AuNPs deposited onto CNF. In the image, the AuNPs are shown with a good clarity and the CNF is faintly visible in the background. The majority of the nanoparticles are spherical with the exception of a few triangular-shaped nanoparticles. The formation of AuNPs with different shapes is a reoccurring observation when AA is used as a reducing agent.[63, 65] The AuNP size distribution is determined by measuring the size of spherical nanoparticles from multiple TEM images. Figure 4-6D is an ASH plot demonstrating the size distribution of the AuNP on CNF. The distribution is unimodal and the rug plot underneath the distribution

shows the frequency throughout the distribution. The average size was measured as 27 ± 10 nm (N=620). Nanoparticles sizes between 10-100 nm are commonly used for SERS measurements.[66]

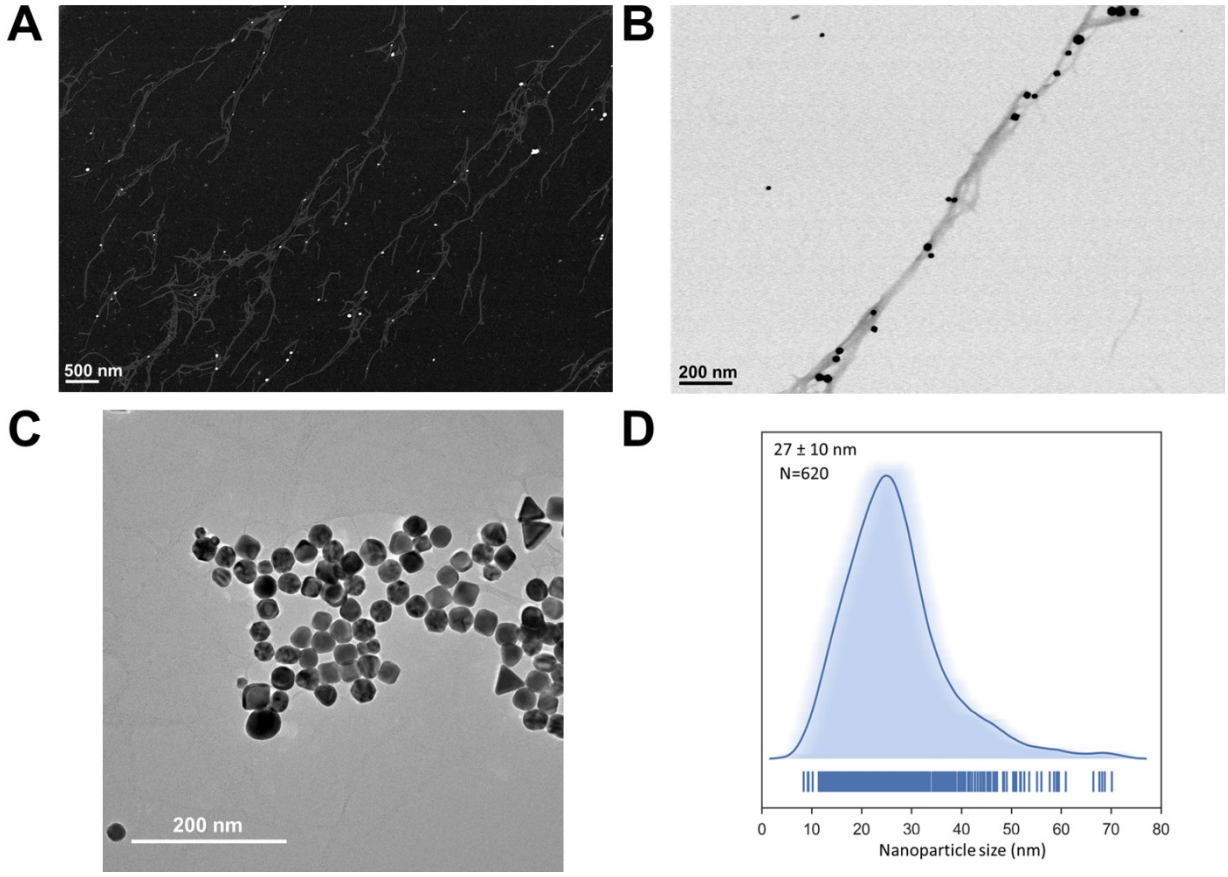

Figure 4-6. Electron microscopy characterization of colloidal Au-CNF. Images of Au-CNF using (A) SEM, (B) STEM and (C) TEM. (D) ASH plot demonstrating the average size and size distribution of Au-CNF. Multiple TEM images were used.

XPS analysis is used to examine the elemental composition of CNF and Au-CNF, and will confirm the reduction of Au^{3+}. Figure 4-7A is a survey scan of CNF and Au-CNF, and Table 4-2 is the corresponding data. The total amount of Au metal in Au-CNF is 0.3%.

Figure 4-7B is high resolution XPS spectra of Au 4f binding energy for CNF and Au-CNF. No Au is observed in the CNF, while Au-CNF shows a Au 4f doublet at 84.2 and 87.9 eV. Similar binding energy assignments for AuNPs have been reported in the literature.[67-68] These results confirm that CNF does not initially contain any Au and the reduction of Au^{3+} to Au^{0} after the synthesis of Au-CNF.

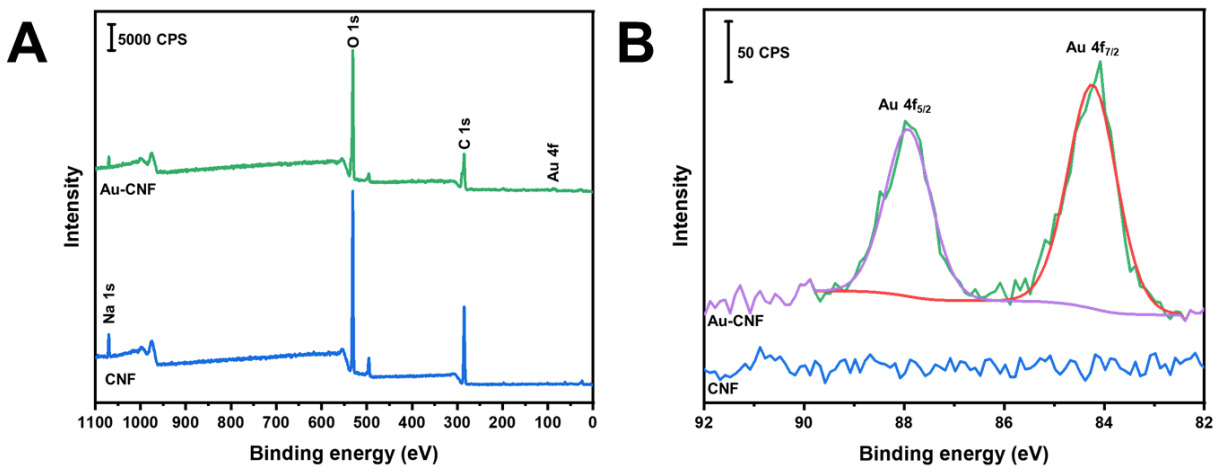

Figure 4-7. X-ray spectroscopy analysis of Au-CNF. (A) Stacked survey spectra of CNF and Au-CNF. (B) High resolution spectra of Au 4f for CNF and Au-CNF.

Table 4-2. X-Ray Photoelectron Spectroscopy Survey Scan Data of CNF and Au-CNF

Sample	Peak	Position	FWHM	Area	At%	R.S.F.
CNF	C 1s	285.0	2.53	28053	57.6	0.278
	O 1s	531.0	2.12	54407	39.8	0.780
	Na 1s	1070.0	2.10	7443	2.5	1.690
Au-CNF	C 1s	285.0	3.80	23275	56.9	0.278
	O 1s	531.0	2.32	47034	41.0	0.780
	Na 1s	1070.0	1.87	3439	1.4	1.690
	Au 4f	88.0	4.17	2341	0.3	6.25
	Cl 2p	198.5	2.10	745	0.6	0.891

XRD analysis is used to determine whether the AuNPs are polycrystalline. Figure 4-8 shows the diffraction spectrum of CNF and Au-CNF. The CNF spectrum contains two broad band peaks at 16.3 ° and 22.8 °. These peaks are attributed to the (110) and (200) crystallographic planes of CNF, respectively. The broad band peaks from CNF are observed in addition to Au metal lattice peaks for the Au-CNF diffraction spectrum. Au metal lattice peaks are observed at 38.3 °, 44.4 °, 64.6 ° and 77.6 ° , and have been attributed to (111), (200), (220) and (311) lattice facets. Chen et al. have reported similar lattice facet assignments in their work consisting of AuNPs on TEMPO-oxidized bacterial CNF.[59] Figure 4-8 demonstrates that the crystallinity of the CNF is unchanged with the deposition of AuNPs. The d-spacing and crystallite size of the AuNPs are shown in Table 4-3. These results confirm that the AuNPs associated with CNF are polycrystalline.

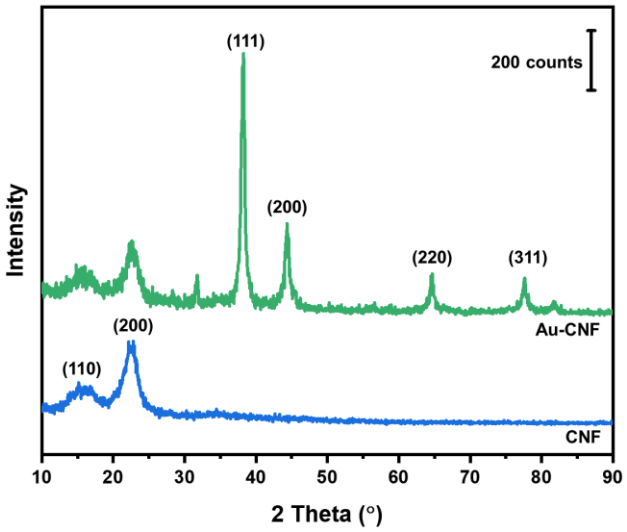

Figure 4-8. X-ray diffraction spectra of CNF and Au-CNF.

Table 4-3. Determination of d-Spacing and Crystallite Size of Gold Nanoparticles on Cellulose Nanofibers From XRD Data

Lattice Facet	2θ	d-spacing (Å)	Crystallite Size (nm)
111	38.2	2.35	16.2
200	44.4	2.04	13.7
220	64.6	1.44	18.4
311	77.6	1.23	22.5

This past section described the synthesis and characterization CNF decorated with AuNPs. This section confirms that: (1) AuNPs interact at the carboxylate group and maintain moderate stability; (2) the majority of the nanoparticles are spherical and have an average diameter of 27 nm; (3) produce a LSPR band characteristic to AuNPs at 533 nm; (4) the nanoparticle composition is confirmed as Au; and (5) the nanoparticles are polycrystalline. The upcoming section will investigate how colloidal Au-CNF can be used as a solution-based SERS substrate.

4.3.2. SERS Enhancement from Au-CNF

In-solution SERS measurements using colloidal Au-CNF were first investigated using 4-mercaptobenzonitrile (MBN). MBN is a thiol Raman probe that ensures high surface coverage and adsorption to Au surfaces due to thiol chemistry. The substrate undergoes a centrifugation step before any measurements as discussed in Chapter 3. Figure 4-9 highlights the effect of this centrifugation step on the dispersible substrate. Figure 4-9A shows the SERS spectra of MBN (5 μM) using centrifuged and non-centrifuged Au-CNF. The spectrum of MBN with non-centrifuged Au-CNF shows very low Raman peak intensities. Conversely, when a centrifuged Au-CNF is used, the Raman peak intensity is increased by ~20×. The band assignments for MBN are shown in Table 4-4.[69-71]

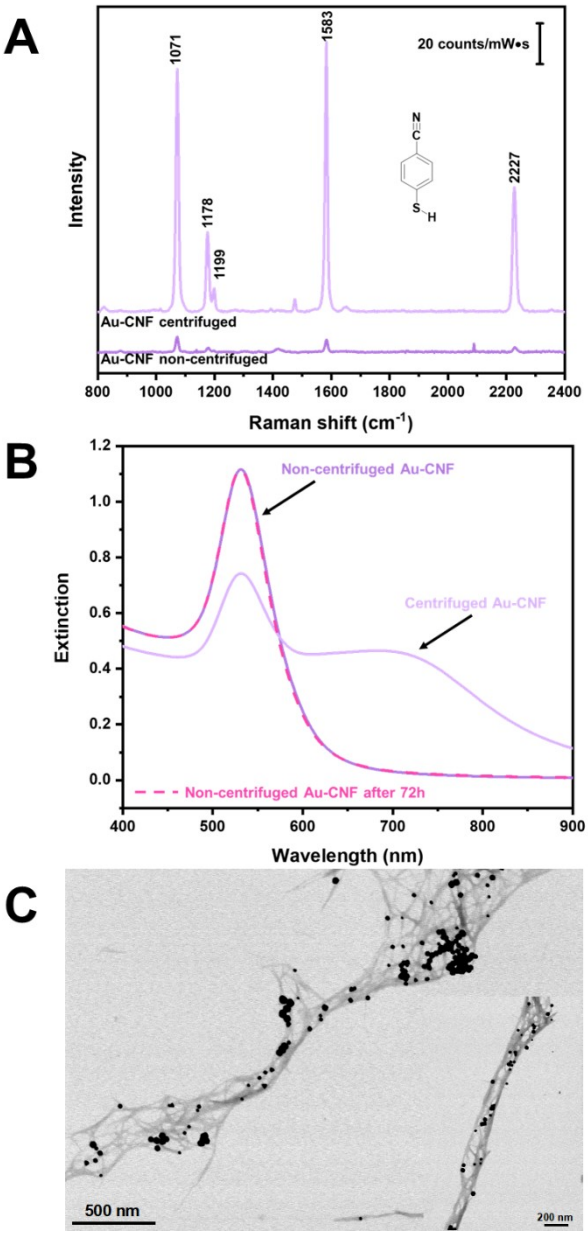

Figure 4-9. SERS capability of Au-CNF. (A) SERS spectra of MBN using centrifuged and non-centrifuged Au-CNF. (B) Comparison of extinction spectra of non-centrifuged and centrifuged Au-CNF, and the stability of non-centrifuged Au-CNF after 72 hours. (C) STEM image of centrifuged Au-CNF.

Table 4-4. Major Bands Assignments Listed for the SERS Spectrum of 4-Mercaptobenzonitrile on Au-CNF

Band position (cm^{-1})	Assignment[69-71]
1071	C–S and C–C stretch
1178	C–H bend and C–C stretch
1199	C–H bend and C–C≡N stretch
1583	C–C stretch
2227	C≡N stretch

Extinction spectroscopy and electron microscopy are used to further understand the enhancement associated with centrifugation. The extinction spectra in Figure 4-9B is of non-centrifuged (dark purple) and centrifuged Au-CNF (light purple). Non-centrifuged Au-CNF shows a single LSPR band at 533 nm, whereas the LSPR of centrifuged Au-CNF decreases in intensity and a second broad LSPR band increases in intensity from 600-800 nm. The Au-CNF solution colour changes from dark red to a purple/blue. STEM imaging is used to image centrifuged Au-CNF and is shown in Figure 4-9C. The images shows bundling of the nanofibers with many nanoparticles in close proximity to each other. These are potential hot spots for in-solution SERS measurements. This effect was first observed in our previous work using CNF decorated with silver nanoparticles (Chapter 3). The zeta potential measurements for non-centrifuged and centrifuged Au-CNF is -25 ± 2 mV (pH ~5) and -30 ± 2 mV (pH ~6-7), respectively. The more negative zeta potential is consistent with the centrifugal force dislodging nanoparticles from the surface carboxylate sites of the CNF.

The short term colloidal stability of an in-solution substrate is important for remote applications and commercialization efforts. The extinction spectra in Figure 4-9B is of non-centrifuged Au-CNF immediately after synthesis (dark purple) and after 72 hours (pink dotted line) at room temperature. The spectra overlap well and there is nearly no change in

extinction after 72 hours. This signifies that Au-CNF is colloidally stable for at least a short period of time.

In this section, the impact of centrifuging Au-CNF on the SERS enhancement is discussed using Raman spectroscopy, extinction spectroscopy and zeta potential measurements. The increase in Raman peak intensity is associated with the bundling of nanofibers and bringing nanoparticles in close proximity. Moreover, the extinction spectra of Au-CNF demonstrates moderate colloidal stability for at least 72 hours. The next section will investigate Au-CNF substrate reproducibility and SERS measurements using different types of analytes. The section will conclude with some proof-of-concept applications using Au-CNF and a handheld Raman spectrometer.

4.3.3. SERS Measurements and Reproducibility of Au-CNF

4.3.3.1. SERS Reproducibility of Au-CNF

Some of the desired features for SERS substrates include a large measurement area (mm^2), uniformity and reproducibility (<20%).[9, 14-15] A solution-based substrate has the potential to provide excellent reproducibility and uniformity due to solution homogeneity. Moreover, the ability to measure at any location on the vial provides a large measurement area. The reproducibility and uniformity of colloidal Au-CNF for in-solution measurements are investigated in Figure 4-10. As a side note, all measurements are taken using centrifuged Au-CNF. The batch-to-batch and sample-to-sample reproducibility are monitored spectrally using MBN adsorbed onto Au-CNF. Figure 4-10A is a 3D plot of MBN using 8 different batches of Au-CNF. We define a batch as Au-CNF synthesized in a different vessel. The MBN spectrum for each batch shown in Figure 4-10A is an average of 4 different samples from

within a batch. We define a sample as a measurement in a separate vial. Figure 4-10B is a column graph showing the peak intensity of the C≡N stretch at 2227 cm^{-1} as a function of Au-CNF batches. The batch-to-batch reproducibility of Au-CNF is determined using the percent relative standard deviation (%RSD) and is determined to be 10%. The sample reproducibility is the %RSD within a single batch. The %RSD for sample-to-sample ranged from 0.6 to 7% depending on the batch. This is comparable to the sample-to-sample reported for gold nanostars (AuNS) and CNF decorated with silver nanoparticles (Ag-CNF) in Chapters 2 and 3, respectively. The reproducibility of 20% or less for SERS measurements is generally considered acceptable.[72]

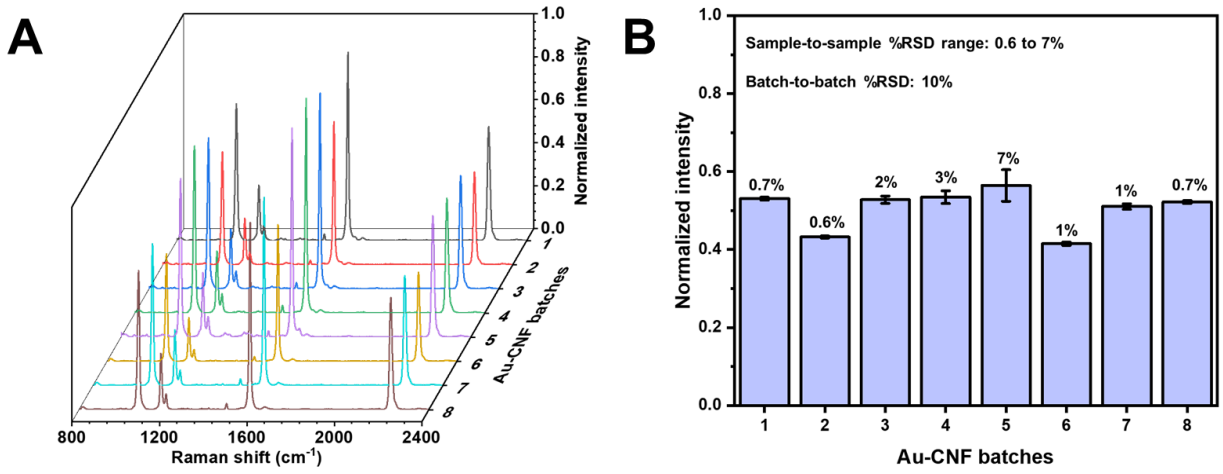

Figure 4-10. Reproducibility of colloidal Au-CNF substrates. (A) SERS spectra of MBN from different Au-CNF batches. (B) Column graph of the normalized peak intensity of the nitrile stretch (n=4 per batch). Normalized to the highest peak intensity (C–C stretch).

4.3.3.2. Applications of Au-CNF for In-Solution SERS Measurements

The applicability of Au-CNF for in-solution SERS is investigated using three different analytes. Figure 4-11 demonstrates the detection of analytes through different adsorption

mechanisms. The analyte SERS spectra are shown in green, while the analyte Raman spectra are shown in purple. The in-solution SERS detection of R6G (5 μM) using Au-CNF is shown in Figure 4-11A. This is a charged analyte that adsorbs to the AuNP surface through a physisorption mechanism, and is detectable within 2 minutes of addition to Au-CNF. Similar results are shown in our previous work using Ag-CNF in Chapter 3. Figure 4-11B and 11C show the SERS spectra of TBZ (1 μM) and MTZ (1 μM) within 2 minutes of mixing with Au-CNF. These analytes are chemisorbed via a metal-thiolate interaction. The SERS measurement of analytes through physisorption and chemisorption mechanisms within 2 minutes demonstrate the potential applications for detecting a wide range of analytes.

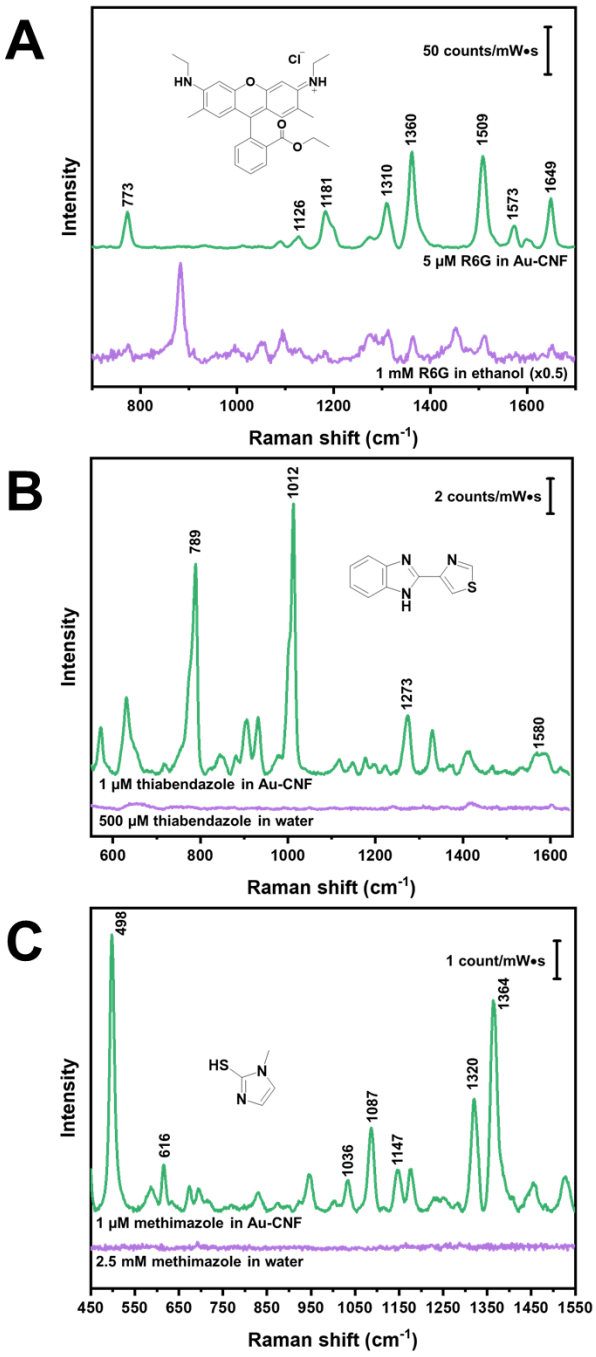

Figure 4-11. Applications of Au-CNF for SERS measurements. SERS spectra of (A) rhodamine 6G, (B) thiabendazole and (C) methimazole. Rhodamine 6G was measured using a 633 nm laser, and thiabendazole and methimazole were measured using a 785 nm laser.

R6G is a fluorescent and commonly used model dye for SERS applications.

Fluorescent molecules, such as R6G, have larger cross-sections (~10^{-16} cm^2) compared to

non-fluorescent molecules (~10^{-30} cm^2), and this facilitates Raman scattering and enables single molecule detection using SERS.[13] Other applications of R6G include being used as a water tracer, and colourant in textile and paper industries.[73] However, due to the toxicity and the carcinogenic effect of R6G, there is a need to monitor its usage and disposal (i.e. water runoff) within industries to avoid any unnecessary environmental contamination and exposures.[73] Figure 4-11A is the in-solution SERS spectrum of 5 μM R6G adsorbed on colloidal Au-CNF. The SERS bands are summarized in Table 4-5.[13, 23] R6G is used as an example to demonstrate the capability of detecting fluorescent dyes and as a potential substrate to monitor R6G in industry.

Table 4-5. Band Assignments for the SERS Spectrum of Rhodamine 6G using Au-CNF

Raman shift (cm^{-1})	Band assignment[13, 23]
773	Out-of-plane C–H bend
1126	In-plane C–H bend
1181	In-plane C–C stretch
1310	In-plane C–C stretch
1360	In-plane C–C stretch
1509	In-plane C–C stretch
1573	In-plane C–C stretch
1649	In-plane C–C stretch

TBZ is generally used for three main purposes: (1) an anthelmintic drug to treat humans and animals infected with parasites; (2) a medicinal chelating agent to prevent metal poisoning; and (3) a fungicide to prevent mould, rot and blight on fruits and

vegetables.[74-76] Whether TBZ is used for medicinal purposes or for its fungicidal properties, there is a need to monitor its usage due to toxicological effects.[77] TBZ adsorption to AuNPs is facilitated through the sulfur and nitrogen moieties. For this reason, a SERS platform for TBZ detection is ideal. Figure 4-11C shows the in-solution SERS spectrum of 1 μM TBZ adsorbed onto colloidal Au-CNF. The major bands for TBZ are assigned in Table 4-6.[75]

Table 4-6. Band Assignments for the SERS Spectrum of Thiabendazole Using Au-CNF

Raman shift (cm^{-1})	Band assignment[75]
789	C–H out-of-plane bend
1012	C–H out-of-plane bend
1273	Ring stretch
1580	Ring stretch and C=N stretch

MTZ is an anti-hormone pharmaceutical used to treat hyperthyroidism and as an illegal animal feed additive used to promote weight gain through increased tissue water retention.[78-80] Over exposure to MTZ can result in skin irritation, allergic reactions, impaired taste, pharyngitis, nephritis, liver cirrhosis and cytotoxic effects.[78, 80-81] MTZ is another analyte containing sulfur and nitrogen moieties, thus making SERS an ideal detection platform. Moreover, MTZ could serve as an unconventional probe for SERS substrate development and optimization. Common SERS probes are usually limited to dyes and thiol-based molecules. These molecules are effective in providing large signal intensities due to large Raman cross-sections, provide high surface coverage and have strong adsorption affinities to metallic nanoparticles. However, there are some limitations when using these probes. For example, dyes generally need to be used at low

concentrations to avoid interference from fluorescence, and their surface coverage on the nanoparticle is limited due steric effects. Moreover, dyes and thiols are generally not water soluble, and this could lead to interference from organic solvents. MTZ as a SERS probe is beneficial because it is a small water soluble thiol molecule. The strong S–Au affinity promotes high surface coverage without the interference from organic solvents. Figure 4-11C shows the in-solution SERS spectrum of 1 μM MTZ adsorbed onto colloidal Au-CNF. Table 4-7 shows the major band assignments for MTZ.[82-87]

Table 4-7. Band Assignments for the SERS Spectrum of Methimazole Using Au-CNF

Raman shift (cm^{-1})	Band assignment[82-87]
498	S–C–N in-plane bend
616	Ring out-of-plane bend, ring C–H and N–H out-of-plane bend
1036	Ring bend, ring C–H bend and C–S–H bend
1087	Ring C–N stretch and ring C–H bend
1147	C–S stretch, ring C–N stretch and C–H bend
1320	Ring C–N stretch, ring bend and ring C–H bend
1364	C–N stretch, ring bend and ring C–H bend

4.3.3.3. Detection and Quantitation of Methimazole in Synthetic Urine

A SERS assay is developed using Au-CNF for the in-solution measurement of MTZ in synthetic urine. Chromatography remains the gold standard technique for the detection and quantitation of MTZ in urine. However, these methods are often time consuming, require expensive equipment, extensive method development, sample pre-treatment and instrumental expertise.[78, 80] Using chromatographic methods, MTZ can be quantitated in

the nM to μM range.[78, 80, 88] The development of a SERS assay using colloidal Au-CNF provides a faster and less strenuous measurement platform. Figure 4-12A shows stacked SERS spectra of MTZ at concentration ranging from 0 to 1 μM. The in-plane S–C–N bending (δ_{S-C-N}) of methimazole at 498 cm^{-1} is the most intense band and is used to construct a calibration curve using Au-CNF as shown in Figure 4-12B. Each point is representative of three samples measured three times at different spots on the sample vial (n=9). The regression line from a linear least squares fit is used to determine the limit of detection and limit of quantitation. These were calculated as 0.09 μM and 0.3 μM, respectively. The linear range is determined to be between 0.3 and 1 μM. The analytical values determined using Au-CNF are competitive with our other work.[30] For example, a similar method was used to quantitate MTZ in-solution using colloidal gold nanostars using a handheld Raman spectrometer (see Chapter 2). While a limit of detection of 0.1 μM was obtained, the method was reliant on the use of NaCl as an aggregating agent. In this work, plasmonic cellulose nanofibers does not require the use of NaCl, conversely, centrifugation is used to generate hot spots in-solution.

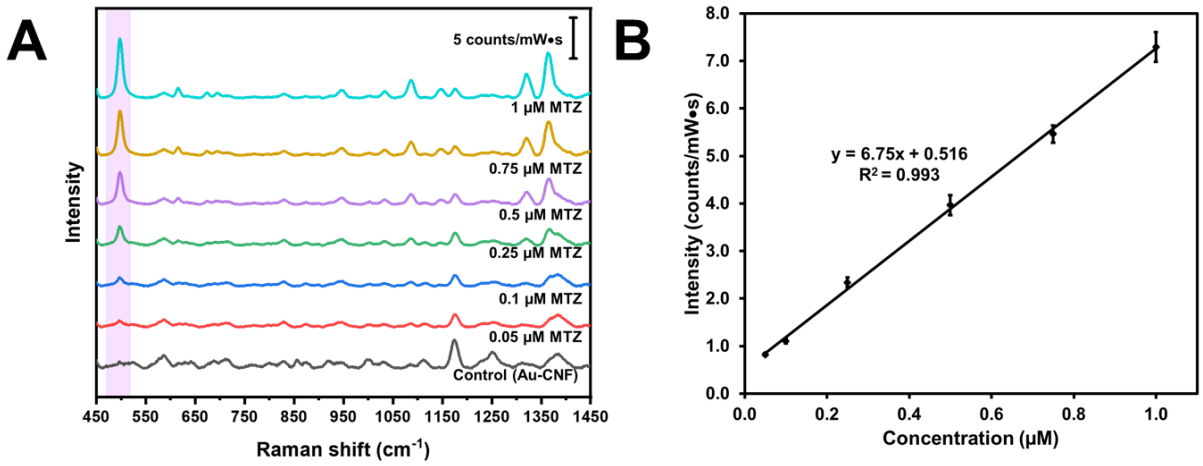

Figure 4-12. Quantitation of methimazole using colloidal Au-CNF. (A) Stacked SERS spectra of methimazole at different concentrations using Au-CNF. (B) Calibration curve of methimazole in solution. Spectra were obtained using a 785 nm laser.

The in-solution SERS enhancement factor of MTZ is determined using Au-CNF. Figure 4-13 shows a comparison the SERS spectra of MTZ at 1 μM in Au-CNF solution, the normal Raman spectrum of 42.4 mM MTZ in water and the normal Raman spectrum of powder MTZ. The δ_{S-C-N} peak intensity is used to determine the in-solution enhancement factor and is shown in Figure 4-13A. In the SERS spectrum, the δ_{S-C-N} vibration appears at 498 cm^{-1}. For the normal Raman spectrum, the δ_{S-C-N} vibration appears at 528 cm^{-1} when in aqueous solution. Figure 4-13B shows the MTZ powder Raman spectrum and the δ_{S-C-N} vibration appears at 530 cm^{-1}. Similar peak shifts for the δ_{S-C-N} vibration have been observed in the literature.[85-87] The enhancement factor of Au-CNF was evaluated using the analytical enhancement factor (A.E.F.) formula (Equation 4-1):[89]

$$A.E.F. = \frac{I_{SERS}/c_{SERS}}{I_{Raman}/c_{Raman}} \quad \textbf{Equation 4-1}$$

where I_{SERS} and I_{Raman} are the peak intensities at the δ_{S-C-N} vibration in Au-CNF and water. Additionally, c_{SERS} and c_{Raman} is the concentration in Au-CNF (1 μM) and water (42.4 mM), respectively. The AEF of Au-CNF was calculated to be ~7.1×10^5. This value is similar to that reported in the literature, and to what is observed for our gold nanostars in Chapter 2.[30, 85-87]

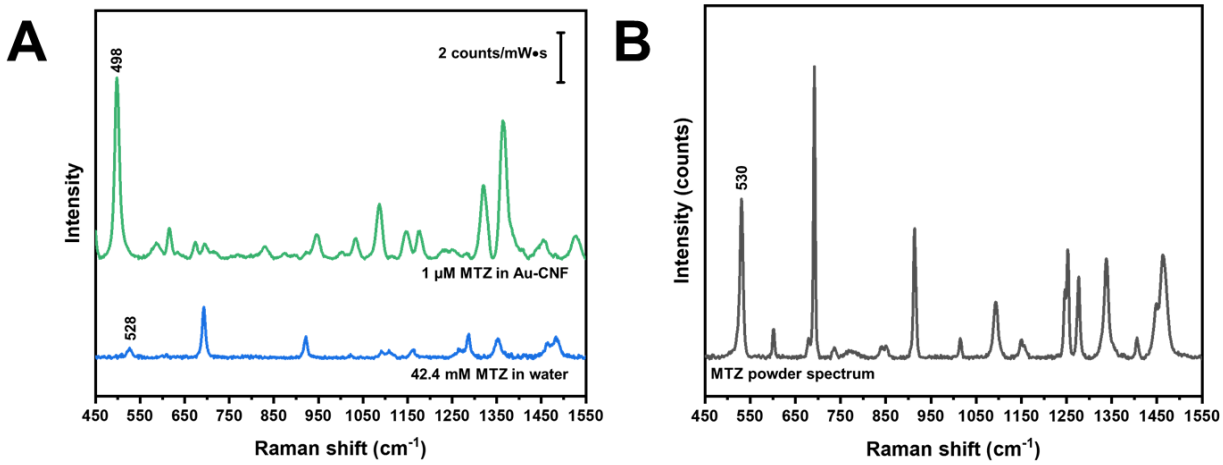

Figure 4-13. Enhancement factor from colloidal Au-CNF. (A) SERS spectra of methimazole in solution with and without Au-CNF to determine the enhancement factor. Spectra were obtained using a 785 nm laser. (B) Powder methimazole Raman spectrum (785 nm, 1% power, 10 s, 1 accumulation).

The retention of MTZ in an individual's body can be monitored through the excretion of excess MTZ in urine.[78, 80] Urine generally consists of non-protein nitrogenous compounds, inorganic salts and water-soluble toxins.[90] Pittman et al. reported that the MTZ excretion in urine after 24 hours is approximately 11-12% of an initial 60 mg dosage.[91] The dosage range of 10-60 mg MTZ has been investigated in previous works.[91-94] The average human being will excrete 2-3 L of urine per day.[95] Using these values, the concentration of MTZ excreted after a 24 hour period can be estimated in the low μM range. In this work,

MTZ is spiked into synthetic urine to investigate the ability of Au-CNF to detect MTZ in a complex matrix. Figure 4-14 shows the SERS spectrum of MTZ in urine using Au-CNF along with the corresponding control experiments. The Raman spectrum of urine shows a peak at 1008 cm^{-1} corresponds to a symmetrical C–N stretch from urea.[90] A spectrum of MTZ in urine specific to this scenario is not available. However, no SERS bands are observed for 2.5 mM MTZ in water, and Chapter 2 demonstrates that 0.2 mM MTZ in urine does not provide any SERS bands (Figure 2-12). The Au-CNF spectrum shows some weak intensity bands suggesting the AuNPs are at the surface of the CNF. When urine is deposited into Au-CNF, some weak bands emerge, however, these are not prominent in intensity and do not significantly overlap with those in MTZ. The disappearance of the C–N stretch from urea is due to the dilution of urine (50×) when mixed with Au-CNF. When MTZ in urine is dispersed into Au-CNF (final concentration of 1 μM), the MTZ band intensity are visible and intense. The percent recoveries of MTZ in urine are calculated using the calibration curve obtained in water. Table 4-8 shows the percent recoveries at 0.2, 0.6, 0.8 and 1 μM MTZ in urine. The recoveries ranged from 67-81%, and the %RSD increased at the lower concentrations. Since the surface of Au-CNF is relatively 'free' (no capping agent) for analyte adsorption, it is possible that the percent recoveries did not reach 100% due to matrix effects from the urine.

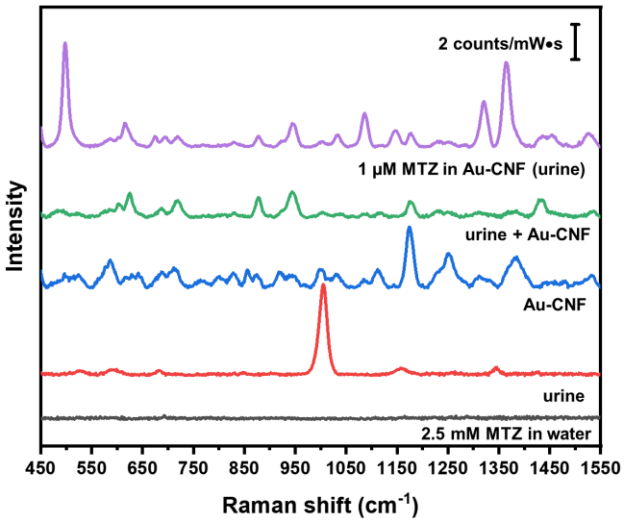

Figure 4-14. Quantitation of methimazole in urine. Detection of methimazole in urine using Au-CNF and the corresponding SERS spectra controls. Spectra was obtained using a 785 nm.

Table 4-8. Percent Recovery of Methimazole in Urine Using Au-CNF

Spiked amount of MTZ (μM)	Calc. amount of MTZ (μM)	%Recovery	%RSD
1	0.81 ± 0.03	81 ± 3	4
0.8	0.59 ± 0.08	74 ± 10	13
0.6	0.40 ± 0.06	67 ± 10	15
0.2	0.15 ± 0.03	74 ± 14	18

4.3.4. Measurements Using a Handheld Raman Spectrometer

The development of compact instrumentation, such as a handheld Raman spectrometer, has been driven by the technological advancement of lasers, wavelength selectors and detectors.[10] Handheld Raman spectrometers can be used for rapid and remote detection and measurement applications. In order to use a SERS measurement platform, substrates must be compatible with handheld Raman spectrometers. There are numerous substrates used for a wide range of applications, including narcotic identification, determination of

food contaminants, pharmaceutical quality control, and monitoring heavy metals and pesticides in the environment.[11, 30, 96-99]

As a proof-of concept, colloidal Au-CNF was tested using a handheld Raman spectrometer and a liquid cell adapter (Chapter 1-5). Figure 4-15 shows the SERS spectra of two different analytes using colloidal Au-CNF. The analytes were measured using the same procedure as for the Raman microscope. Figure 4-15A is the SERS spectrum of TBZ and has been discussed in Section 4.3.3.2. Briefly, TBZ is commonly applied to fruits and vegetables to prevent mould, rot and blight.[74] However, the use of pesticides and fungicides can lead to unintentional exposure, and there is a need to monitor its use. For example, grapes treated with TBZ and other pesticides could lead to contamination in wine and other goods down the processing line.[100] The TBZ SERS spectrum from Au-CNF and a handheld device demonstrates similar peaks to that observed in Figure 4-11B, and the band assignments are found in Table 4-6. With the development of an appropriate SERS detection method and a process to mitigate matrix effects, colloidal Au-CNF coupled with a handheld Raman device could be used as a quality control system to verify the absence of TBZ in wine.

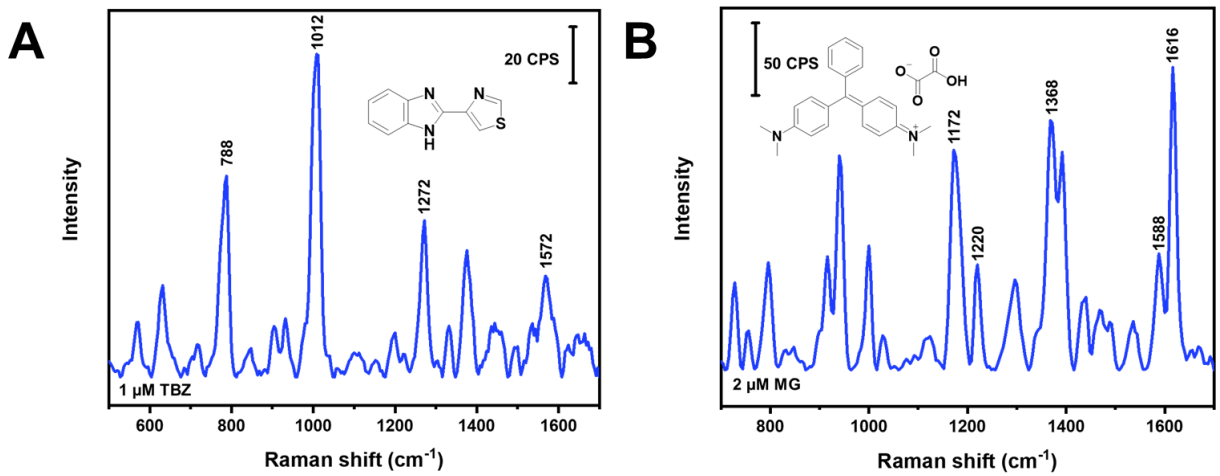

Figure 4-15. Potential applications for colloidal Au-CNF using a handheld Raman spectrometer. (A) 1 μM thiabendazole and (B) 2 μM malachite green. Spectra were obtained with a 785 nm laser (300 mW).

MG is another fluorescent dye with a variety of different applications such as a biological stain, a dye for textiles, and an additive for paper and ceramics.[101] MG is also known for its fungicidal properties relating in the aquaculture industry.[101-102] The use of MG in the aquaculture industry has been banned in numerous countries, including Canada, due to the toxicological effects of MG on humans.[103-104] However, in Canada while the use of MG on food-producing fish is prohibited, aquarium fish can be treated with MG.[103] The potential use of MG illegally in the aquaculture industry and improper disposal of treated aquarium fish and water can lead to human and environmental exposure. Figure 4-15B shows the in-solution SERS spectrum of 2 μM MG adsorbed onto colloidal Au-CNF, and Table 4-9 lists the MG band assignments.[105-108]

Table 4-9. Band Assignments for the SERS Spectrum of Malachite Green Using Au-CNF

Raman shift (cm^{-1})	Band assignment[105-108]
1171	In-plane C–H ring vibration
1219	C–H rock
1366	N–phenyl stretch
1591	C–C stretch
1615	C–C stretch

In this section, the reproducibility of Au-CNF and detection of analytes through physisorption and chemisorption mechanisms were investigated. The detection and quantification of MTZ in urine was examined using Au-CNF. Finally, a couple of proof-of-concept examples were discussed as potential applications for a dispersible substrate and a handheld Raman spectrometer.

4.4. Conclusions

A water dispersible SERS substrate consisting of CNF decorated with AuNPs was synthesized and characterized using electron microscopy, spectroscopic and elemental techniques. The AuNPs have an average size of 27 nm and interact with the nanofibers. CNF plays a vital role in the enhancement of the substrate. Centrifugation causes bundling of the nanofibers and produces dispersible bundles of CNF with AuNPs in close proximity to each other with an increase in intensity by ~20×. The Au-CNF demonstrated a sample-to-sample reproducibility ranging between 0.6 and 7 %, and the batch-to-batch reproducibility of 10%. Colloidal Au-CNF showed the ability to detect various analytes through chemisorption and physisorption mechanisms in 2 minutes. A SERS assay for the detection

and quantitation of MTZ in urine demonstrated a limit of detection of 0.09 μM and a recovery as high as 81% in urine. Measurements were taken with a handheld Raman spectrometer and colloidal Au-CNF as a proof-of-concept for rapid on-site SERS analysis.

4.5. References

1. Bell, S. E. J.; Sirimuthu, N. M. S., Quantitative surface-enhanced Raman spectroscopy. *Chem. Soc. Rev.* **2008,** *37* (5), 1012-1024.

2. Langer, J.; Jimenez de Aberasturi, D.; Aizpurua, J.; Alvarez-Puebla, R. A.; Auguié, B.; Baumberg, J. J.; Bazan, G. C.; Bell, S. E. J.; Boisen, A.; Brolo, A. G.; Choo, J.; Cialla-May, D.; Deckert, V.; Fabris, L.; Faulds, K.; García de Abajo, F. J.; Goodacre, R.; Graham, D.; Haes, A. J.; Haynes, C. L.; Huck, C.; Itoh, T.; Käll, M.; Kneipp, J.; Kotov, N. A.; Kuang, H.; Le Ru, E. C.; Lee, H. K.; Li, J.-F.; Ling, X. Y.; Maier, S. A.; Mayerhöfer, T.; Moskovits, M.; Murakoshi, K.; Nam, J.-M.; Nie, S.; Ozaki, Y.; Pastoriza-Santos, I.; Perez-Juste, J.; Popp, J.; Pucci, A.; Reich, S.; Ren, B.; Schatz, G. C.; Shegai, T.; Schlücker, S.; Tay, L.-L.; Thomas, K. G.; Tian, Z.-Q.; Van Duyne, R. P.; Vo-Dinh, T.; Wang, Y.; Willets, K. A.; Xu, C.; Xu, H.; Xu, Y.; Yamamoto, Y. S.; Zhao, B.; Liz-Marzán, L. M., Present and Future of Surface-Enhanced Raman Scattering. *ACS Nano* **2020,** *14* (1), 28-117.

3. Hakonen, A.; Andersson, P. O.; Stenbæk Schmidt, M.; Rindzevicius, T.; Käll, M., Explosive and chemical threat detection by surface-enhanced Raman scattering: A review. *Anal. Chim. Acta* **2015,** *893*, 1-13.

4. Hakonen, A.; Wu, K.; Stenbæk Schmidt, M.; Andersson, P. O.; Boisen, A.; Rindzevicius, T., Detecting forensic substances using commercially available SERS substrates and handheld Raman spectrometers. *Talanta* **2018,** *189*, 649-652.

5. Li, Y.-S.; Church, J. S., Raman spectroscopy in the analysis of food and pharmaceutical nanomaterials. *J. Food Drug Anal.* **2014,** *22* (1), 29-48.

6. Shi, R.; Liu, X.; Ying, Y., Facing Challenges in Real-Life Application of Surface-Enhanced Raman Scattering: Design and Nanofabrication of Surface-Enhanced Raman Scattering Substrates for Rapid Field Test of Food Contaminants. *J. Agric. Food. Chem.* **2018,** *66* (26), 6525-6543.

7. Wei, H.; Hossein Abtahi, S. M.; Vikesland, P. J., Plasmonic colorimetric and SERS sensors for environmental analysis. *Environ. Sci.: Nano* **2015,** *2* (2), 120-135.

8. Zong, C.; Xu, M.; Xu, L.-J.; Wei, T.; Ma, X.; Zheng, X.-S.; Hu, R.; Ren, B., Surface-Enhanced Raman Spectroscopy for Bioanalysis: Reliability and Challenges. *Chem. Rev.* **2018,** *118* (10), 4946-4980.

9. Pilot, R.; Signorini, R.; Durante, C.; Orian, L.; Bhamidipati, M.; Fabris, L., A Review on Surface-Enhanced Raman Scattering. *Biosensors* **2019,** *9* (2), 57.

10. Crocombe, R. A., Portable Spectroscopy. *Appl. Spectrosc.* **2018,** *72* (12), 1701-1751.

11. Pilot, R., SERS detection of food contaminants by means of portable Raman instruments. *J. Raman Spectrosc.* **2018,** *49* (6), 954-981.

12. Kneipp, K.; Wang, Y.; Kneipp, H.; Perelman, L. T.; Itzkan, I.; Dasari, R. R.; Feld, M. S., Single Molecule Detection Using Surface-Enhanced Raman Scattering (SERS). *Phys. Rev. Lett.* **1997,** *78* (9), 1667-1670.

13. Nie, S.; Emory, S. R., Probing Single Molecules and Single Nanoparticles by Surface-Enhanced Raman Scattering. *Science* **1997,** *275* (5303), 1102-1106.

14. Lin, X.-M.; Cui, Y.; Xu, Y.-H.; Ren, B.; Tian, Z.-Q., Surface-enhanced Raman spectroscopy: substrate-related issues. *Anal. Bioanal. Chem.* **2009,** *394* (7), 1729-1745.

15. Natan, M. J., Concluding Remarks Surface enhanced Raman scattering. *Faraday Discuss.* **2006,** *132* (0), 321-328.

16. Mosier-Boss, P. A., Review of SERS Substrates for Chemical Sensing. *Nanomaterials* **2017,** *7* (6), 142.

17. Yu, W. W.; White, I. M., Inkjet Printed Surface Enhanced Raman Spectroscopy Array on Cellulose Paper. *Anal. Chem.* **2010,** *82* (23), 9626-9630.

18. Yu, W. W.; White, I. M., Inkjet-printed paper-based SERS dipsticks and swabs for trace chemical detection. *Analyst* **2013,** *138* (4), 1020-1025.

19. Ogundare, S. A.; van Zyl, W. E., A review of cellulose-based substrates for SERS: fundamentals, design principles, applications. *Cellulose* **2019,** *26* (11), 6489-6528.

20. Liou, P.; Nayigiziki, F. X.; Kong, F.; Mustapha, A.; Lin, M., Cellulose nanofibers coated with silver nanoparticles as a SERS platform for detection of pesticides in apples. *Carbohydr. Polym.* **2017,** *157*, 643-650.

21. Chen, J.; Huang, M.; Kong, L.; Lin, M., Jellylike flexible nanocellulose SERS substrate for rapid in-situ non-invasive pesticide detection in fruits/vegetables. *Carbohydr. Polym.* **2019,** *205*, 596-600.

22. Chen, R.; Zhang, L.; Li, X.; Ong, L.; Soe, Y. G.; Sinsua, N.; Gras, S. L.; Tabor, R. F.; Wang, X.; Shen, W., Trace Analysis and Chemical Identification on Cellulose Nanofibers-Textured SERS Substrates Using the "Coffee Ring" Effect. *ACS Sens.* **2017,** *2* (7), 1060-1067.

23. Jiang, F.; Hsieh, Y.-L., Synthesis of Cellulose Nanofibril Bound Silver Nanoprism for Surface Enhanced Raman Scattering. *Biomacromolecules* **2014,** *15* (10), 3608-3616.

24. Zhang, L.; Li, X.; Ong, L.; Tabor, R. F.; Bowen, B. A.; Fernando, A. I.; Nilghaz, A.; Garnier, G.; Gras, S. L.; Wang, X.; Shen, W., Cellulose nanofibre textured SERS substrate. *Colloids Surf., A* **2015,** *468*, 309-314.

25. Zhang, S.; Xiong, R.; Mahmoud, M. A.; Quigley, E. N.; Chang, H.; El-Sayed, M.; Tsukruk, V. V., Dual-Excitation Nanocellulose Plasmonic Membranes for Molecular and Cellular SERS Detection. *ACS Appl. Mater. Interfaces* **2018,** *10* (21), 18380-18389.

26. Cunningham, D.; Littleford, R. E.; Smith, W. E.; Lundahl, P. J.; Khan, I.; McComb, D. W.; Graham, D.; Laforest, N., Practical control of SERRS enhancement. *Faraday Discuss.* **2006,** *132* (0), 135-145.

27. Faulds, K.; Smith, W. E.; Graham, D.; Lacey, R. J., Assessment of silver and gold substrates for the detection of amphetamine sulfate by surface enhanced Raman scattering (SERS). *Analyst* **2002,** *127* (2), 282-286.

28. Graham, D.; Thompson, D. G.; Smith, W. E.; Faulds, K., Control of enhanced Raman scattering using a DNA-based assembly process of dye-coded nanoparticles. *Nat. Nanotechnol.* **2008,** *3* (9), 548-551.

29. Lu, G.; Forbes, T. Z.; Haes, A. J., SERS detection of uranyl using functionalized gold nanostars promoted by nanoparticle shape and size. *Analyst* **2016,** *141* (17), 5137-5143.

30. Mahmoud, A. Y. F.; Rusin, C. J.; McDermott, M. T., Gold nanostars as a colloidal substrate for in-solution SERS measurements using a handheld Raman spectrometer. *Analyst* **2020,** *145* (4), 1396-1407.

31. Vander Ende, E.; Bourgeois, M. R.; Henry, A.-I.; Chávez, J. L.; Krabacher, R.; Schatz, G. C.; Van Duyne, R. P., Physicochemical Trapping of Neurotransmitters in Polymer-Mediated Gold Nanoparticle Aggregates for Surface-Enhanced Raman Spectroscopy. *Anal. Chem.* **2019,** *91* (15), 9554-9562.

32. Li, J.-M.; Ma, W.-F.; Wei, C.; You, L.-J.; Guo, J.; Hu, J.; Wang, C.-C., Detecting Trace Melamine in Solution by SERS Using Ag Nanoparticle Coated Poly(styrene-co-acrylic acid) Nanospheres as Novel Active Substrates. *Langmuir* **2011,** *27* (23), 14539-14544.

33. Nabeela, K.; Thomas, R. T.; Nair, J. B.; Maiti, K. K.; Warrier, K. G. K.; Pillai, S., TEMPO-Oxidized Nanocellulose Fiber-Directed Stable Aqueous Suspension of Plasmonic Flower-like Silver Nanoconstructs for Ultra-Trace Detection of Analytes. *ACS Appl. Mater. Interfaces* **2016,** *8* (43), 29242-29251.

34. Ogundare, S. A.; van Zyl, W. E., Nanocrystalline cellulose as reducing- and stabilizing agent in the synthesis of silver nanoparticles: Application as a surface-enhanced Raman scattering (SERS) substrate. *Surf. Interfaces* **2018,** *13*, 1-10.

35. Ogundare, S. A.; van Zyl, W. E., Amplification of SERS "hot spots" by silica clustering in a silver-nanoparticle/nanocrystalline-cellulose sensor applied in malachite green detection. *Colloids Surf., A* **2019,** *570*, 156-164.

36. Mayer, K. M.; Hafner, J. H., Localized Surface Plasmon Resonance Sensors. *Chem. Rev.* **2011,** *111* (6), 3828-3857.

37. Abalde-Cela, S.; Aldeanueva-Potel, P.; Mateo-Mateo, C.; Rodríguez-Lorenzo, L.; Alvarez-Puebla, R. A.; Liz-Marzán, L. M., Surface-enhanced Raman scattering biomedical applications of plasmonic colloidal particles. *J. R. Soc. Interface* **2010,** *7* (suppl_4), S435-S450.

38. Murphy, C. J.; Gole, A. M.; Stone, J. W.; Sisco, P. N.; Alkilany, A. M.; Goldsmith, E. C.; Baxter, S. C., Gold Nanoparticles in Biology: Beyond Toxicity to Cellular Imaging. *Acc. Chem. Res.* **2008,** *41* (12), 1721-1730.

39. Saito, T.; Isogai, A., TEMPO-Mediated Oxidation of Native Cellulose. The Effect of Oxidation Conditions on Chemical and Crystal Structures of the Water-Insoluble Fractions. *Biomacromolecules* **2004,** *5* (5), 1983-1989.

40. Saito, T.; Kimura, S.; Nishiyama, Y.; Isogai, A., Cellulose Nanofibers Prepared by TEMPO-Mediated Oxidation of Native Cellulose. *Biomacromolecules* **2007,** *8* (8), 2485-2491.

41. Anderson, S. L.; Luber, E. J.; Olsen, B. C.; Buriak, J. M., Substance over Subjectivity: Moving beyond the Histogram. *Chem. Mater.* **2016,** *28* (17), 5973-5975.

42. Menges, F. Spectragryph - optical spectroscopy software. http://www.effemm2.de/spectragryph/ (accessed April 23, 2020).

43. Islam, M. S.; Chen, L.; Sisler, J.; Tam, K. C., Cellulose nanocrystal (CNC)-inorganic hybrid systems: synthesis, properties and applications. *J. Mater. Chem. B* **2018,** *6* (6), 864-883.

44. Foster, E. J.; Moon, R. J.; Agarwal, U. P.; Bortner, M. J.; Bras, J.; Camarero-Espinosa, S.; Chan, K. J.; Clift, M. J. D.; Cranston, E. D.; Eichhorn, S. J.; Fox, D. M.; Hamad, W. Y.; Heux, L.; Jean, B.; Korey, M.; Nieh, W.; Ong, K. J.; Reid, M. S.; Renneckar, S.; Roberts, R.; Shatkin, J. A.; Simonsen, J.; Stinson-Bagby, K.; Wanasekara, N.; Youngblood, J., Current characterization methods for cellulose nanomaterials. *Chem. Soc. Rev.* **2018,** *47* (8), 2609-2679.

45. Siró, I.; Plackett, D., Microfibrillated cellulose and new nanocomposite materials: a review. *Cellulose* **2010,** *17* (3), 459-494.

46. Miao, X.; Lin, J.; Tian, F.; Li, X.; Bian, F.; Wang, J., Cellulose nanofibrils extracted from the byproduct of cotton plant. *Carbohydr. Polym.* **2016,** *136*, 841-850.

47. Soni, B.; Hassan, E. B.; Mahmoud, B., Chemical isolation and characterization of different cellulose nanofibers from cotton stalks. *Carbohydr. Polym.* **2015,** *134*, 581-589.

48. Moon, R. J.; Martini, A.; Nairn, J.; Simonsen, J.; Youngblood, J., Cellulose nanomaterials review: structure, properties and nanocomposites. *Chem. Soc. Rev.* **2011,** *40* (7), 3941-3994.

49. Isogai, A.; Saito, T.; Fukuzumi, H., TEMPO-oxidized cellulose nanofibers. *Nanoscale* **2011,** *3* (1), 71-85.

50. Kafy, A.; Kim, H. C.; Zhai, L.; Kim, J. W.; Hai, L. V.; Kang, T. J.; kim, J., Cellulose long fibers fabricated from cellulose nanofibers and its strong and tough characteristics. *Sci. Rep.* **2017,** *7* (1), 17683.

51. Yu, L.; Lin, J.; Tian, F.; Li, X.; Bian, F.; Wang, J., Cellulose nanofibrils generated from jute fibers with tunable polymorphs and crystallinity. *J. Mater. Chem. A* **2014,** *2* (18), 6402-6411.

52. Zhu, C.; Soldatov, A.; Mathew, A. P., Advanced microscopy and spectroscopy reveal the adsorption and clustering of Cu(ii) onto TEMPO-oxidized cellulose nanofibers. *Nanoscale* **2017,** *9* (22), 7419-7428.

53. Liu, P.; Oksman, K.; Mathew, A. P., Surface adsorption and self-assembly of Cu(II) ions on TEMPO-oxidized cellulose nanofibers in aqueous media. *J. Colloid Interface Sci.* **2016,** *464*, 175-182.

54. Van Rie, J.; Thielemans, W., Cellulose–gold nanoparticle hybrid materials. *Nanoscale* **2017,** *9* (25), 8525-8554.

55. He, J.; Kunitake, T.; Nakao, A., Facile In Situ Synthesis of Noble Metal Nanoparticles in Porous Cellulose Fibers. *Chem. Mater.* **2003,** *15* (23), 4401-4406.

56. Johnston, J. H.; Nilsson, T., Nanogold and nanosilver composites with lignin-containing cellulose fibres. *J. Mater. Sci.* **2012,** *47* (3), 1103-1112.

57. Koga, H.; Tokunaga, E.; Hidaka, M.; Umemura, Y.; Saito, T.; Isogai, A.; Kitaoka, T., Topochemical synthesis and catalysis of metal nanoparticles exposed on crystalline cellulose nanofibers. *Chem. Commun.* **2010,** *46* (45), 8567-8569.

58. Wu, X.; Lu, C.; Zhou, Z.; Yuan, G.; Xiong, R.; Zhang, X., Green synthesis and formation mechanism of cellulose nanocrystal-supported gold nanoparticles with enhanced catalytic performance. *Environ. Sci.: Nano* **2014,** *1* (1), 71-79.

59. Chen, Y.; Chen, S.; Wang, B.; Yao, J.; Wang, H., TEMPO-oxidized bacterial cellulose nanofibers-supported gold nanoparticles with superior catalytic properties. *Carbohydr. Polym.* **2017,** *160*, 34-42.

60. Englebienne, P., Use of colloidal gold surface plasmon resonance peak shift to infer affinity constants from the interactions between protein antigens and antibodies specific for single or multiple epitopes. *Analyst* **1998,** *123* (7), 1599-1603.

61. Willets, K. A.; Van Duyne, R. P., Localized surface plasmon resonance spectroscopy and sensing. *Annu. Rev. Phys. Chem.* **2007,** *58*, 267-97.

62. Malassis, L.; Dreyfus, R.; Murphy, R. J.; Hough, L. A.; Donnio, B.; Murray, C. B., One-step green synthesis of gold and silver nanoparticles with ascorbic acid and their versatile surface post-functionalization. *RSC Adv.* **2016,** *6* (39), 33092-33100.

63. Jana, N. R.; Gearheart, L.; Murphy, C. J., Evidence for Seed-Mediated Nucleation in the Chemical Reduction of Gold Salts to Gold Nanoparticles. *Chem. Mater.* **2001,** *13* (7), 2313-2322.

64. Kimling, J.; Maier, M.; Okenve, B.; Kotaidis, V.; Ballot, H.; Plech, A., Turkevich Method for Gold Nanoparticle Synthesis Revisited. *J. Phys. Chem. B* **2006,** *110* (32), 15700-15707.

65. Ziegler, C.; Eychmüller, A., Seeded Growth Synthesis of Uniform Gold Nanoparticles with Diameters of 15−300 nm. *J. Phys. Chem. C* **2011,** *115* (11), 4502-4506.

66. Moskovits, M., Surface-enhanced Raman spectroscopy: a brief retrospective. *J. Raman Spectrosc.* **2005,** *36* (6-7), 485-496.

67. Gopiraman, M.; Deng, D.; Saravanamoorthy, S.; Chung, I.-M.; Kim, I. S., Gold, silver and nickel nanoparticle anchored cellulose nanofiber composites as highly active catalysts for the rapid and selective reduction of nitrophenols in water. *RSC Adv.* **2018,** *8* (6), 3014-3023.

68. Sahoo, G. P.; Bhui, D. K.; Bar, H.; Sarkar, P.; Samanta, S.; Pyne, S.; Misra, A., Synthesis and characterization of gold nanoparticles adsorbed in methyl cellulose micro fibrils. *J. Mol. Liq.* **2010,** *155* (2), 91-95.

69. Gkogkou, D.; Schreiber, B.; Shaykhutdinov, T.; Ly, H. K.; Kuhlmann, U.; Gernert, U.; Facsko, S.; Hildebrandt, P.; Esser, N.; Hinrichs, K.; Weidinger, I. M.; Oates, T. W. H., Polarization- and Wavelength-Dependent Surface-Enhanced Raman Spectroscopy Using Optically Anisotropic Rippled Substrates for Sensing. *ACS Sens.* **2016,** *1* (3), 318-323.

70. Holze, R., Competition of anchoring groups in adsorption on gold electrodes—a comparative spectroelectrochemical study of 4-mercaptobenzonitrile and aromatic nitriles. *J. Solid State Electrochem.* **2013,** *17* (7), 1869-1879.

71. Villarreal, E.; Li, G. G.; Zhang, Q.; Fu, X.; Wang, H., Nanoscale Surface Curvature Effects on Ligand–Nanoparticle Interactions: A Plasmon-Enhanced Spectroscopic Study of

Thiolated Ligand Adsorption, Desorption, and Exchange on Gold Nanoparticles. *Nano Lett.* **2017,** *17* (7), 4443-4452.

72. Panneerselvam, R.; Liu, G.-K.; Wang, Y.-H.; Liu, J.-Y.; Ding, S.-Y.; Li, J.-F.; Wu, D.-Y.; Tian, Z.-Q., Surface-enhanced Raman spectroscopy: bottlenecks and future directions. *Chem. Commun.* **2018,** *54* (1), 10-25.

73. Ranjbari, E.; Hadjmohammadi, M. R., Optimization of magnetic stirring assisted dispersive liquid–liquid microextraction of rhodamine B and rhodamine 6G by response surface methodology: Application in water samples, soft drink, and cosmetic products. *Talanta* **2015,** *139*, 216-225.

74. Alsammarraie, F. K.; Lin, M.; Mustapha, A.; Lin, H.; Chen, X.; Chen, Y.; Wang, H.; Huang, M., Rapid determination of thiabendazole in juice by SERS coupled with novel gold nanosubstrates. *Food Chem.* **2018,** *259*, 219-225.

75. Kim, M. S.; Kim, M. K.; Lee, C. J.; Jung, Y. M.; Lee, M.-S., Surface-enhanced Raman Spectroscopy of Benzimidazolic Fungicides: Benzimidazole and Thiabendazole. *Bull. Korean Chem. Soc.* **2009,** *30* (12), 2930-2934.

76. Satou, T.; Koga, M.; Koike, K.; Tada, I.; Nikaido, T., Nematocidal activities of thiabendazole and ivermectin against the larvae of Strongyloides ratti and S. venezuelensis. *Vet. Parasitol.* **2001,** *99* (4), 311-322.

77. Jamieson, J. D.; Smith, E. B.; Dalvie, D. K.; Stevens, G. J.; Yanochko, G. M., Myeloperoxidase-mediated bioactivation of 5-hydroxythiabendazole: A possible mechanism of thiabendazole toxicity. *Toxicol. In Vitro* **2011,** *25* (5), 1061-1066.

78. Ebrahimzadeh, H.; Asgharinezhad, A. A.; Adlnasab, L.; Shekari, N., Optimization of ion-pair based hollow fiber liquid phase microextraction combined with HPLC–UV for the

determination of methimazole in biological samples and animal feed. *J. Sep. Sci.* **2012,** *35* (16), 2040-2047.

79. Kong, D.; Chi, Y.; Chen, L.; Dong, Y.; Zhang, L.; Chen, G., Determination of thyreostatics in animal feeds by CE with electrochemical detector. *Electrophoresis* **2009,** *30* (19), 3489-3495.

80. Kuśmierek, K.; Bald, E., Determination of methimazole in urine by liquid chromatography. *Talanta* **2007,** *71* (5), 2121-2125.

81. Genter, M. B., Evaluation of olfactory and auditory system effects of the antihyperthyroid drug carbimazole in the Long-Evans rat. *J. Biochem. Mol. Toxicol.* **1998,** *12* (5), 305-314.

82. Fei, J.; Wu, L.; Zhang, Y.; Zong, S.; Wang, Z.; Cui, Y., Pharmacokinetics-on-a-Chip Using Label-Free SERS Technique for Programmable Dual-Drug Analysis. *ACS Sens.* **2017,** *2* (6), 773-780.

83. Ma, P.; Liang, F.; Yang, Q.; Wang, D.; Sun, Y.; Wang, X.; Gao, D.; Song, D., Highly sensitive SERS probe for mercury(II) using cyclodextrin-protected silver nanoparticles functionalized with methimazole. *Microchim. Acta* **2014,** *181* (9), 975-981.

84. Muniz-Miranda, M.; Muniz-Miranda, F.; Pedone, A., Raman and DFT study of methimazole chemisorbed on gold colloidal nanoparticles. *PCCP* **2016,** *18* (8), 5974-5980.

85. Saleh, T. A.; Al-Shalalfeh, M. M.; Al-Saadi, A. A., Graphene Dendrimer-stabilized silver nanoparticles for detection of methimazole using Surface-enhanced Raman scattering with computational assignment. *Sci. Rep.* **2016,** *6*, 32185.

86. Saleh, T. A.; Al-Shalalfeh, M. M.; Al-Saadi, A. A., Silver nanoparticles for detection of methimazole by surface-enhanced Raman spectroscopy. *Mater. Res. Bull.* **2017,** *91*, 173-178.

87. Saleh, T. A.; Al-Shalalfeh, M. M.; Onawole, A. T.; Al-Saadi, A. A., Ultra-trace detection of methimazole by surface-enhanced Raman spectroscopy using gold substrate. *Vib. Spectrosc* **2017,** *90*, 96-103.

88. Zakrzewski, R., Determination of methimazole in urine with the iodine-azide detection system following its separation by reversed-phase high-performance liquid chromatography. *J. Chromatogr. B: Anal. Technol. Biomed. Life Sci.* **2008,** *869* (1-2), 67-74.

89. Le Ru, E. C.; Blackie, E.; Meyer, M.; Etchegoin, P. G., Surface Enhanced Raman Scattering Enhancement Factors: A Comprehensive Study. *J. Phys. Chem. C* **2007,** *111* (37), 13794-13803.

90. Moreira, L. P.; Silveira, L.; Pacheco, M. T. T.; da Silva, A. G.; Rocco, D. D. F. M., Detecting urine metabolites related to training performance in swimming athletes by means of Raman spectroscopy and principal component analysis. *J. Photochem. Photobiol., B* **2018,** *185*, 223-234.

91. Pittman, J. A.; Beschi, R. J.; Smitherman, T. C., Methimazole: Its Absorption and Excretion in Man and Tissue Distribution in Rats. *J. Clin. Endocrinol. Metab.* **1971,** *33* (2), 182-185.

92. Hengstmann, J. H.; Hohn, H., Pharmacokinetics of methimazole in humans. *Klin. Wochenschr.* **1985,** *63* (23), 1212-1217.

93. Jansson, R.; Lindström, B.; Dahlberg, P. A., Pharmacokinetic Properties and Bioavailability of Methimazole. *Clin. Pharmacokinet.* **1985,** *10* (5), 443-450.

94. Okamura, Y.; Shigemasa, C.; Tatsuhara, T., Pharmacokinetics of Methimazole in Normal Subjects and Hyperthyroid Patients. *Endocrinol. Jpn.* **1986,** *33* (5), 605-615.

95. Hebert, L. A.; Greene, T.; Levey, A.; Falkenhain, M. E.; Klahr, S., High urine volume and low urine osmolality are risk factors for faster progression of renal disease1 1No reprints are available. *Am. J. Kidney Dis.* **2003,** *41* (5), 962-971.

96. Bumbrah, G. S.; Sharma, R. M., Raman spectroscopy – Basic principle, instrumentation and selected applications for the characterization of drugs of abuse. *Egypt. J. Forensic Sci.* **2016,** *6* (3), 209-215.

97. Lanzarotta, A.; Lorenz, L.; Batson, J. S.; Flurer, C., Development and implementation of a pass/fail field-friendly method for detecting sildenafil in suspect pharmaceutical tablets using a handheld Raman spectrometer and silver colloids. *J. Pharm. Biomed. Anal.* **2017,** *146*, 420-425.

98. Sarfo, D. K.; Sivanesan, A.; Izake, Emad L.; Ayoko, G. A., Rapid detection of mercury contamination in water by surface enhanced Raman spectroscopy. *RSC Adv.* **2017,** *7* (35), 21567-21575.

99. Zheng, J.; Pang, S.; Labuza, T. P.; He, L., Semi-quantification of surface-enhanced Raman scattering using a handheld Raman spectrometer: a feasibility study. *Analyst* **2013,** *138* (23), 7075-7078.

100. Pazzirota, T.; Martin, L.; Mezcua, M.; Ferrer, C.; Fernandez-Alba, A. R., Processing factor for a selected group of pesticides in a wine-making process: distribution of pesticides during grape processing. *Food Addit. Contam. A* **2013,** *30* (10), 1752-1760.

101. Culp, S. J.; Beland, F. A., Malachite Green: A Toxicological Review. *J. Am. Coll. Toxicol.* **1996,** *15* (3), 219-238.

102. Sudova, E.; Machova, J.; Svobodova, Z.; Vesely, T., Negative effects of malachite green and possibilities of its replacement in the treatment of fish eggs and fish: a review. *Vet. Med.* **2007,** *52* (12), 527-539.

103. CFIA Malachite Green - Questions and Answers. Canadian Food Inspection Agency. http://www.inspection.gc.ca/food/information-for-consumers/fact-sheets-and-infographics/products-and-risks/chemical-hazards/malachite-green/eng/1332268890141/1332268947157 (accessed April 2, 2019).

104. Deng, D.; Lin, Q.; Li, H.; Huang, Z.; Kuang, Y.; Chen, H.; Kong, J., Rapid detection of malachite green residues in fish using a surface-enhanced Raman scattering-active glass fiber paper prepared by in situ reduction method. *Talanta* **2019,** *200*, 272-278.

105. Chamuah, N.; Bhuyan, N.; Das, P. P.; Ojah, N.; Choudhary, A. J.; Medhi, T.; Nath, P., Gold-coated electrospun PVA nanofibers as SERS substrate for detection of pesticides. *Sens. Actuators, B* **2018,** *273*, 710-717.

106. Jin, Y.; Ma, P.; Liang, F.; Gao, D.; Wang, X., Determination of malachite green in environmental water using cloud point extraction coupled with surface-enhanced Raman scattering. *Anal. Methods* **2013,** *5* (20), 5609-5614.

107. Xu, K.-X.; Guo, M.-H.; Huang, Y.-P.; Li, X.-D.; Sun, J.-J., Rapid and sensitive detection of malachite green in aquaculture water by electrochemical preconcentration and surface-enhanced Raman scattering. *Talanta* **2018,** *180*, 383-388.

108. Zhao, Y.; Tian, Y.; Ma, P.; Yu, A.; Zhang, H.; Chen, Y., Determination of melamine and malachite green by surface-enhanced Raman scattering spectroscopy using starch-coated silver nanoparticles as substrates. *Anal. Methods* **2015,** *7* (19), 8116-8122.

Chapter 5. Comparison of the SERS Performance of Plasmonic Cellulose Nanofibers in Solid and Solution Format

5.1. Introduction

Surface-enhancement Raman scattering (SERS) is a sensitive chemical sensing platform with the capability of single molecule detection.[1-3] The development of SERS substrates has led to its advancement as a powerful analytical technique. There are many of different types of substrates reported in the literature in both solid- and solution-based formats. Detailed information can be found in one of many available review articles.[3-7] This chapter will focus on producing solid-phase SERS substrates of metal decorated cellulose nanofibers in two different ways and comparing with solution phase measurements. Cellulose-based substrates are of interest because of their versatility to act as a solid- and solution-based SERS substrate. Ogundare and van Zyl have published a recent review on cellulose-based SERS substrates.[7] Developing cellulose-based SERS substrates is popular due to a range of benefits. These benefits of using cellulose include (1) good availability; (2) cellulose can act as a reducing and stabilizing agent for metal nanoparticles; (3) easy surface functionalization; (4) biocompatibility and biodegradability; (5) weak Raman scattering from cellulose.[7] The authors created a comprehensive table to highlight the different types of cellulose-based substrates, their preparation method and their performance.[7]

Many different approaches have been used in making cellulose-based SERS substrates. Some of these approaches include drop-casting, thermal evaporation, in-situ coating, immersion, inkjet printing and vacuum filtration.[7-13] For example, Chen et al. drop-casted CNF and AuNPs onto glass slides for trace analysis and chemical identification applications.[11] In another example, Yu and White developed an inexpensive paper-based SERS substrate using an inkjet printer.[12] In a third example, Kim et al. developed a SERS substrate for pesticide detection using a vacuum filtration method to deposit 2,2,6,6-tetramethylpiperidinyl-1-oxyl (TEMPO) oxidized CNF, AuNPs and gold nanorods onto cellulose ester filter membranes.[13] These are just a few examples of solid-based substrates out of the many substrates developed. Cellulose materials have also been used for in-solution measurements. Ogundare and van Zyl used cellulose nanocrystals as a reducing and stabilizing agent for AgNPs, and used their material as a solution-based SERS substrate.[14] Chapter 3 shows CNF decorated with AgNPs being used for in-solution measurements of malachite green. Moreover, Chapter 4 shows in-solution measurements of methimazole using CNF decorated with AuNPs. Cellulose-based substrates are versatile and create different opportunities for SERS measurements. It is obvious that there are differences between taking measurements on a surface versus in solution. For example, the focusing procedure for a surface measurement is different than that of a solution measurement. Hence, it is useful to understand the benefits and challenges of taking measurements using a solid- and solution-based substrate.

Herein, cellulose nanofibers decorated with gold nanoparticles (Au-CNF) is used as a solid- and solution-based SERS substrate. Colloidal Au-CNF synthesized in Chapter 4 is used to develop different solid-based substrates. A vacuum filtration and drop-casting

protocols are used to create these substrates. Four different Au-CNF filter membranes are developed using vacuum filtration, and Au-CNF/glass slide substrates are developed using a drop-casting method. This chapter discusses the different procedures for taking measurements on a surface versus in solution. Rhodamine 6G (R6G) is used as a Raman probe to assess the SERS performance of the substrates. Both solid- and solution-based substrates show excellent performance and SERS capability. Discussions around the advantages and disadvantages of each measurement platform highlight the potential for different applications.

5.2. Experimental

5.2.1. Chemicals

Commercial Bleached Chemi-Thermo Mechanical Pulp (BCTMP, 60% water content) was obtained from a local company and used to synthesize the CNF. Laboratory grade 2,2,6,6-tetramethylpiperidinyl-1-oxyl radical (TEMPO), sodium bromide (NaBr, 99%), sodium hypochlorite solution (NaOCl, 13%), hydrochloric acid (HCl, 37.5%), gold (III) chloride trihydrate (99.995%, $HAuCl_4$), rhodamine 6G (R6G, 95%) and hydrogen peroxide (30% w/w) were purchased from Sigma-Aldrich Canada (Oakville, Ontario). The sulfuric acid (95-98%) is purchased from Caledon. L-ascorbic acid (AA) was purchased from Anachemia. Sodium hydroxide (NaOH) was purchased from Fisher Scientific Canada. Absolute ethanol was purchased from Commercial Alcohols. Deionized (DI) water (18.2 MΩ·cm) was used for all syntheses and measurements.

5.2.2. Synthesis of Plasmonic Cellulose Nanofibers

The synthesis of CNF decorated with AuNPs was developed in a previous work (Chapter 4). TEMPO-oxidation of CNF can be found in Chapters 3 and 4. A solution of TEMPO-oxidized CNF (0.02 %) was heated and mixed to 70 °C and 400 rpm, respectively. An aliquot of $HAuCl_4$ (0.2 mM final concentration) was added to the CNF and mixed for 5 minutes. An aliquot of AA (0.3 mM final concentration) was then added to the solution and mixed for another 5 minutes.

5.2.3. Development of Au-CNF Planar SERS Substrates

A schematic for the development of Au-CNF planar SERS substrate is shown in Figure 5-1. Figure 5-1A demonstrates the synthesis of membrane-based Au-CNF substrates. Four types of membranes were investigated: (1) Whatman #1 (11 μm pore size); (2) polyvinylidene fluoride (PVDF) (0.45 μm pore size); (3) nitrocellulose (0.22μm pore size) and (4) nylon filter membranes (0.22 μm pore size). The membranes are cut into smaller circles using a hole puncher and placed on a vacuum filtration system as shown in Figure 5-1A. Aliquots (0.2 mL) of pre-synthesized Au-CNF are added to the membrane up to a total volume of 0.4 mL and 2 mL. The membranes are left on the vacuum apparatus until dry. The circle substrates are then cut into 4 individual substrates.

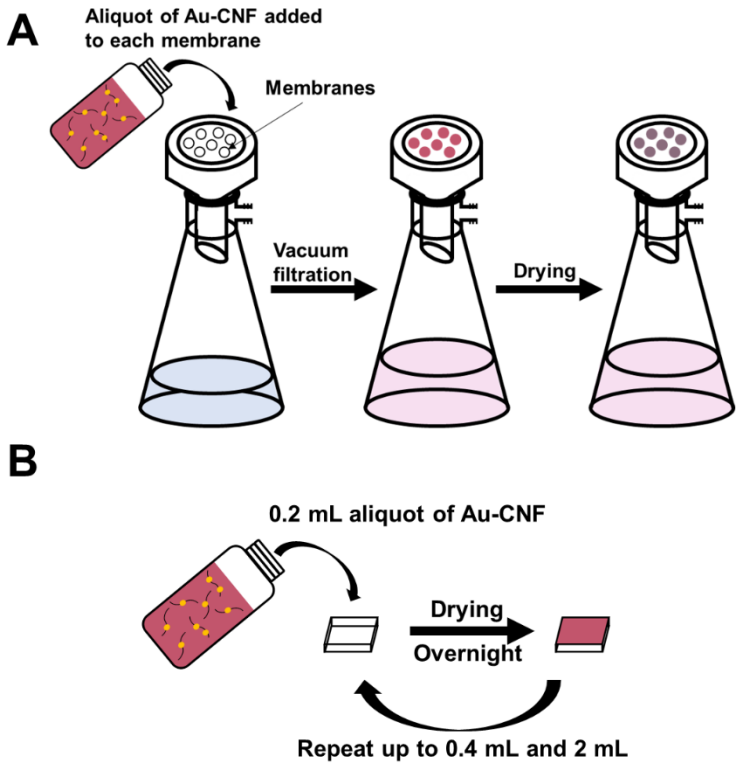

Figure 5-1. Schematic of the development of Au-CNF solid-based SERS substrates. (A) Au-CNF vacuum filtered onto membrane substrates and (B) Au-CNF drop-casted on glass slides.

Figure 5-1B demonstrates the synthesis of a glass slide based Au-CNF substrate. Glass slides (1 cm × 1 cm) were washed using piranha cleaning protocol. Similarly, an aliquot (0.2 mL) was added to the glass slides up to a total volume of 0.4 mL and 2 mL. An aliquot of 0.2 mL was left overnight to evaporate before another aliquot was added.

5.2.4. SERS Measurements Using Solid and Solution Substrates

SERS measurements were taken using a Renishaw inVia Raman microscope. The instrument is equipped with a RL633 50 mW HeNe laser and a 300 mW 785 nm diode laser. Measurements on a planar surface were taken using the 20× objective. The microscope was modified with a 90 ° liquid cell adapter (f=30 mm objective) for solution

measurements. Colloidal Au-CNF was centrifuged at 14000 rpm for 10 minutes (Eppendorf Centrifuge 5417 R) and re-dispersed. Solution measurements were taken in clear shell vials (1 mL). Nearly all data was acquired using the following conditions: 632.8 nm laser, 100% power (for solution), 10% power (for solid), 1 second and 5 accumulations. Data was collected using Wire 3.4 software and analyzed using Spectragryph open-source software.[15] The adsorption time for solution analysis was 2 minutes, while planar substrates were left for 10 minutes to allow for evaporation.

5.3. Results and Discussion

This section is divided into four sections: (1) Discussions on taking measurements on a surface; (2) discussions on taking measurements in solution; (3) the performance of solid- and solution-based substrates; and (4) a comparison between Au-CNF used for solid- and solution-based measurements. For sections 1 and 2, the discussion will focus on measurements with a Raman microscope. This is a common instrument platform in many labs. In-solution spectra are collected with a solution adapter, in this case the adapter is for a Renishaw InVia microscope. Other microscopes and instrument formats will require slightly varied procedures.

5.3.1. Taking Measurements on a Surface

The aim of this section is to describe the measurement process using a solid-based SERS substrate. Figure 5-2 illustrates a general procedure used for setting up the measurements. The substrates are placed onto a clean glass slide as shown in Figure 5-2A. R6G is used as a Raman probe, and a 5 μL ethanolic aliquot of 1.4 mM R6G (7 nmol) in ethanol is drop-

casted onto the substrate. The samples are left for 10 minutes to ensure complete evaporation of ethanol. After the deposition of R6G onto the solid-based substrates, the glass slide is placed onto the microscope stage as shown in Figure 5-2B. The objective (20×) is centred onto the substrate using the microscope light, and focused onto the substrate using the microscope's focusing knob (red box) and on-screen camera. It is important to note that determining whether the microscope is in focus can be challenging. The 3D nature of the planar substrates, such as filter paper membranes, does not allow the microscope to be in focus over the entire surface. This is an important consideration when using an instrument without an auto-focus function because it can negatively impact the spot-to-spot reproducibility.

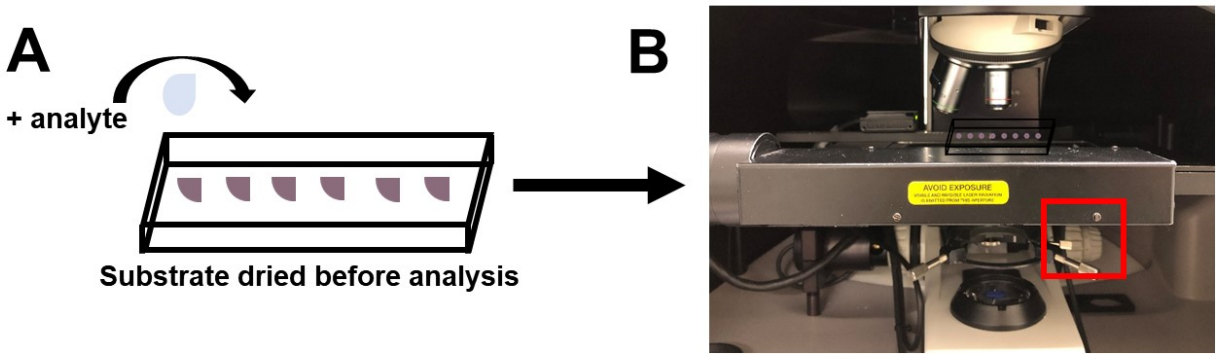

Figure 5-2. Schematic of the experimental procedure for solid-based substrates.

5.3.2. Taking In-Solution Measurements

This section describes the experimental set up and the measurement process for the solution-based substrates. Figure 5-3 illustrates the experimental procedure for taking measurements in solution. It is worth noting that there are significantly less substrate

preparation steps (i.e. filtration or drop-casting of Au-CNF). After the synthesis of Au-CNF, the substrate is centrifuged and re-dispersed. The substrate is then mixed with an aliquot of R6G (5 µM; 5 µL of 1 mM R6G) for 2 minutes. The sample is then placed into the Raman microscope equipped with a 90 ° liquid cell adapter for measurement.

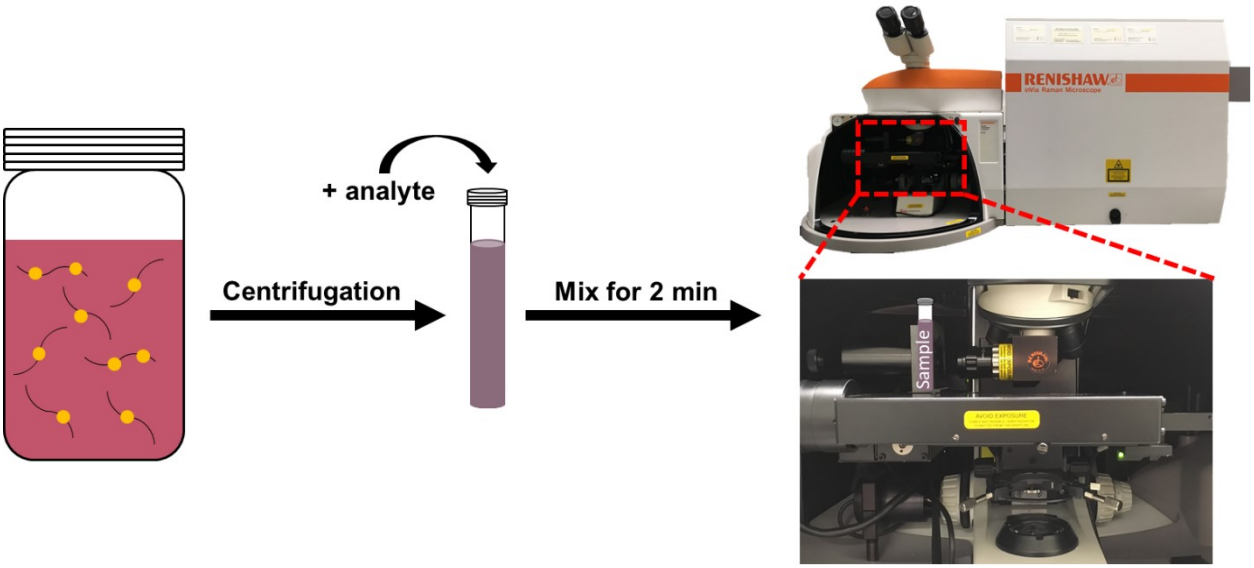

Figure 5-3. Schematic of experimental procedure for solution-based substrates.

A key consideration that is not applicable to solid-based substrates is the type of measurement vessel. Figure 5-4 shows different types of measurement containers including a quartz cuvette on the left and glass vials of different volumes on the right. Raman spectra for ethanol is shown for the quartz cuvette and a glass vial using a 633 nm and 785 nm lasers (focused at edge of the container). In the case of the quartz cuvette, there is a little to no fluorescence interference from the measurement container. Conversely, fluorescence interference is observed from the glass vial, particularly with the 785 nm laser. While these effects can be mitigated with background and baseline

subtractions, one needs to consider the container type for their particular application. A quartz cuvette provides a little to no background interference, however, it needs to be cleaned and dried after every measurement. The benefit of using a glass vial for measurements is that they are disposable, and a new vial can be used for each sample. Since there is a bottleneck effect to use a quartz cuvette for large amounts of measurements, a glass vial (far right) and a 633 nm laser is used in the sections to come.

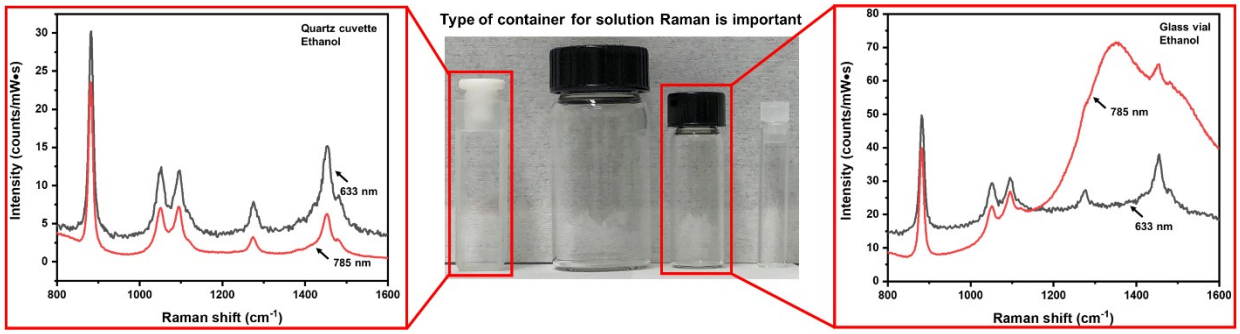

Figure 5-4. Containers for solution analysis. Raman spectra of ethanol in a quartz cuvette and glass vial using a 633 nm and 785 nm laser.

Another factor to consider is the alignment of the solution container in the liquid cell adapter. Figure 5-5 shows the key components and set up for solution measurements. Figure 5-5A and 5-5B shows the 90 ° objective attachment, and the stage attachment and sample holder, respectively. In Figure 5-5B the plunger at the end of the attachment is pulled outwards to load the sample. More discussion on loading the sample is in the next paragraph. Figure 5-5C and 5-5D are images demonstrating the final set up for solution measurement.

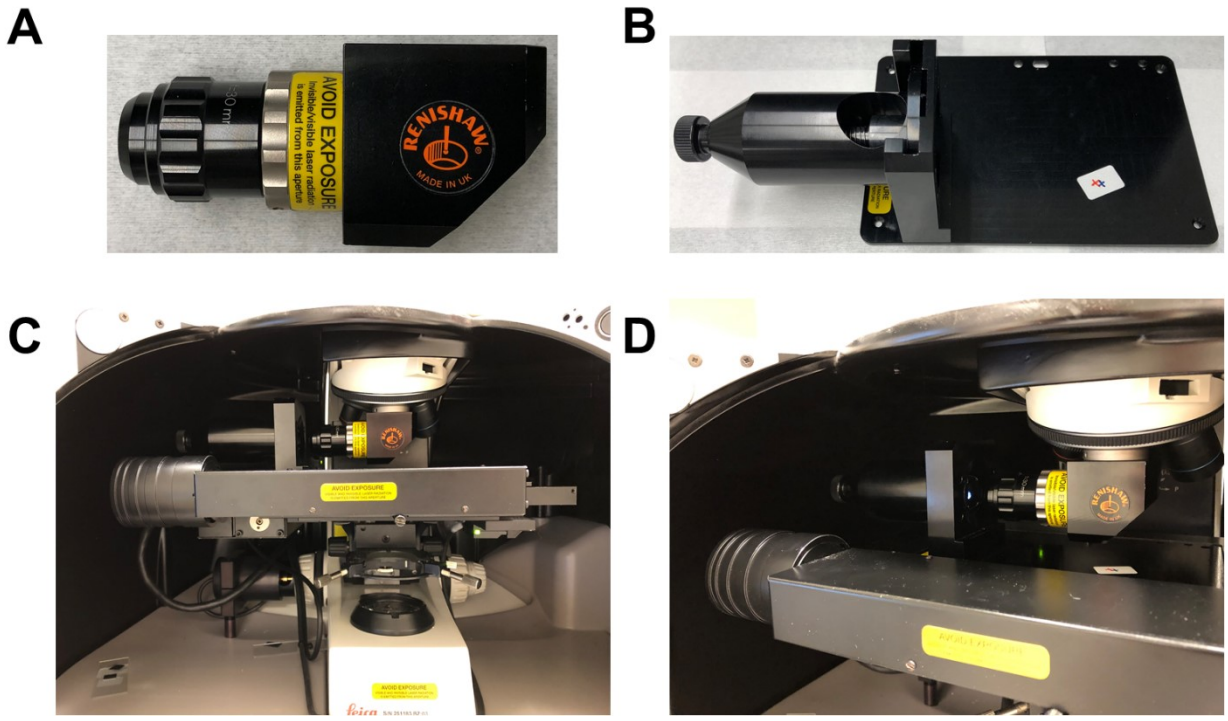

Figure 5-5. Liquid cell adapter components. Images showing (A) 90 ° objective attachment (B) stage platform and sample holder, (C-D) liquid cell set up for solution measurement.

Next, the sample needs to be loaded into the holder. Figure 5-6 shows images demonstrating the placement of a glass vial (A) and a quartz cuvette (B). These positions are achieved by rotating the plunger holding the container in place. Initial centring of the stage can be accomplished by ensuring the microscope light lines up with the dotted line in Figure 5-6A. The stage can also be moved upwards and downwards accordingly. In Figure 5-6A, the plunger is notched (V-shaped) so that the vial can be held securely in place, and can be removed and replaced reproducibly. The image on the right in Figure 5-6A demonstrates a vial being held in place. Similar steps are taken for when a cuvette is used. In Figure 5-6B, protruding corners (indicated with arrows) hold the quartz cuvette in place and do not allow that cuvette to move side to side. The image on the right in Figure 5-6B

demonstrates a cuvette being held in place. It is important to develop a standard protocol for aligning the solution container in order to obtain reproducible results. While there will always be slight changes in alignment and configuration for day-to-day measurements, these basic steps can help reduce the amount of uncertainty in the measurement set up.

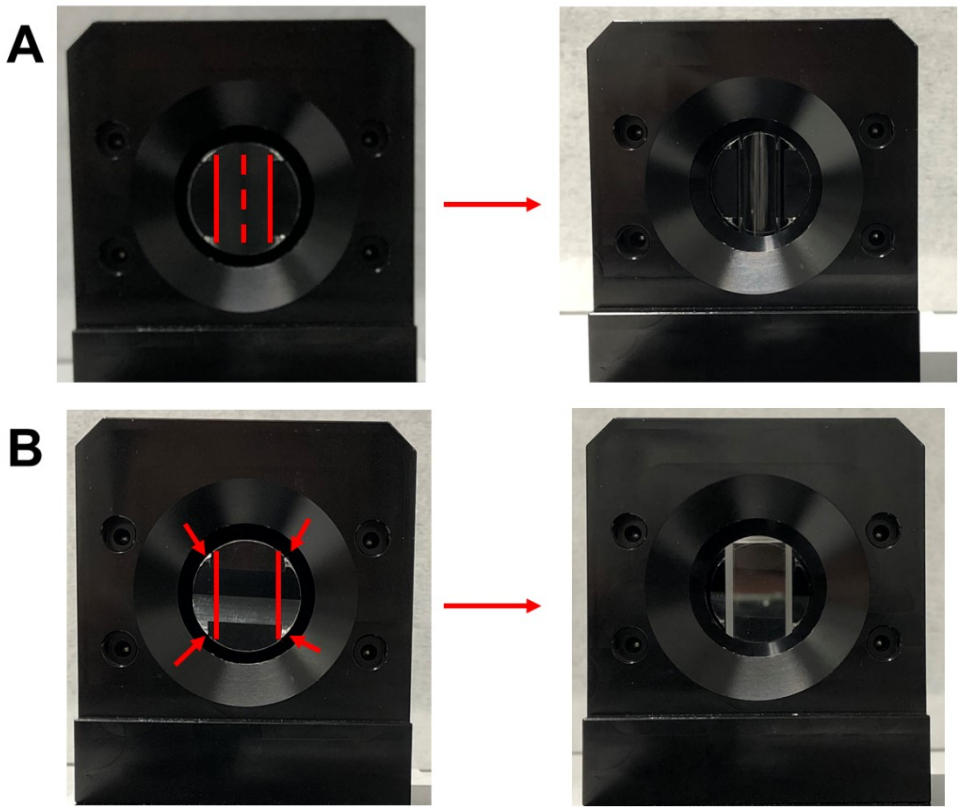

Figure 5-6. Initial placement of solution containers into the Raman spectrometer. Front facing view of the stage attachment and sample holder. (A) Configuration for a glass vial and (B) a quartz cuvette.

Raman spectroscopy is used to determine the optimal laser focus point on the vial. This is specific to the type of vial being used and 1 mL sampling vials are used in this case. After the vial has been placed into the holder, the stage needs to be adjusted so that the laser is aligned and focused. Figure 5-7 shows images and the Raman spectra of ethanol at

different locations on the vial. There are two important benchmarks when aligning and focusing the laser: (1) the front and (2) back of the vial. Using the arbitrary values provided by the microscope and all other locations within the vial can be determined mathematically. The middle of the vial is used as a starting point for the upcoming discussion. Figure 5-7A is the Raman spectra of ethanol as the laser moves across the vial. The Raman intensity is lowest when the laser is focused along the edges of the vial (positions 1 and 5), while there is no change in intensity as long as the laser is focused inside the vial (positions 2-4). There also seems to be some fluorescence interference along the edges of the vial. Figure 5-7B examines the effect of laser position and depth within the vial. Similar to above, the edges of the vial (position 6 and 10) provide lower Raman intensity and show evidence of fluorescence interference from the vial. The largest Raman spectral intensities are observed when the laser is focused within the vial (positions 7-9). Figure 5-7C examines the effect of taking measurements at different heights on the vial (focused in the middle). As expected, there are no changes in the Raman intensities at different height locations. When performing measurements in solution the laser needs to be focused somewhere within the vial rather than at the edges of the vial. This differs from surface measurements as the laser is generally focused at the surface of the substrate. Note that these estimates are made based on normal Raman scattering, and we assume that the same effect will be observed for SERS measurements.

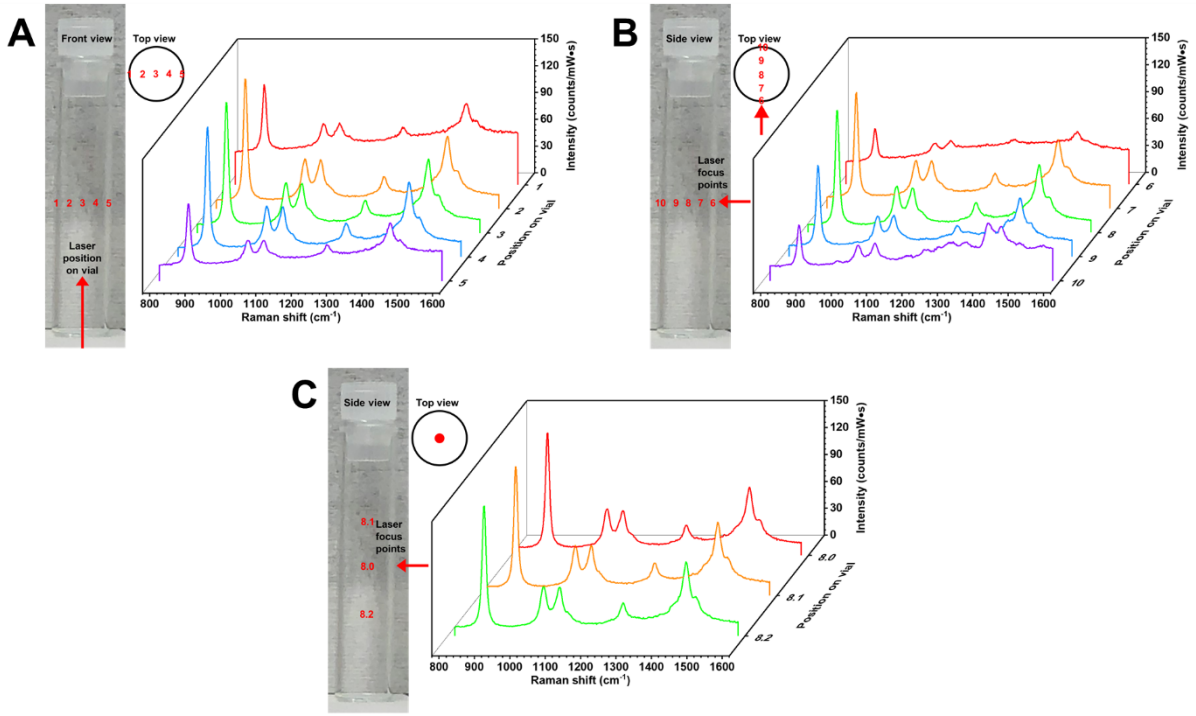

Figure 5-7. Alignment of the laser on the vial. The alignment is based on (A) the position across the vial, (B) the depth within the vial and (C) height within the vial. Raman spectrum is of ethanol using a 633 nm laser.

5.3.3. Performance of Solid-Based Substrates

In the upcoming section the SERS performance from solid-based Au-CNF substrates using different membranes and glass slides are examined using R6G. The spectra shown in the following sections are treated with two baseline subtractions. Figure 5-8 provides insight of the R6G spectrum on membranes and a glass slide containing 2 mL of Au-CNF before the baseline subtractions.

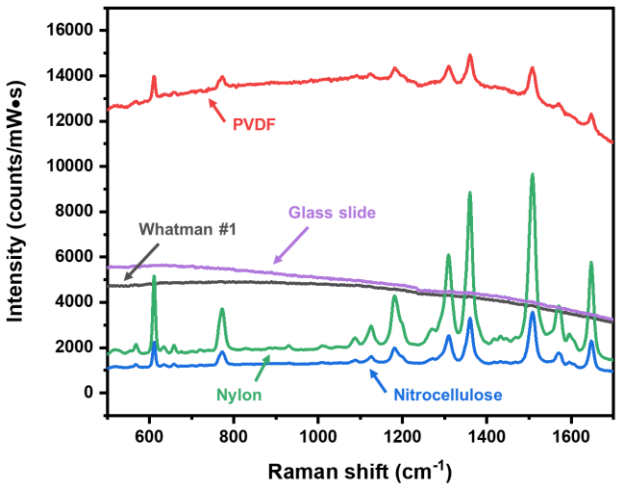

Figure 5-8. SERS performance spectrum treatment. SERS spectra of R6G before spectral baseline subtractions for membrane-based and glass slide substrates.

5.3.3.1. Membrane Supported SERS Substrates

Membrane supported Au-CNF substrates are prepared using a vacuum filtration protocol and evaluated by their SERS performance. Similar filtration protocols have been used to prepare cellulose-based nanocomposites.[13, 16] For example, Kim et al. used a vacuum filtration protocol to deposit CNF-AuNP nanocomposites onto a cellulose ester membrane, and the membrane was peeled off afterwards.[16] In this work, four types of membranes are examined, including Whatman #1 filter papers, polyvinylidene fluoride (PVDF) membranes, nitrocellulose membranes and nylon membranes. The use of these types of membranes have been previously reported for SERS substrates (not necessarily via filtration).[17-22] The key aspects that are considered in this work include the preparation time, pore size, type of substrate/membrane and amount of Au-CNF added to the substrate. Two different Au-CNF volumes (0.4 mL and 2 mL) are compared for membrane supported Au-CNF substrates. Figure 5-9 shows a 3D plots of the SERS spectrum of R6G when 0.4 mL

of Au-CNF is deposited onto the membranes. The inset images show the membrane supported Au-CNF substrates after preparation, and each membrane is cut into four individual membranes.

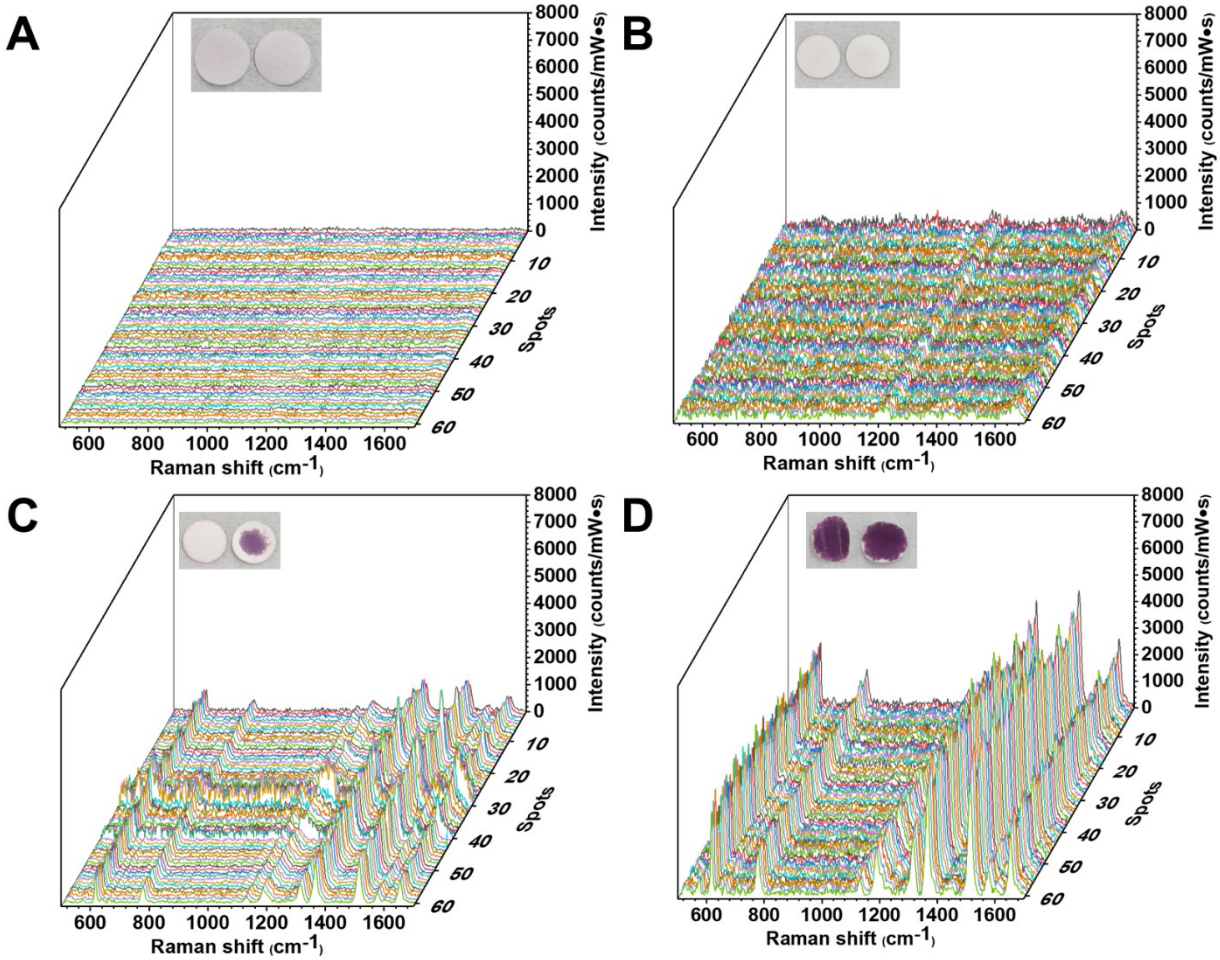

Figure 5-9. 3D plots of the SERS spectrum for rhodamine 6G (7 nmol) from Au-CNF (0.4 mL) deposited onto different types of membranes. (A) Whatman #1 filter paper, (B) polyvinylidene fluoride (PVDF) membrane, (C) nitrocellulose membrane and (D) nylon membrane. The spectra are from 3 substrates (substrate 1: spots 1-20; substrate 2: spots 21-40; substrate 3: spots 41-60).

The membrane used in Figure 5-9A is Whatman #1 filter paper with a pore size of 11 μm. The membrane does not retain the Au-CNF likely due to the large pore size. As a result, there is no observable SERS spectrum of R6G when using these substrates. Figure 5-

9B demonstrates the performance of PVDF membranes with a pore size of 0.45 μm. Similar to the Whatman #1 filter paper, the PVDF membrane does not retain most of the deposited Au-CNF. There is no observable SERS spectrum for R6G using a PVDF membrane with 0.4 mL Au-CNF. Membranes with smaller pore sizes yield an overall better SERS performance, but with a dependence on membrane material. The performance of Au-CNF deposited on a nitrocellulose membrane with a pore size of 0.22 μm is shown in Figure 5-9C. In this case the SERS spectrum for R6G is observable. The inset image shows that the filtered Au-CNF only covers a portion of the membrane, which could impact the substrate reproducibility. Moreover, there were instances where very little Au-CNF was retained, and those substrates were not used in measurements. The in-plane C–C stretch at 1509 cm^{-1} is used to investigate the SERS performance. The average spot-to-spot reproducibility within a single substrate is 18% (n=20; based on 3 substrates), while the substrate-to-substrate reproducibility is 19%. Finally, Figure 5-9D demonstrates the performance of Au-CNF deposited onto nylon membranes with a pore size of 0.22 μm. These substrates show excellent SERS intensities compared to the previously discussed substrates. The inset image shows that nearly the entire membrane is covered with Au-CNF. The average spot-to-spot reproducibility within a single substrate is 10% (n=20; based on 3 substrates), while the substrate-to-substrate reproducibility is 14%. Two factors to consider in preparing these substrates are the pore size and the membrane composition. As the pore size decreases, visually, more Au-CNF is retained by the membrane. However, as the pore size decreases, the filtration time also increases, which requires longer preparation times. The membrane composition could also impact the retention of Au-CNF during the vacuum filtration process. The differences between each membrane could be attributed to stronger

and/or weaker intermolecular forces between the membrane and oxidized CNF. However, to fully understand the impact from intermolecular forces between each membrane and oxidized CNF, the membranes should be compared at the same pore size. Moving forward, it is clear that the substrates are not completely covered by Au-CNF after the filtration process. The next section will examine the effect of filtering a larger volume of Au-CNF through the membrane.

The amount of Au-CNF filtered through the membranes is increased from 0.4 mL to 2 mL in order to achieve a higher coverage of Au-CNF on the membrane and to improve on the SERS performance. Figure 5-10 shows 3D plots of the SERS spectrum of R6G when 2 mL of Au-CNF is deposited onto the membranes.

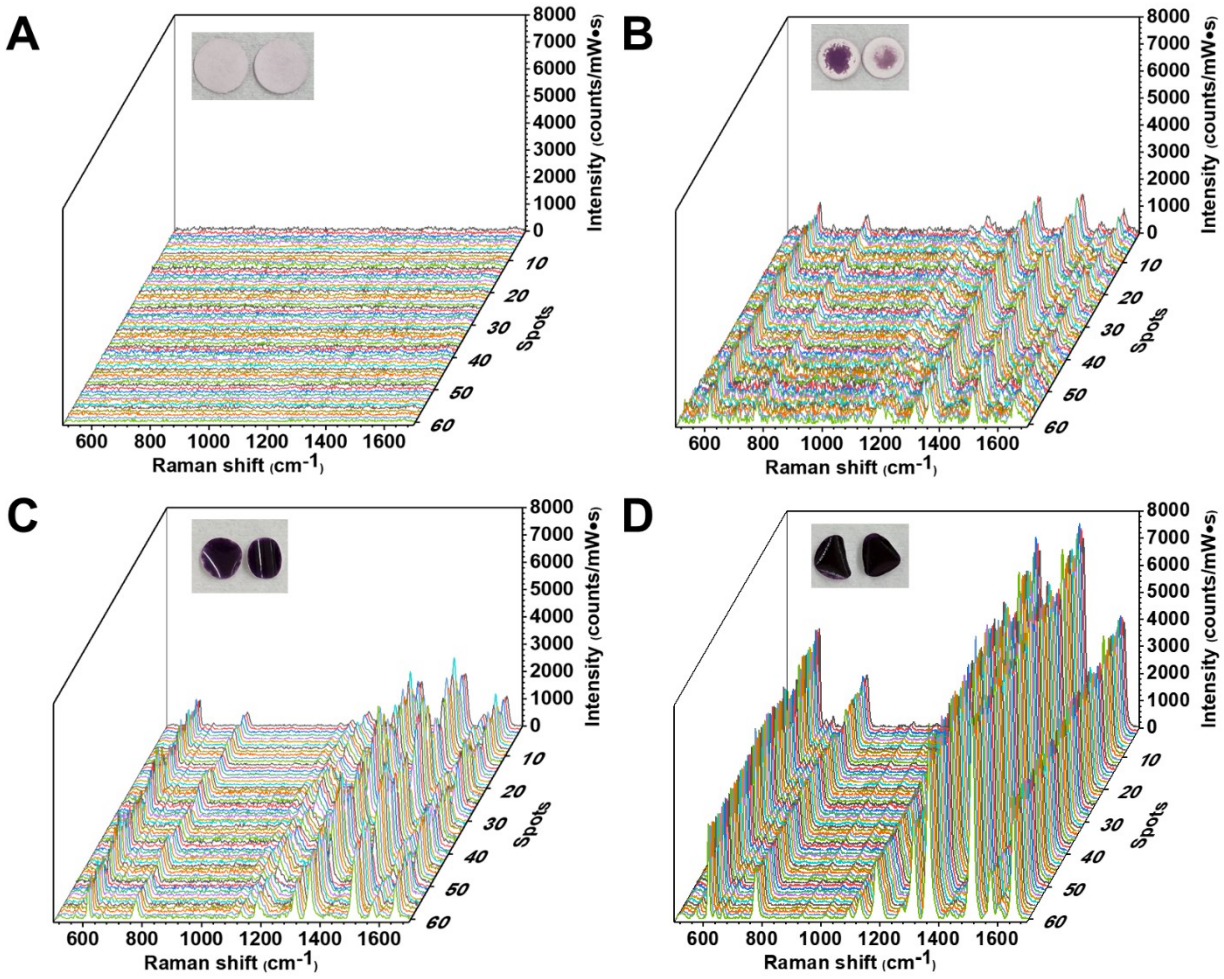

Figure 5-10. 3D plots of the SERS spectrum for rhodamine 6G (7 nmol) from Au-CNF (2 mL) deposited onto different types of membranes. (A) Whatman #1 filter paper, (B) polyvinylidene fluoride (PVDF) membrane, (C) nitrocellulose membrane and (D) nylon membrane. The spectra is from 3 substrates (substrate 1: spots 1-20; substrate 2: spots 21-40; substrate 3: spots 41-60).

The membrane used in Figure 5-10A is Whatman #1 filter paper. Similar to the results above, no SERS intensities are observed, and very little Au-CNF is retained by the filter paper. In this case, the use of Whatman #1 filter paper with large pore sizes, or without further treatment is not an ideal option for the development of SERS substrates. Figure 5-10B shows the SERS performance of Au-CNF filtered onto a PVDF membrane. There is a significant improvement in the amount of Au-CNF retained by the membrane and in the

SERS performance in comparison to Figure 5-9B. It is hypothesized that with the deposition of more Au-CNF, it will begin to block the pores within the membrane and capture more Au-CNF. While the membrane's entire surface is not covered with Au-CNF and we expect this to have an impact on the reproducibility, measurements were only taken where the Au-CNF can be observed. The average spot-to-spot reproducibility within a single substrate is 15% (n=20; based on 3 substrates), while the substrate-to-substrate reproducibility is 8%. Figure 5-10C shows the SERS performance associated with Au-CNF deposited onto nitrocellulose membranes. The entire membrane surface is covered with Au-CNF, and cellulose hornification wrinkling is observed. The overall SERS peak intensities have increased in comparison to before. The average spot-to-spot reproducibility within a single substrate is 22% (n=20; based on 3 substrates) and the substrate-to-substrate reproducibility is 14%. There is no significant improvement in reproducibility with the addition of more Au-CNF on nitrocellulose membranes. Finally, the deposition of 2 mL of Au-CNF onto nylon membranes shows large SERS peak intensities (Figure 5-10D). The nylon membrane is completely covered with Au-CNF and has become a dark purple in comparison to when only 0.4 mL of Au-CNF was added. There is evidence of hornification wrinkling from the cellulose upon drying. The average spot-to-spot reproducibility within a single substrate is 5% (n=20; based on 3 substrates) and the substrate-to-substrate reproducibility is 3%. The addition of more Au-CNF has resulted in an increase in SERS peak intensities and improved SERS reproducibility.

Overall, four different membrane-based Au-CNF substrates were prepared and examined in terms of their SERS performance. Briefly, the pore size and type of membrane played key roles in the substrate preparation. Substrates with 2 mL Au-CNF performed

better than those with only 0.4 mL of Au-CNF, and the nylon-based Au-CNF substrates demonstrated excellent SERS performance and reproducibility.

5.3.3.2. Drop-Casted SERS Substrates

A second method is used to prepare a solid- and cellulose-based SERS substrate. Different volumes (0.4 mL and 2 mL) of Au-CNF are drop-casted onto 1x1 cm glass slides and left to dry overnight. One immediate disadvantage to this method is the amount of time required to prepare these substrates. For instance, 0.2 mL of Au-CNF is added daily to the glass slide and is left overnight to dry. A substrate containing 0.4 mL only takes 2 days of preparation, however, a substrate containing 2 mL of Au-CNF requires 10 days of preparation. Figure 5-11 shows the SERS performance of drop-casting 0.4 mL and 2 mL onto glass slides. Measurements are taken using the same conditions as above. Figure 5-11A shows the substrate containing 0.4 mL of Au-CNF. There is a fairly good distribution on the surface, with the presence of a coffee-ring effect around the edges. Figure 5-11B shows the substrate containing 2 mL of Au-CNF. The substrate is a dark purple and demonstrates a good distribution of Au-CNF. However, in both cases, the SERS spectra for R6G are not observed. It is clear that the Au-CNF is retained on the surface of the glass slides, but it is unclear to us why no spectrum is observed. It is possible that the R6G solution is too concentrated, and the SERS peaks are overwhelmed with background fluorescence (before baseline subtractions) (see Figure 5-8). In the case of the membranes, excess R6G could be wicked away by the membrane, where this is not possible with the glass slides.

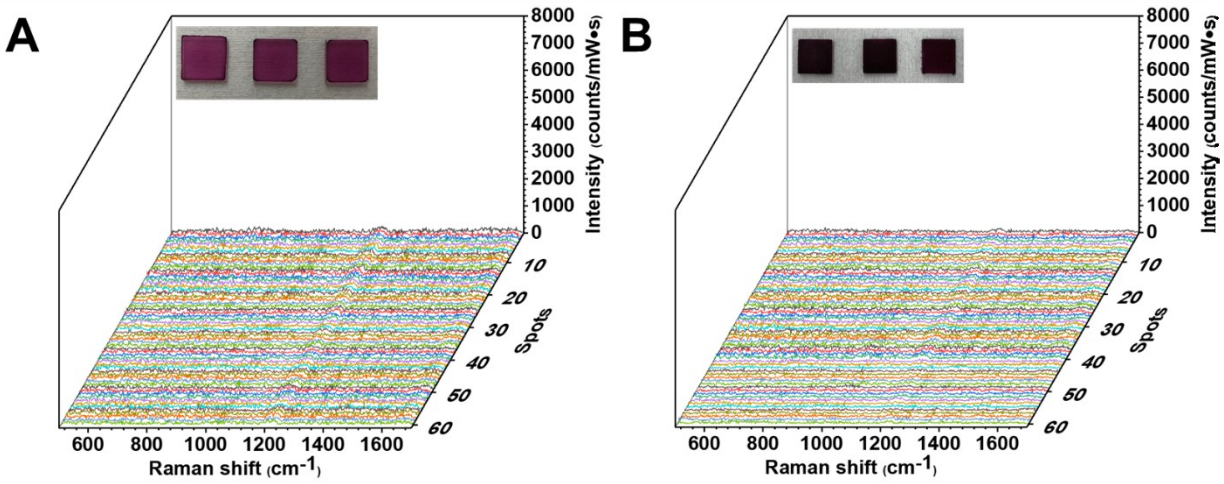

Figure 5-11. Raman spectra of rhodamine 6G (7 nmol) from Au-CNF deposited onto glass slides. (A) 0.4 mL and (B) 2 mL deposited onto 1x1 cm glass slides. The spectra is from 3 substrates (substrate 1: spots 1-20; substrate 2: spots 21-40; substrate 3: spots 41-60).

5.3.4. Performance of Solution-Based SERS Substrates

The merits of in-solution SERS measurements have been thoroughly discussed in Chapter 2-4. The in-solution SERS spectra of R6G using the dispersed Au-CNF substrate is shown in Figure 5-12. Similar to above, the in-plane C–C stretch at 1509 cm^{-1} is used to investigate the SERS performance. The aim of this section is to highlight the ability to use colloidal Au-CNF as a dispersible substrate, and to compare its capabilities to a solid-based substrate. The performance is investigated using 16 batches of colloidal Au-CNF. Each batch consists of 5 samples, and each vial was analyzed 3 times (Note: batch 1 contains only 3 samples). The average spot-to-spot reproducibility is determined as 2 ± 1 %. This is the measurement reproducibility within a vial and is based on a total of 78 vials. This is a comparable reproducibility value to the CNF decorated with silver nanoparticles susbtrate developed in

Chapter 3. The sample-to-sample and batch-to-batch reproducibility is shown in Figure 5-12.

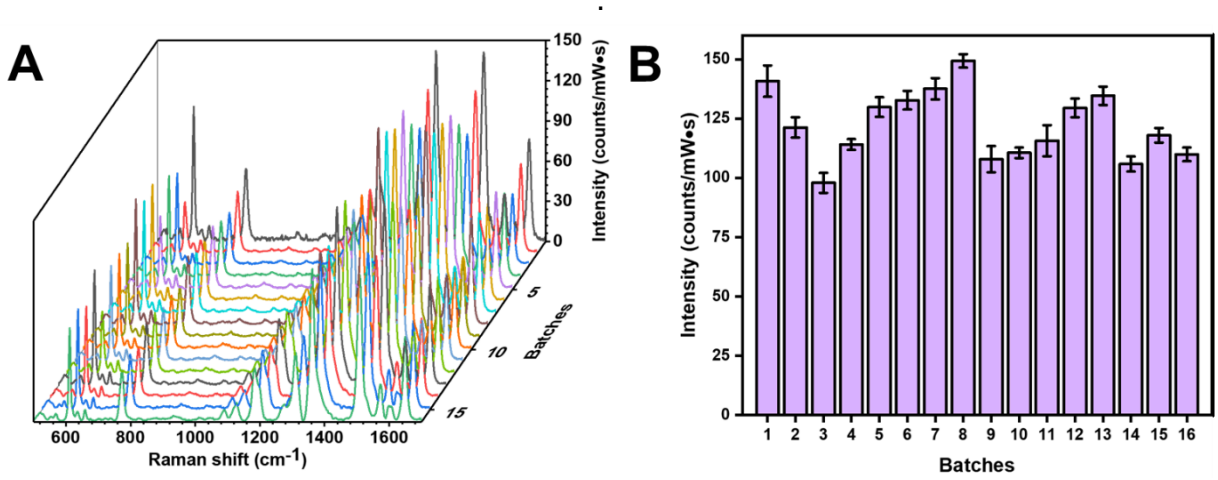

Figure 5-12. In-solution analysis of rhodamine 6G (5 µM) using Au-CNF. (A) Raman spectra of rhodamine 6G from different Au-CNF batches. (B) Column graph of the peak intensity of C-C stretch at 1509 cm^{-1}. Each batch consists of 5 different samples.

The sample reproducibility within a single batch is shown as the percent relative standard deviation (%RSD) of the average peak intensity within a measurement vial (n=5). The sample-to-sample reproducibility (within a single batch) ranges from 3 to 6%. The average sample reproducibility across all batches is 3 ± 1 %. The batch-to-batch reproducibility is shown as the %RSD of the average peak intensity from each Au-CNF batch, and is determined as 12%. These values associate well with what has been observed in Chapters 3 and 4. These results demonstrate that colloidal Au-CNF is capable of providing rapid SERS measurements with comparable reproducibility to solid-based Au-CNF substrates. The next section will compare and discuss some of the advantages and disadvantages of using solid- and solution-based Au-CNF substrates.

5.3.5. Comparative Examination of Solid and Solution SERS Analysis

The intent of this section is not to determine whether one type of measurement is superior to the other or not. There are many factors to consider when choosing a substrate and measurement format. Some of these factors include the synthesis time, the scalability and the performance of the substrate, how the measurements are to be taken, the desired application, etc. The aim of this section is to highlight some of these key factors. The discussions about the advantages and disadvantages pertain specifically to the synthesis/preparation of the substrate, the ability to take measurements and the measurement time, and the substrate performance/reproducibility.

The preparation of the substrate is the first part of the discussion. The synthesis of colloidal Au-CNF is a simple fairly inexpensive preparation method. It is obvious that the synthesis of a solution-based Au-CNF substrate requires less time overall. Moreover, the synthesis of Au-CNF is easily scalable for large volume analysis. The preparation of a solid-based Au-CNF is at a disadvantage in comparison to the solution-based substrates. All the solid-based Au-CNF substrates require additional preparation steps, i.e. filtration and drop-casting. The preparation and optimization could vary in time based on the pore size of the membrane, the type of membrane, or the amount of Au-CNF added to the membrane. Additionally, the preparation time can be days longer in the case of drop-casting onto a glass slide. Another consideration in the development of solid-based substrates is the random distribution of Au-CNF on the membrane via filtration, or the formation of a Au-CNF coffee-ring upon solvent evaporation via a drop-casting method.

Another important area of consideration pertains to the measurement style between the two substrates. The set up for a solid-based substrate is relatively straightforward (in relation to the sections above), but can become tedious and time consuming when analyzing a large amounts of samples. Moreover, the focus of the laser spot changes as the stage moves from spot-to-spot, and could negatively impact the substrate reproducibility. Additionally, if the Au-CNF is not well distributed on the surface it could lead to reproducibility issues. Crawford et al. have shown that a sampling error can be introduced into SERS measurements, particularly when a smaller laser spot size is used.[23]

In the case of the solution-based substrates, there is a long initial set up and alignment procedure, but it is simple to remove and insert samples without re-adjusting the microscope. This allows for analysis of a large amounts of samples. The issue of spot-to-spot reproducibility is not as large of a concern compared to the Au-CNF solid-substrates. Since the substrate is colloidally stable and is well dispersed, the solution homogeneity reduces the spot-to-spot irreproducibility.

When it comes to taking measurements with each substrate there are some key differences between the two measurement styles. In this case of a solid-based Au-CNF, a key advantage is the versatility in taking a measurement, such as wiping, drop-casting and dipping in solution, and these substrates are easily transportable. The White group has developed highly sensitive and flexible SERS substrates on paper using inkjet printing, and these sensors are used as a swab, dipstick and in lateral flow assays.[24] Jiang and Hsieh adsorbed R6G to their cellulose nanofibril silver nanoprism substrate using an immersion

method.[22] Others have used a drop-casting method to deposit the analyte onto the substrate.[11, 25] The deposition of analyte can become time consuming because these types of methods often require longer adsorption times, and rinsing and drying steps. In this chapter, the solid-based substrates were used with a drop-casting technique. There are two main concerns with drop-casting an analyte on a substrate (1) the formation of a coffee-ring of the analyte and (2) the re-distribution of the nanoparticles/hot spots. These could have an impact on the substrate reproducibility. While all of the solid-based substrates are susceptible to these conditions, an excellent substrate was developed after some preliminary optimization steps (2 mL of Au-CNF on nylon membrane).

When using a solution-based substrate, it is fairly limited to solution-bound analytes and the substrate typically needs to be aggregated to some extent. There is also the potential to experience interference from the sampling vial. However, there are some benefits to taking measurements in solution. There are no rinsing and drying steps, and no solvent evaporation required. This includes excellent and competitive SERS reproducibility due to solution homogeneity of the substrate, and rapid analysis times due to substrate/analyte mixing capability.

Comparing the performance between solid- and solution-based substrates is extremely challenging largely due to differences in the measurement styles. This chapter aimed at keeping parameters relatively close in order to gain an understanding of performance differences. It is clear that solid-based substrates produced larger and slightly sharper peak intensities in comparison to the solution-based substrates. When measurements are taken in solution, Raman scattered photons are competing with the

surrounding solution and the sample container. This results in a lower peak intensity and peak broadening of the analyte. Regardless, solution-based substrates have shown to be comparable in performance to a solid-based substrate. One type of substrate is not necessarily "better" than the other as both offer advantages over the other, and could be used to their advantage in specific scenarios.

5.4. Conclusions

This chapter highlights the capability of Au-CNF to be used as a solid-based and solution-based SERS substrate. The different measurement set ups and procedures for taking measurements on a surface and in solution were discussed in detail. Setting up measurements using a solid-based substrate is relatively straightforward, however, it is important to consider focus and defocus spots when taking measurements. Also, solid-based substrates generally require additional analysis time due to solvent evaporation. When taking measurements in solution, the set up procedure can be tedious and time consuming, but is only required at the beginning of the measurements. This promotes rapid sample to sample measurements. The development of a consistent procedure in order to achieve reproducible results is crucial, and the laser needs to be focused somewhere within the solution container (in the middle) to achieve the optimal intensities. Nylon membranes with deposited Au-CNF (2 mL) showed excellent reproducibility and large SERS intensities of R6G. The nylon-based membranes were competitive with colloidal Au-CNF in terms of reproducibility, and this highlights the potential and versatility of Au-CNF as a SERS substrate.

5.5. References

1. Nie, S.; Emory, S. R., Probing Single Molecules and Single Nanoparticles by Surface-Enhanced Raman Scattering. *Science* **1997,** *275* (5303), 1102-1106.

2. Kneipp, K.; Wang, Y.; Kneipp, H.; Perelman, L. T.; Itzkan, I.; Dasari, R. R.; Feld, M. S., Single Molecule Detection Using Surface-Enhanced Raman Scattering (SERS). *Phys. Rev. Lett.* **1997,** *78* (9), 1667-1670.

3. Mosier-Boss, P. A., Review of SERS Substrates for Chemical Sensing. *Nanomaterials* **2017,** *7* (6), 142.

4. Pilot, R.; Signorini, R.; Durante, C.; Orian, L.; Bhamidipati, M.; Fabris, L., A Review on Surface-Enhanced Raman Scattering. *Biosensors* **2019,** *9* (2), 57.

5. Shi, R.; Liu, X.; Ying, Y., Facing Challenges in Real-Life Application of Surface-Enhanced Raman Scattering: Design and Nanofabrication of Surface-Enhanced Raman Scattering Substrates for Rapid Field Test of Food Contaminants. *J. Agric. Food. Chem.* **2018,** *66* (26), 6525-6543.

6. Guerrini, L.; Graham, D., Molecularly-mediated assemblies of plasmonic nanoparticles for Surface-Enhanced Raman Spectroscopy applications. *Chem. Soc. Rev.* **2012,** *41* (21), 7085-7107.

7. Ogundare, S. A.; van Zyl, W. E., A review of cellulose-based substrates for SERS: fundamentals, design principles, applications. *Cellulose* **2019,** *26* (11), 6489-6528.

8. Park, M.; Hwang, C. S. H.; Jeong, K.-H., Nanoplasmonic Alloy of Au/Ag Nanocomposites on Paper Substrate for Biosensing Applications. *ACS Appl. Mater. Interfaces* **2018,** *10* (1), 290-295.

9. Li, Y.; Zhang, K.; Zhao, J.; Ji, J.; Ji, C.; Liu, B., A three-dimensional silver nanoparticles decorated plasmonic paper strip for SERS detection of low-abundance molecules. *Talanta* **2016,** *147*, 493-500.

10. Hasi, W.-L.-J.; Lin, S.; Lin, X.; Lou, X.-T.; Yang, F.; Lin, D.-Y.; Lu, Z.-W., Rapid fabrication of self-assembled interfacial film decorated filter paper as an excellent surface-enhanced Raman scattering substrate. *Anal. Methods* **2014,** *6* (24), 9547-9553.

11. Chen, R.; Zhang, L.; Li, X.; Ong, L.; Soe, Y. G.; Sinsua, N.; Gras, S. L.; Tabor, R. F.; Wang, X.; Shen, W., Trace Analysis and Chemical Identification on Cellulose Nanofibers-Textured SERS Substrates Using the "Coffee Ring" Effect. *ACS Sens.* **2017,** *2* (7), 1060-1067.

12. Yu, W. W.; White, I. M., Inkjet Printed Surface Enhanced Raman Spectroscopy Array on Cellulose Paper. *Anal. Chem.* **2010,** *82* (23), 9626-9630.

13. Kim, D.; Ko, Y.; Kwon, G.; Kim, U.-J.; Lee, J. H.; You, J., 2,2,6,6-Tetramethylpiperidine-1-oxy-Oxidized Cellulose Nanofiber-Based Nanocomposite Papers for Facile In Situ Surface-Enhanced Raman Scattering Detection. *ACS Sustainable Chem. Eng.* **2019,** *7* (18), 15640-15647.

14. Ogundare, S. A.; van Zyl, W. E., Nanocrystalline cellulose as reducing- and stabilizing agent in the synthesis of silver nanoparticles: Application as a surface-enhanced Raman scattering (SERS) substrate. *Surf. Interfaces* **2018,** *13*, 1-10.

15. Menges, F. Spectragryph - optical spectroscopy software. http://www.effemm2.de/spectragryph/ (accessed April 23, 2020).

16. Kim, D.; Ko, Y.; Kwon, G.; Choo, Y.-M.; You, J., Low-cost, high-performance plasmonic nanocomposites for hazardous chemical detection using surface enhanced Raman scattering. *Sens. Actuators, B* **2018,** *274*, 30-36.

17. Lee, C. H.; Hankus, M. E.; Tian, L.; Pellegrino, P. M.; Singamaneni, S., Highly Sensitive Surface Enhanced Raman Scattering Substrates Based on Filter Paper Loaded with Plasmonic Nanostructures. *Anal. Chem.* **2011,** *83* (23), 8953-8958.

18. Schmucker, A. L.; Tadepalli, S.; Liu, K.-K.; Sullivan, C. J.; Singamaneni, S.; Naik, R. R., Plasmonic paper: a porous and flexible substrate enabling nanoparticle-based combinatorial chemistry. *RSC Adv.* **2016,** *6* (5), 4136-4144.

19. Zhang, K.; Ji, J.; Fang, X.; Yan, L.; Liu, B., Carbon nanotube/gold nanoparticle composite-coated membrane as a facile plasmon-enhanced interface for sensitive SERS sensing. *Analyst* **2015,** *140* (1), 134-139.

20. Liu, R.; Tang, J.; Yang, H.; Jin, W.; Liu, M.; Liu, S.; Hu, J., In situ decoration of plasmonic silver nanoparticles on poly(vinylidene fluoride) membrane for versatile SERS detection. *New J. Chem.* **2019,** *43* (18), 6965-6972.

21. Torul, H.; Çiftçi, H.; Çetin, D.; Suludere, Z.; Boyacı, I. H.; Tamer, U., Paper membrane-based SERS platform for the determination of glucose in blood samples. *Anal. Bioanal. Chem.* **2015,** *407* (27), 8243-8251.

22. Jiang, F.; Hsieh, Y.-L., Synthesis of Cellulose Nanofibril Bound Silver Nanoprism for Surface Enhanced Raman Scattering. *Biomacromolecules* **2014,** *15* (10), 3608-3616.

23. Crawford, A. C.; Skuratovsky, A.; Porter, M. D., Sampling Error: Impact on the Quantitative Analysis of Nanoparticle-Based Surface-Enhanced Raman Scattering Immunoassays. *Anal. Chem.* **2016,** *88* (12), 6515-6522.

24. Hoppmann, E. P.; Yu, W. W.; White, I. M., Highly sensitive and flexible inkjet printed SERS sensors on paper. *Methods* **2013,** *63* (3), 219-224.

25. Zhang, L.; Li, X.; Ong, L.; Tabor, R. F.; Bowen, B. A.; Fernando, A. I.; Nilghaz, A.; Garnier, G.; Gras, S. L.; Wang, X.; Shen, W., Cellulose nanofibre textured SERS substrate. *Colloids Surf., A* **2015,** *468*, 309-314.

Chapter 6. Conclusion

6.1. Chapter Summaries

The motivation behind the work in this thesis was to develop surface-enhanced Raman scattering (SERS) substrates for rapid and reproducible in-solution measurements. This thesis presented three different types of solution-based SERS substrates based on using buffers and cellulose nanofibers (CNF) as nanoparticle supports. The use of these substrates using handheld Raman spectrometer was highlighted to emphasize the ability and potential for rapid and on-site analysis. Finally, CNF decorated with gold nanoparticles was compared and discussed as a solution- and solid-based substrate highlighting the advantages and disadvantages of using different measurement platforms.

Cellulose nanomaterials are excellent for the development of SERS substrates because of the versatility of the material. There are many types of cellulose-based substrates used as a solid substrate. However, this thesis highlights their use as a dispersible SERS substrate. In-solution measurements provide the opportunity for rapid analysis and reproducible measurements relating to the homogeneity of the solution. This thesis demonstrate both of these aspects and was competitive with other solid- and cellulose-based substrates.

In Chapter 2, the use of gold nanostars (AuNS) coupled with a handheld Raman spectrometer was explored as an in-solution SERS substrate. The synthesis of the AuNS using 4-(2-hydroxyethyl)-1-piperazineethanesulfonic acid (HEPES) and 4-(2-

hydroxyethyl)-1-piperazinepropanesulfonic acid (EPPS) buffers were optimized based on the buffer type and the buffer-to-gold molar ratios. Different buffers and ratios produced AuNS with different branch lengths, thus impacting the SERS intensities of 4-mercaptobenzonitrile (MBN). It was initially thought that longer branches would provide larger peak intensities. However, the results were counterintuitive in that AuNS synthesized using HEPES at ratio 100 produced the highest signal intensities. The differences in SERS intensities are due to the surface coverage of MBN on the AuNS rather than enhanced electromagnetic effects. The AuNS were stored in the refrigerator at 4 °C for over 78 days with a signal intensity %RSD of 8%. The capability to detect different analytes through chemisorption and physisorption mechanisms were investigated. Additional enhancement was provided with the addition of NaCl. The SERS intensity increased by a factor of 10 with the addition of NaCl through the formation of nanoaggregates. Methimazole (MTZ) was detected and quantified in urine using a SERS assay. The colloidal AuNS substrate showed a limit of detection of 0.1 μM and a recovery of nearly 100% when MTZ was spiked in synthetic urine. The coupling of colloidal AuNS and a handheld Raman device introduce the potential for rapid and remote SERS analysis.

In Chapter 3, a water dispersible SERS substrate comprising of cellulose nanofibers (CNF) decorated with silver nanoparticles (Ag NPs) was developed to provide rapid and reproducible in-solution measurements. The chemical reduction of the Ag onto CNF is explored and characterized using spectroscopic, elemental and imaging techniques. It was discovered that CNF has a key role in the synthesis by acting as a support and dispersing agent for the hybrid nanomaterial. Spherical Ag NPs about 45 nm in diameter are anchored to the CNF and remained colloidally stable. The optimal SERS activity was determined

using MBN as a probe species. Centrifugation was used to produce colloidally stable bundles of nanofibers to bring the Ag NPs into close proximity. Ag-CNF bundles produce dispersible SERS hot spots resulting in signal enhancement as high as 30×. Ag-CNF as a water dispersible substrate showed potential for rapid and reproducible detection of analytes through chemisorption and physisorption adsorption mechanisms. A SERS assay was developed to detect malachite green (MG), a banned fungicide, lower than the maximum allowable limit (~5 nM). Chemical modification of the CNF can be explored in the future to control the fibre entanglement and introduce selectivity to the measurement platform.

Chapter 4 explores the use of CNF decorated with gold nanoparticles (Au-CNF) as a water dispersible SERS substrate. A couple benefits to using Au over Ag is the inertness of Au and the localized surface plasmon resonance (LSPR) being shifts to a longer wavelength. This allows for more overlap between the LSPR and laser wavelength. The synthesis and characterization is modelled after the Ag-CNF substrate. We determined that the majority of the AuNPs of ~27nm in diameter are attached to the CNF. As before, the CNF plays an important role in the substrate synthesis by acting as a support and dispersing agent. Centrifugation of Au-CNF resulted in a signal enhancement of ~20× for MBN. The adsorption through chemisorption and physisorption mechanism were examined using thiabendazole, MTZ and rhodamine 6G (R6G). The detection and quantitation of MTZ in urine was investigated using a SERS assay. In-solution measurements using colloidal Au-CNF resulted in a limit of detection of 0.09 μM and a recovery of spiked MTZ in synthetic urine to be as high as 81%. Discussions about using colloidal Au-CNF and a handheld

Raman device are presented. As a proof-of-concept, a handheld Raman spectrometer was used to detect thiabendazole and MG in-solution with Au-CNF.

Chapter 5 compares the use of Au-CNF as a planar and solution SERS substrate. Colloidal Au-CNF was deposited on glasses slides, Whatman #1, polyvinylidene fluoride, nitrocellulose and nylon filter membranes. The performance of the planar and solution based substrates were investigated and compared using R6G. In general, the solution based substrate required less sample and analysis preparation. However, Au-CNF deposited on nylon filter membranes provided excellent signal intensities and reproducibility. This highlights the versatility of Au-CNF in planar and solution measurements.

6.2. Future Directions

The work in this thesis primarily focuses on the development of solution-based SERS substrates. The upcoming sections provide an opportunity for future research work to continue. These sections highlight ideas that could improve cellulose-based SERS substrates for in-solution measurements, introduce detection specificity/selectivity and investigate other in-solution platforms.

6.2.1. Anisotropic Nanoparticles on Cellulose Nanofibers

This thesis work highlights two general solution-based SERS substrates: (1) AuNS supported by Good's buffers and (2) Ag and Au nanoparticles supported by CNF. Given that one synthesis yields anisotropic nanoparticles and the other yields isotropic nanoparticles, these synthesis methods could be combined to synthesize anisotropic nanoparticles on CNF. In this case, the final product would be AuNS attached to CNF. The synthesis of AuNS

and Au-CNF both use a seedless method. However, another method to synthesize nanoparticles is a seed-mediated synthesis. For example, a seed-mediated approach has been taken to synthesize AuNS with Good's buffers.[1] With this in mind, pre-synthesized Au-CNF could be used as a seed and the anisotropic structure could be grown onto the Au-CNF with the addition of a Good's buffer and $HAuCl_4$. The motivation behind growing or attaching AuNS to CNF is to generate additional electromagnetic enhancement at the tip of the nanostar. This effect is called the "lightning rod" effect.[2] Anisotropic nanoparticles are known to provide more stronger SERS signal intensities in comparison to spherical nanoparticles.[3]

6.2.2. Specificity and Selectivity In-Solution Measurements

The work in this thesis highlights the development of solution-based substrates and demonstrates how these can be used in real-world applications. The analytes used in this thesis adsorb to the nanoparticle surface through chemisorption or physisorption mechanisms. Currently, the substrates lack specificity and selectivity capabilities. In short, as long as the target analyte has a stronger affinity to the surface than the other matrix analytes, it is likely to be detected. Future work is required to develop indirect measurement platforms in solution, and to measure analytes with a low affinity to the nanoparticle. Figure 6-1 is a schematic that illustrates future steps that can be taken to introduce specificity and selectively for in-solution measurements. For example, Orelma et al. have modified carboxymethyl cellulose using 1-ethyl-3-[3-dimethylaminopropyl]carbodiimide hydrochloride (EDC) and N-hydroxysuccinimide (NHS) (EDC/NHS) chemistry to covalently link antibodies to the carboxymethyl cellulose.[4]

Similar approaches could be applied to oxidized cellulose nanofibers decorated with metallic nanoparticles. In Figure 6-1A, the nanoparticles of Ag-CNF or Au-CNF are modified with a Raman reporter, i.e. MBN, and CNF are modified with an antibody or aptamer. When the target molecule is added to the solution, it will interact with the modified CNF causing the CNF bundle. This will bring the nanoparticles in close proximity to one another, and provide many hot spots for SERS analysis. Only the target analyte is expected to cause this increase in signal intensity, thus creating specificity within the substrate.

The addition of selectively to Ag-CNF and Au-CNF can be done in a similar fashion. Figure 6-1B is a schematic of how a Ag-CNF or Au-CNF substrate could be used for selective analyte measurements. In this case, two different CNF samples are modified with a different reporter and a different antibody/aptamer. Following modification, the CNF samples are mixed into the vessel. When the solution is exposed to the target analyte for that specific antibody/aptamer, there will be an increase in signal intensity for that specific reporter.

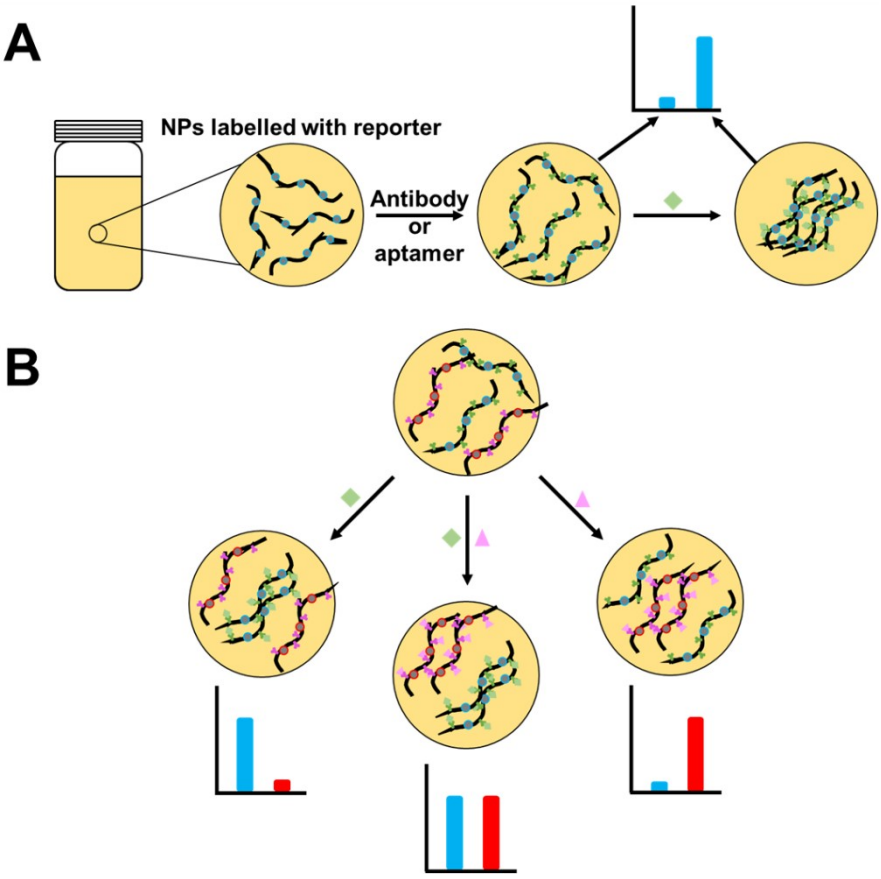

Figure 6-1. Introducing selectivity for in-solution measurements using colloidal plasmonic cellulose nanofibers. Schematic demonstrating the use of antibodies or aptamers to introduce specificity and selectivity for (A) a single target and (B) multiple targets.

6.2.3. Other Methods for Taking Measurements In-Solution

The work in this thesis highlights developing solution-based substrates. An alternative method for in-solution measurements could be fabricating the substrate onto the inside of a vial or capillary tube. Chapter 5 shows that the Raman signal intensity of ethanol is increased when the laser is focused into the solution rather than at the edge. However, metallic nanoparticles adsorbed to the inside of a vial or capillary tube brings nanoparticles in close proximity to each other and produces potential hot spots along the edge of the vial/capillary. Recently, Yu et al. have coated the inside of capillaries with gold nanorods

for the detection of thiram.[5] The inside of the capillaries are coated with nanorods using silane-chemistry treatment. Gold nanorods are adsorbed to the -NH_2 modified capillary wall.[5] For a future direction, anisotropic nanoparticles such as nanostars could provide the opportunity for increased SERS signal intensities. The analysis using these types of substrates have the potential to be straightforward, as only an aliquot would need to be added to the vial/capillary. I envision that these types of substrates have the potential to be commericialized since they could be easily transported and compatible with a handhand device for remote measurements.

6.3. References

1. Pallares, R. M.; Stilson, T.; Choo, P.; Hu, J.; Odom, T. W., Using Good's Buffers To Control the Anisotropic Structure and Optical Properties of Spiky Gold Nanoparticles for Refractive Index Sensing. *ACS Appl. Nano Mater.* **2019,** *2* (8), 5266-5271.

2. Gersten, J. I., The effect of surface roughness on surface enhanced Raman scattering. *J. Chem. Phys.* **1980,** *72* (10), 5779-5780.

3. Tian, F.; Bonnier, F.; Casey, A.; Shanahan, A. E.; Byrne, H. J., Surface enhanced Raman scattering with gold nanoparticles: effect of particle shape. *Anal. Methods* **2014,** *6* (22), 9116-9123.

4. Orelma, H.; Teerinen, T.; Johansson, L.-S.; Holappa, S.; Laine, J., CMC-Modified Cellulose Biointerface for Antibody Conjugation. *Biomacromolecules* **2012,** *13* (4), 1051-1058.

5. Yu, Y.; Zeng, P.; Yang, C.; Gong, J.; Liang, R.; Ou, Q.; Zhang, S., Gold-Nanorod-Coated Capillaries for the SERS-Based Detection of Thiram. *ACS Appl. Nano Mater.* **2019,** *2* (1), 598-606.

Bibliography

Abalde-Cela, S.; Aldeanueva-Potel, P.; Mateo-Mateo, C.; Rodríguez-Lorenzo, L.; Alvarez-Puebla, R. A.; Liz-Marzán, L. M., Surface-enhanced Raman scattering biomedical applications of plasmonic colloidal particles. *J. R. Soc. Interface* **2010,** *7* (suppl_4), S435-S450.

Agilent. Handheld Chemical Identification - Resolve Handheld Through-Barrier Identification System. https://www.agilent.com/en/products/raman-spectroscopy/raman-spectroscopy-systems/handheld-chemical-identification/resolve (accessed April 18, 2020).

Agilent. Pharmaceutical Analysis - Vaya Raman Raw Material Identity Verification System. https://www.agilent.com/en/products/raman-spectroscopy/raman-spectroscopy-systems/pharmaceutical-analysis/vaya-raman-raw-material-identity-verification-system (accessed April 18, 2020).

Ahsan, H.; Masaaki, T.; Guang, W. Y., Formation of Gold Nanoparticles by Good's Buffers. *Bull. Chem. Soc. Jpn.* **2005,** *78* (2), 262-269.

Albrecht, M. G.; Creighton, J. A., Anomalously intense Raman spectra of pyridine at a silver electrode. *J. Am. Chem. Soc.* **1977,** *99* (15), 5215-5217.

Alsammarraie, F. K.; Lin, M.; Mustapha, A.; Lin, H.; Chen, X.; Chen, Y.; Wang, H.; Huang, M., Rapid determination of thiabendazole in juice by SERS coupled with novel gold nanosubstrates. *Food Chem.* **2018,** *259*, 219-225.

An, L.; Deng, J.; Zhou, L.; Li, H.; Chen, F.; Wang, H.; Liu, Y., Simultaneous spectrophotometric determination of trace amount of malachite green and crystal violet in water after cloud point extraction using partial least squares regression. *J. Hazard. Mater.* **2010,** *175* (1), 883-888.

Anderson, S. L.; Luber, E. J.; Olsen, B. C.; Buriak, J. M., Substance over Subjectivity: Moving beyond the Histogram. *Chem. Mater.* **2016,** *28* (17), 5973-5975.

Anton Paar. Handheld Raman spectrometer: Cora 100. https://www.anton-paar.com/ca-en/products/details/handheld-raman-spectrometer-cora-100/ (accessed April 18, 2020).

B&W Tek. NanoRam - 1064 Handheld Raman Spectrometer. https://bwtek.com/products/nanoram-1064/ (accessed April 18, 2020).

B&W Tek. NanoRam Handheld Raman Spectrometer. https://bwtek.com/products/nanoram/ (accessed April 18, 2020).

B&W Tek. TacticID-1064 All-Inclusive Handheld Raman for Identification of Explosives, Hazmat, Narcotics & More. https://bwtek.com/products/tacticid-1064/ (accessed April 18, 2020).

B&W Tek. TacticID-GP Plus All-Inclusive Handheld Analyzer for Hazmat, Narcotics and More. https://bwtek.com/products/tacticid-gp/ (accessed April 18, 2020).

B&W Tek. TacticID-N Plus Handheld Raman Analyzer for Narcotics Identification. https://bwtek.com/products/tacticid-n/ (accessed April 18, 2020).

Banholzer, M. J.; Millstone, J. E.; Qin, L.; Mirkin, C. A., Rationally designed nanostructures for surface-enhanced Raman spectroscopy. *Chem. Soc. Rev.* **2008,** *37* (5), 885-897.

Bell, S. E. J.; Sirimuthu, N. M. S., Quantitative surface-enhanced Raman spectroscopy. *Chem. Soc. Rev.* **2008,** *37* (5), 1012-1024.

Bell, S. E. J.; Sirimuthu, N. M. S., Surface-Enhanced Raman Spectroscopy (SERS) for Sub-Micromolar Detection of DNA/RNA Mononucleotides. *J. Am. Chem. Soc.* **2006,** *128* (49), 15580-15581.

Berger, A. G.; Restaino, S. M.; White, I. M., Vertical-flow paper SERS system for therapeutic drug monitoring of flucytosine in serum. *Anal. Chim. Acta* **2017,** *949*, 59-66.

Betz, J. F.; Yu, W. W.; Cheng, Y.; White, I. M.; Rubloff, G. W., Simple SERS substrates: powerful, portable, and full of potential. *PCCP* **2014,** *16* (6), 2224-2239.

Bouchard, M.; Smith, D. C., Catalogue of 45 reference Raman spectra of minerals concerning research in art history or archaeology, especially on corroded metals and coloured glass. *Spectrochim. Acta, Part A* **2003,** *59* (10), 2247-2266.

Brolo, A. G.; Irish, D. E.; Smith, B. D., Applications of surface enhanced Raman scattering to the study of metal-adsorbate interactions. *J. Mol. Struct.* **1997,** *405* (1), 29-44.

Bruker. BRAVO Handheld Raman Spectrometer. https://www.bruker.com/products/infrared-near-infrared-and-raman-spectroscopy/raman/bravo.html (accessed April 18, 2020).

Bumbrah, G. S.; Sharma, R. M., Raman spectroscopy – Basic principle, instrumentation and selected applications for the characterization of drugs of abuse. *Egypt. J. Forensic Sci.* **2016,** *6* (3), 209-215.

Cai, J.; Raghavan, V.; Bai, Y. J.; Zhou, M. H.; Liu, X. L.; Liao, C. Y.; Ma, P.; Shi, L.; Dockery, P.; Keogh, I.; Fan, H. M.; Olivo, M., Controllable synthesis of tetrapod gold nanocrystals with precisely tunable near-infrared plasmon resonance towards highly efficient surface enhanced Raman spectroscopy bioimaging. *J. Mater. Chem. B* **2015,** *3* (37), 7377-7385.

CBRNE Tech Index. Chem 500. https://www.cbrnetechindex.com/p/4131/SciAps-Inc/Chem-500 (accessed April 19, 2020).

CFIA Malachite Green - Questions and Answers. Canadian Food Inspection Agency. http://www.inspection.gc.ca/food/information-for-consumers/fact-sheets-and-infographics/products-and-risks/chemical-hazards/malachite-green/eng/1332268890141/1332268947157 (accessed April 2, 2019).

Chamuah, N.; Bhuyan, N.; Das, P. P.; Ojah, N.; Choudhary, A. J.; Medhi, T.; Nath, P., Gold-coated electrospun PVA nanofibers as SERS substrate for detection of pesticides. *Sens. Actuators, B* **2018,** *273*, 710-717.

Chandra, K.; Culver, K. S. B.; Werner, S. E.; Lee, R. C.; Odom, T. W., Manipulating the Anisotropic Structure of Gold Nanostars using Good's Buffers. *Chem. Mater.* **2016,** *28* (18), 6763-6769.

Chen, J.; Huang, M.; Kong, L.; Lin, M., Jellylike flexible nanocellulose SERS substrate for rapid in-situ non-invasive pesticide detection in fruits/vegetables. *Carbohydr. Polym.* **2019,** *205*, 596-600.

Chen, R.; Wu, J.; Li, H.; Cheng, G.; Lu, Z.; Che, C.-M., Fabrication of gold nanoparticles with different morphologies in HEPES buffer. *Rare Met.* **2010,** *29* (2), 180-186.

Chen, R.; Zhang, L.; Li, X.; Ong, L.; Soe, Y. G.; Sinsua, N.; Gras, S. L.; Tabor, R. F.; Wang, X.; Shen, W., Trace Analysis and Chemical Identification on Cellulose Nanofibers-Textured SERS Substrates Using the "Coffee Ring" Effect. *ACS Sens.* **2017,** *2* (7), 1060-1067.

Chen, Y.; Chen, S.; Wang, B.; Yao, J.; Wang, H., TEMPO-oxidized bacterial cellulose nanofibers-supported gold nanoparticles with superior catalytic properties. *Carbohydr. Polym.* **2017,** *160*, 34-42.

Crawford, A. C.; Skuratovsky, A.; Porter, M. D., Sampling Error: Impact on the Quantitative Analysis of Nanoparticle-Based Surface-Enhanced Raman Scattering Immunoassays. *Anal. Chem.* **2016,** *88* (12), 6515-6522.

Crocombe, R. A., Portable Spectroscopy. *Appl. Spectrosc.* **2018,** *72* (12), 1701-1751.

Culp, S. J.; Beland, F. A., Malachite Green: A Toxicological Review. *J. Am. Coll. Toxicol.* **1996,** *15* (3), 219-238.

Cunningham, D.; Littleford, R. E.; Smith, W. E.; Lundahl, P. J.; Khan, I.; McComb, D. W.; Graham, D.; Laforest, N., Practical control of SERRS enhancement. *Faraday Discuss.* **2006,** *132* (0), 135-145.

Dam, D. H. M.; Lee, J. H.; Sisco, P. N.; Co, D. T.; Zhang, M.; Wasielewski, M. R.; Odom, T. W., Direct Observation of Nanoparticle–Cancer Cell Nucleus Interactions. *ACS Nano* **2012,** *6* (4), 3318-3326.

de Puig, H.; Tam, J. O.; Yen, C.-W.; Gehrke, L.; Hamad-Schifferli, K., Extinction Coefficient of Gold Nanostars. *J. Phys. Chem. C* **2015,** *119* (30), 17408-17415.

Deidda, R.; Sacre, P.-Y.; Clavaud, M.; Coïc, L.; Avohou, H.; Hubert, P.; Ziemons, E., Vibrational spectroscopy in analysis of pharmaceuticals: Critical review of innovative portable and handheld NIR and Raman spectrophotometers. *TrAC, Trends Anal. Chem.* **2019,** *114*, 251-259.

Deng, D.; Lin, Q.; Li, H.; Huang, Z.; Kuang, Y.; Chen, H.; Kong, J., Rapid detection of malachite green residues in fish using a surface-enhanced Raman scattering-active glass fiber paper prepared by in situ reduction method. *Talanta* **2019,** *200*, 272-278.

Docherty, J.; Mabbott, S.; Smith, E.; Faulds, K.; Davidson, C.; Reglinski, J.; Graham, D., Detection of potentially toxic metals by SERS using salen complexes. *Analyst* **2016,** *141* (20), 5857-5863.

Ebrahimzadeh, H.; Asgharinezhad, A. A.; Adlnasab, L.; Shekari, N., Optimization of ion-pair based hollow fiber liquid phase microextraction combined with HPLC–UV for the

determination of methimazole in biological samples and animal feed. *J. Sep. Sci.* **2012,** *35* (16), 2040-2047.

Eisa, W. H.; Abdelgawad, A. M.; Rojas, O. J., Solid-State Synthesis of Metal Nanoparticles Supported on Cellulose Nanocrystals and Their Catalytic Activity. *ACS Sustainable Chem. Eng.* **2018,** *6* (3), 3974-3983.

Englebienne, P., Use of colloidal gold surface plasmon resonance peak shift to infer affinity constants from the interactions between protein antigens and antibodies specific for single or multiple epitopes. *Analyst* **1998,** *123* (7), 1599-1603.

Fan, M.; Andrade, G. F. S.; Brolo, A. G., A review on recent advances in the applications of surface-enhanced Raman scattering in analytical chemistry. *Anal. Chim. Acta* **2020,** *1097*, 1-29.

Fan, M.; Andrade, G. F. S.; Brolo, A. G., A review on the fabrication of substrates for surface enhanced Raman spectroscopy and their applications in analytical chemistry. *Anal. Chim. Acta* **2011,** *693* (1), 7-25.

Faulds, K.; Littleford, R. E.; Graham, D.; Dent, G.; Smith, W. E., Comparison of Surface-Enhanced Resonance Raman Scattering from Unaggregated and Aggregated Nanoparticles. *Anal. Chem.* **2004,** *76* (3), 592-598.

Faulds, K.; Smith, W. E.; Graham, D.; Lacey, R. J., Assessment of silver and gold substrates for the detection of amphetamine sulfate by surface enhanced Raman scattering (SERS). *Analyst* **2002,** *127* (2), 282-286.

Fei, J.; Wu, L.; Zhang, Y.; Zong, S.; Wang, Z.; Cui, Y., Pharmacokinetics-on-a-Chip Using Label-Free SERS Technique for Programmable Dual-Drug Analysis. *ACS Sens.* **2017,** *2* (6), 773-780.

Fisher Scientific. Raman Handheld Analyzers. https://www.fishersci.com/us/en/products/I9C8KOH0/raman-handheld-analyzers.html (accessed April 19, 2020).

Fisher Scientific. Thermo Scientific First Defender RMX Handheld Chemical Identification. https://www.fishersci.com/shop/products/thermo-scientific-firstdefender-rmx-handheld-chemical-identification-5/p-4006497 (accessed April 19, 2020).

Fisher Scientific. Thermo Scientific Gemini Analyzer. https://www.fishersci.com/shop/products/gemini-analyzer/18001149 (accessed April 19, 2020).

Fisher Scientific. Thermo Scientific TruNarc. https://www.fishersci.com/shop/products/thermo-scientific-trunarc-4/p-4351112 (accessed April 19, 2020).

Fleischmann, M.; Hendra, P. J.; McQuillan, A. J., Raman spectra of pyridine adsorbed at a silver electrode. *Chem. Phys. Lett.* **1974,** *26* (2), 163-166.

Foster, E. J.; Moon, R. J.; Agarwal, U. P.; Bortner, M. J.; Bras, J.; Camarero-Espinosa, S.; Chan, K. J.; Clift, M. J. D.; Cranston, E. D.; Eichhorn, S. J.; Fox, D. M.; Hamad, W. Y.; Heux, L.; Jean, B.; Korey, M.; Nieh, W.; Ong, K. J.; Reid, M. S.; Renneckar, S.; Roberts, R.; Shatkin, J. A.; Simonsen, J.; Stinson-Bagby, K.; Wanasekara, N.; Youngblood, J., Current characterization methods for cellulose nanomaterials. *Chem. Soc. Rev.* **2018,** *47* (8), 2609-2679.

Gao, S. Y.; Glasser, J.; He, L. L., A Filter-based Surface Enhanced Raman Spectroscopic Assay for Rapid Detection of Chemical Contaminants. *J. Visualized Exp.* **2016,** (108).

Genter, M. B., Evaluation of olfactory and auditory system effects of the antihyperthyroid drug carbimazole in the Long-Evans rat. *J. Biochem. Mol. Toxicol.* **1998,** *12* (5), 305-314.

Gersten, J. I., The effect of surface roughness on surface enhanced Raman scattering. *J. Chem. Phys.* **1980,** *72* (10), 5779-5780.

Gkogkou, D.; Schreiber, B.; Shaykhutdinov, T.; Ly, H. K.; Kuhlmann, U.; Gernert, U.; Facsko, S.; Hildebrandt, P.; Esser, N.; Hinrichs, K.; Weidinger, I. M.; Oates, T. W. H., Polarization- and Wavelength-Dependent Surface-Enhanced Raman Spectroscopy Using Optically Anisotropic Rippled Substrates for Sensing. *ACS Sens.* **2016,** *1* (3), 318-323.

Gkogkou, D.; Shaykhutdinov, T.; Kratz, C.; Oates, T. W. H.; Hildebrandt, P.; Weidinger, I. M.; Ly, K. H.; Esser, N.; Hinrichs, K., Gradient metal nanoislands as a unified surface enhanced Raman scattering and surface enhanced infrared absorption platform for analytics. *Analyst* **2019,** *144* (17), 5271-5276.

Gole, A.; Murphy, C. J., Seed-Mediated Synthesis of Gold Nanorods: Role of the Size and Nature of the Seed. *Chem. Mater.* **2004,** *16* (19), 3633-3640.

Goodacre, R.; Graham, D.; Faulds, K., Recent developments in quantitative SERS: Moving towards absolute quantification. *TrAC, Trends Anal. Chem.* **2018,** *102*, 359-368.

Gopiraman, M.; Deng, D.; Saravanamoorthy, S.; Chung, I.-M.; Kim, I. S., Gold, silver and nickel nanoparticle anchored cellulose nanofiber composites as highly active catalysts for the rapid and selective reduction of nitrophenols in water. *RSC Adv.* **2018,** *8* (6), 3014-3023.

Grady, J. K.; Chasteen, N. D.; Harris, D. C., Radicals from "Good's" buffers. *Anal. Biochem.* **1988,** *173* (1), 111-115.

Graham, D.; Thompson, D. G.; Smith, W. E.; Faulds, K., Control of enhanced Raman scattering using a DNA-based assembly process of dye-coded nanoparticles. *Nat. Nanotechnol.* **2008,** *3* (9), 548-551.

Guerrini, L.; Garcia-Ramos, J. V.; Domingo, C.; Sanchez-Cortes, S., Building Highly Selective Hot Spots in Ag Nanoparticles Using Bifunctional Viologens: Application to the SERS Detection of PAHs. *J. Phys. Chem. C* **2008,** *112* (20), 7527-7530.

Guerrini, L.; Garcia-Ramos, J. V.; Domingo, C.; Sanchez-Cortes, S., Functionalization of Ag Nanoparticles with Dithiocarbamate Calix[4]arene As an Effective Supramolecular Host for the Surface-Enhanced Raman Scattering Detection of Polycyclic Aromatic Hydrocarbons. *Langmuir* **2006,** *22* (26), 10924-10926.

Guerrini, L.; Garcia-Ramos, J. V.; Domingo, C.; Sanchez-Cortes, S., Nanosensors Based on Viologen Functionalized Silver Nanoparticles: Few Molecules Surface-Enhanced Raman Spectroscopy Detection of Polycyclic Aromatic Hydrocarbons in Interparticle Hot Spots. *Anal. Chem.* **2009,** *81* (4), 1418-1425.

Guerrini, L.; Garcia-Ramos, J. V.; Domingo, C.; Sanchez-Cortes, S., Sensing Polycyclic Aromatic Hydrocarbons with Dithiocarbamate-Functionalized Ag Nanoparticles by Surface-Enhanced Raman Scattering. *Anal. Chem.* **2009,** *81* (3), 953-960.

Guerrini, L.; Graham, D., Molecularly-mediated assemblies of plasmonic nanoparticles for Surface-Enhanced Raman Spectroscopy applications. *Chem. Soc. Rev.* **2012,** *41* (21), 7085-7107.

Guo, J.; Filpponen, I.; Su, P.; Laine, J.; Rojas, O. J., Attachment of gold nanoparticles on cellulose nanofibrils via click reactions and electrostatic interactions. *Cellulose* **2016,** *23* (5), 3065-3075.

Habibi, Y.; Lucia, L. A.; Rojas, O. J., Cellulose Nanocrystals: Chemistry, Self-Assembly, and Applications. *Chem. Rev.* **2010,** *110* (6), 3479-3500.

Hakonen, A.; Andersson, P. O.; Stenbæk Schmidt, M.; Rindzevicius, T.; Käll, M., Explosive and chemical threat detection by surface-enhanced Raman scattering: A review. *Anal. Chim. Acta* **2015,** *893*, 1-13.

Hakonen, A.; Wu, K.; Stenbæk Schmidt, M.; Andersson, P. O.; Boisen, A.; Rindzevicius, T., Detecting forensic substances using commercially available SERS substrates and handheld Raman spectrometers. *Talanta* **2018,** *189*, 649-652.

Hao, E.; Schatz, G. C., Electromagnetic fields around silver nanoparticles and dimers. *J. Chem. Phys.* **2004,** *120* (1), 357-366.

Hao, F.; Nehl, C. L.; Hafner, J. H.; Nordlander, P., Plasmon Resonances of a Gold Nanostar. *Nano Lett.* **2007,** *7* (3), 729-732.

Hargreaves, M. D.; Page, K.; Munshi, T.; Tomsett, R.; Lynch, G.; Edwards, H. G. M., Analysis of seized drugs using portable Raman spectroscopy in an airport environment—a proof of principle study. *J. Raman Spectrosc.* **2008,** *39* (7), 873-880.

Hasi, W.-L.-J.; Lin, S.; Lin, X.; Lou, X.-T.; Yang, F.; Lin, D.-Y.; Lu, Z.-W., Rapid fabrication of self-assembled interfacial film decorated filter paper as an excellent surface-enhanced Raman scattering substrate. *Anal. Methods* **2014,** *6* (24), 9547-9553.

Haynes, C. L.; Van Duyne, R. P., Nanosphere Lithography: A Versatile Nanofabrication Tool for Studies of Size-Dependent Nanoparticle Optics. *J. Phys. Chem. B* **2001,** *105* (24), 5599-5611.

He, J.; Kunitake, T.; Nakao, A., Facile In Situ Synthesis of Noble Metal Nanoparticles in Porous Cellulose Fibers. *Chem. Mater.* **2003,** *15* (23), 4401-4406.

Hebert, L. A.; Greene, T.; Levey, A.; Falkenhain, M. E.; Klahr, S., High urine volume and low urine osmolality are risk factors for faster progression of renal disease. *Am. J. Kidney Dis.* **2003,** *41* (5), 962-971.

Hengstmann, J. H.; Hohn, H., Pharmacokinetics of methimazole in humans. *Klin. Wochenschr.* **1985,** *63* (23), 1212-1217.

Hidi, I. J.; Heidler, J.; Weber, K.; Cialla-May, D.; Popp, J., Ciprofloxacin: pH-dependent SERS signal and its detection in spiked river water using LoC-SERS. *Anal. Bioanal. Chem.* **2016,** *408* (29), 8393-8401.

History of the Division: Cellulose, Paper and Textile. ACS: Cellulose and Renewable Materials Division. https://cell.sites.acs.org/history.htm (accessed May 5, 2020).

Holze, R., Competition of anchoring groups in adsorption on gold electrodes—a comparative spectroelectrochemical study of 4-mercaptobenzonitrile and aromatic nitriles. *J. Solid State Electrochem.* **2013,** *17* (7), 1869-1879.

Hoppmann, E. P.; White, I. M., A paper-based inkjet-fabricated substrate for SERS detection and differentiation of PCR products. In *Advanced Environmental, Chemical, and Biological Sensing Technologies X*, VoDinh, T.; Lieberman, R. A.; Gauglitz, G. G., Eds. 2013; Vol. 8718.

Hoppmann, E. P.; Yu, W. W.; White, I. M., Detection of Deoxyribonucleic Acid (DNA) Targets Using Polymerase Chain Reaction (PCR) and Paper Surface-Enhanced Raman Spectroscopy (SERS) Chromatography. *Appl. Spectrosc.* **2014,** *68* (8), 909-915.

Hoppmann, E. P.; Yu, W. W.; White, I. M., Highly sensitive and flexible inkjet printed SERS sensors on paper. *Methods* **2013,** *63* (3), 219-224.

Hoppmann, E. P.; Yu, W. W.; White, I. M., Inkjet-Printed Fluidic Paper Devices for Chemical and Biological Analytics Using Surface Enhanced Raman spectroscopy. *IEEE J. Sel. Top. Quantum Electron.* **2014,** *20* (3).

Huang, X.; Neretina, S.; El-Sayed, M. A., Gold Nanorods: From Synthesis and Properties to Biological and Biomedical Applications. *Adv. Mater.* **2009,** *21* (48), 4880-4910.

Hulteen, J. C.; Duyne, R. P. V., Nanosphere lithography: A materials general fabrication process for periodic particle array surfaces. *J. Vac. Sci. Technol., A* **1995**, *13* (3), 1553-1558.

Ifuku, S.; Tsuji, M.; Morimoto, M.; Saimoto, H.; Yano, H., Synthesis of Silver Nanoparticles Templated by TEMPO-Mediated Oxidized Bacterial Cellulose Nanofibers. *Biomacromolecules* **2009,** *10* (9), 2714-2717.

III, N. C.; Chidsey, C. E. D.; Liu, G. y.; Scoles, G., Substrate dependence of the surface structure and chain packing of docosyl mercaptan self-assembled on the (111), (110), and (100) faces of single crystal gold. *J. Chem. Phys.* **1993,** *98* (5), 4234-4245.

Indrasekara, A. S. D. S.; Meyers, S.; Shubeita, S.; Feldman, L. C.; Gustafsson, T.; Fabris, L., Gold nanostar substrates for SERS-based chemical sensing in the femtomolar regime. *Nanoscale* **2014,** *6* (15), 8891-8899.

Islam, M. S.; Chen, L.; Sisler, J.; Tam, K. C., Cellulose nanocrystal (CNC)-inorganic hybrid systems: synthesis, properties and applications. *J. Mater. Chem. B* **2018,** *6* (6), 864-883.

Isogai, A.; Saito, T.; Fukuzumi, H., TEMPO-oxidized cellulose nanofibers. *Nanoscale* **2011,** *3* (1), 71-85.

Jalani, G.; Cerruti, M., Nano graphene oxide-wrapped gold nanostars as ultrasensitive and stable SERS nanoprobes. *Nanoscale* **2015,** *7* (22), 9990-9997.

Jamieson, J. D.; Smith, E. B.; Dalvie, D. K.; Stevens, G. J.; Yanochko, G. M., Myeloperoxidase-mediated bioactivation of 5-hydroxythiabendazole: A possible mechanism of thiabendazole toxicity. *Toxicol. In Vitro* **2011,** *25* (5), 1061-1066.

Jana, N. R.; Gearheart, L.; Murphy, C. J., Evidence for Seed-Mediated Nucleation in the Chemical Reduction of Gold Salts to Gold Nanoparticles. *Chem. Mater.* **2001,** *13* (7), 2313-2322.

Jansson, R.; Lindström, B.; Dahlberg, P. A., Pharmacokinetic Properties and Bioavailability of Methimazole. *Clin. Pharmacokinet.* **1985,** *10* (5), 443-450.

Jeanmaire, D. L.; Van Duyne, R. P., Surface raman spectroelectrochemistry: Part I. Heterocyclic, aromatic, and aliphatic amines adsorbed on the anodized silver electrode. *J. Electroanal. Chem. Interfacial Electrochem.* **1977,** *84* (1), 1-20.

Jiang, F.; Hsieh, Y.-L., Super water absorbing and shape memory nanocellulose aerogels from TEMPO-oxidized cellulose nanofibrils via cyclic freezing-thawing. *J. Mater. Chem. A* **2014,** *2* (2), 350-359.

Jiang, F.; Hsieh, Y.-L., Synthesis of Cellulose Nanofibril Bound Silver Nanoprism for Surface Enhanced Raman Scattering. *Biomacromolecules* **2014,** *15* (10), 3608-3616.

Jin, Y.; Ma, P.; Liang, F.; Gao, D.; Wang, X., Determination of malachite green in environmental water using cloud point extraction coupled with surface-enhanced Raman scattering. *Anal. Methods* **2013,** *5* (20), 5609-5614.

Johnston, J. H.; Nilsson, T., Nanogold and nanosilver composites with lignin-containing cellulose fibres. *J. Mater. Sci.* **2012,** *47* (3), 1103-1112.

Joke, D. G.; Kris, D. G.; Peter, V.; Luc, M., Reference database of Raman spectra of biological molecules. *J. Raman Spectrosc.* **2007,** *38* (9), 1133-1147.

Kafy, A.; Kim, H. C.; Zhai, L.; Kim, J. W.; Hai, L. V.; Kang, T. J.; kim, J., Cellulose long fibers fabricated from cellulose nanofibers and its strong and tough characteristics. *Sci. Rep.* **2017,** *7* (1), 17683.

Kambhampati, P.; Child, C. M.; Foster, M. C.; Campion, A., On the chemical mechanism of surface enhanced Raman scattering: Experiment and theory. *J. Chem. Phys.* **1998,** *108* (12), 5013-5026.

Kim, D.; Ko, Y.; Kwon, G.; Choo, Y.-M.; You, J., Low-cost, high-performance plasmonic nanocomposites for hazardous chemical detection using surface enhanced Raman scattering. *Sens. Actuators, B* **2018,** *274*, 30-36.

Kim, D.; Ko, Y.; Kwon, G.; Kim, U.-J.; Lee, J. H.; You, J., 2,2,6,6-Tetramethylpiperidine-1-oxy-Oxidized Cellulose Nanofiber-Based Nanocomposite Papers for Facile In Situ Surface-Enhanced Raman Scattering Detection. *ACS Sustainable Chem. Eng.* **2019,** *7* (18), 15640-15647.

Kim, M. S.; Kim, M. K.; Lee, C. J.; Jung, Y. M.; Lee, M.-S., Surface-enhanced Raman Spectroscopy of Benzimidazolic Fungicides: Benzimidazole and Thiabendazole. *Bull. Korean Chem. Soc.* **2009,** *30* (12), 2930-2934.

Kim, W.; Lee, J.-C.; Shin, J.-H.; Jin, K.-H.; Park, H.-K.; Choi, S., Instrument-Free Synthesizable Fabrication of Label-Free Optical Biosensing Paper Strips for the Early Detection of Infectious Keratoconjunctivitides. *Anal. Chem.* **2016,** *88* (10), 5531-5537.

Kimling, J.; Maier, M.; Okenve, B.; Kotaidis, V.; Ballot, H.; Plech, A., Turkevich Method for Gold Nanoparticle Synthesis Revisited. *J. Phys. Chem. B* **2006,** *110* (32), 15700-15707.

Kneipp, K.; Kneipp, H.; Manoharan, R.; Hanlon, E. B.; Itzkan, I.; Dasari, R. R.; Feld, M. S., Extremely Large Enhancement Factors in Surface-Enhanced Raman Scattering for Molecules on Colloidal Gold Clusters. *Appl. Spectrosc.* **1998,** *52* (12), 1493-1497.

Kneipp, K.; Wang, Y.; Kneipp, H.; Perelman, L. T.; Itzkan, I.; Dasari, R. R.; Feld, M. S., Single Molecule Detection Using Surface-Enhanced Raman Scattering (SERS). *Phys. Rev. Lett.* **1997,** *78* (9), 1667-1670.

Koga, H.; Tokunaga, E.; Hidaka, M.; Umemura, Y.; Saito, T.; Isogai, A.; Kitaoka, T., Topochemical synthesis and catalysis of metal nanoparticles exposed on crystalline cellulose nanofibers. *Chem. Commun.* **2010,** *46* (45), 8567-8569.

Kong, D.; Chi, Y.; Chen, L.; Dong, Y.; Zhang, L.; Chen, G., Determination of thyreostatics in animal feeds by CE with electrochemical detector. *Electrophoresis* **2009,** *30* (19), 3489-3495.

Kou, X.; Ni, W.; Tsung, C. K.; Chan, K.; Lin, H. Q.; Stucky, G. D.; Wang, J., Growth of Gold Bipyramids with Improved Yield and Their Curvature-Directed Oxidation. *Small* **2007,** *3* (12), 2103-2113.

Krishnan, R. S.; Shankar, R. K., Raman effect: History of the discovery. *J. Raman Spectrosc.* **1981,** *10* (1), 1-8.

Kuśmierek, K.; Bald, E., Determination of methimazole in urine by liquid chromatography. *Talanta* **2007,** *71* (5), 2121-2125.

Langer, J.; Jimenez de Aberasturi, D.; Aizpurua, J.; Alvarez-Puebla, R. A.; Auguié, B.; Baumberg, J. J.; Bazan, G. C.; Bell, S. E. J.; Boisen, A.; Brolo, A. G.; Choo, J.; Cialla-May, D.; Deckert, V.; Fabris, L.; Faulds, K.; García de Abajo, F. J.; Goodacre, R.; Graham, D.; Haes, A. J.; Haynes, C. L.; Huck, C.; Itoh, T.; Käll, M.; Kneipp, J.; Kotov, N. A.; Kuang, H.; Le Ru, E. C.; Lee, H. K.; Li, J.-F.; Ling, X. Y.; Maier, S. A.; Mayerhöfer, T.; Moskovits, M.; Murakoshi, K.; Nam, J.-M.; Nie, S.; Ozaki, Y.; Pastoriza-Santos, I.; Perez-Juste, J.; Popp, J.; Pucci, A.; Reich, S.; Ren, B.; Schatz, G. C.; Shegai, T.; Schlücker, S.; Tay, L.-L.; Thomas, K. G.; Tian, Z.-Q.; Van Duyne, R. P.; Vo-Dinh, T.; Wang, Y.; Willets, K. A.; Xu, C.; Xu, H.; Xu, Y.; Yamamoto, Y. S.; Zhao, B.; Liz-Marzán, L. M., Present and Future of Surface-Enhanced Raman Scattering. *ACS Nano* **2020,** *14* (1), 28-117.

Lanzarotta, A.; Lorenz, L.; Batson, J. S.; Flurer, C., Development and implementation of a pass/fail field-friendly method for detecting sildenafil in suspect pharmaceutical tablets using a handheld Raman spectrometer and silver colloids. *J. Pharm. Biomed. Anal.* **2017,** *146*, 420-425.

Larmour, I. A.; Faulds, K.; Graham, D., Improved Versatility of Silver Nanoparticle Dimers for Surface-Enhanced Raman Spectroscopy. *J. Phys. Chem. C* **2010,** *114* (31), 13249-13254.

Lavoine, N.; Desloges, I.; Dufresne, A.; Bras, J., Microfibrillated cellulose – Its barrier properties and applications in cellulosic materials: A review. *Carbohydr. Polym.* **2012,** *90* (2), 735-764.

Le Ru, E. C.; Blackie, E.; Meyer, M.; Etchegoin, P. G., Surface Enhanced Raman Scattering Enhancement Factors: A Comprehensive Study. *J. Phys. Chem. C* **2007,** *111* (37), 13794-13803.

Lee, C. H.; Hankus, M. E.; Tian, L.; Pellegrino, P. M.; Singamaneni, S., Highly Sensitive Surface Enhanced Raman Scattering Substrates Based on Filter Paper Loaded with Plasmonic Nanostructures. *Anal. Chem.* **2011,** *83* (23), 8953-8958.

Lee, P. C.; Meisel, D., Adsorption and surface-enhanced Raman of dyes on silver and gold sols. *J. Phys. Chem.* **1982,** *86* (17), 3391-3395.

Lee, S.; Choi, J.; Chen, L.; Park, B.; Kyong, J. B.; Seong, G. H.; Choo, J.; Lee, Y.; Shin, K.-H.; Lee, E. K.; Joo, S.-W.; Lee, K.-H., Fast and sensitive trace analysis of malachite green using a surface-enhanced Raman microfluidic sensor. *Anal. Chim. Acta* **2007,** *590* (2), 139-144.

Lee, S. J.; Morrill, A. R.; Moskovits, M., Hot Spots in Silver Nanowire Bundles for Surface-Enhanced Raman Spectroscopy. *J. Am. Chem. Soc.* **2006,** *128* (7), 2200-2201.

Li, J.-M.; Ma, W.-F.; Wei, C.; You, L.-J.; Guo, J.; Hu, J.; Wang, C.-C., Detecting Trace Melamine in Solution by SERS Using Ag Nanoparticle Coated Poly(styrene-co-acrylic acid) Nanospheres as Novel Active Substrates. *Langmuir* **2011,** *27* (23), 14539-14544.

Li, Y.-S.; Church, J. S., Raman spectroscopy in the analysis of food and pharmaceutical nanomaterials. *J. Food Drug Anal.* **2014,** *22* (1), 29-48.

Li, Y.; Zhang, K.; Zhao, J.; Ji, J.; Ji, C.; Liu, B., A three-dimensional silver nanoparticles decorated plasmonic paper strip for SERS detection of low-abundance molecules. *Talanta* **2016,** *147*, 493-500.

Liang, D.; Bowers, J. E., Recent progress in lasers on silicon. *Nat. Photonics* **2010,** *4* (8), 511-517.

Liao, W.-J.; Roy, P. K.; Chattopadhyay, S., An ink-jet printed, surface enhanced Raman scattering paper for food screening. *RSC Adv.* **2014,** *4* (76), 40487-40493.

Lin, X.-M.; Cui, Y.; Xu, Y.-H.; Ren, B.; Tian, Z.-Q., Surface-enhanced Raman spectroscopy: substrate-related issues. *Anal. Bioanal. Chem.* **2009,** *394* (7), 1729-1745.

Liou, P.; Nayigiziki, F. X.; Kong, F.; Mustapha, A.; Lin, M., Cellulose nanofibers coated with silver nanoparticles as a SERS platform for detection of pesticides in apples. *Carbohydr. Polym.* **2017,** *157*, 643-650.

Liu, H.; Xu, Y.; Qin, Y.; Sanderson, W.; Crowley, D.; Turner, C. H.; Bao, Y., Ligand-Directed Formation of Gold Tetrapod Nanostructures. *J. Phys. Chem. C* **2013,** *117* (33), 17143-17150.

Liu, P.; Oksman, K.; Mathew, A. P., Surface adsorption and self-assembly of Cu(II) ions on TEMPO-oxidized cellulose nanofibers in aqueous media. *J. Colloid Interface Sci.* **2016,** *464*, 175-182.

Liu, R.; Tang, J.; Yang, H.; Jin, W.; Liu, M.; Liu, S.; Hu, J., In situ decoration of plasmonic silver nanoparticles on poly(vinylidene fluoride) membrane for versatile SERS detection. *New J. Chem.* **2019,** *43* (18), 6965-6972.

Lokanathan, A. R.; Uddin, K. M. A.; Rojas, O. J.; Laine, J., Cellulose Nanocrystal-Mediated Synthesis of Silver Nanoparticles: Role of Sulfate Groups in Nucleation Phenomena. *Biomacromolecules* **2014,** *15* (1), 373-379.

Lombardi, J. R.; Birke, R. L., A Unified Approach to Surface-Enhanced Raman Spectroscopy. *J. Phys. Chem. C* **2008,** *112* (14), 5605-5617.

Lu, G.; Forbes, T. Z.; Haes, A. J., SERS detection of uranyl using functionalized gold nanostars promoted by nanoparticle shape and size. *Analyst* **2016,** *141* (17), 5137-5143.

Lu, G.; Johns, A. J.; Neupane, B.; Phan, H. T.; Cwiertny, D. M.; Forbes, T. Z.; Haes, A. J., Matrix-Independent Surface-Enhanced Raman Scattering Detection of Uranyl Using Electrospun

Amidoximated Polyacrylonitrile Mats and Gold Nanostars. *Anal. Chem.* **2018,** *90* (11), 6766-6772.

Ma, P.; Liang, F.; Yang, Q.; Wang, D.; Sun, Y.; Wang, X.; Gao, D.; Song, D., Highly sensitive SERS probe for mercury(II) using cyclodextrin-protected silver nanoparticles functionalized with methimazole. *Microchim. Acta* **2014,** *181* (9), 975-981.

Mahmoud, A. Y. F.; Rusin, C. J.; McDermott, M. T., Gold nanostars as a colloidal substrate for in-solution SERS measurements using a handheld Raman spectrometer. *Analyst* **2020,** *145* (4), 1396-1407.

Malassis, L.; Dreyfus, R.; Murphy, R. J.; Hough, L. A.; Donnio, B.; Murray, C. B., One-step green synthesis of gold and silver nanoparticles with ascorbic acid and their versatile surface post-functionalization. *RSC Adv.* **2016,** *6* (39), 33092-33100.

Mayer, K. M.; Hafner, J. H., Localized Surface Plasmon Resonance Sensors. *Chem. Rev.* **2011,** *111* (6), 3828-3857.

McCreery, R. L., Raman spectroscopy for chemical analysis. John Wiley & Sons: New York :, 2000.

McFarland, A. D.; Young, M. A.; Dieringer, J. A.; Van Duyne, R. P., Wavelength-Scanned Surface-Enhanced Raman Excitation Spectroscopy. *J. Phys. Chem. B* **2005,** *109* (22), 11279-11285.

Menges, F. Spectragryph - optical spectroscopy software. http://www.effemm2.de/spectragryph/ (accessed April 23, 2020).

Metrohm. Mira DS Basic. https://www.metrohm.com/en/products-overview/spectroscopy/mira%20handheld%20raman%20spectrometer/29260010?fromProductFinder=true (accessed April 19, 2020).

Metrohm. Mira DS: Identify hazardous and illicit substances quickly and safely. https://www.metrohm.com/en/products/spectroscopy/mira-handheld-raman-spectrometers/mira-ds-landing-page/ (accessed April 19, 2020).

Metrohm. Mira P Basic. https://www.metrohm.com/en/products-overview/spectroscopy/mira%20handheld%20raman%20spectrometer/29270010?fromProductFinder=true (accessed April 19, 2020).

Meyer, M.; Le Ru, E. C.; Etchegoin, P. G., Self-Limiting Aggregation Leads to Long-Lived Metastable Clusters in Colloidal Solutions. *J. Phys. Chem. B* **2006,** *110* (12), 6040-6047.

Miao, X.; Lin, J.; Tian, F.; Li, X.; Bian, F.; Wang, J., Cellulose nanofibrils extracted from the byproduct of cotton plant. *Carbohydr. Polym.* **2016,** *136*, 841-850.

Moon, R. J.; Martini, A.; Nairn, J.; Simonsen, J.; Youngblood, J., Cellulose nanomaterials review: structure, properties and nanocomposites. *Chem. Soc. Rev.* **2011,** *40* (7), 3941-3994.

Moore, D. S., Instrumentation for trace detection of high explosives. *Rev. Sci. Instrum.* **2004,** *75* (8), 2499-2512.

Moreira, L. P.; Silveira, L.; Pacheco, M. T. T.; da Silva, A. G.; Rocco, D. D. F. M., Detecting urine metabolites related to training performance in swimming athletes by means of Raman spectroscopy and principal component analysis. *J. Photochem. Photobiol., B* **2018,** *185*, 223-234.

Morton, S. M.; Ewusi-Annan, E.; Jensen, L., Controlling the non-resonant chemical mechanism of SERS using a molecular photoswitch. *PCCP* **2009,** *11* (34), 7424-7429.

Mosier-Boss, P. A., Review of SERS Substrates for Chemical Sensing. *Nanomaterials* **2017,** *7* (6), 142.

Moskovits, M., Surface-enhanced Raman spectroscopy: a brief retrospective. *J. Raman Spectrosc.* **2005,** *36* (6-7), 485-496.

Moskovits, M., Surface-enhanced spectroscopy. *Rev. Mod. Phys.* **1985,** *57* (3), 783-826.

Moskovits, M., Surface roughness and the enhanced intensity of Raman scattering by molecules adsorbed on metals. *J. Chem. Phys.* **1978,** *69* (9), 4159-4161.

Muniz-Miranda, M.; Muniz-Miranda, F.; Pedone, A., Raman and DFT study of methimazole chemisorbed on gold colloidal nanoparticles. *PCCP* **2016,** *18* (8), 5974-5980.

Murphy, C. J.; Gole, A. M.; Hunyadi, S. E.; Stone, J. W.; Sisco, P. N.; Alkilany, A.; Kinard, B. E.; Hankins, P., Chemical sensing and imaging with metallic nanorods. *Chem. Commun.* **2008,** (5), 544-557.

Murphy, C. J.; Gole, A. M.; Stone, J. W.; Sisco, P. N.; Alkilany, A. M.; Goldsmith, E. C.; Baxter, S. C., Gold Nanoparticles in Biology: Beyond Toxicity to Cellular Imaging. *Acc. Chem. Res.* **2008,** *41* (12), 1721-1730.

Nabeela, K.; Thomas, R. T.; Nair, J. B.; Maiti, K. K.; Warrier, K. G. K.; Pillai, S., TEMPO-Oxidized Nanocellulose Fiber-Directed Stable Aqueous Suspension of Plasmonic Flower-like Silver Nanoconstructs for Ultra-Trace Detection of Analytes. *ACS Appl. Mater. Interfaces* **2016,** *8* (43), 29242-29251.

Nalbant Esenturk, E.; Hight Walker, A. R., Surface-enhanced Raman scattering spectroscopy via gold nanostars. *J. Raman Spectrosc.* **2009,** *40* (1), 86-91.

Natan, M. J., Concluding Remarks Surface enhanced Raman scattering. *Faraday Discuss.* **2006,** *132* (0), 321-328.

Nehl, C. L.; Hafner, J. H., Shape-dependent plasmon resonances of gold nanoparticles. *J. Mater. Chem.* **2008,** *18* (21), 2415-2419.

Nergiz, S. Z.; Gandra, N.; Singamaneni, S., Self-assembled high aspect ratio gold nanostar/graphene oxide hybrid nanorolls. *Carbon* **2014,** *66*, 585-591.

Neugebauer, U.; Szeghalmi, A.; Schmitt, M.; Kiefer, W.; Popp, J.; Holzgrabe, U., Vibrational spectroscopic characterization of fluoroquinolones. *Spectrochim. Acta, Part A* **2005,** *61* (7), 1505-1517.

Nie, S.; Emory, S. R., Probing Single Molecules and Single Nanoparticles by Surface-Enhanced Raman Scattering. *Science* **1997,** *275* (5303), 1102-1106.

Nikoobakht, B.; El-Sayed, M. A., Preparation and Growth Mechanism of Gold Nanorods (NRs) Using Seed-Mediated Growth Method. *Chem. Mater.* **2003,** *15* (10), 1957-1962.

Njoki, P. N.; Lim, I. I. S.; Mott, D.; Park, H.-Y.; Khan, B.; Mishra, S.; Sujakumar, R.; Luo, J.; Zhong, C.-J., Size Correlation of Optical and Spectroscopic Properties for Gold Nanoparticles. *J. Phys. Chem. C* **2007,** *111* (40), 14664-14669.

O'Sullivan, A. C., Cellulose: the structure slowly unravels. *Cellulose* **1997,** *4* (3), 173-207.

Ogundare, S. A.; van Zyl, W. E., Amplification of SERS "hot spots" by silica clustering in a silver-nanoparticle/nanocrystalline-cellulose sensor applied in malachite green detection. *Colloids Surf., A* **2019,** *570*, 156-164.

Ogundare, S. A.; van Zyl, W. E., Nanocrystalline cellulose as reducing- and stabilizing agent in the synthesis of silver nanoparticles: Application as a surface-enhanced Raman scattering (SERS) substrate. *Surf. Interfaces* **2018,** *13*, 1-10.

Ogundare, S. A.; van Zyl, W. E., A review of cellulose-based substrates for SERS: fundamentals, design principles, applications. *Cellulose* **2019,** *26* (11), 6489-6528.

Okamura, Y.; Shigemasa, C.; Tatsuhara, T., Pharmacokinetics of Methimazole in Normal Subjects and Hyperthyroid Patients. *Endocrinol. Jpn.* **1986,** *33* (5), 605-615.

Omrani, A. A.; Taghavinia, N., Photo-induced growth of silver nanoparticles using UV sensitivity of cellulose fibers. *Appl. Surf. Sci.* **2012,** *258* (7), 2373-2377.

Orelma, H.; Teerinen, T.; Johansson, L.-S.; Holappa, S.; Laine, J., CMC-Modified Cellulose Biointerface for Antibody Conjugation. *Biomacromolecules* **2012,** *13* (4), 1051-1058.

Osinkina, L.; Lohmüller, T.; Jäckel, F.; Feldmann, J., Synthesis of Gold Nanostar Arrays as Reliable, Large-Scale, Homogeneous Substrates for Surface-Enhanced Raman Scattering Imaging and Spectroscopy. *J. Phys. Chem. C* **2013,** *117* (43), 22198-22202.

Padalkar, S.; Capadona, J. R.; Rowan, S. J.; Weder, C.; Won, Y.-H.; Stanciu, L. A.; Moon, R. J., Natural Biopolymers: Novel Templates for the Synthesis of Nanostructures. *Langmuir* **2010,** *26* (11), 8497-8502.

Pallares, R. M.; Stilson, T.; Choo, P.; Hu, J.; Odom, T. W., Using Good's Buffers To Control the Anisotropic Structure and Optical Properties of Spiky Gold Nanoparticles for Refractive Index Sensing. *ACS Appl. Nano Mater.* **2019,** *2* (8), 5266-5271.

Panneerselvam, R.; Liu, G.-K.; Wang, Y.-H.; Liu, J.-Y.; Ding, S.-Y.; Li, J.-F.; Wu, D.-Y.; Tian, Z.-Q., Surface-enhanced Raman spectroscopy: bottlenecks and future directions. *Chem. Commun.* **2018,** *54* (1), 10-25.

Park, M.; Hwang, C. S. H.; Jeong, K.-H., Nanoplasmonic Alloy of Au/Ag Nanocomposites on Paper Substrate for Biosensing Applications. *ACS Appl. Mater. Interfaces* **2018,** *10* (1), 290-295.

Pawcenis, D.; Chlebda, D. K.; Jędrzejczyk, R. J.; Leśniak, M.; Sitarz, M.; Łojewska, J., Preparation of silver nanoparticles using different fractions of TEMPO-oxidized nanocellulose. *Eur. Polym. J.* **2019,** *116*, 242-255.

Pazzirota, T.; Martin, L.; Mezcua, M.; Ferrer, C.; Fernandez-Alba, A. R., Processing factor for a selected group of pesticides in a wine-making process: distribution of pesticides during grape processing. *Food Addit. Contam. A* **2013,** *30* (10), 1752-1760.

Pelaz, B.; Grazu, V.; Ibarra, A.; Magen, C.; del Pino, P.; de la Fuente, J. M., Tailoring the Synthesis and Heating Ability of Gold Nanoprisms for Bioapplications. *Langmuir* **2012,** *28* (24), 8965-8970.

Pilot, R., SERS detection of food contaminants by means of portable Raman instruments. *J. Raman Spectrosc.* **2018,** *49* (6), 954-981.

Pilot, R.; Signorini, R.; Durante, C.; Orian, L.; Bhamidipati, M.; Fabris, L., A Review on Surface-Enhanced Raman Scattering. *Biosensors* **2019,** *9* (2), 57.

Pittman, J. A.; Beschi, R. J.; Smitherman, T. C., Methimazole: Its Absorption and Excretion in Man and Tissue Distribution in Rats. *J. Clin. Endocrinol. Metab.* **1971,** *33* (2), 182-185.

Pope, C. G., X-Ray Diffraction and the Bragg Equation. *J. Chem. Educ.* **1997,** *74* (1), 129.

Porter, M. D.; Bright, T. B.; Allara, D. L.; Chidsey, C. E. D., Spontaneously organized molecular assemblies. 4. Structural characterization of n-alkyl thiol monolayers on gold by optical ellipsometry, infrared spectroscopy, and electrochemistry. *J. Am. Chem. Soc.* **1987,** *109* (12), 3559-3568.

Prikhozhdenko, E. S.; Bratashov, D. N.; Gorin, D. A.; Yashchenok, A. M., Flexible surface-enhanced Raman scattering-active substrates based on nanofibrous membranes. *Nano Research* **2018,** *11* (9), 4468-4488.

Qin, Y.; Ji, X.; Jing, J.; Liu, H.; Wu, H.; Yang, W., Size control over spherical silver nanoparticles by ascorbic acid reduction. *Colloids Surf., A* **2010,** *372* (1), 172-176.

Raman, C. V.; Krishnan, K. S., A New Type of Secondary Radiation. *Nature* **1928,** *121* (3048), 501-502.

Ranjbari, E.; Hadjmohammadi, M. R., Optimization of magnetic stirring assisted dispersive liquid–liquid microextraction of rhodamine B and rhodamine 6G by response surface methodology: Application in water samples, soft drink, and cosmetic products. *Talanta* **2015,** *139*, 216-225.

Restaino, S. M.; White, I. M., A critical review of flexible and porous SERS sensors for analytical chemistry at the point-of-sample. *Anal. Chim. Acta* **2019,** *1060*, 17-29.

Rigaku. Progeny. https://www.rigaku.com/products/raman/progeny (accessed April 19, 2020).

Rigaku. Progeny ResQ. https://www.rigaku.com/products/raman/resq (accessed April 19, 2020).

Rigaku. Progeny ResQ FLX. https://www.rigaku.com/products/raman/flx (accessed April 19, 2020).

Rigaku. ResQ CQL. https://www.rigaku.com/products/raman/cql (accessed April 19, 2020).

Rodríguez-Lorenzo, L.; Álvarez-Puebla, R. A.; Pastoriza-Santos, I.; Mazzucco, S.; Stéphan, O.; Kociak, M.; Liz-Marzán, L. M.; García de Abajo, F. J., Zeptomol Detection Through Controlled Ultrasensitive Surface-Enhanced Raman Scattering. *J. Am. Chem. Soc.* **2009,** *131* (13), 4616-4618.

Rusin, C. J.; El Bakkari, M.; Du, R.; Boluk, Y.; McDermott, M. T., Plasmonic Cellulose Nanofibers as Water-Dispersible Surface-Enhanced Raman Scattering Substrates. *ACS Appl. Nano Mater.* **2020**, *3* (7), 6584-6597.

Rycenga, M.; Langille, M. R.; Personick, M. L.; Ozel, T.; Mirkin, C. A., Chemically Isolating Hot Spots on Concave Nanocubes. *Nano Lett.* **2012,** *12* (12), 6218-6222.

Sacui, I. A.; Nieuwendaal, R. C.; Burnett, D. J.; Stranick, S. J.; Jorfi, M.; Weder, C.; Foster, E. J.; Olsson, R. T.; Gilman, J. W., Comparison of the Properties of Cellulose Nanocrystals and Cellulose Nanofibrils Isolated from Bacteria, Tunicate, and Wood Processed Using Acid, Enzymatic, Mechanical, and Oxidative Methods. *ACS Appl. Mater. Interfaces* **2014,** *6* (9), 6127-6138.

Sahoo, G. P.; Bhui, D. K.; Bar, H.; Sarkar, P.; Samanta, S.; Pyne, S.; Misra, A., Synthesis and characterization of gold nanoparticles adsorbed in methyl cellulose micro fibrils. *J. Mol. Liq.* **2010,** *155* (2), 91-95.

Saito, T.; Isogai, A., Ion-exchange behavior of carboxylate groups in fibrous cellulose oxidized by the TEMPO-mediated system. *Carbohydr. Polym.* **2005,** *61* (2), 183-190.

Saito, T.; Isogai, A., TEMPO-Mediated Oxidation of Native Cellulose. The Effect of Oxidation Conditions on Chemical and Crystal Structures of the Water-Insoluble Fractions. *Biomacromolecules* **2004,** *5* (5), 1983-1989.

Saito, T.; Kimura, S.; Nishiyama, Y.; Isogai, A., Cellulose Nanofibers Prepared by TEMPO-Mediated Oxidation of Native Cellulose. *Biomacromolecules* **2007,** *8* (8), 2485-2491.

Saleh, T. A.; Al-Shalalfeh, M. M.; Al-Saadi, A. A., Graphene Dendrimer-stabilized silver nanoparticles for detection of methimazole using Surface-enhanced Raman scattering with computational assignment. *Sci. Rep.* **2016,** *6*, 32185.

Saleh, T. A.; Al-Shalalfeh, M. M.; Al-Saadi, A. A., Silver nanoparticles for detection of methimazole by surface-enhanced Raman spectroscopy. *Mater. Res. Bull.* **2017,** *91*, 173-178.

Saleh, T. A.; Al-Shalalfeh, M. M.; Onawole, A. T.; Al-Saadi, A. A., Ultra-trace detection of methimazole by surface-enhanced Raman spectroscopy using gold substrate. *Vib. Spectrosc* **2017,** *90*, 96-103.

Sánchez-Purrà, M.; Carré-Camps, M.; de Puig, H.; Bosch, I.; Gehrke, L.; Hamad-Schifferli, K., Surface-Enhanced Raman Spectroscopy-Based Sandwich Immunoassays for Multiplexed Detection of Zika and Dengue Viral Biomarkers. *ACS Infect. Dis.* **2017,** *3* (10), 767-776.

Sánchez-Purrà, M.; Roig-Solvas, B.; Rodriguez-Quijada, C.; Leonardo, B. M.; Hamad-Schifferli, K., Reporter Selection for Nanotags in Multiplexed Surface Enhanced Raman Spectroscopy Assays. *ACS Omega* **2018,** *3* (9), 10733-10742.

Sarfo, D. K.; Sivanesan, A.; Izake, Emad L.; Ayoko, G. A., Rapid detection of mercury contamination in water by surface enhanced Raman spectroscopy. *RSC Adv.* **2017,** *7* (35), 21567-21575.

Satou, T.; Koga, M.; Koike, K.; Tada, I.; Nikaido, T., Nematocidal activities of thiabendazole and ivermectin against the larvae of Strongyloides ratti and S. venezuelensis. *Vet. Parasitol.* **2001,** *99* (4), 311-322.

Sau, T. K.; Murphy, C. J., Room Temperature, High-Yield Synthesis of Multiple Shapes of Gold Nanoparticles in Aqueous Solution. *J. Am. Chem. Soc.* **2004,** *126* (28), 8648-8649.

Saute, B.; Narayanan, R., Solution-based direct readout surface enhanced Raman spectroscopic (SERS) detection of ultra-low levels of thiram with dogbone shaped gold nanoparticles. *Analyst* **2011,** *136* (3), 527-532.

Saute, B.; Narayanan, R., Solution-based SERS method to detect dithiocarbamate fungicides in different real-world matrices. *J. Raman Spectrosc.* **2013,** *44* (11), 1518-1522.

Saute, B.; Premasiri, R.; Ziegler, L.; Narayanan, R., Gold nanorods as surface enhanced Raman spectroscopy substrates for sensitive and selective detection of ultra-low levels of dithiocarbamate pesticides. *Analyst* **2012,** *137* (21), 5082-5087.

Schlücker, S., Surface-Enhanced Raman Spectroscopy: Concepts and Chemical Applications. *Angew. Chem. Int. Ed.* **2014,** *53* (19), 4756-4795.

Schmucker, A. L.; Tadepalli, S.; Liu, K.-K.; Sullivan, C. J.; Singamaneni, S.; Naik, R. R., Plasmonic paper: a porous and flexible substrate enabling nanoparticle-based combinatorial chemistry. *RSC Adv.* **2016,** *6* (5), 4136-4144.

SciAps. CHEM-200 Raman Analyzer. https://www.sciaps.com/raman-spectrometers/chem-200/ (accessed April 19, 2020).

SciAps. Inspector 300. https://www.sciaps.com/raman-spectrometers/legacy-products/inspector-300 (accessed April 19, 2020).

SciAps. Inspector 500. https://www.sciaps.com/raman-spectrometers/inspector-500/ (accessed April 19, 2020).

SciAps. ObserveR. https://www.sciaps.com/raman-spectrometers/legacy-products/ (accessed April 19, 2020).

SciAps. ReporteR. https://www.sciaps.com/raman-spectrometers/legacy-products/ (accessed April 19, 2020).

Seney, C. S.; Gutzman, B. M.; Goddard, R. H., Correlation of Size and Surface-Enhanced Raman Scattering Activity of Optical and Spectroscopic Properties for Silver Nanoparticles. *J. Phys. Chem. C* **2009,** *113* (1), 74-80.

Senthil Kumar, P.; Pastoriza-Santos, I.; Rodríguez-González, B.; Javier García de Abajo, F.; Liz-Marzán, L. M., High-yield synthesis and optical response of gold nanostars. *Nanotechnology* **2007,** *19* (1), 015606.

Shi, R.; Liu, X.; Ying, Y., Facing Challenges in Real-Life Application of Surface-Enhanced Raman Scattering: Design and Nanofabrication of Surface-Enhanced Raman Scattering

Substrates for Rapid Field Test of Food Contaminants. *J. Agric. Food. Chem.* **2018,** *66* (26), 6525-6543.

Siró, I.; Plackett, D., Microfibrillated cellulose and new nanocomposite materials: a review. *Cellulose* **2010,** *17* (3), 459-494.

Skrabalak, S. E.; Au, L.; Li, X.; Xia, Y., Facile synthesis of Ag nanocubes and Au nanocages. *Nat. Protoc.* **2007,** *2* (9), 2182-2190.

Soni, B.; Hassan, E. B.; Mahmoud, B., Chemical isolation and characterization of different cellulose nanofibers from cotton stalks. *Carbohydr. Polym.* **2015,** *134*, 581-589.

Stiles, P. L.; Dieringer, J. A.; Shah, N. C.; Duyne, R. P. V., Surface-Enhanced Raman Spectroscopy. *Annu. Rev. Anal. Chem.* **2008,** *1* (1), 601-626.

Sudova, E.; Machova, J.; Svobodova, Z.; Vesely, T., Negative effects of malachite green and possibilities of its replacement in the treatment of fish eggs and fish: a review. *Vet. Med.* **2007,** *52* (12), 527-539.

Tan, E.-Z.; Yin, P.-G.; You, T.-t.; Wang, H.; Guo, L., Three Dimensional Design of Large-Scale TiO2 Nanorods Scaffold Decorated by Silver Nanoparticles as SERS Sensor for Ultrasensitive Malachite Green Detection. *ACS Appl. Mater. Interfaces* **2012,** *4* (7), 3432-3437.

Tantra, R.; Brown, R. J. C.; Milton, M. J. T., Strategy to improve the reproducibility of colloidal SERS. *J. Raman Spectrosc.* **2007,** *38* (11), 1469-1479.

Tao, A.; Kim, F.; Hess, C.; Goldberger, J.; He, R.; Sun, Y.; Xia, Y.; Yang, P., Langmuir−Blodgett Silver Nanowire Monolayers for Molecular Sensing Using Surface-Enhanced Raman Spectroscopy. *Nano Lett.* **2003,** *3* (9), 1229-1233.

Thanh, N. T. K.; Maclean, N.; Mahiddine, S., Mechanisms of Nucleation and Growth of Nanoparticles in Solution. *Chem. Rev.* **2014,** *114* (15), 7610-7630.

ThermoFisher Scientific Gemini handheld analyzer - Integrated Raman and FTIR for chemical and explosives ID. https://www.thermofisher.com/document-connect/document-connect.html?url=https%3A%2F%2Fassets.thermofisher.com%2FTFS-Assets%2FCAD%2Fbrochures%2Fgemini-analyzer-brochure.pdf&title=QnJvY2h1cmU6IEdlbWluaSBIYW5kaGVsZCAgQW5hbHl6ZXI= (accessed April 19, 2020).

ThermoFisher Scientific. FirstDefender RMX Handheld Chemical Identification. https://www.thermofisher.com/order/catalog/product/FIRSTDEFENDERRMX?SID=srch-srp-FIRSTDEFENDERRMX#/FIRSTDEFENDERRMX?SID=srch-srp-FIRSTDEFENDERRMX (accessed April 19, 2020).

ThermoFisher Scientific. Gemini Analyzer https://www.thermofisher.com/order/catalog/product/GEMINI?SID=srch-srp-GEMINI#/GEMINI?SID=srch-srp-GEMINI (accessed April 19, 2020).

ThermoFisher Scientific. TruNarc Handheld Narcotics Analyzer. https://www.thermofisher.com/order/catalog/product/TRUNARC?SID=srch-srp-TRUNARC#/TRUNARC?SID=srch-srp-TRUNARC (accessed April 19, 2020).

ThermoFisher Scientific. TruScan RM Handheld Raman Analyzer. https://www.thermofisher.com/order/catalog/product/TRUSCANRM#/TRUSCANRM (accessed April 19, 2020).

Tian, F.; Bonnier, F.; Casey, A.; Shanahan, A. E.; Byrne, H. J., Surface enhanced Raman scattering with gold nanoparticles: effect of particle shape. *Anal. Methods* **2014,** *6* (22), 9116-9123.

Torul, H.; Çiftçi, H.; Çetin, D.; Suludere, Z.; Boyacı, I. H.; Tamer, U., Paper membrane-based SERS platform for the determination of glucose in blood samples. *Anal. Bioanal. Chem.* **2015,** *407* (27), 8243-8251.

Tran, C. D., Subnanogram detection of dyes on filter paper by surface-enhanced Raman scattering spectrometry. *Anal. Chem.* **1984,** *56* (4), 824-826.

Uddin, K. M. A.; Arcot Raghupathi, L.; Liljeström, A.; Chen, X.; Rojas, O. J.; Laine, J., Silver nanoparticle synthesis mediated by carboxylated cellulose nanocrystals. *Green Mater.* **2014,** *2* (4), 183-192.

USDA Pesticide Data Program Annual Summary, Calendar Year 2017. United States Department of Agriculture: 2017. https://www.ams.usda.gov/sites/default/files/media/2017PDPAnnualSummary.pdf (accessed March 31, 2019).

USEPA EPA reregistration eligibility decision thiabendazole. United States Environmental Protection Agency: 2002. https://archive.epa.gov/pesticides/reregistration/web/pdf/thiabendazole_red.pdf (accessed March 31, 2019).

Valley, N.; Greeneltch, N.; Van Duyne, R. P.; Schatz, G. C., A Look at the Origin and Magnitude of the Chemical Contribution to the Enhancement Mechanism of Surface-Enhanced Raman Spectroscopy (SERS): Theory and Experiment. *J. Phys. Chem. Lett.* **2013,** *4* (16), 2599-2604.

Van Rie, J.; Thielemans, W., Cellulose–gold nanoparticle hybrid materials. *Nanoscale* **2017,** *9* (25), 8525-8554.

Vander Ende, E.; Bourgeois, M. R.; Henry, A.-I.; Chávez, J. L.; Krabacher, R.; Schatz, G. C.; Van Duyne, R. P., Physicochemical Trapping of Neurotransmitters in Polymer-Mediated Gold

Nanoparticle Aggregates for Surface-Enhanced Raman Spectroscopy. *Anal. Chem.* **2019,** *91* (15), 9554-9562.

Villarreal, E.; Li, G. G.; Zhang, Q.; Fu, X.; Wang, H., Nanoscale Surface Curvature Effects on Ligand–Nanoparticle Interactions: A Plasmon-Enhanced Spectroscopic Study of Thiolated Ligand Adsorption, Desorption, and Exchange on Gold Nanoparticles. *Nano Lett.* **2017,** *17* (7), 4443-4452.

Vo-Dinh, T.; Hiromoto, M. Y. K.; Begun, G. M.; Moody, R. L., Surface-enhanced Raman spectrometry for trace organic analysis. *Anal. Chem.* **1984,** *56* (9), 1667-1670.

Vo-Dinh, T.; Uziel, M.; Morrison, A. L., Surface-Enhanced Raman Analysis of Benzo[A]Pyrene-DNA Adducts on Silver-Coated Cellulose Substrates. *Appl. Spectrosc.* **1987,** *41* (4), 605-610.

VWR. NanoRam Handheld RAMAN System, B&W Tek. https://ca.vwr.com/store/product/en/13244534/nanoram-handheld-raman-system-b-w-tek (accessed April 18, 2020).

Webb, J. A.; Erwin, W. R.; Zarick, H. F.; Aufrecht, J.; Manning, H. W.; Lang, M. J.; Pint, C. L.; Bardhan, R., Geometry-Dependent Plasmonic Tunability and Photothermal Characteristics of Multibranched Gold Nanoantennas. *J. Phys. Chem. C* **2014,** *118* (7), 3696-3707.

Wei, H.; Hossein Abtahi, S. M.; Vikesland, P. J., Plasmonic colorimetric and SERS sensors for environmental analysis. *Environ. Sci.: Nano* **2015,** *2* (2), 120-135.

White, I. M., Optofluidic SERS on inkjet-fabricated paper-based substrates. In *Integrated Optics: Devices, Materials, and Technologies Xvi*, Broquin, J. E.; Conti, G. N., Eds. 2012; Vol. 8264.

Willets, K. A.; Van Duyne, R. P., Localized surface plasmon resonance spectroscopy and sensing. *Annu. Rev. Phys. Chem.* **2007,** *58*, 267-97.

Wu, C.-N.; Fuh, S.-C.; Lin, S.-P.; Lin, Y.-Y.; Chen, H.-Y.; Liu, J.-M.; Cheng, K.-C., TEMPO-Oxidized Bacterial Cellulose Pellicle with Silver Nanoparticles for Wound Dressing. *Biomacromolecules* **2018,** *19* (2), 544-554.

Wu, X.; Lu, C.; Zhou, Z.; Yuan, G.; Xiong, R.; Zhang, X., Green synthesis and formation mechanism of cellulose nanocrystal-supported gold nanoparticles with enhanced catalytic performance. *Environ. Sci.: Nano* **2014,** *1* (1), 71-79.

Xi, W.; Haes, A. J., Elucidation of HEPES Affinity to and Structure on Gold Nanostars. *J. Am. Chem. Soc.* **2019,** *141* (9), 4034-4042.

Xia, Y.; Halas, N. J., Shape-Controlled Synthesis and Surface Plasmonic Properties of Metallic Nanostructures. *MRS Bull.* **2011,** *30* (5), 338-348.

Xiao, G.; Li, Y.; Shi, W.; Shen, L.; Chen, Q.; Huang, L., Highly sensitive, reproducible and stable SERS substrate based on reduced graphene oxide/silver nanoparticles coated weighing paper. *Appl. Surf. Sci.* **2017,** *404*, 334-341.

Xie, J.; Lee, J. Y.; Wang, D. I. C., Seedless, Surfactantless, High-Yield Synthesis of Branched Gold Nanocrystals in HEPES Buffer Solution. *Chem. Mater.* **2007,** *19* (11), 2823-2830.

Xiong, Z.; Lin, M.; Lin, H.; Huang, M., Facile synthesis of cellulose nanofiber nanocomposite as a SERS substrate for detection of thiram in juice. *Carbohydr. Polym.* **2018,** *189*, 79-86.

Xu, K.-X.; Guo, M.-H.; Huang, Y.-P.; Li, X.-D.; Sun, J.-J., Rapid and sensitive detection of malachite green in aquaculture water by electrochemical preconcentration and surface-enhanced Raman scattering. *Talanta* **2018,** *180*, 383-388.

Yaffe, N. R.; Ingram, A.; Graham, D.; Blanch, E. W., A multi-component optimisation of experimental parameters for maximising SERS enhancements. *J. Raman Spectrosc.* **2010,** *41* (6), 618-623.

Yang, L.; Qin, X.; Jiang, X.; Gong, M.; Yin, D.; Zhang, Y.; Zhao, B., SERS investigation of ciprofloxacin drug molecules on TiO2 nanoparticles. *PCCP* **2015,** *17* (27), 17809-17815.

Yu, L.; Lin, J.; Tian, F.; Li, X.; Bian, F.; Wang, J., Cellulose nanofibrils generated from jute fibers with tunable polymorphs and crystallinity. *J. Mater. Chem. A* **2014,** *2* (18), 6402-6411.

Yu, W. W.; White, I. M., Chromatographic separation and detection of target analytes from complex samples using inkjet printed SERS substrates. *Analyst* **2013,** *138* (13), 3679-3686.

Yu, W. W.; White, I. M., Inkjet-printed paper-based SERS dipsticks and swabs for trace chemical detection. *Analyst* **2013,** *138* (4), 1020-1025.

Yu, W. W.; White, I. M., Inkjet Printed Surface Enhanced Raman Spectroscopy Array on Cellulose Paper. *Anal. Chem.* **2010,** *82* (23), 9626-9630.

Yu, W. W.; White, I. M., Paper-based optofluidic SERS using ink-jet-printed substrates. In *Plasmonics in Biology and Medicine Viii*, VoDinh, T.; Lakowicz, J. R., Eds. 2011; Vol. 7911.

Yu, W. W.; White, I. M., A simple filter-based approach to surface enhanced Raman spectroscopy for trace chemical detection. *Analyst* **2012,** *137* (5), 1168-1173.

Yu, Y.; Zeng, P.; Yang, C.; Gong, J.; Liang, R.; Ou, Q.; Zhang, S., Gold-Nanorod-Coated Capillaries for the SERS-Based Detection of Thiram. *ACS Appl. Nano Mater.* **2019,** *2* (1), 598-606.

Yu, Z.; Grasso, M. F.; Sorensen, H. H.; Zhang, P., Ratiometric SERS detection of polycyclic aromatic hydrocarbons assisted by β-cyclodextrin-modified gold nanoparticles. *Microchim. Acta* **2019,** *186* (6), 391.

Yuan, H.; Khoury, C. G.; Hwang, H.; Wilson, C. M.; Grant, G. A.; Vo-Dinh, T., Gold nanostars: surfactant-free synthesis, 3D modelling, and two-photon photoluminescence imaging. *Nanotechnology* **2012,** *23* (7), 075102.

Yue, W.; Wang, Z.; Yang, Y.; Chen, L.; Syed, A.; Wong, K.; Wang, X., Electron-beam lithography of gold nanostructures for surface-enhanced Raman scattering. *J. Micromech. Microeng.* **2012,** *22* (12), 125007.

Zakrzewski, R., Determination of methimazole in urine with the iodine-azide detection system following its separation by reversed-phase high-performance liquid chromatography. *J. Chromatogr. B: Anal. Technol. Biomed. Life Sci.* **2008,** *869* (1-2), 67-74.

Zhang, K.; Ji, J.; Fang, X.; Yan, L.; Liu, B., Carbon nanotube/gold nanoparticle composite-coated membrane as a facile plasmon-enhanced interface for sensitive SERS sensing. *Analyst* **2015,** *140* (1), 134-139.

Zhang, K.; Shen, M.; Liu, H.; Shang, S.; Wang, D.; Liimatainen, H., Facile synthesis of palladium and gold nanoparticles by using dialdehyde nanocellulose as template and reducing agent. *Carbohydr. Polym.* **2018,** *186*, 132-139.

Zhang, L.; Li, X.; Ong, L.; Tabor, R. F.; Bowen, B. A.; Fernando, A. I.; Nilghaz, A.; Garnier, G.; Gras, S. L.; Wang, X.; Shen, W., Cellulose nanofibre textured SERS substrate. *Colloids Surf., A* **2015,** *468*, 309-314.

Zhang, S.; Xiong, R.; Mahmoud, M. A.; Quigley, E. N.; Chang, H.; El-Sayed, M.; Tsukruk, V. V., Dual-Excitation Nanocellulose Plasmonic Membranes for Molecular and Cellular SERS Detection. *ACS Appl. Mater. Interfaces* **2018,** *10* (21), 18380-18389.

Zhang, T.; Wang, W.; Zhang, D.; Zhang, X.; Ma, Y.; Zhou, Y.; Qi, L., Biotemplated Synthesis of Gold Nanoparticle–Bacteria Cellulose Nanofiber Nanocomposites and Their Application in Biosensing. *Adv. Funct. Mater.* **2010,** *20* (7), 1152-1160.

Zhao, J.; Lin, J.; Li, X.; Zhao, G.; Zhang, W., Silver nanoparticles deposited inverse opal film as a highly active and uniform SERS substrate. *Appl. Surf. Sci.* **2015,** *347*, 514-519.

Zhao, Y.; Tian, Y.; Ma, P.; Yu, A.; Zhang, H.; Chen, Y., Determination of melamine and malachite green by surface-enhanced Raman scattering spectroscopy using starch-coated silver nanoparticles as substrates. *Anal. Methods* **2015,** *7* (19), 8116-8122.

Zheng, J.; Pang, S.; Labuza, T. P.; He, L., Semi-quantification of surface-enhanced Raman scattering using a handheld Raman spectrometer: a feasibility study. *Analyst* **2013,** *138* (23), 7075-7078.

Zhu, C.; Soldatov, A.; Mathew, A. P., Advanced microscopy and spectroscopy reveal the adsorption and clustering of Cu(ii) onto TEMPO-oxidized cellulose nanofibers. *Nanoscale* **2017,** *9* (22), 7419-7428.

Ziegler, C.; Eychmüller, A., Seeded Growth Synthesis of Uniform Gold Nanoparticles with Diameters of 15−300 nm. *J. Phys. Chem. C* **2011,** *115* (11), 4502-4506.

Zong, C.; Xu, M.; Xu, L.-J.; Wei, T.; Ma, X.; Zheng, X.-S.; Hu, R.; Ren, B., Surface-Enhanced Raman Spectroscopy for Bioanalysis: Reliability and Challenges. *Chem. Rev.* **2018,** *118* (10), 4946-4980.